Taking Magnetic Resonance into Industrial Applications

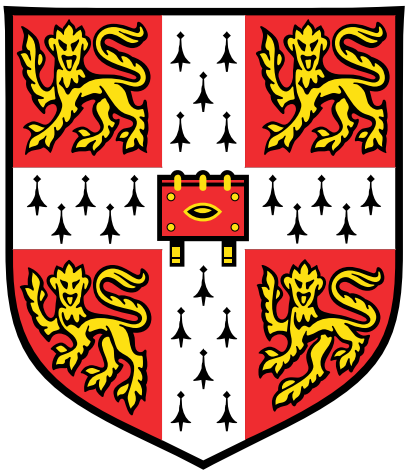

Thomas Whitney Blythe

Darwin College

This dissertation is submitted for the degree of

Doctor of Philosophy

July 2017

Magnetic Resonance Research Centre

Department of Chemical Engineering and Biotechnology

University of Cambridge

Taking Magnetic Resonance into Industrial Applications

Thomas Whitney Blythe

Magnetic resonance (MR) is a highly versatile technique with great potential for use in industrial applications; from the *in situ* study of unit operations to the optimisation of product properties. This thesis, concerned with the latter, is divided into two parts.

Firstly, dynamic MR is applied to characterise the flow behaviour, or rheology, of process fluids. Such characterisation is typically performed using conventional rheometry methods operating offline, with an online, or inline, method sought for process control and optimisation. Until recently, MR was an unlikely choice for this application due to the requirement of high-field MR hardware. However, recent developments in low-field MR hardware mean that the potential of MR in such applications can now be realised. Since the implementation of MR flow imaging is challenging on low-field MR hardware, two new approaches to MR rheometry are described using pulsed field gradient (PFG) MR. A cumulant analysis of the PFG MR signal is first used to characterise the rheology of model power-law fluids, namely xanthan gum-in-water solutions, accurate to within 5% of conventional rheometry, the data being acquired in only 6% of the time required when using MR flow imaging. The second approach utilises a Bayesian analysis of the PFG MR signal to characterise the rheology of model Herschel–Bulkley fluids, namely Carbopol 940-in-water solutions; data are acquired in only 12% of the time required for analysis using MR flow imaging. The suitability of the Bayesian MR approach to study process fluids is demonstrated through experimental study on an alumina-in-acetic acid slurry used by Johnson Matthey.

Secondly, MR imaging is used to provide insights into the origins and mechanisms of colloidal gel collapse. Many industrial products are colloidal gels, a space-spanning network of attractive particles with a yield stress. Colloidal gels are, however, known to undergo gravitational collapse after a latency period, thus limiting the shelf-life of products. This remains poorly understood, with a more detailed understanding of both fundamental interest and practical importance. To this end, MR imaging is applied offline to investigate the phase behaviour of colloidal gels. In particular, a comparison of the simulated and experimental phase diagrams suggests gravitational gel collapse to be gravity-driven. Furthermore, measurement of the colloid volume fraction using MR imaging indicates the formation of clusters of colloids at the top of the samples. Whether such clusters initiate gravitational gel collapse is yield stress-dependent; the gravitational stress exerted by a cluster must be sufficient to yield the colloidal gel.

For my family and friends.

Declaration

This dissertation is the result of my own work and includes nothing which is the outcome of work done in collaboration except as specified in the text and Acknowledgements. The work described herein has not been submitted previously in part, or in whole, for any other degree, diploma or qualification. All research was performed at the Magnetic Resonance Research Centre in the Department of Chemical Engineering and Biotechnology, University of Cambridge, between October 2012 and March 2017. This dissertation contains not more than 65 000 words.

Thomas Whitney Blythe
July 2017

Acknowledgements

Firstly, I would like to thank my supervisor, Professor Lynn Gladden, for presenting me with the opportunity to study at the Magnetic Resonance Research Centre (MRRC) and for providing me with continuous support and advice. The guidance of Dr Andrew Sederman has been invaluable, whilst not forgetting the efforts of Dr Jonathan Mitchell during my formative years. I would also like to take this opportunity to express my gratitude to colleagues at the MRRC—particularly Luke Baker, Mohamed Ainte, and Dr Nicholas Ramskill—for many helpful discussions and for their assistance with both data acquisition and processing.

Secondly, I am indebted to my industrial supervisors, namely Professor Hugh Stitt and Dr Andrew York of Johnson Matthey (JM), for providing great insights into the rheological characterisation of process fluids and for the supply of alumina-in-acetic acid slurry investigated in Chapter 6. Dr Simon Butler of the University of Cambridge is thanked for the provision of and assistance with the conventional rheometry measurements described in Chapters 3 to 6. Also acknowledged are Professor Wilson Poon and Dr Michiel Hermes of the University of Edinburgh for many helpful discussions and assistance with gravitational gel collapse, specifically the visual observations and molecular dynamics simulations described in Chapter 7. Dr Andrew Schofield is also acknowledged for synthesising the colloidal gels used in Chapters 7 and 8, and JM and the Engineering and Physical Sciences Research Council are thanked for financing this iCASE award studentship.

Finally, I would like to express gratitude to family and friends, both in Cambridge and elsewhere, for their continuous love, support, and guidance throughout my time in Cambridge. Most notably, I would like to thank mum, dad, Lauren, and my amazing grandparents, without whom this incredible adventure would never have been possible. I will forever be indebted to my wonderful partner, Rebecca, for moving to Cambridge without question and/or hesitation and for providing me with unwavering support and encouragement during our time in Cambridge. This is for you.

Publications

Work contained in this Thesis has been published in journal articles and presented at various conferences, as outlined below.

Journal articles

- Blythe, T.W., Sederman, A.J., Stitt, E.H., York, A.P.E., and Gladden, L.F., 2017, PFG NMR and Bayesian analysis to characterise non-Newtonian fluids. *J. Magn. Reson.*, **274**, 103-114.
- Harich, R., Blythe, T.W., Hermes, M., Zaccarelli, E., Sederman, A.J., Gladden, L.F., and Poon, W.C.K., 2016, Gravitational collapse of depletion-induced colloidal gels. *Soft Matter*, **12**, 4300-4308.
- Blythe, T.W., Sederman, A.J., Mitchell, J., Stitt, E.H., York, A.P.E., and Gladden, L.F., 2015, Characterising the rheology of non-Newtonian fluids using PFG NMR and cumulant analysis. *J. Magn. Reson.*, **255**, 122-132.

Conferences

- Blythe, T.W., Stitt, E.H., York, A.P.E., Sederman, A.J., and Gladden, L.F., Johnson Matthey Academic Conference. 8th-9th April 2015. Holywell Park, Loughborough University, Loughborough, GB. Oral presentation.
- Blythe, T.W., Gladden, L.F., Sederman, A.J., York, A.P.E., and Stitt, E.H., Johnson Matthey Academic Conference. 15th-16th April 2014. Holywell Park, Loughborough University, Loughborough, GB. Poster and flash presentation.
- Blythe, T.W., Gladden, L.F., Mitchell, J., Sederman, A.J., York, A.P.E., and Stitt, E.H., International Conference on Magnetic Resonance Microscopy. 25th-29th August 2013. Fitzwilliam College, University of Cambridge, Cambridge, GB. Poster presentation.
- Blythe, T.W., Gladden, L.F., Mitchell, J., and Stitt, E.H., Johnson Matthey Academic Conference. 16th-17th April 2013. Holywell Park, Loughborough University, Loughborough, GB. Poster presentation.

Contents

1 Introduction **1**

1.1 Applications of MR in chemical engineering 2

1.1.1 *In situ* study of unit operations 5

1.1.2 Optimisation of product properties 8

1.2 Rheological characterisation 12

1.3 Scope of thesis 19

1.4 References 22

2 Magnetic resonance theory **33**

2.1 Basic principles of MR 34

2.1.1 Nuclear spin and Zeeman splitting 34

2.1.2 Excitation, detection, and the rotating frame 36

2.1.3 Relaxometry 38

2.1.4 Echoes 42

2.1.5 Chemical shift 45

2.2 Principles of MR imaging 46

2.2.1 Image encoding and **k**-space 46

2.2.2 Slice selection 50

2.3 Dynamics and MR 52

2.3.1 Displacement encoding and **q**-space 52

2.3.2 Imaging **k**-space and **q**-space 55

2.4 Application of MR to complex fluids 57

2.4.1 Rheological characterisation 57
2.4.2 Colloidal dispersions 63
2.5 References 64

3 Characterising power-law fluids using cumulant analysis 71
3.1 Introduction 72
3.2 Model development 79
3.3 Materials and methods 86
3.3.1 Simulations 86
3.3.2 Experimental 87
3.4 Results and discussion 92
3.4.1 Sensitivity to the flow behaviour index 92
3.4.2 Sensitivity to noisy data and reduced sampling 95
3.4.3 Experimental validation using MR 96
3.5 Conclusions 102
3.6 References 104

4 Extension to Herschel–Bulkley fluids 109
4.1 Introduction 110
4.2 Cumulant analysis 114
4.2.1 Model development 114
4.2.2 Simulations 119
4.2.3 Results and discussion 120
4.2.4 Conclusions 122
4.3 Bayesian analysis 123
4.3.1 Model development 123
4.3.2 Simulations 129
4.3.3 Results and discussion 130
4.3.4 Conclusions 133
4.4 Conclusions 133

4.5 References 135

5 Characterising Herschel–Bulkley fluids using Bayesian analysis 139

5.1 Introduction 140

5.2 Materials and methods 145

5.2.1 Simulations 145

5.2.2 Experimental 146

5.3 Results and discussion 149

5.3.1 Sensitivity to the Herschel–Bulkley parameters 149

5.3.2 Sensitivity to noisy data and reduced sampling 151

5.3.3 Experimental validation using MR 152

5.4 Conclusions 158

5.5 References 160

6 Case study: washcoating slurry 165

6.1 Introduction 166

6.2 Materials and methods 171

6.2.1 Simulations 171

6.2.2 Experimental 171

6.3 Results and discussion 175

6.3.1 Bayesian MR methods 175

6.3.2 Comparison with non-Bayesian MR methods 176

6.4 Conclusions 180

6.5 References 181

7 Gravitational collapse of depletion-induced colloidal gels 185

7.1 Introduction 186

7.2 Materials and methods 193

7.2.1 Simulations 193

7.2.2 Experimental 196

7.3 Results and discussion 201

7.3.1 Simulations . . . 201
7.3.2 Experimental . . . 204
7.4 Conclusions . . . 215
7.5 References . . . 216

8 On the stability of colloidal gels using MR 221
8.1 Introduction . . . 222
8.2 Materials and methods . . . 226
8.2.1 Materials and experimental set-up . . . 226
8.2.2 Magnetic resonance . . . 227
8.3 Results and discussion . . . 228
8.3.1 Time-dependent interface height . . . 229
8.3.2 Volume fraction . . . 233
8.3.3 The origins of gravitational gel collapse . . . 242
8.4 Conclusions . . . 244
8.5 References . . . 246

9 Conclusions and future work 251
9.1 Conclusions . . . 252
9.2 Future work . . . 256
9.3 References . . . 258

Nomenclature

Roman symbols

A	area	m^2
$\mathbf{a}$	acceleration vector	$\mathrm{m\,s}^{-2}$
a	Arrhenius parameter	$\mathrm{Pa\,s}$
a_G	acceleration due to gravity	$\mathrm{m\,s}^{-2}$
$\mathbf{B}$	magnetic field vector	T
B	magnetic field strength	T
b	Arrhenius parameter	K
b_2	reduced second virial coefficient	-
C	Cross time constant	s
c	Richardson and Zaki parameter	-
$\mathbf{D}$	self-diffusion tensor	$\mathrm{m}^2\,\mathrm{s}^{-1}$
D	self-diffusion coefficient	$\mathrm{m}^2\,\mathrm{s}^{-1}$
d	diameter	m
E	energy	J
e	noise	-
$\mathbf{F}$	force vector	N
F	force	N
f	noise-free signal intensity	a.u.
$\mathbf{G}$	spatial encoding gradient vector	$\mathrm{T\,m}^{-1}$
G	spatial encoding gradient strength	$\mathrm{T\,m}^{-1}$

$\mathbf{g}$	flow encoding gradient vector	$\mathrm{T\,m^{-1}}$
g	flow encoding gradient strength	$\mathrm{T\,m^{-1}}$
H	height	m
h	Planck's constant	J s
I	spin quantum number	-
i	index	-
j	index	-
K	consistency factor	$\mathrm{Pa\,s}^n$
$\mathbf{k}$	reciprocal space vector	$\mathrm{m^{-1}}$
$\mathbf{k}_0$	kernel matrix	-
k	Boltzmann's constant	$\mathrm{J\,K^{-1}}$
k_0	kernel	-
$\mathbf{L}$	smoothness criterion operator	-
L	length	m
l	hydrodynamic entrance length	m
$\mathbf{M}$	net magnetisation vector	T
M	net magnetisation	T
M_w	molecular weight	$\mathrm{kg\,mol^{-1}}$
m	Cross rate constant	-
m_I	magnetic quantum number	-
N	number	-
n	flow behaviour index	-
O	dimensionless yield stress parameter	-
o	Merkak parameter	-
P	pressure	Pa
p	probability	-
Q	goodness-of-fit parameter	-
$\mathbf{q}$	reciprocal displacement vector	$\mathrm{m^{-1}}$

q	reciprocal displacement scalar	m^{-1}
$\mathbf{R}$	displacement vector	m
R	radius	m
$\mathbf{r}$	position vector	m
r	radial position or separation	m
r_0	radial position corresponding to τ_0	m
$\mathbf{S}$	signal intensity vector	a.u.
S	signal intensity	a.u.
s	gamma function parameter	-
T	temperature	K
T_1	spin-lattice relaxation time	s
T_2	true spin-spin relaxation time	s
T_2^*	apparent spin-spin relaxation time	s
T_2'	inhomogeneity-related spin-spin relaxation time	s
T_{str}	characteristic time constant	s
t	time	s
U	depletion potential	J
u	Kobelev and Schweizer parameter	Pa
V	volume	m^3
$\dot{V}$	volumetric flow rate	$\mathrm{m}^3\,\mathrm{s}^{-1}$
$\mathbf{v}$	velocity vector	$\mathrm{m}\,\mathrm{s}^{-1}$
v	velocity	$\mathrm{m}\,\mathrm{s}^{-1}$
W	isothermal compressibility	Pa^{-1}
$\mathbf{w}$	solution vector	-
w	probability (on logarithmic scale)	-
X	Chilton and Stainsby or Lekkerkerker parameter	-
x	x-position or direction	m
Y	Chilton and Stainsby or Lekkerkerker parameter	-

y	y-position or direction	m
$\hat{y}$	experimental observations	-
Z	Chilton and Stainsby or Lekkerkerker parameter	-
z	z-position or direction	m

Greek symbols

α	smoothing parameter	-
β	stretching exponent	-
γ	gyromagnetic ratio	$\mathrm{rad\,s^{-1}\,T^{-1}}$
$\dot{\gamma}$	shear rate	$\mathrm{s^{-1}}$
Δ	flow contrast time	s
δ	flow encoding gradient duration	s
ϵ	attraction strength	J
ε	Kobelev and Schweizer parameter	-
ζ	fluid displacement	m
η	shear viscosity	Pa s
η_0	zero-shear viscosity	Pa s
η_∞	infinite-shear viscosity	Pa s
Θ	hypothesis	-
θ	angle	rad
ι	Chilton and Stainsby or Lekkerkerker parameter	-
κ_j	j^{th} cumulant	m^j
Λ	ratio of ζ to L	-
λ	expected value	a.u.
μ_j	j^{th} moment	-
ν	cyclic frequency	Hz
Ξ	ratio of r to R_o	-
ξ	ratio of $2R_\mathrm{g}$ to d	-
ρ	density	-

σ	standard deviation of the noise	a.u.
τ	shear stress	Pa
τ_0	yield stress	Pa
Υ	ratio of R_i to R_o	-
υ	degrees of freedom	-
Φ	volume fraction	-
ϕ	phase shift	rad
χ	Kobelev and Schweizer parameter	-
χ^2	sum of squared residuals	a.u.
Ψ	Kilfoil parameter	-
ψ	ratio of Φ_P to $\Phi_\mathrm{P}^\mathrm{free}$	-
Ω	angular frequency	$\mathrm{rad\,s^{-1}}$
ω	Larmor frequency	$\mathrm{rad\,s^{-1}}$

Superscripts

final	final (infinite time)
free	in the free volume
glass	at the glass transition line
perc	at the percolation line
rcp	at random close packing

Subscripts

a	apparent
c	critical
D	drag
d	dwell
G	gravitational
g	gyration
H	hindered
h	homospoil gradient

i	inner or input
inc	increment
l	latency
max	maximum
o	outer or output
P	polymer
p	phase gradient
pulse	pulse
r	read gradient
ref	reference
S	solvent
s	slice gradient
store	store
t	tube
w	wall

Other symbols

Γ	gamma function
$\Im$	imaginary component
∞	infinity
$\int$	integration
$\langle ... \rangle$	average
$\lvert ... \rvert$	absolute value (modulus)
$\mathbb{E}$	expected value
$\prod$	product
$\Re$	real component
$\sum$	summation
$\{...\}$	set
J_0	modified zeroth order Bessel function of the first kind

Acronyms

1D, 2D, 3D	one-, two-, three-dimensional
AO	Asakura–Oosawa
APGSTE	alternating pulsed gradient stimulated echo
BD	Brownian dynamics
CFD	computational fluid dynamics
CPMG	Carr–Purcell Meiboom–Gill
CRT®	continuously regenerating trap
CSF®	catalysed soot filter
cCRT®	catalysed continuously regenerating trap
cDPF	catalysed diesel particulate filter
DOC	diesel oxidation catalyst
DPF	diesel particulate filter
ED	event-driven
ELCS	extended law of corresponding states
EPI	echo planar imaging
FID	free induction decay
FLASH	fast low angle shot
FOF	field-of-flow
FOV	field-of-view
HC	hydrocarbons
HI	hydrodynamic interactions
i.d.	inner diameter
JM	Johnson Matthey
LJ	Lennard–Jones
LLS	linear least squares
LNT	lean NO_x trap
MCT	mode coupling theory

MD	molecular dynamics
MR	magnetic resonance
NLLS	non-linear least squares
o.d.	outer diameter
PFG	pulsed field gradient
PGSE	pulsed gradient spin echo
PGSTE	pulsed gradient stimulated echo
PHSA	poly-12-hydroxystearic acid
PM	particulate matter
PMMA	poly(methyl methacrylate)
PS	polystyrene
PSD	particle size distribution
PTFE	polytetrafluoroethylene
PVC	polyvinyl chloride
RARE	rapid imaging with refocused echoes
RCP	random close packing
r.f.	radiofrequency
SCR	selective catalytic reduction
SCRF®	selective catalytic reducing filter
SNR	signal-to-noise ratio
SPI	single point imaging
SPRITE	single point ramped imaging with T_1 enhancement
SW	square-well
TOF	time-of-flight
VNR	velocity-to-noise ratio

Chapter 1

Introduction

In 1946, both Purcell *et al.* [1] and Bloch *et al.* [2] observed that certain nuclei, in the presence of an external magnetic field, could absorb and subsequently emit radiofrequency radiation; a phenomenon termed magnetic resonance (MR). Later, in 1950, Proctor and Yu [3] attracted the attention of the chemistry community when they observed that the resonant frequency of the emitting nuclei depends on their chemical environment. This attention was extended, in 1971, to the medical community when Damadian [4] reported the ability of MR to distinguish between the emitting nuclei of different tissues. In 1973, prompted by this work, Lauterbur [5] and Mansfield and Grannell [6] showed that, by application of a spatially-dependent external magnetic field, the position of different emitting nuclei, *i.e.* the different tissues, could be determined non-invasively; a process now known as MR imaging. Since those early days, MR techniques have established themselves in these communities; MR spectroscopy has developed into a multi-dimensional technique for analytical chemistry, enabling the elucidation of molecular structure and the study of chemical exchange [7], and MR imaging has revolutionised medical diagnosis, allowing the black box approach to medical diagnosis to be abandoned [8].

More recently, MR techniques have attracted the attention of the chemical engineering community, interested in probing unit operations—including mixing, reaction, and transport processes—and improving design and scientific understanding [9–11]. The structure of this Chapter is as follows. Firstly, a brief introduction to chemical engineering is provided. Secondly, the current applications of MR techniques to problems of relevance to chemical engineering, from the raw materials to the desired products, are reviewed. Finally, the concept of flow behaviour, or rheology, is introduced.

1.1 Applications of MR in chemical engineering

Chemical engineering is a multi-disciplinary subject that combines natural and experimental sciences with mathematics and economics to enable the design, development, and operation of industrial processes for converting raw materials to desired products. Figure 1.1, which attempts to put the major contributions to the subject of chemical engineering into perspective, shows that chemical engineering may be divided into three separate, though often interconnected, disciplines.

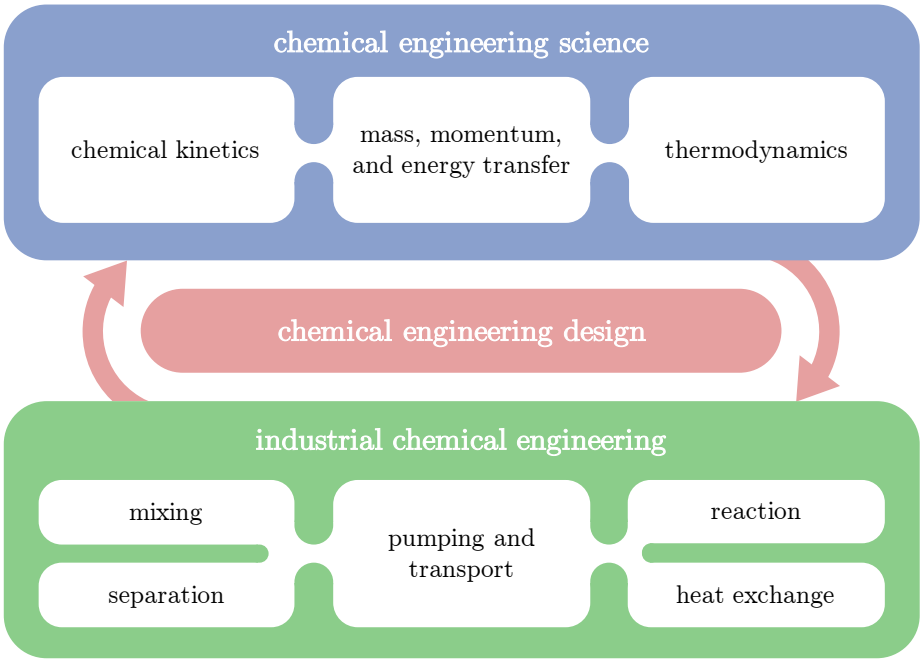

Fig. 1.1: A schematic of the major contributions to the subject of chemical engineering. Adapted from Mantle and Sederman [12].

The application of magnetic resonance (MR) to problems of relevance to the subject of chemical engineering has long been realised. In 1954, prompted by earlier work [13], Shoolery [14] predicted the use of MR spectroscopy as a tool to provide a non-invasive, real-time measurement of moisture content. Since those early days, and following the realisation of MR imaging, the capabilities of MR have expanded considerably. Although a detailed introduction to MR is provided in Chapter 2, a general introduction to the four main elements of MR—namely spectroscopy, relaxometry, imaging, and dynamics—is required before the applications of MR in chemical engineering can be reviewed.

MR involves the manipulation of nuclear spin, with spin a fundamental property of all sub-atomic particles. Following the application of a radiofrequency (r.f.) excitation pulse of appropriate frequency, signal is observed from the nucleus under study; often ^{1}H, ^{13}C, or ^{19}F. The frequency of the signal is sensitive to the local chemical environment, whilst its intensity is proportional to the nuclear spin density. MR spectroscopy is a quantitative technique used to differentiate between emitting nuclei in different chemical environments. For example, MR spectroscopy may be used to distinguish between ^{1}H in water (experiencing an O–H bond) and in oil (experiencing a C–H bond). Moreover, the signal following excitation will return to thermal equilibrium at a rate dependent upon the local physical environment. The study of signal relaxation, termed MR relaxometry and requiring the measurement of several relaxation constants, may be applied to differentiate between emitting nuclei in different physical environments. Lastly, through the application of a spatially-dependent external magnetic field, or a magnetic field gradient, the position of the emitting nuclei can also be determined non-invasively; a process known as MR imaging. The application of multiple magnetic field gradients may be used to study the motion of emitting nuclei, *i.e.* their displacements over a specified observation time, and hence their velocities. These measurements are referred to as dynamic MR and used to study both coherent and incoherent motion.

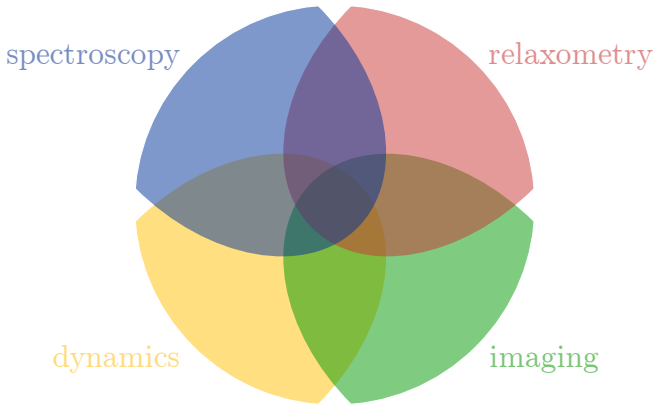

Fig. 1.2: The four main elements of MR and their combinations.

The toolkit of MR techniques is now available to chemical engineers, where they may be joined in almost any combination, as shown in Fig. 1.2, to probe length scales ranging from 10^{-10}–10^{0} m over time scales of 10^{-10}–10^{0} s. For example, dynamic MR is sensitive to molecular displacements in the range of 10^{-9}–10^{-4} m. The length and time scales associated with the four main MR techniques are summarised in Fig. 1.3. MR

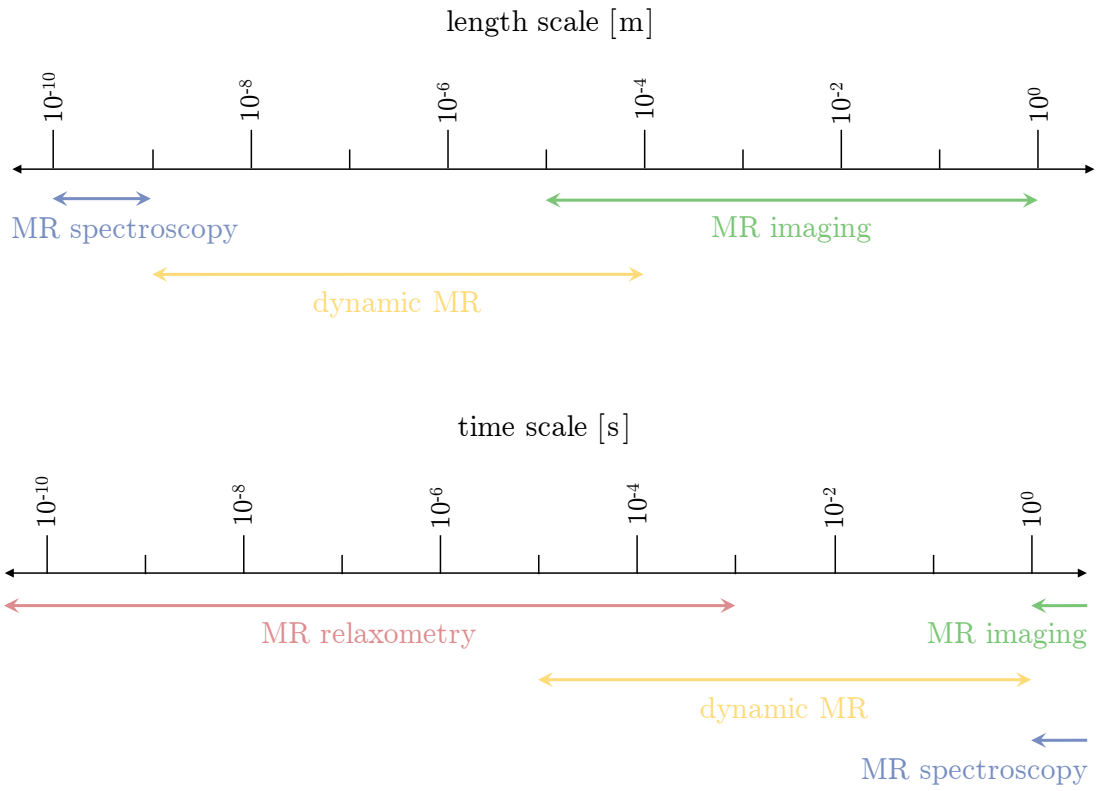

Fig. 1.3: A demonstration of the length and time scales associated with the four main elements of MR. Adapted from Callaghan [15].

techniques are, therefore, not restricted to the measurement of moisture content, but suitable for a wide range of industrial applications following two main themes [10]:

- ***In situ* study of unit operations.** MR techniques can be applied to industrial chemical engineering unit operations, such as mixing, to provide quantitative information *in situ*. This information can be used to improve chemical engineering science and enable the development or refinement of theoretical models.
- **Optimisation of product properties.** At the simplest level, MR techniques can be used online, or inline, for process control and optimisation, or offline to aid chemical engineering design by allowing the effect of the process parameters on the final product to be investigated.

The subject of the present thesis is the development of MR techniques for the optimisation of product properties. For completeness, and to provide a general introduction to the *in situ* study of unit operations, the application of the toolkit of MR techniques to problems of both main themes will now be reviewed.

1.1.1 *In situ* study of unit operations

Over recent years, the toolkit of MR techniques has successfully been applied to study many unit operations. These include, but are not limited to, reaction, heat exchange, transport, mixing, drying, and filtration [12]. In these unit operations, MR techniques have been applied to provide quantitative information *in situ* for the improvement of chemical engineering science. This section describes the application of MR techniques to three unit operations; namely reaction, mixing, and drying. For a more complete description, the interested reader is directed towards the review articles of Gladden [9,11] and Mantle and Sederman [12].

Reaction

Reactions represent one of the most popular areas of MR research, with many studies—including those involving continuous stirred tank, trickle bed, packed bed, and fluidised bed reactors—focused on the problem of scale-up, the process during which a laboratory invention becomes a successful commercial product [12]. The process of scale-up remains poorly understood due to the complex heat and mass transfer properties and chemical kinetics. Using MR it is possible to examine some of the issues associated with scale-up. In particular, the black box approach to reactor characterisation can be complemented with spatially-resolved measurements of conversion and selectivity by combining MR spectroscopy and MR imaging techniques. Furthermore, *operando* conditions, *i.e.* industrial temperatures and pressures, can now be achieved, enabling the detailed study of phase behaviour during operation [16]. Collectively, this information can be used for the development of theoretical scale-up models, or computational fluid dynamics (CFD) codes [17], to facilitate improved reactor design and enable reactor optimisation.

Mixing

Mixing may be defined as a reduction in inhomogeneity; the inhomogeneity may be one of concentration, phase, or temperature [18]. Traditionally, mixing has been achieved using batch stirred tank systems, agitated using specialised impeller designs [19]. However, owing to an increasing shift towards continuous processing [18], there has been recent interest in assessing the performance of inline static mixers to enable improved mixer design. In this application, dynamic MR imaging has successfully been used to

obtain spatially-resolved measurements of velocity and concentration and enable the identification of dead zones in the mixing geometry [20,21]. This information can be used for the validation of CFD codes [22], where validation has previously been difficult due to the complex mixing geometry, to improve static mixer design and enable an increased mixing efficiency.

Drying

Drying, the process during which a fluid is removed from a substance, plays an important role in a large number of industrial processes; including, but not limited to, the manufacture of diesel particulate filters (DPFs) in the automotive industry. Internal combustion engines, whether petrol or diesel fuel, produce a number of species harmful to both health and the environment. Although automotive manufacturers have optimised engine design to improve efficiency, aftertreatment systems are required, in the form of autocatalysts, for the abatement of harmful species and to ensure compliance with increasingly stringent emission limit legislation.

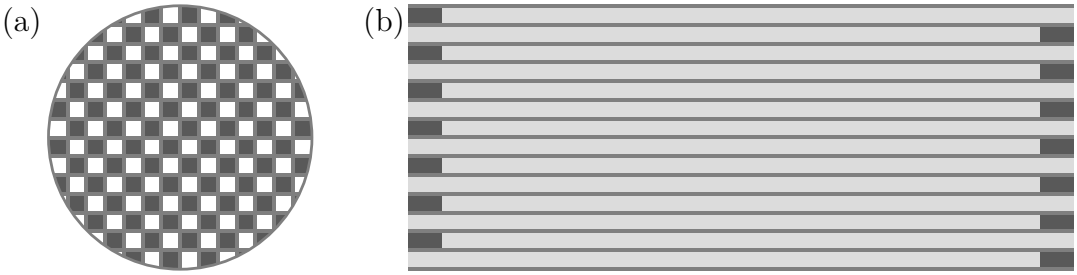

Fig. 1.4: Schematic representations of the (a) end and (b) side views of a DPF, showing the alternate plugged channels of the wall-flow monolith which force the exhaust gases to flow through the permeable wall.

At their simplest level, DPFs are bare, wall-flow ceramic monoliths, as depicted in Fig. 1.4, consisting of alternate permeable channels plugged at opposite ends. However, DPFs that incorporate a catalyst for the abatement of nitrogen oxides have also been developed [23]. The catalyst is applied, in the form of a washcoating solution or slurry, in a process termed washcoating [24]. During washcoating, the slurry—containing the catalyst, binder material, acid, and water [25]—is applied to the surface of the DPF and dried to remove the water content and deposit a layer of catalyst. The drying process is represented schematically in Fig. 1.5. Previous studies have indicated that non-ideal drying can be responsible for a non-uniform distribution of catalyst [24,26]. Traditional

techniques used for the monitoring of drying, including gravimetric methods and/or humidity and temperature measurements [27], are unable to provide sufficient insight into the drying mechanism. However, MR offers a non-invasive technique enabling the study of moisture content and mass transfer phenomena.

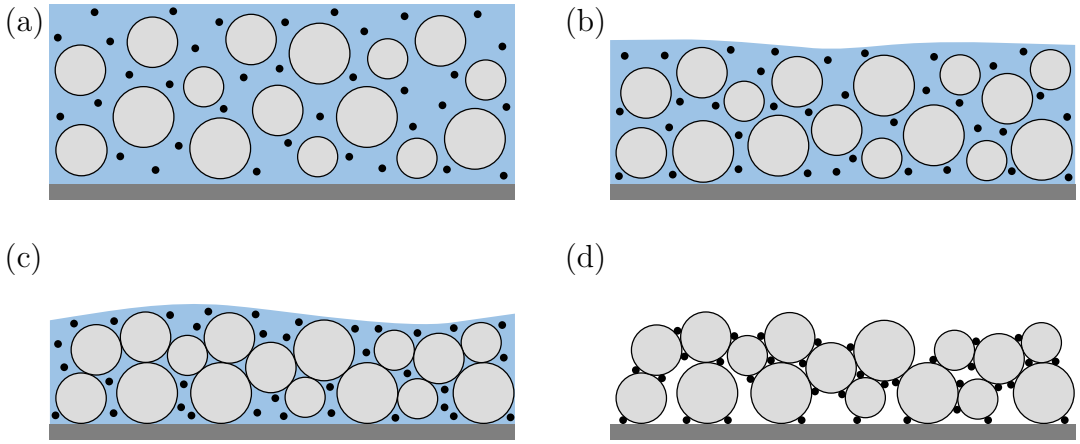

Fig. 1.5: A schematic representation of the drying process, showing the (○) catalyst, (●) binder, and (●) liquid on (●) the surface of the DPF. The four stages of drying are as follows: (a) the wet slurry is initially on the surface; (b) the first stage of drying, with the catalyst and binder suspended in the liquid; (c) the catalyst begins to coat the surface but the binder is still suspended; and (d) the final stage of drying, with the binder deposited at the interfaces between the catalyst. Adapted from Nijhuis *et al.* [24].

The characterisation of drying using MR was first reported by Gummerson *et al.* [28] in 1979. Since those early days, MR imaging has been used to study the drying mechanism in a flow-through monolith, consisting of impermeable, unplugged channels [29]. This work was extended by Ismagilov *et al.* [30] who observed the enrichment of the catalyst in the slurry layer at the surface of the monolith. Whilst, superficially, flow-through monoliths are similar to DPFs, the impermeable, unplugged channels of a flow-through monolith give rise to fundamentally different mass transfer characteristics. Ramskill *et al.* [31] compared the drying processes occurring within a DPF and a flow-through monolith, with such measurements used for the optimisation of drying and for the development of CFD codes. Furthermore, spatially-resolved measurements of velocity obtained using dynamic MR imaging were used to characterise the flow field through a DPF as a precursor to future work involving the *in situ* study of soot deposition, which has previously been shown to reduce performance [32–34].

1.1.2 Optimisation of product properties

The potential use of MR for the optimisation of product properties has been realised in a diverse range of industrial applications. For example, MR techniques have been used offline to enable the effect of process parameters on the final product to be investigated without compromising the structural integrity of the product. Alternatively, the online, or inline, use of MR techniques may provide information necessary for process control and optimisation and/or quality control; an advantage of MR is that it is non-invasive and can be applied to optically opaque samples. The application of the toolkit of MR techniques for the optimisation of product properties is now reviewed.

Offline

Over recent years, the offline application of MR techniques for the study of product properties has expanded considerably, motivated by a shift from hypothesis testing to generation [35]. For example, MR techniques have successfully been applied to study the structural inhomogeneities within composite tyre samples [36] and the marination process of chicken [37]. In this Section, the application of MR techniques to two major industries, namely the pharmaceutical and food industries, will be reviewed.

In the pharmaceutical industry, or, more generally, polymer science and technology, MR techniques have been used to examine the influence of processing parameters on the structural properties of drug release formulations and assess the performance of real product materials [10]. Since early work by Rajabi-Siahboomi *et al.* [38] and Hyde *et al.* [39,40], and following a shift in attention within the pharmaceutical community to medium-to-fast drug release formulations, MR imaging methods have been improved considerably, with quantitative, two-dimensional (2D) images of water and polymer concentration now routinely acquired, simultaneously, in several minutes [41,42]. Such images may be used for the study of water ingress and polymer egress during swelling and dissolution, a more detailed understanding of which is necessary for the development of theoretical models and the optimisation of formulation design [43].

In the food industry, MR has been used to investigate food stability, the prediction of which remains difficult due to the complexity of even the most simple foodstuffs, and crystallisation, which becomes important when partial melting occurs during handling or storage [10]. Consider, for example, the application of MR techniques for the study of food stability. Many food products—including whipped cream, butter, and cheese—are

Table 1.1: Types of colloidal dispersions. Adapted from Simoneau *et al.* [44].

dispersion medium	dispersed phase		
	gas	liquid	solid
gas	—	liquid aerosol *e.g.* fog, mist	solid aerosol *e.g.* smoke, dust
liquid	foam *e.g.* whipped cream	emulsion *e.g.* butter, cream	sol *e.g.* paint
solid	solid foam *e.g.* cakes, bread	gel *e.g.* cheese, gelatin	solid sol *e.g.* ruby glass

thermodynamically unstable, multiphase, colloidal dispersions. Colloidal dispersions, involving a dispersed phase sized between 10 nm and 1 µm distributed throughout a dispersion medium, encountered in the food industry and elsewhere are summarised in Table 1.1. Colloidal products typically exhibit a limited shelf-life; collisions between particles result from thermal and gravitational motion, the latter due to a difference in density between the dispersed phase and the dispersion medium, often responsible for flocculation or coalescence. Depending on the density difference between the dispersed phase and the dispersion medium, sedimentation or creaming may ensue.

Improved product design is necessary to enhance shelf-lives, requiring a more complete understanding of colloidal and interface science. To this end, MR has been applied to study the stability of various colloidal dispersions, including emulsions [45], suspensions [46], and foams [47]. Kauten *et al.* [48] used MR imaging to obtain one-dimensional (1D) measurements of the oil volume fraction in various oil-in-water emulsions, later extended to 2D by Pilhofer *et al.* [49], with the aim of model development and validation. For the study of water-in-oil emulsions, Balinov *et al.* [50] used dynamic MR to investigate the influence of ageing, volume fraction, and the addition of emulsifiers on the emulsion droplet size distribution. Emulsifiers are added to emulsions, where they absorb on to the interface between the dispersed phase and the dispersion medium, to provide increased stability. Demulsifiers, responsible for decreased emulsion stability, have also been investigated [51]. Further applications of MR techniques to emulsions include the study of flow behaviour [52], freezing [53], and the investigation of concentrated [54] and multiple emulsions, such as water-oil-water [55]. For a more comprehensive review of the application of MR to emulsions, or, more generally, the food industry, the interested reader is directed towards the review articles of Simoneau *et al.* [44] and Mariette [56].

Colloidal products are not unique to food, but ubiquitous in industry; from agriculture to oilfields. For example, dynamic MR has recently been used to select the ideal emulsifier for use in the oilfield industry [57]. Therefore, despite the progress currently being made in colloidal and interface science, more detailed experimental studies are still required to develop understanding and facilitate an improved product design, including, for example, the theory of the flow behaviour of colloidal dispersions [58] and the transient gelation in otherwise stable colloidal dispersions [59].

Online

Although the online, or inline, use of MR techniques for process control and optimisation was first proposed in 1954 [14], the requirement of large, high field strength superconducting magnet technology has restricted the use of MR to highly controlled and specialised environments. Moreover, so-called high-field MR hardware is expensive [60]. Over recent years, however, developments in small, low field strength permanent magnet technology have removed such restrictions. Furthermore, so-called low-field MR hardware is highly portable, inexpensive, and does not require cryogenic cooling. A summary of the magnetic field strengths associated with high-field and low-field MR is included in Fig. 1.6, shown complete with a high-field, 300 MHz Oxford Spectrospin Cryomagnet and a low-field, 2 MHz Oxford Instruments GeoSpec2.

The widespread availability of low-field MR has the potential to revolutionise process control and optimisation. However, whilst MR imaging is routinely used at high field strengths to perform spatially-resolved 2D or 3D measurements, the reduction in signal-to-noise ratio (SNR) at low field strengths makes such measurements problematic. To this end, recent research has focused on the development of robust, real-time MR techniques, requiring no calibration, ideally suited to low SNR, low-field MR applications [62]. For example, Osán *et al.* [63] exploited the sensitivity of MR relaxometry to fluid flow to provide a fast measurement of volumetric flow rate using low-field MR. Dalitz *et al.* [62] investigated the use of low-field MR for reaction monitoring, where MR spectroscopy enables the investigation of reaction processes in real-time. A further online, or inline, application now attracting significant interest is the characterisation of the flow behaviour, or rheology, of process fluids [64].

Consumers are familiar with the informal concept of thickness, often perceived as a measure of quality or concentration [65]; premium yoghurts are described as ‘thick and creamy’, whilst consumers are charged a premium for ‘thick’ bleach. Furthermore,

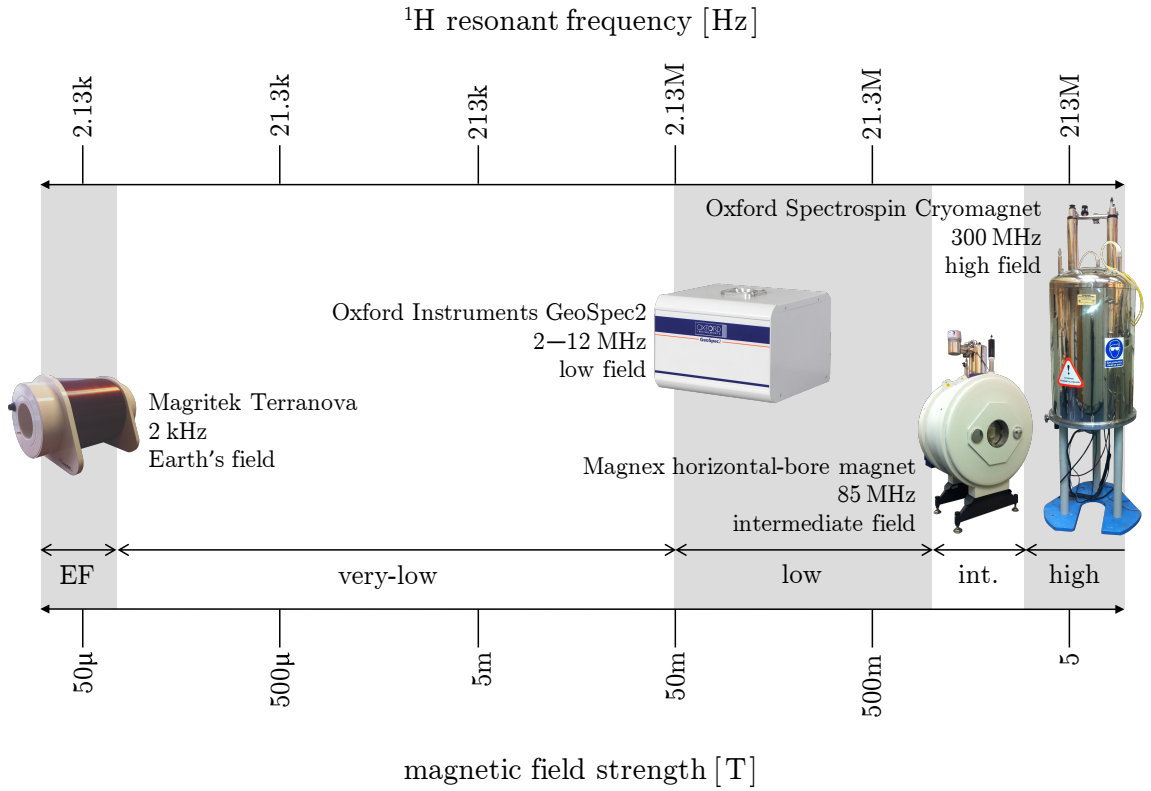

Fig. 1.6: Summary of magnetic field strengths, including photographs showing typical hardware encountered at those strengths. The ranges encompassing Earth's field (20–65 µT), very-low (65 µT–50 mT), low (50 mT–1 T), intermediate (1–3 T), and high-field (> 3 T) are indicated, with very-low a subsection of the low-field regime. Adapted from Mitchell *et al.* [61].

many industrial processes—including spraying, mixing, drying, and coating—are sensitive to the rheology of process fluids [66]. In Section 1.1.1, for example, the application of MR techniques to study the drying mechanism in the manufacture of a catalysed DPF was described. Whilst an improved understanding of the drying mechanism would ensure a uniform coating of catalyst on the surface of the DPF, the coating thickness is known to be sensitive to the rheology of the slurry. This may be influenced by the pH value of the slurry and the catalyst and/or binder concentration [67–69]. The optimisation of product properties therefore requires an accurate measurement of rheology.

The rheology of simple fluids is well understood; the linear relationship between shear stress and shear rate can be characterised by a single, temperature- and pressure-dependent shear viscosity, where an increase in shear viscosity represents an increase in the resistance of a fluid to flow. Furthermore, the shear viscosity of so-called New-

tonian fluids can be accurately characterised using conventional rheometry methods. However, a number of process fluids—from adhesives and polymers, to foodstuffs and paints—exhibit a non-linear relationship between shear stress and shear rate. Paint, for example, demonstrates a decrease in shear viscosity with an increase in shear rate. The rheology of so-called complex fluids is, therefore, of both practical and fundamental interest [70].

Complex fluids contain structures on the mesoscopic scale, between molecular and macroscopic and ranging from 10 nm to 10 µm, often referred to as microstructure [71]. The length scales associated with complex fluids, when compared to molecular dimensions, can lead to interactions between the flow field and microstructure. Therefore, changes in the flow field may induce changes in the microstructure which can, in turn, induce additional changes in the flow field [72]. Due to this coupling between the microstructure and flow field, complex fluids typically exhibit non-Newtonian behaviour including a shear dependence of shear viscosity (as described previously for paint) and viscoselasticity (both solid- and liquid-like behaviour). For many fluids, this non-linear behaviour can be described using a model relating shear stress and shear rate, however, the characterisation of such behaviour using conventional rheometry methods can be problematic due to flow heterogeneities and discontinuities which may arise during the measurement [73]. For a more complete introduction to complex fluids, the interested reader is directed towards the texts of Larson [70] and Gelbart and Ben-Shaul [71].

The potential application of high-field MR for the study of the rheology of complex fluids has long been realised [74]. Dynamic MR imaging has successfully been applied for the purpose of rheological characterisation and also for the study of shear banding, wall slip, and particle migration [72]. In contrast, applications of low-field MR for this purpose are limited [64]. Undoubtedly, low-field MR has the potential to revolutionise rheological characterisation in industrial applications—facilitating the transition from offline to online, or inline, characterisation—thus ensuring the optimisation of product properties through process control. For completeness, an introduction to rheological characterisation is provided in Section 1.2.

1.2 Rheological characterisation

The study of a fluid subjected to flow is termed rheology. Two different, though often interconnected, areas of rheology exist depending on whether the fluid under study is

subjected to shear or extensional flow. In shear flow, adjacent molecules move over or past each other, whereas in extensional flow, adjacent molecules move away from or towards each other. The difference between shear and extensional flow is demonstrated schematically in Fig. 1.7. This section aims to provide an introduction to shear flow, with the interested reader directed towards the comprehensive textbooks of Collyer and Clegg [66] and Barnes [75] for a more detailed description of extensional flow.

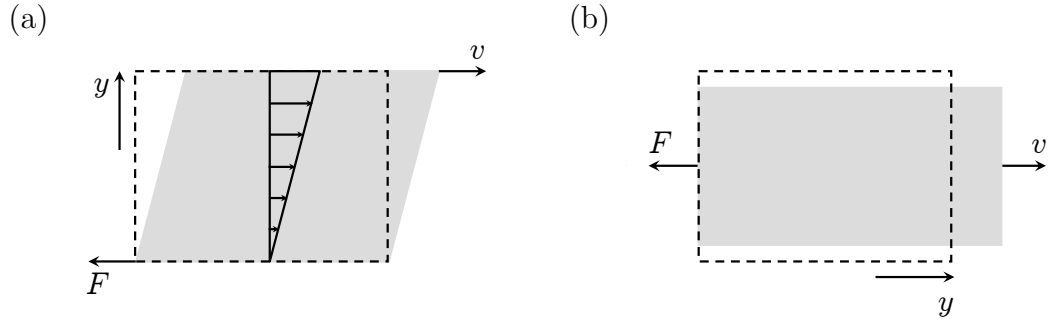

Fig. 1.7: A schematic representation of (a) shear and (b) extensional flow, where F is the force creating or created by the flow, of velocity v, and v is a function of position, y, from a fixed surface.

Figure 1.7(a) shows that the velocity, v, of a fluid under shear increases linearly with distance, y, from a fixed surface, with the gradient of velocity, termed shear rate and denoted $\dot{\gamma}$, given by v/y. The force per unit area corresponding to $\dot{\gamma}$, referred to as shear stress and denoted τ, is given by F/A, where A is the area over which the force is applied. Rheometry involves the characterisation of τ with respect to $\dot{\gamma}$, commonly referred to as the flow curve, where

$$\tau \propto \dot{\gamma}. \tag{1.1}$$

The characterisation of the flow curve using conventional rheometry methods can be achieved by measuring shear stress for a controlled shear rate, or, conversely, measuring shear rate for a controlled shear stress. Whilst a comparison of the advantages and disadvantages of controlled-rate and controlled-stress rheometry will not be provided here, the interested reader is directed towards the journal article of Brunn and Asoud [76]. In the following discussion, controlled-rate rheometry will be assumed.

Flow is resisted by internal friction, a result of molecular momentum transfer and intermolecular forces [77]. In gases, the contribution due to intermolecular forces is small, with internal friction dominated by molecular momentum transfer; the greater the molecular momentum transfer, the greater the internal friction. Conversely, intermolecular forces dominate the internal friction of liquids; the stronger the intermolecular forces between the molecules, the greater the internal friction. For example, polar molecules demonstrate a greater internal friction than non-polar molecules, although internal friction can also be affected by other factors, including the shape, size, and structure of the molecules [78]. Internal friction is also known to be affected by the microstructure [79]. To quantify internal friction, *i.e.* the resistance of a fluid to flow, Newton [80] introduced the concept of shear viscosity, denoted η, where

$$\eta = \frac{\tau}{\dot{\gamma}}. \tag{1.2}$$

Therefore, for a given shear stress, an increase in shear viscosity is responsible for a decrease in shear rate. Similarly, for a given shear rate, an increase in shear viscosity is responsible for an increase in shear stress. Shear viscosity information is required by process engineers for process control, while design engineers use shear viscosity information for process optimisation and the determination of dimensionless groups, such as Reynolds number [81]. For the case of a fluid demonstrating Newtonian rheology, shear viscosity is independent of shear rate and the flow curve can be characterised by a single shear viscosity, such that

$$\tau\left(\dot{\gamma}\right) = \eta\dot{\gamma}. \tag{1.3}$$

Examples of fluids demonstrating Newtonian rheology include water and glycerol. The shear viscosity of glycerol, on the order of 1 Pa s, is three orders of magnitude greater than that of water, which has a shear viscosity at room temperature of 1 mPa s. Glycerol is more viscous than water; the elongated shape of the polar glycerol molecules allow them to become entangled, increasing the resistance to flow.

Shear viscosity is independent of shear rate for only a small number of fluids; the shear viscosity of many fluids will increase or decrease with an increase in shear rate. The flow curves of these so-called non-Newtonian fluids cannot be accurately described

using Eq. (1.3), and therefore alternative expressions are required. Constitutive equations, or rheological equations of state, are relatively simple expressions that describe the flow curves of non-Newtonian fluids in terms of rheological parameters. These expressions, or models, may be empirical, theoretical, or based on a structural understanding [82]. A significant number of models have been developed to characterise the flow curves of many non-Newtonian fluids over a wide range of shear rates. For example, the Cross model [83] describes $\eta(\dot{\gamma})$ for a fluid whose shear viscosity decreases with increasing shear rate according to

$$\frac{\eta(\dot{\gamma}) - \eta_\infty}{\eta_0 - \eta_\infty} = \frac{1}{1 + (C\dot{\gamma})^m}, \tag{1.4}$$

where η_0 and η_∞ refer to the asymptotic values of shear viscosity at very low and very high shear rates, respectively, with C the Cross time constant and m a dimensionless Cross rate constant. Other popular models include, but are not limited to, the Carreau [84] and Carreau–Yasuda [85] models. Assuming $\eta \ll \eta_0$ and $\eta \gg \eta_\infty$, the Cross model simplifies to

$$\eta(\dot{\gamma}) = \frac{\eta_0}{(C\dot{\gamma})^m}, \tag{1.5}$$

which, with $K = \eta_0/C^m$ and $n = 1 - m$, reduces to the Ostwald–de Waele, or power-law, model [86]:

$$\eta(\dot{\gamma}) = K\dot{\gamma}^{n-1}, \tag{1.6}$$

or

$$\tau(\dot{\gamma}) = K\dot{\gamma}^n, \tag{1.7}$$

where K represents the consistency factor, which quantifies the shear viscosity of the

fluid at a shear rate of $1\,\mathrm{s}^{-1}$, and n is the dimensionless flow behaviour index. According to Eq. (1.7), the linear contributions to $\tau\left(\dot{\gamma}\right)$ for a power-law fluid are captured by K, whilst the non-linear contributions are captured by n. The non-linear contributions, shown in Fig. 1.8, may fall into one of three categories:

- $\boldsymbol{n = 1}$. Non-linear contributions to the shear stress response become zero and the shear viscosity becomes independent of the shear rate, *i.e.* Newtonian, with Eq. (1.7) reducing to Eq. (1.3).

- $\boldsymbol{n < 1}$. A decrease in shear viscosity with an increase in shear rate is known as shear-thinning, or pseudo-plastic, behaviour, corresponding to an n value of less than unity. The smaller the value of n, the greater the degree of shear-thinning behaviour. For the example shown in Fig. 1.8(b), $n = 0.5$ such that the shear viscosity decreases by one order of magnitude across an increase in shear rate of two orders of magnitude.

  Shear-thinning behaviour is often attributed to the alignment of molecules and/or particles with the direction of flow, deflocculation, or a temporary rearrangement of the microstructure in suspension and emulsion flow [87]. Examples of fluids that demonstrate such behaviour include mayonnaise and aqueous xanthan gum solution, with the latter investigated in Chapter 3.

- $\boldsymbol{n > 1}$. For a fluid demonstrating shear-thickening, or dilatant, behaviour, shear viscosity increases with increasing shear rate, corresponding to an n value greater than unity. The larger the value of n, the greater the degree of shear-thickening behaviour. For the example shown in Fig. 1.8(b), $n = 1.5$ such that the shear viscosity increases by one order of magnitude while the shear rate increases by two orders of magnitude.

  Although the mechanisms of shear-thickening behaviour remain unclear [88–92], it has been suggested that such behaviour will always be observed for concentrated suspensions, for example corn starch-in-water [93,94], across an appropriate range of shear rates; this range dependant upon phase volume, particle size and shape, and the shear viscosity of the continuous phase [95]. Shear-thickening behaviour will not be considered further in this thesis, with the interested reader directed towards the review articles of Barnes [95] and Brown and Jaeger [96] for more information.

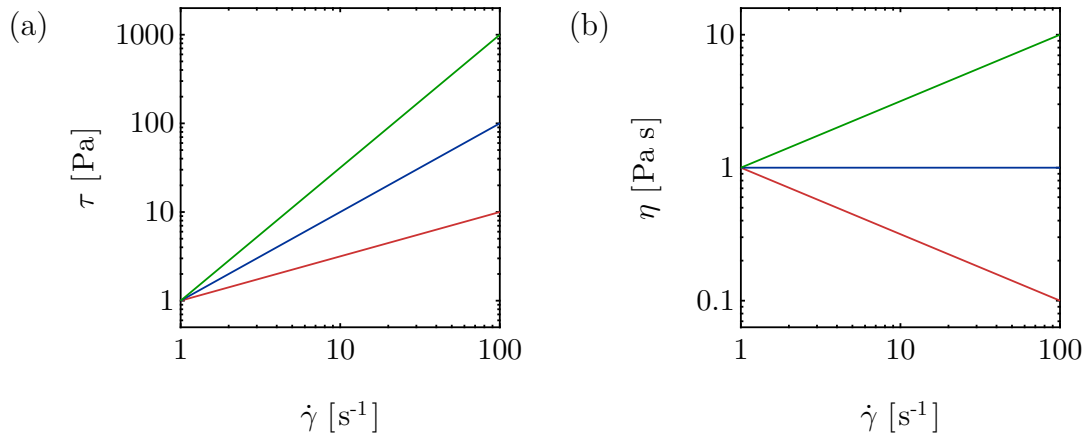

Fig. 1.8: Plots to show the relationship between shear rate and (a) shear stress and (b) shear viscosity for three example fluids demonstrating Newtonian and power-law behaviour; (—) $n = 1.0$, (—) $n = 0.5$, and (—) $n = 1.5$. The data were simulated across a shear rate range of 1–100 s^{-1} using Eqs. (1.2) to (1.7) with $K = 1\,\mathrm{Pa\,s}^{n}$.

If $\eta \ll \eta_0$ but $\eta \not\gg \eta_\infty$, the Cross model instead simplifies to the Sisko model [97]:

$$\eta\left(\dot{\gamma}\right) = \eta_\infty + \frac{\eta_0}{\left(C\dot{\gamma}\right)^m}, \tag{1.8}$$

which, with redefinition of the rheological parameters, reduces to the Herschel–Bulkley model [98]:

$$\tau\left(\dot{\gamma}\right) = \tau_0 + K\dot{\gamma}^n, \tag{1.9}$$

where τ_0 is the yield stress of the fluid under study, *i.e.* the stress at which the fluid begins to flow. Therefore, the fluid behaves as a solid below τ_0, such that $\dot{\gamma} = 0\,\mathrm{s}^{-1}$ for $\tau \leq \tau_0$, but a liquid above τ_0. Despite the controversial concept of τ_0 as a material property [99–102], it nevertheless provides a convenient way for engineers to model, or predict, flow behaviour for process design and operation [103]. Note that when $n = 1$, Eq. (1.9) simplifies to the Bingham model [104].

In industrial applications, a fluid may encounter a wide range of shear rates spanning up to twelve orders of magnitude; from 10^{-6}–$10^{-4}\,\mathrm{s}^{-1}$ during sedimentation up to 10^{5}–$10^{6}\,\mathrm{s}^{-1}$ during high-speed coating [75]. It is important to note that, in most cases,

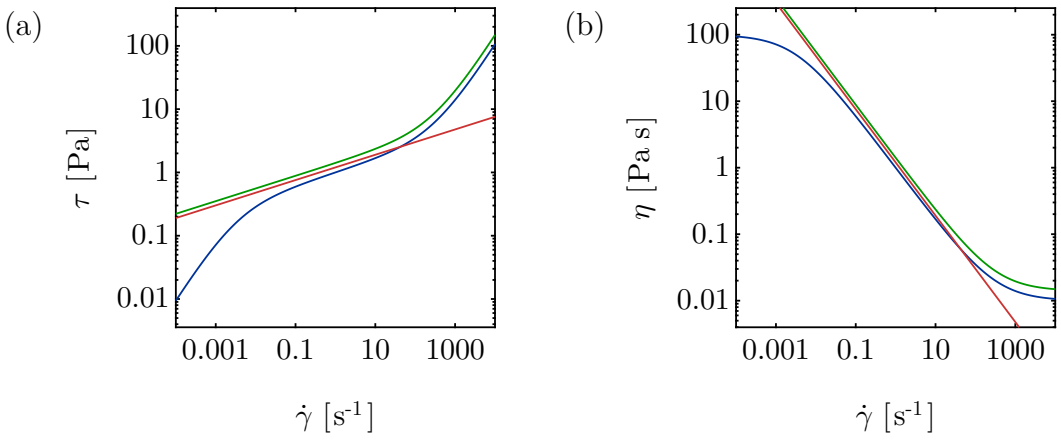

Fig. 1.9: Plots to show the relationship between shear rate and (a) shear stress and (b) shear viscosity for an example fluid; where $n = 0.2$, $\eta_0 = 100\,\mathrm{Pa\,s}$, $\eta_\infty = 0.01\,\mathrm{Pa\,s}$, and $K = 1\,\mathrm{Pa\,s}^n$. The data were simulated using (—) Cross, (—) power-law, and (—) Sisko models and have been vertically shifted for clarity.

constitutive equations are unable to accurately describe the rheology of a fluid over an infinite shear rate range. To demonstrate this, Fig. 1.9 compares the Cross, power-law, and Sisko models for an example fluid across a shear rate range of 10^{-4}–$10^{4}\,\mathrm{s}^{-1}$; a fluid whose rheology can be accurately described using the Cross model can be described using the power-law model over a finite shear rate range of only 0.1–$10\,\mathrm{s}^{-1}$. Caution must therefore be exercised to ensure that the rheology of the fluid under study, across the experimental shear rate range, can be accurately described using the selected rheological model. Large errors may ensue if the model is insufficient to accurately describe the rheology of the fluid under study, thus requiring a different model to be selected or the experimental procedure modified to adjust the range of shear rates investigated.

Aside from the variation of shear viscosity with shear rate, shear viscosity can, for a fixed shear rate, be affected by a number of factors, including:

- **Time.** The continuous decrease of shear viscosity with time, when flow is applied to a sample that was initially at rest, and the subsequent recovery, when the flow is discontinued, is called thixotropy [105]. Many suspensions and emulsions demonstrate thixotropic behaviour, including blood [106] and ice cream [107], with such behaviour often attributed to a temporary rearrangement of the microstructure [79]. A number of models have been developed to describe thixotropic behaviour, including, but not limited to, the Weltmann [108] and Tiu-Boger [109] models.

Although less common than thixotropy, an increase in shear viscosity with time can also occur, called anti-thixotropy, often due to temporary flocculation [79]. For a more complete discussion on thixotropy and anti-thixotropy, the interested reader is directed towards the general reviews of Mewis [110] and Barnes [87].

- **Temperature.** Shear viscosity decreases with an increase in temperature, often attributed to a decrease in the strength of the intermolecular forces with increasing volume. Such behaviour can be approximated, over a suitable temperature range, according to the Arrhenius relationship [111]:

$$\eta = a \exp\left[\frac{b}{T}\right], \tag{1.10}$$

where T is the absolute temperature of the fluid and a and b are constants dependant on the fluid under study, although other relationships have also been proposed [112]. For the case of water, at room temperature, a temperature fluctuation of $\pm 1\,^{\circ}\mathrm{C}$ is responsible for a change in shear viscosity of $\pm 3\%$ [75].

- **Pressure.** The shear viscosity of many fluids increases exponentially with increasing pressure due to an increase in the strength of the intermolecular forces with decreasing volume. Water, below a temperature of $33\,^{\circ}\mathrm{C}$, is an exception to this rule, with shear viscosity first decreasing with pressure before subsequently increasing [113]. Nevertheless, at (or near to) atmospheric pressure, any changes in shear viscosity are negligible [75].

In the present thesis, unless otherwise stated, isothermal and isobaric conditions are ensured to negate temperature- and pressure-dependent rheology, respectively. Note that only controlled-rate rheometry was considered in this discussion. Similar derivations may be performed for controlled-stress rheometry by using, for example, the Ellis model [114].

1.3 Scope of thesis

The aim of the present thesis is the development and application of MR techniques for the study of product properties, thus enabling accurate process control and optimisation or the development and refinement of theoretical models. Firstly, two acquisition

and processing strategies are developed to enable the online, or inline, rheological characterisation of process fluids in real-time using MR. The suitability of these strategies for the rheological characterisation of a real process fluid, as used by Johnson Matthey (JM) in the manufacture of catalysed DPFs (cDPFs), is considered. Secondly, MR is used to provide insight into the origins and mechanisms of colloidal gel collapse, which limits the shelf-life of many industrial products. To this end, this thesis is arranged as follows:

Chapter 2 provides an introduction into the background and theory of MR—including spectroscopy, relaxometry, imaging, and dynamics—using firstly a quantum mechanical description of spin behaviour before adopting vector notation. An overview of MR rheometry is also provided.

Chapter 3 describes the development of an approach using cumulant analysis and dynamic MR to enable the estimation of n describing the rheology of fluids demonstrating power-law rheology using only single-axis gradient hardware in a pipe flow geometry. Simulation experiments are performed to determine the minimum number of data points required to be sampled to ensure accurate parameter estimation, before experimental validation is performed on a model power-law fluid of xanthan gum-in-water using MR and conventional rheometry methods.

Chapter 4 extends the methodology developed in Chapter 3 to enable the rheological characterisation of Herschel–Bulkley fluids. Numerical simulation experiments indicate that cumulant analysis is unsuitable for use with Herschel–Bulkley fluids due to the interdependence between the Herschel–Bulkley rheological parameters. To this end, an alternative approach utilising Bayesian analysis is developed. Bayesian analysis is a probabilistic approach that does enable the unambiguous determination of the Herschel–Bulkley rheological parameters.

Chapter 5 uses the Bayesian analysis approach developed in Chapter 4. Numerical simulation experiments are performed to determine the minimum number of data points required to be sampled for accurate parameter estimation. Experimental validation is performed on a model Herschel–Bulkley fluid of Carbopol 940-in-water using MR and conventional rheometry methods.

Chapter 6 assesses the suitability of the methodologies developed in Chapters 4 and 5 to enable the study of a real process fluid provided by JM. The process fluid under study is an alumina-in-acetic acid washcoating slurry used in the manufacture of cDPFs. Conventional rheometry is used to characterise the rheology of this particle-

laden process fluid and characterisation is also performed using MR rheometry; namely MR flow imaging and Bayesian MR. An issue associated with the use of real, particle-laden process fluids is described.

Chapter 7 investigates the ageing and ultimate gravitational collapse of depletion-induced colloidal gels. The experimental state diagram obtained using visual observations is mapped onto a theoretical state diagram obtained from computer simulations and theoretical calculations, and the discrepancies between these two approaches are considered. To extend visual observations, MR imaging is applied to provide a quantitative, spatio-temporally resolved measurement of colloid volume fraction in these rapidly collapsing gels. MR imaging reveals that gravitational gel collapse is initiated by processes at the top of the sample.

Chapter 8 extends work described in Chapter 7 by investigating the gravitational collapse of colloidal gels using 2D MR imaging. Spatio-temporally resolved measurements of colloid volume fraction, and the height of the gas-liquid interface, are used to reveal that gravitational gel collapse is initiated by processes at the top of the sample and at the wall. Onset times and rates of subsequent gravitational gel collapse are also quantified.

Chapter 9 provides a summary of the conclusions and gives recommendations for future work.

1.4 References

[1] Purcell, E.M., Torrey, H.C. and Pound, R.V., 1946, Resonance absorption by nuclear magnetic moments in a solid. *Phys. Rev.*, **69**, 37–38.

[2] Bloch, F., Hansen, W.W. and Packard, M.E., 1946, Nuclear induction. *Phys. Rev.*, **69**, 127.

[3] Proctor, W.G. and Yu, F.C., 1950, The dependence of a nuclear magnetic resonance frequency upon chemical compound. *Phys. Rev.*, **77**, 717.

[4] Damadian, R., 1971, Tumor detection by nuclear magnetic resonance. *Science*, **171**, 1151–1153.

[5] Lauterbur, P.C., 1973, Image formation by induced local interactions: examples employing nuclear magnetic resonance. *Nature*, **242**, 190–191.

[6] Mansfield, P. and Grannell, P.K., 1973, NMR 'diffraction' in solids? *J. Phys. C: Solid State Phys.*, **6**, L422–L426.

[7] Aue, W.P., Bartholdi, E. and Ernst, R.R., 1976, Two-dimensional spectroscopy. Application to nuclear magnetic resonance. *J. Chem. Phys.*, **64**, 2229–2246.

[8] Wehrli, F.W., 1992, The origins and future of nuclear magnetic resonance imaging. *Phys. Today*, **45**, 34–42.

[9] Gladden, L.F., 1994, Nuclear magnetic resonance in chemical engineering: principles and applications. *Chem. Eng. Sci.*, **49**, 3339–3408.

[10] Gladden, L.F., 1995, Industrial applications of nuclear magnetic resonance. *Chem. Eng. J.*, **56**, 149–158.

[11] Gladden, L.F. and Alexander, P., 1996, Applications of nuclear magnetic resonance imaging in process engineering. *Meas. Sci. Technol.*, **7**, 423–435.

[12] Mantle, M.D. and Sederman, A.J., 2003, Dynamic MRI in chemical process and reaction engineering. *Prog. Nucl. Magn. Reson. Spectrosc.*, **43**, 3–60.

[13] Shaw, T.M., Elsken, R.H. and Kunsman, C.H., 1953, Moisture determination of foods by hydrogen nuclei magnetic resonance. *J. Assoc. Off. Agric. Chem.*, **36**, 1070–1076.

[14] Shoolery, J.N., 1954, Nuclear magnetic resonance spectroscopy. *Anal. Chem.*, **26**, 1400–1403.

[15] Callaghan, P.T., 1999, Rheo-NMR: nuclear magnetic resonance and the rheology of complex fluids. *Rep. Prog. Phys.*, **62**, 599–670.

[16] Roberts, S.T., Renshaw, M.P., Lutecki, M., McGregor, J., Sederman, A.J., Mantle, M.D. and Gladden, L.F., 2013, *Operando* magnetic resonance: monitoring the evolution of conversion and product distribution during the heterogeneous catalytic ethene oligomerisation reaction. *Chem. Commun.*, **49**, 10519–10521.

[17] Robbins, D.J., El-Bachir, M.S., Gladden, L.F., Cant, R.S. and Harbou, E. von, 2012, CFD modeling of single-phase flow in a packed bed with MRI validation. *AIChE J.*, **58**, 3904–3915.

[18] Paul, E.L., Atiemo-Obeng, V. and Kresta, S.M., *Handbook of Industrial Mixing: Science and Practice*, John Wiley & Sons, Hoboken, US, 2003.

[19] Ramsay, J., Simmons, M.J.H., Ingram, A. and Stitt, E.H., 2016, Mixing performance of viscoelastic fluids in a Kenics KM in-line static mixer. *Chem. Eng. Res. Des.*, **115**, 310–324.

[20] Herold, H., Hardy, E.H., Brodhagen, A., Müller, C. and Nestle, N., 2015, Direct velocity imaging by magnetic resonance in a static mixer model produced using stereo lithography. *Chem. Eng. Sci.*, **134**, 599–604.

[21] Mihailova, O., Lim, V., McCarthy, M.J., McCarthy, K.L. and Bakalis, S., 2015, Laminar mixing in a SMX static mixer evaluated by positron emission particle tracking (PEPT) and magnetic resonance imaging (MRI). *Chem. Eng. Sci.*, **137**, 1014–1023.

[22] Tozzi, E.J., McCarthy, K.L., Bacca, L.A., Hartt, W.H. and McCarthy, M.J., 2012, Quantifying mixing using magnetic resonance imaging. *J. Vis. Exp.*, e3493.

[23] Watling, T.C., Ravenscroft, M.R. and Avery, G., 2012, Development, validation and application of a model for an SCR catalyst coated diesel particulate filter. *Catal. Today*, **188**, 32–41.

[24] Nijhuis, T.A., Beers, A.E.W., Vergunst, T., Hoek, I., Kapteijn, F. and Moulijn, J.A., 2001, Preparation of monolithic catalysts. *Catal. Rev.*, **43**, 345–380.

[25] Pennemann, H., Dobra, M., Wichert, M. and Kolb, G., 2013, Optimization of wash-coating slurries as catalyst carrier for screen printing into microstructured reactors. *Chem. Eng. Technol.*, **36**, 1033–1041.

[26] Vergunst, T., Kapteijn, F. and Moulijn, J.A., 2001, Monolithic catalysts—non-uniform active phase distribution by impregnation. *Appl. Catal., A*, **213**, 179–187.

[27] Molnár, K., *Experimental techniques in drying*, CRC Press, Boca Raton, US, 2014, pp. 31–50.

[28] Gummerson, R.J., Hall, C., Hoff, W.D., Hawkes, R., Holland, G.N. and Moore, W.S., 1979, Unsaturated water flow within porous materials observed by NMR imaging. *Nature*, **281**, 56–57.

[29] Koptyug, I.V., Sagdeev, R.Z., Khitrina, L.Y. and Parmon, V.N., 2000, A nuclear magnetic resonance microscopy study of mass transport in porous materials. *Appl. Magn. Reson.*, **18**, 13–28.

[30] Ismagilov, Z.R., Yashnik, S.A., Matveev, A.A., Koptyug, I.V. and Moulijn, J.A., 2005, Characteristics of drying and active component distribution in alumina monoliths using ^{1}H-NMR imaging. *Catal. Today*, **105**, 484–491.

[31] Ramskill, N.P., Gladden, L.F., York, A.P.E., Sederman, A.J., Mitchell, J. and Hardstone, K.A., 2013, Understanding the operation and preparation of diesel particulate filters using a multi-faceted nuclear magnetic resonance approach. *Catal. Today*, **216**, 104–110.

[32] Bensaid, S., Marchisio, D.L., Fino, D., Saracco, G. and Specchia, V., 2009, Modelling of diesel particulate filtration in wall-flow traps. *Chem. Eng. J.*, **154**, 211–218.

[33] Bensaid, S., Marchisio, D.L., Russo, N. and Fino, D., 2009, Experimental investigation of soot deposition in diesel particulate filters. *Catal. Today*, **147S**, S295–S300.

[34] Bensaid, S., Marchisio, D.L. and Fino, D., 2010, Numerical simulation of soot filtration and combustion within diesel particulate filters. *Chem. Eng. Sci.*, **65**, 357–363.

[35] Duynhoven, J.P.M. van, Haiduc, A., Dorsten, F. van and Velzen, E. van, in *Magnetic Resonance in Food Science: From Molecules to Man*, Royal Society of Chemistry, Cambridge, GB, 2007, pp. 1–14.

[36] Blümler, P. and Blümich, B., 1992, Magnetization filters: applications to NMR imaging of elastomers. *Magn. Reson. Imaging*, **10**, 779–788.

[37] Blumenthal, H., *Further adventures in search of perfection: reinventing kitchen classics*, Bloomsbury, London, GB, 2007.

[38] Rajabi-Siahboomi, A.R., Bowtell, R.W., Mansfield, P., Henderson, A., Davies, M.C. and Melia, C.D., 1994, Structure and behaviour in hydrophilic matrix sustained release dosage forms: 2. NMR-imaging studies of dimensional changes in the gel layer and core of HPMC tablets undergoing hydration. *J. Control. Release*, **31**, 121–128.

[39] Hyde, T.M., Gladden, L.F. and Payne, R., 1995, A nuclear magnetic resonance imaging study of the effect of incorporating a macromolecular drug in poly (glycolic acid-co-DL-lactic acid). *J. Control. Release*, **36**, 261–275.

[40] Hyde, T.M. and Gladden, L.F., 1998, Simultaneous measurement of water and polymer concentration profiles during swelling of poly(ethylene oxide) using magnetic resonance imaging. *Polymer*, **39**, 811–819.

[41] Chen, Y.Y., Hughes, L.P., Gladden, L.F. and Mantle, M.D., 2010, Quantitative ultra-fast MRI of HPMC swelling and dissolution. *J. Pharm. Sci.*, **99**, 3462–3472.

[42] Chen, C., Gladden, L.F. and Mantle, M.D., 2014, Direct visualization of *in vitro* drug mobilization from Lescol XL tablets using two-dimensional ^{19}F and ^{1}H magnetic resonance imaging. *Mol. Pharm.*, **11**, 630–637.

[43] Yassin, S., Goodwin, D.J., Anderson, A., Sibik, J., Wilson, D.I., Gladden, L.F. and Zeitler, J.A., 2015, The disintegration process in microcrystalline cellulose based tablets, part 1: influence of temperature, porosity and superdisintegrants. *J. Pharm. Sci.*, **104**, 3440–3450.

[44] Simoneau, C., McCarthy, M.J. and German, J.B., 1993, Magnetic resonance imaging and spectroscopy for food systems. *Food Res. Int.*, **26**, 387–398.

[45] Johns, M.L. and Hollingsworth, K.G., 2007, Characterisation of emulsion systems using NMR and MRI. *Prog. Nucl. Magn. Reson. Spectrosc.*, **50**, 51–70.

[46] Cooper, C.L., Cosgrove, T., Duijneveldt, J.S. van, Murray, M. and Prescott, S.W., 2013, The use of solvent relaxation NMR to study colloidal suspensions. *Soft Matter*, **9**, 7211–7228.

[47] Smith, K., Burbidge, A., Apperley, D., Hodgkinson, P., Markwell, F.A., Topgaard, D. and Hughes, E., 2016, Stray-field NMR diffusion q-space diffraction imaging of monodisperse coarsening foams. *J. Colloid Interf. Sci.*, **476**, 1–27.

[48] Kauten, R.J., Maneval, J.E. and McCarthy, M.J., 1991, Fast determination of spatially localized volume fractions in emulsions. *J. Food Sci.*, **56**, 799–801.

[49] Pilhofer, G.M., McCarthy, M.J., German, J.B. and Kauten, R.J., 1993, Phase separation in optically opaque emulsions. *J. Food Eng.*, **20**, 369–380.

[50] Balinov, B., Urdahl, O., Söderman, O. and Sjöblom, J., 1994, Characterization of water-in-crude oil emulsions by the NMR self-diffusion technique. *Colloids Surf. A: Physicochem. Eng. Aspects*, **82**, 173–181.

[51] Peña, A.A., Hirasaki, G.J. and Miller, C.A., 2005, Chemically induced destabilization of water-in-crude oil emulsions. *Ind. Eng. Chem. Res.*, **44**, 1139–1149.

[52] Callaghan, P.T., Jolley, K.W., Lelievre, J. and Wong, R.B.K., 1983, Nuclear magnetic resonance studies of wheat starch pastes. *J. Colloid Interf. Sci.*, **92**, 332–337.

[53] Hindmarsh, J.P., Hollingsworth, K.G., Wilson, D.I. and Johns, M.L., 2004, An NMR study of the freezing of emulsion-containing drops. *J. Colloid Interf. Sci.*, **275**, 165–171.

[54] Balinov, B., Söderman, O. and Ravey, J.C., 1994, Diffraction-like effects observed in the PGSE experiment when applied to a highly concentrated water/oil emulsion. *J. Phys. Chem.*, **98**, 393–395.

[55] Lönnqvist, I., Håkansson, B., Balinov, B. and Söderman, O., 1997, NMR self-diffusion studies of the water and the oil components in a W/O/W emulsion. *J. Colloid Interf. Sci.*, **192**, 66–73.

[56] Mariette, F., 2009, Investigations of food colloids by NMR and MRI. *Curr. Opin. Colloid Interface Sci.*, **14**, 203–211.

[57] Carneiro, G.F., Silva, R.C., Barbosa, L.L., Freitas, J.C.C., Sad, C.M.S., Tose, L.V., Vaz, B.G., Romão, W., De Castro, E.V.R., Neto, A.C. and Lacerda, V., 2015, Characterisation and selection of demulsifiers for water-in-crude oil emulsions using low-field ^{1}H NMR and ESI-FT-ICR MS. *Fuel*, **140**, 762–769.

[58] Bergenholtz, J., 2001, Theory of rheology of colloidal dispersions. *Curr. Opin. Colloid Interface Sci.*, **6**, 484–488.

[59] Bergenholtz, J., Poon, W.C.K. and Fuchs, M., 2003, Gelation in model colloid-polymer mixtures. *Langmuir*, **19**, 4493–4503.

[60] Blümich, B., Casanova, F. and Appelt, S., 2009, NMR at low magnetic fields. *Chem. Phys. Lett.*, **477**, 231–240.

[61] Mitchell, J., Chandrasekera, T.C., Holland, D.J., Gladden, L.F. and Fordham, E.J., 2013, Magnetic resonance imaging in laboratory petrophysical core analysis. *Phys. Rep.*, **526**, 165–225.

[62] Dalitz, F., Cudaj, M., Maiwald, M. and Guthausen, G., 2012, Process and reaction monitoring by low-field NMR spectroscopy. *Prog. Nucl. Magn. Reson. Spectrosc.*, **60**, 52–70.

[63] Osán, T.M., Ollé, J.M., Carpinella, M., Cerioni, L.M.C., Pusiol, D.J., Appel, M., Freeman, J. and Espejo, I., 2011, Fast measurements of average flow velocity by low-field ^{1}H NMR. *J. Magn. Reson.*, **209**, 116–122.

[64] Herold, H., Hardy, E.H., Ranft, M., Wassmer, K.H. and Nestle, N., 2013, Online rheo-TD NMR for analysing batch polymerisation processes. *Microporous Mesoporous Mater.*, **178**, 74–78.

[65] Barnes, H.A., 1999, Delivering rheology to the consumer-the challenges facing process engineering science in the manufacture of liquid products. *Ingenia*, 46–48.

[66] Collyer, A.A. and Clegg, D.W., *Rheological Measurement*, Springer, Dordrecht, NL, 1998.

[67] Meille, V., Pallier, S., Santa Cruz Bustamante, G.V., Roumanie, M. and Reymond, J.-P., 2005, Deposition of γ-Al_2O_3 layers on structured supports for the design of new catalytic reactors. *Appl. Catal., A*, **286**, 232–238.

[68] Hwang, S.-M., Kwon, O.J. and Kim, J.J., 2007, Method of catalyst coating in micro-reactors for methanol steam reforming. *Appl. Catal., A*, **316**, 83–89.

[69] Stefanescu, A., Veen, A.C. van, Mirodatos, C., Beziat, J.C. and Duval-Brunel, E., 2007, Wall coating optimization for microchannel reactors. *Catal. Today*, **125**, 16–23.

[70] Larson, R.G., *The Structure and Rheology of Complex Fluids*, Oxford University Press, New York, US, 1999.

[71] Gelbart, W.M. and Ben-Shaul, A., 1996, The "new" science of complex fluids. *J. Phys. Chem.*, **100**, 13169–13189.

[72] Bonn, D., Rodts, S., Groenink, M., Rafaï, S., Shahidzadeh-Bonn, N. and Coussot, P., 2008, Some applications of magnetic resonance imaging in fluid mechanics: complex flows and complex fluids. *Annu. Rev. Fluid Mech.*, **40**, 209–233.

[73] Callaghan, P.T., 2006, Rheo-NMR and velocity imaging. *Curr. Opin. Colloid Interface Sci.*, **11**, 13–18.

[74] Callaghan, P.T., in *Encyclopedia of Nuclear Magnetic Resonance*, John Wiley & Sons, Chichester, GB, 2002, vol. 9, pp. 737–750.

[75] Barnes, H.A., Hutton, J.F. and Walters, K., *An Introduction to Rheology*, Elsevier, Amsterdam, NL, 1989.

[76] Brunn, P.O. and Asoud, H., 2002, Analysis of shear rheometry of yield stress materials and apparent yield stress materials. *Rheol. Acta*, **41**, 524–531.

[77] Massey, B.S. and Ward-Smith, J., *Mechanics of Fluids*, Taylor & Francis, London, GB, 2006.

[78] Reger, D.L., Goode, S.R. and Ball, D.W., *Chemistry: Principles and Practice*, Cengage Learning, Belmont, US, 2009.

[79] Mewis, J. and Wagner, N.J., 2009, Thixotropy. *Adv. Colloid Interface Sci.*, **147-148**, 214–227.

[80] Newton, I., *Philosophiæ naturalis principia mathematica*, Royal Society, London, GB, 1687.

[81] Viswanath, D.S., Ghosh, T., Prasad, D.H.L., Dutt, N.V.K. and Rani, K.Y., *Viscosity of Liquids: Theory, Estimation, Experiment, and Data*, Springer, Dordrecht, NL, 2007.

[82] Rao, M.A., in *Rheology of Fluid, Semisolid, and Solid Foods: Principles and Applications*, Springer, New York, US, 2013, pp. 27–61.

[83] Cross, M.M., 1965, Rheology of non-Newtonian fluids: a new flow equation for pseudoplastic systems. *J. Colloid Sci.*, **20**, 417–437.

[84] Carreau, P.J., Ph.D. Thesis, University of Wisconsin, US, 1968.

[85] Yasuda, K., Armstrong, R.C. and Cohen, R.E., 1981, Shear flow properties of concentrated solutions of linear and star branched polystyrenes. *Rheol. Acta*, **20**, 163–178.

[86] Ostwald, W., 1929, Ueber die rechnerische darstellung des strukturgebietes der viskosität. *Kolloid-Z.*, **47**, 176–187.

[87] Barnes, H.A., 1997, Thixotropy—a review. *J. Non-Newton. Fluid Mech.*, **70**, 1–33.

[88] Brady, J.F. and Morris, J.F., 1997, Microstructure of strongly sheared suspensions and its impact on rheology and diffusion. *J. Fluid Mech.*, **348**, 103–139.

[89] Wagner, N.J. and Brady, J.F., 2009, Shear thickening in colloidal dispersions. *Phys. Today*, **62**, 27–32.

[90] Brown, E. and Jaeger, H.M., 2012, The role of dilation and confining stresses in shear thickening of dense suspensions. *J. Rheol.*, **56**, 875–923.

[91] Wyart, M. and Cates, M.E., 2014, Discontinuous shear thickening without inertia in dense non-Brownian suspensions. *Phys. Rev. Lett.*, **112**, 098302.

[92] Lin, N.Y.C., Guy, B.M., Hermes, M., Ness, C., Sun, J., Poon, W.C.K. and Cohen, I., 2015, Hydrodynamic and contact contributions to continuous shear thickening in colloidal suspensions. *Phys. Rev. Lett.*, **115**, 228304.

[93] Fall, A., Bertrand, F., Ovarlez, G. and Bonn, D., 2012, Shear thickening of cornstarch suspensions. *J. Rheol.*, **56**, 575–591.

[94] Fall, A., Bertrand, F., Hautemayou, D., Mezière, C., Moucheront, P., Lemaître, A. and Ovarlez, G., 2015, Macroscopic discontinuous shear thickening versus local shear jamming in cornstarch. *Phys. Rev. Lett.*, **114**, 098301.

[95] Barnes, H.A., 1989, Shear-thickening ("dilatancy") in suspensions of nonaggregating solid particles dispersed in Newtonian liquids. *J. Rheol.*, **33**, 329–366.

[96] Brown, E. and Jaeger, H.M., 2014, Shear thickening in concentrated suspensions: phenomenology, mechanisms and relations to jamming. *Rep. Prog. Phys.*, **77**, 046602.

[97] Sisko, A.W., 1958, The flow of lubricating greases. *Ind. Eng. Chem.*, **50**, 1789–1792.

[98] Herschel, W.H. and Bulkley, R., 1926, Konsistenzmessungen von gummi-benz-ollösungen. *Kolloid-Z.*, **39**, 291–300.

[99] Barnes, H.A. and Walters, K., 1985, The yield stress myth? *Rheol. Acta*, **24**, 323–326.

[100] Hartnett, J.P. and Hu, R.Y.Z., 1989, Technical note: the yield stress—an engineering reality. *J. Rheol.*, **33**, 671–679.

[101] Astarita, G., 1990, Letter to the editor: the engineering reality of the yield stress. *J. Rheol.*, **34**, 275–277.

[102] Barnes, H.A., 1999, The yield stress—a review or '$\pi\alpha\nu\tau\alpha\ \rho\epsilon\iota$'—everything flows? *J. Non-Newton. Fluid Mech.*, **81**, 133–178.

[103] Nguyen, Q.D. and Boger, D.V., 1992, Measuring the flow properties of yield stress fluids. *Annu. Rev. Fluid Mech.*, **24**, 47–88.

[104] Bingham, E.C., 1916, An investigation of the laws of plastic flow. *Bull. Bur. Stand.*, **13**, 309–353.

[105] Péterfi, T.W., 1927, Die abhebung der befruchtungsmembran bei seeigeleiern. *Arch. Entwickl. Org.*, **112**, 660–695.

[106] Huang, C.R., Siskovic, N., Robertson, R.W., Fabisiak, W., Smitherberg, E.H. and Copley, A.L., 1975, Quantitative characterization of thixotropy of whole human blood. *Biorheology*, **12**, 279–282.

[107] Stokes, J.R. and Telford, J.H., 2004, Measuring the yield behaviour of structured fluids. *J. Non-Newton. Fluid Mech.*, **124**, 137–146.

[108] Weltmann, R.N., 1943, Breakdown of thixotropic structure as function of time. *J. Appl. Phys.*, **14**, 343–350.

[109] Tiu, C. and Boger, D.V., 1974, Complete rheological characterization of time-dependent food products. *J. Texture Stud.*, **5**, 329–338.

[110] Mewis, J., 1979, Thixotropy—a general review. *J. Non-Newton. Fluid Mech.*, **6**, 1–20.

[111] Guzman, J. de, 1913, Relación entre la fluidez y el calor de fusion. *An. R. Soc. Esp. Fis. Quím.*, **11**, 353–362.

[112] Brush, S.G., 1962, Theories of liquid viscosity. *Chem. Rev.*, **62**, 513–548.

[113] Wonham, J., 1967, Effect of pressure on the viscosity of water. *Nature*, **215**, 1053–1054.

[114] Ellis, S.B., Thesis, Lafayette College, US, 1927.

Chapter 2

Magnetic resonance theory

Magnetic resonance (MR) is a highly versatile technique involving the manipulation of nuclear spin, with spin a fundamental property of all sub-atomic particles. The four main elements of MR, as introduced in Section 1.1, are:

- **Spectroscopy.** The frequency of the signal is dependent upon the local chemical environment, whilst the intensity of the signal is proportional to the nuclear spin density. This may be used to elucidate chemical structure.
- **Relaxometry.** Signal relaxation, the rate at which the signal returns to thermal equilibrium, is sensitive to the local physical environment. This may be used to provide an insight into microstructure.
- **Imaging.** The position of the emitting nuclei can be determined non-invasively through the application of a spatially-dependent external magnetic field, or magnetic field gradient, to study macrostructure.
- **Dynamics.** A series of magnetic field gradients may be used to study the displacements of emitting nuclei over a specified observation time. This enables the investigation of both coherent and incoherent motion.

In this Chapter, the basic principles of the four main elements of MR are introduced. A quantum mechanical approach is initially employed to describe the physical basis of these measurements, before a more intuitive vector model is then adopted. Only the basic theory is presented. A more comprehensive description of MR is presented in the literature [1,2] and, in the cases where standard techniques have been modified, the relevant Chapters of this thesis.

2.1 Basic principles of MR

2.1.1 Nuclear spin and Zeeman splitting

Magnetic resonance (MR) involves the manipulation of nuclear spin. Spin is an intrinsic form of angular momentum and fundamental property of all sub-atomic particles, with nuclear spin described by the spin quantum number, I, and quantised in increments of $1/2$. The phenomenon of nuclear spin arises due to unpaired nucleons, *i.e.* odd numbers of protons or neutrons, each of which are spin-$1/2$ and may be positive or negative. For example, a hydrogen nucleus (^{1}H) consists of a single unpaired proton and is spin-$1/2$, whilst a deuterium nucleus (^{2}H) also contains an unpaired neutron and is spin-1.

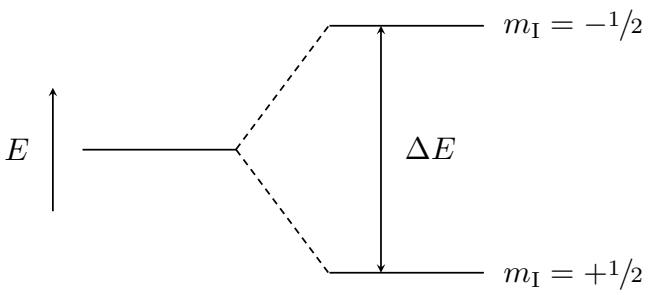

Fig. 2.1: An energy level diagram showing the Zeeman splitting of a spin-$1/2$ nucleus, where $+1/2$ and $-1/2$ are the low and high energy spin states, respectively.

A nucleus may adopt one of $2I + 1$ spin states between $-I$ and I, as defined by the magnetic quantum number, m_I. Therefore, ^{1}H can occupy two spin states; $m_\mathrm{I} = \pm 1/2$. In the absence of a magnetic field, the spin states are degenerate, *i.e.* all spin states are of equal energy. This degeneracy is broken in the presence of a magnetic field, with each spin state occupying a different energy level, E, as given by

$$E = -\frac{1}{2\pi} h\gamma m_\mathrm{I} B_0, \tag{2.1}$$

where h is Planck's constant, γ is the gyromagnetic ratio of the nucleus under study, and B_0 is the strength of the external magnetic field, $\mathbf{B}_0$, aligned with the z-axis. This phenomenon is known as Zeeman splitting. Figure 2.1 shows the Zeeman splitting of

the spin states of a spin-$^1/_2$ nucleus. A transition between two adjacent, non-degenerate spin states, *i.e.* $\Delta m_\mathrm{I} = \pm 1$, is possible by the absorption or emission of a photon:

$$\Delta E = \frac{1}{2\pi} h\gamma B_0, \tag{2.2}$$

where ΔE is the energy required to induce a transition between spin states. Only the difference in the populations of these spin states is observable using MR. Therefore, only nuclei with a non-zero net spin are MR active. It is for this reason that several common nuclei such as carbon (^{12}C) and oxygen (^{16}O) are unsuitable for study using MR. Although a number of the isotopes of these nuclei are MR active, the low natural abundance of such isotopes reduces the sensitivity of the measurement, *i.e.* a reduction in the signal-to-noise ratio (SNR). The natural abundance of ^{13}C, for example, is only 1.07%.

The difference in the populations between the low energy spin state, $N_{+1/2}$, and the high energy spin state, $N_{-1/2}$, of a spin-$^1/_2$ nucleus at thermal equilibrium with B_0 is given by a Boltzmann distribution:

$$\frac{N_{-1/2}}{N_{+1/2}} = \exp\left[-\frac{\Delta E}{kT}\right], \tag{2.3}$$

where k and T represent Boltzmann's constant and the absolute temperature, respectively. The low energy spin state is more populous than the high energy spin state; for a sample at room temperature and an external field strength of 7 T, the relative difference between low and high energy spin state populations is around 1 in 10^5. This small difference is responsible for the inherent lack of sensitivity of MR. Due to the large number of nuclei contained within a sample, it is possible to consider the population difference as a bulk property, *i.e.* averaged over the large spin ensemble, and thus define a net magnetisation vector, $\mathbf{M}$. This is known as the Bloch vector model and allows $\mathbf{M}$ to be described in terms of classical mechanics [3]. The evolution of $\mathbf{M}$ with time, t, in the presence of $\mathbf{B}_0$ may now be described as

$$\frac{\mathrm{d}\mathbf{M}}{\mathrm{d}t} = \mathbf{M} \times \gamma \mathbf{B}_0, \tag{2.4}$$

which, for a static magnetic field aligned with the z-axis, gives

$$\omega_0 = \gamma B_0, \tag{2.5}$$

where ω_0 is the Larmor frequency, ω, at B_0, and $\omega_0 = 2\pi\nu_0$, with ν_0 the corresponding cyclic frequency, ν. Equation (2.5) implies that $\mathbf{M}$ precesses about an applied magnetic field at a rate proportional to B; a packet of nuclear spins experiencing the same B is called an isochromat. At $B_0 = 7\,\mathrm{T}$, $\nu_0 = 300\,\mathrm{MHz}$ for the ^{1}H resonance.

2.1.2 Excitation, detection, and the rotating frame

At thermal equilibrium, $\mathbf{M}$ is aligned with $\mathbf{B}_0$ along the z-, or longitudinal, axis. For signal detection, $\mathbf{M}$ must be perturbed from equilibrium such that a component of $\mathbf{M}$ acts in the xy-, or transverse, plane; a process termed excitation. During this process, a temporary magnetic field, $\mathbf{B}_1$, is applied perpendicular to $\mathbf{B}_0$ through the application of a pulse of radiofrequency (r.f.) radiation. It is important that $\mathbf{B}_1$ oscillates in resonance with the precession about $\mathbf{B}_0$ to induce the transition between spin states. Under these conditions, $\mathbf{M}$ is perturbed from equilibrium due to the simultaneous precession of $\mathbf{M}$ about $\mathbf{B}_0$ and $\mathbf{B}_1$. Note that the frequency, ω_1, at which $\mathbf{M}$ precesses about $\mathbf{B}_1$ is lower than ω_0 as B_1 is weaker than B_0, with B_1 the strength of $\mathbf{B}_1$.

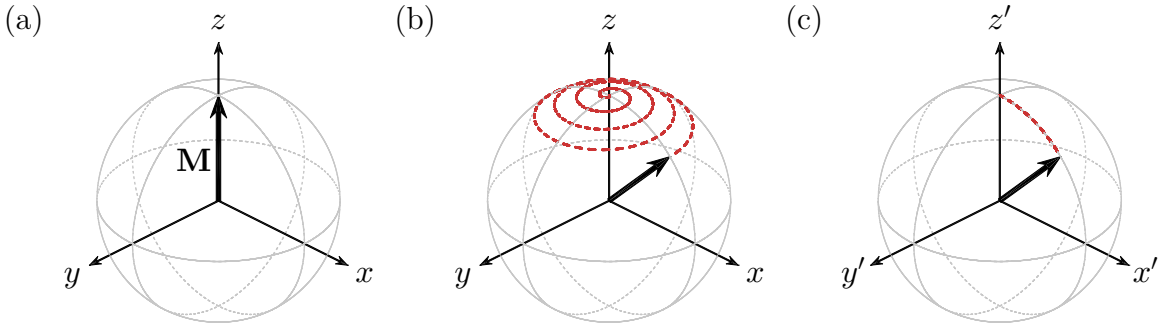

Fig. 2.2: The net magnetisation vector (a) at thermal equilibrium with B_0 and following the application of an r.f. pulse along the y'-axis, as shown in the (b) laboratory and (c) rotating frames of reference. The $x'y'$-plane rotates about z' at ω_0, and the dashed lines (- - -) show the path of $\mathbf{M}$, as defined.

The complex precession of $\mathbf{M}$ about both $\mathbf{B}_0$ and $\mathbf{B}_1$ is difficult to describe in the

fixed, or laboratory, frame of reference. For this reason, a rotating frame of reference is adopted. In the rotating frame, the transverse plane is considered to rotate about the z-axis at a frequency of ω_0. The effect of $\mathbf{B}_1$, or the r.f. pulse, in the rotating frame of reference is a simple rotation of $\mathbf{M}$ about the axis along which the pulse is applied, as shown in Fig. 2.2. By controlling the power and duration of the r.f. pulse it is possible to control the rotation, θ, of $\mathbf{M}$ about $\mathbf{B}_1$, with

$$\theta = \gamma B_1 t_{\text{pulse}} \tag{2.6}$$

and where t_{pulse} is the duration of the r.f. pulse. As shown in Fig. 2.3, the transverse components of the net magnetisation vector, denoted $M_{x,y}$, may be maximised through the application of an r.f. pulse to rotate $\mathbf{M}$ by 90°, commonly referred to as an excitation pulse. Alternatively, a 180° r.f. pulse, termed an inversion pulse, may be applied to invert the longitudinal component of the net magnetisation vector, M_z.

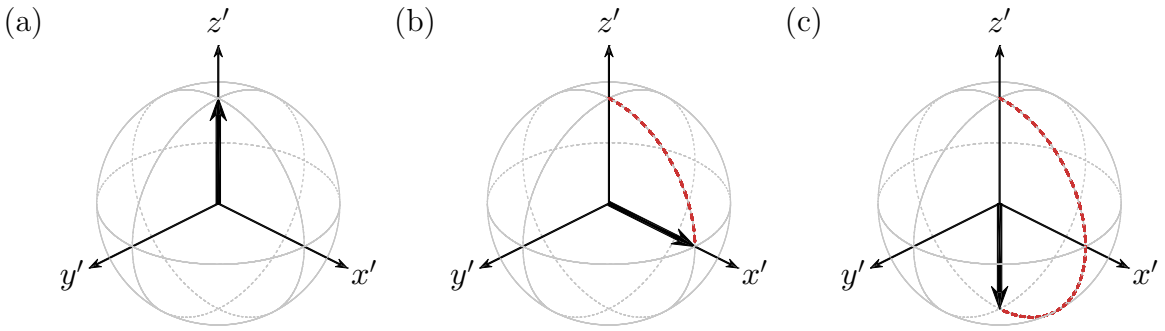

Fig. 2.3: The net magnetisation vector (a) at thermal equilibrium with B_0 and following the application of (b) 90° excitation and (c) 180° inversion pulses, respectively.

Following the application of a 90° excitation pulse, the precession of $\mathbf{M}$ about $\mathbf{B}_0$ at ω_0 causes $M_{x,y}(t)$ to induce a voltage in a coil aligned parallel with the transverse plane, with the voltage induced in the coil proportional to $M_{x,y}(t)$. Voltage is converted into a signal which is detected in quadrature, requiring the signal to be sampled in both the x- and y-directions, to provide both magnitude and phase information. The resulting free induction decay (FID) decays exponentially to 0 due to the return of $\mathbf{M}$ to thermal equilibrium with B_0. This process, termed relaxation, is discussed in detail in Section 2.1.3. Figure 2.4(a) shows the pulse-acquire pulse sequence, complete with the time-domain FID signal. Note that in the simplest case, pulse sequences describe

the series of r.f. pulses applied during a particular experiment to achieve the desired result. A Fourier transform of the time-domain FID signal provides a frequency-domain spectrum of the sample under study. Figure 2.4(b) shows the spectrum corresponding to the FID signal shown in Fig. 2.4(a). Due to the requirement of the Fourier transform and digitisation of the FID signal, a sampling frequency of at least twice the maximum frequency under study must be selected [4]. The sampling frequency, or sweep width, is defined by the dwell time, t_{d}, which characterises the delay between the sampling of successive points in the FID signal. Sweep width is given by $1/t_{\mathrm{d}}$.

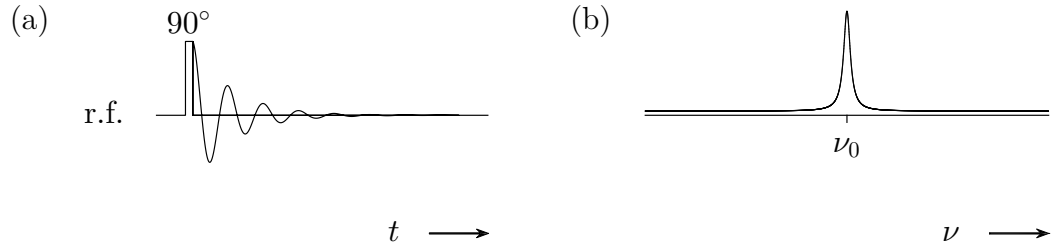

Fig. 2.4: (a) A pulse-acquire pulse sequence showing a 90° excitation pulse followed by an oscillating time-domain FID signal demonstrating an exponential decay of the signal due to relaxation. (b) The corresponding frequency-domain spectrum showing a single (Lorentzian) distribution of frequencies at ν_0, often referred to as a peak. The spectrum is obtained following the Fourier transform of the FID signal.

The SNR of a time-domain signal is improved through signal averaging; the signal increases linearly with the number of averages, N, whilst the noise increases with $\sqrt{N}$. For this reason, SNR increases with $\sqrt{N}$. Any increase in SNR using signal averaging, however, is limited due to practical constraints, with the experimental acquisition time proportional to N.

2.1.3 Relaxometry

During the application of a 90° excitation pulse, energy is provided necessary to induce the transition between spin states. The process by which the spins return to thermal equilibrium, as defined by Eq. (2.3), is termed relaxation. Relaxation is an important element of MR, required for the design of experimental procedure and the elucidation of microstructure. The two mechanisms of relaxation will now be discussed; namely spin-lattice and spin-spin relaxation. For a more complete discussion of MR relaxometry, the interested reader is directed towards the textbooks of Levitt [5] and Keeler [6].

Spin-lattice relaxation

The return of M_z to thermal equilibrium with B_0 is known as spin-lattice relaxation. During spin-lattice relaxation, interactions between the individual spins and the external environment, *i.e.* the lattice, are responsible for energy transfer. This transfer may result in the translation, rotation, or internal motion of molecules within the lattice. Spin-lattice relaxation, characterised by time constant T_1, is expressed as

$$\frac{\mathrm{d}M_z}{\mathrm{d}t} = -\frac{(M_z - M_0)}{T_1}, \tag{2.7}$$

where M_0 is the magnitude of $\mathbf{M}$ in thermal equilibrium with B_0. Note that T_1 represents the time taken for $M_z(t)$ to recover from 0 to 63.2% of M_0. Assuming the initial condition $M_z(0)$, Eq. (2.7) becomes

$$M_z(t) = M_z(0) \exp\left[-\frac{t}{T_1}\right] + M_0\left(1 - \exp\left[-\frac{t}{T_1}\right]\right). \tag{2.8}$$

The estimation of T_1 is commonly achieved using either saturation or inversion recovery. During saturation recovery, a series of 90° excitation pulses are applied to saturate the spin ensemble, such that $M_z(0) = 0$ and

$$M_z(t) = M_0\left(1 - \exp\left[-\frac{t}{T_1}\right]\right). \tag{2.9}$$

Following saturation, spin-lattice relaxation is responsible for the exponential recovery of $M_z(t)$ from 0 to M_0. After a short delay, τ, a 90° excitation pulse is applied to rotate $M_z(t)$ into the transverse plane and the signal is detected. By adjusting the duration of τ it is possible to characterise the extent of spin-lattice relaxation, with the least squares regression of Eq. (2.9) to the experimental dataset used to provide an estimate of T_1. An accurate estimate of T_1 is required for the design of experimental procedure, with a recycle time of 5 times T_1 necessary to ensure the recovery of $M_z(t)$ to 99.3% of M_0. Due to the sensitivity of the recycle time, *i.e.* experimental acquisition time, to T_1, it is often desirable to reduce T_1 by adding paramagnetic ions, such as gadolinium or dysprosium, containing unpaired electrons.

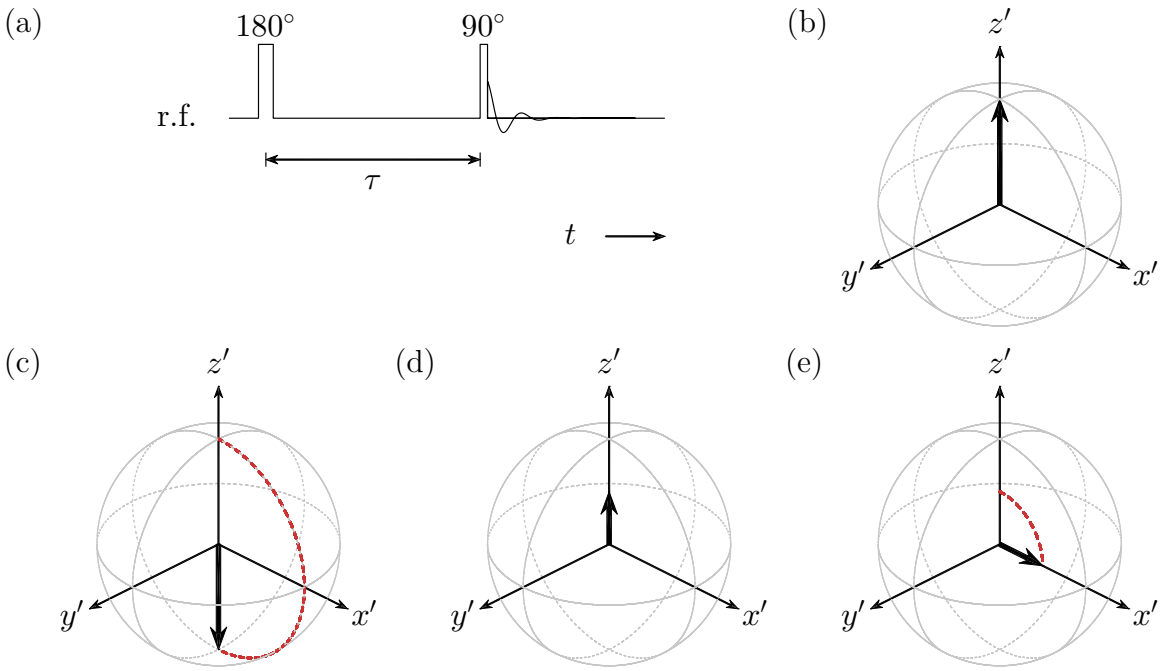

Fig. 2.5: (a) An inversion recovery pulse sequence: (b) M_z equals M_0 at thermal equilibrium with B_0; (c) the 180° pulse inverts $\mathbf{M}$, with $M_z\,(0)$ equal to $-M_0$; (d) following inversion, spin-lattice relaxation is responsible for the exponential recovery of $M_z\,(t)$ from $-M_0$ to M_0; (e) after a short delay, τ, a 90° excitation pulse rotates $\mathbf{M}$ into the transverse plane for signal detection. The extent of spin-lattice relaxation, studied by adjusting the duration of τ, is used to provide an estimate of T_1.

An alternative, more common approach to T_1 characterisation is inversion recovery, performed using the pulse sequence shown in Fig. 2.5 [7]. Unlike saturation recovery, a 180° inversion pulse is initially applied, such that $M_z\,(0) = -M_0$ and

$$M_z\,(t) = M_0\left(1 - 2\exp\left[-\frac{t}{T_1}\right]\right). \tag{2.10}$$

An estimate of T_1 is achieved by adjusting the duration of τ before the application of a 90° excitation pulse and the subsequent least squares regression of Eq. (2.10) to the experimental dataset. For spin-lattice relaxation to occur, an individual spin requires a local magnetic field in the transverse plane oscillating at, or near to, ω_0 to induce a transition between spin states. This local magnetic field is commonly generated by the reorientation of a dipolar interaction due to molecular motion, or tumbling. Spin-lattice relaxation is, therefore, dependent on the distribution of tumbling frequencies.

Spin-spin relaxation

The fluctuating local magnetic fields generated during molecular tumbling cause local variations in B_0 and ω_0. Therefore, following the application of a 90° excitation pulse, $M_{x,y}(t)$ decays to 0 due to a loss of phase coherence, *i.e.* through dephasing of the spin ensemble. In the rotating frame of reference, those isochromats experiencing a higher-than-average ω_0 are observed to accrue a positive phase shift whilst those experiencing a lower-than-average ω_0 accrue a negative phase shift. This process is known as spin-spin relaxation and expressed as

$$\frac{\mathrm{d}M_{x,y}}{\mathrm{d}t} = -\frac{M_{x,y}}{T_2}, \tag{2.11}$$

where T_2 is a time constant representing the time taken for $M_{x,y}(t)$ to decay to 36.8% of $M_{x,y}(0)$. For the initial condition $M_{x,y}(0) = M_0$, Eq. (2.11) becomes

$$M_{x,y}(t) = M_0 \exp\left[-\frac{t}{T_2}\right]. \tag{2.12}$$

The estimation of T_2, which can be achieved using a number of different approaches, is discussed in Section 2.1.4. Spin-spin relaxation is caused by fluctuating local magnetic fields in any orientation and at any frequency, with T_2 always less than, or equal to, T_1. The transient nature of the local variations in ω_0 means that spin-spin relaxation is irreversible.

Although inhomogeneities in B_0 are minimised, or shimmed, using a shim magnetic field, it is impossible to render B_0 perfectly homogeneous. In addition to the dephasing of the spin ensemble caused by spin-spin relaxation, such dephasing may also occur due to local variations in ω_0 resulting from inhomogeneities in B_0. For this reason, it is necessary to define an apparent spin-spin relaxation time constant, T_2^*, which combines both true spin-spin relaxation and relaxation due to B_0 field inhomogeneities, with

$$\frac{1}{T_2^*} = \frac{1}{T_2} + \frac{1}{T_2'}, \tag{2.13}$$

where T_2' characterises dephasing due to B_0 inhomogeneity. Note that T_2^* approaches T_2

as T_2' tends to infinity, *i.e.* as B_0 becomes homogeneous. Apparent spin-spin relaxation is responsible for the exponential decay of the time-domain FID signal and defines the extent of line broadening in the frequency-domain MR spectrum, as given by

$$T_2^* = \frac{1}{\pi \Delta \nu}, \tag{2.14}$$

where $\Delta\nu$ is the full width of the peak at half the peak maximum. From Eq. (2.14), a decrease in T_2^*, caused by a reduction in either T_2 or T_2', is responsible for increased line broadening in the MR spectrum. Line broadening limits the spectral resolution in MR spectroscopy and causes a reduction in spatial resolution in MR imaging. Unlike the local variations in ω_0 caused by molecular tumbling, the local variations in ω_0 due to B_0 field inhomogeneities do not change appreciably over the experimental time scale. Therefore, the relaxation of $M_{x,y}(t)$ resulting from B_0 field inhomogeneities is reversible through the use of echoes, as described in Section 2.1.4.

2.1.4 Echoes

Spin-spin relaxation and B_0 field inhomogeneities are responsible for the dephasing of the spin ensemble at a rate characterised by T_2^*; in the rotating frame of reference, isochromats experiencing a higher-than-average B_0 accrue a positive phase shift whilst those experiencing a lower-than-average B_0 accrue a negative phase shift. This limits the time available for signal encoding and acquisition. Fortunately, dephasing can be mitigated through the application of echoes; namely spin and stimulated echoes.

Spin echo

The spin, or Hahn, echo pulse sequence is shown in Fig. 2.6 [8]. During a spin echo, a 90° excitation pulse is initially applied to rotate $\mathbf{M}$ into the transverse plane. Following excitation, spin-spin relaxation and B_0 field inhomogeneities cause the dephasing of the spin ensemble at a rate defined by T_2^*. After a short delay, τ, a 180° pulse is applied to invert $M_{x,y}(t)$ and the accrued phase shifts. Inhomogeneities in B_0 remain unaltered and the spin ensemble rephases at a rate defined by T_2' such that, at a time 2τ after excitation and assuming no molecular displacement, dephasing of the spin ensemble due to B_0 field inhomogeneities is rephased and a spin echo is formed. For this reason,

a 180° pulse following a 90° excitation pulse is known as a refocusing pulse. Dephasing resulting from spin-spin relaxation is not rephased during a spin echo, enabling the extent of spin-spin relaxation to be characterised by adjusting the duration of τ. The least squares regression of Eq. (2.12) to the experimental dataset provides an estimate of T_2.

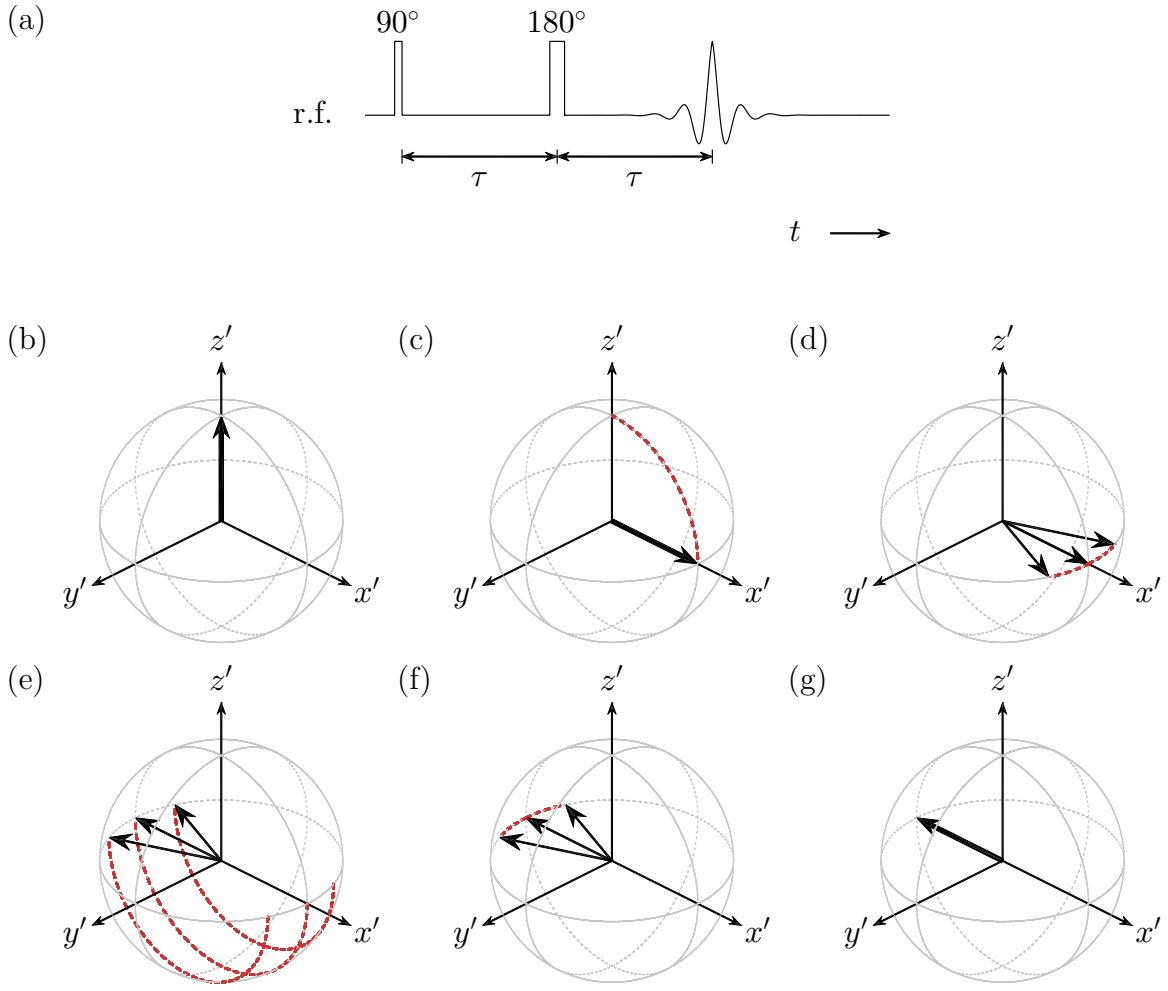

Fig. 2.6: (a) A spin echo pulse sequence: (b) M_z equals M_0 at thermal equilibrium with B_0 and $M_{x,y}$ is 0; (c) the 90° excitation pulse rotates $\mathbf{M}$ into the transverse plane, with $M_{x,y}(0)$ equal to M_0; (d) following excitation, B_0 field inhomogeneities are responsible for the dephasing of the spin ensemble, causing the relaxation of $M_{x,y}(t)$ from M_0 to 0; (e) after a short delay, τ, a 180° pulse is applied to rotate $\mathbf{M}$ about the y'-axis and invert the accrued phase shifts; (f) following the 180° pulse, B_0 field inhomogeneities are responsible for the rephasing of the spin ensemble, causing the recovery of $M_{x,y}(t)$ from 0 to M_0; (g) at a time τ after application of the 180° pulse, the spin ensemble is in phase, with $M_{x,y}(t)$ equal to M_0. Note that spin-spin relaxation has been ignored in this description of a spin echo.

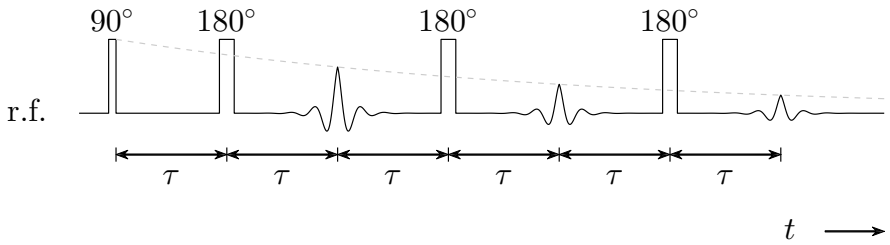

Fig. 2.7: A CPMG pulse sequence, showing a 90° excitation pulse followed by a train of N 180° refocusing pulses, where $N = 3$, with a spin echo formed every $2N\tau$ after excitation. The dashed line (- - -) shows the resulting envelope of T_2 relaxation.

For long τ, an incomplete rephasing of the spin ensemble may result due to molecular displacement; the phase shift accrued between 0 and τ, *i.e.* the 90 and 180° pulses, due to B_0 field inhomogeneities may differ to that accrued between τ and 2τ, *i.e.* the 180° pulse and the spin echo. To minimise the effect of molecular displacement, a more common approach to T_2 estimation involves a very short τ and the application of a train of 180° refocusing pulses. Following the formation of a spin echo as described, the spin ensemble again dephases at a rate defined by T_2^* due to spin-spin relaxation and B_0 field inhomogeneities. The application of a second 180° refocusing pulse, at a time τ after spin echo formation, may be used once again to rephase the spin ensemble at a rate defined by T_2'. A train of 180° refocusing pulses may thus be applied to continuously refocus the spin ensemble for a fixed τ, with a spin echo formed every $2N\tau$ after excitation and where N represents the number of 180° refocusing pulses. Using this approach, the extent of spin-spin relaxation can be characterised by increasing N. The Carr–Purcell Meiboom–Gill (CPMG) pulse sequence [9,10] used for this purpose is shown in Fig. 2.7, where an estimate of T_2 is obtained by performing a least squares regression of Eq. (2.12) to the resulting envelope of T_2 relaxation.

Stimulated echo

Although dephasing of the spin ensemble due to B_0 field inhomogeneities is completely rephased during the formation of a spin echo, dephasing resulting from spin-spin relaxation causes a reduction in SNR and limits the time available for signal encoding and acquisition. These effects may be mitigated through the use of a stimulated echo, as demonstrated in Fig. 2.8 [11]. During a stimulated echo, a 90° excitation pulse is initially applied to rotate $\mathbf{M}$ into the transverse plane. Following excitation, spin-spin relaxation and B_0 field inhomogeneities are responsible for the dephasing of the spin

ensemble at a rate defined by T_2^*. After a short delay, τ, a second 90° pulse is applied to rotate $M_x(t)$ (or $M_y(t)$) into the $-z$-axis such that no further dephasing due to spin-spin relaxation can occur. Instead, $M_z(t)$ returns to thermal equilibrium with B_0 due to spin-lattice relaxation. Although only one component of $M_{x,y}(t)$ can be stored in the $-z$-axis, an increase in SNR is associated with a stimulated echo if $T_1 \gg T_2$. After t_{store}, a final 90° pulse is applied to rotate $M_z(t)$ into the transverse plane and invert the accrued phase shifts. Inhomogeneities in B_0 are not affected by the pair of 90° pulses and the spin ensemble rephases at a rate defined by T_2'. At a time τ after the application of the final 90° pulse, dephasing of the spin ensemble due to B_0 field inhomogeneities is reversed and a stimulated echo is formed.

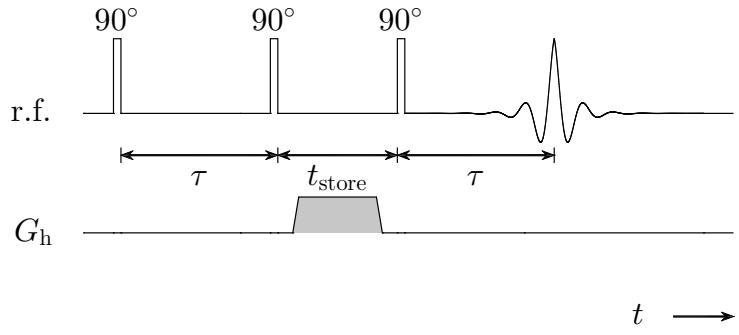

Fig. 2.8: A stimulated echo pulse sequence, showing a 90° excitation pulse followed, after a delay τ, by a pair of 90° pulses separated by a delay t_{store}. The stimulated echo is formed at a time τ after the application of the final 90° pulse and any unwanted $M_{x,y}(t)$ is dephased during t_{store} using a homospoil gradient, G_{h}.

The second component of $M_{x,y}(t)$ is dephased during t_{store} by the application of a magnetic field gradient, termed a homospoil. Magnetic field gradients, introduced in Section 2.2, involve a spatially-dependent magnetic field strength such that ω varies linearly with spatial position. Homospoils are also useful for dephasing unwanted $M_{x,y}(t)$ arising due to imperfect 90° pulses which may otherwise lead to the formation of spin echoes.

2.1.5 Chemical shift

Nuclei within a molecule may experience slightly different B_0 due to orbiting electrons causing local magnetic shielding, with the extent of local magnetic shielding dependent upon the local electron density and polar effects. Therefore, the slight differences

in ν_0 due to local magnetic shielding, termed chemical shift, are sensitive to the local chemical environment. Chemical shift is responsible for multiple peaks and peak splitting in the frequency-domain, as used in MR spectroscopy to identify specific chemical groups and elucidate chemical structure. The dependence of ν_0 on B_0, as implied by Eq. (2.5), is removed by comparing the resonant frequency of the nuclei under study, ν, with that of a reference nuclei, ν_{ref}, using

$$\delta = \frac{\nu - \nu_{\text{ref}}}{\nu_{\text{ref}}} \times 10^6, \tag{2.15}$$

where δ, the chemical shift, is measured in parts per million. Note, therefore, that line broadening, defined by T_2^*, limits the spectral resolution due to peak overlap.

2.2 Principles of MR imaging

It is known, from Section 2.1.1, that the Larmor frequency is dependent on the strength of the applied magnetic field. This dependence can be exploited, by the application of a spatially-dependent magnetic field strength, to enable the position of the emitting nuclei to be determined; a process known as MR imaging. In this section, the principles of MR imaging are introduced.

2.2.1 Image encoding and k-space

Equation (2.5) implies that the Larmor frequency, ω, is directly proportional to the magnetic field strength, B. It follows that a magnetic field gradient, $\mathbf{G}$, may be used to render ω spatially-dependent, thus enabling the position of the emitting nuclei to be determined. The Larmor frequency for an isochromat at position $\mathbf{r}$ is given by

$$\omega(\mathbf{r}) = \gamma(B_0 + \mathbf{G} \cdot \mathbf{r}). \tag{2.16}$$

This is demonstrated schematically in Fig. 2.9, showing the linear variation of ω with $\mathbf{r}$ in the presence of a magnetic field gradient. Note that in the absence of a magnetic field gradient, *i.e.* when $G_x = G_y = G_z = 0$ and where G is the strength of $\mathbf{G}$, Eq. (2.16) reduces to Eq. (2.5) with ω independent of $\mathbf{r}$ and dependent only on B_0.

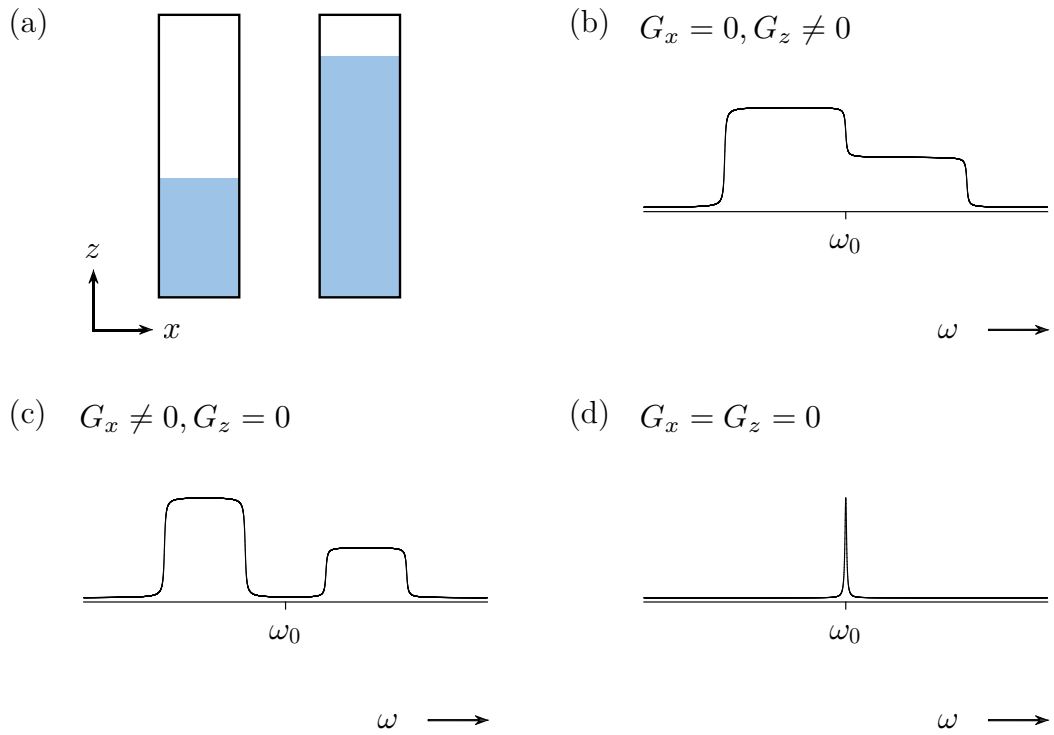

Fig. 2.9: (a) A schematic representation of two, partially-filled tubes and the corresponding MR spectra in the presence of magnetic field gradients applied in the (b) z- and (c) x-directions, where ω depends linearly on $\mathbf{r}$. (d) In the absence of a magnetic field gradient, the MR spectrum shows a single (Lorentzian) peak, with ω independent of $\mathbf{r}$ and dependent only on B_0. Note that line broadening, defined by T_2^*, also affects MR imaging and limits the spatial resolution.

In Fig. 2.9, the signal intensity is shown, in the absence of spin-spin and spin-lattice relaxation, to be proportional to the number of spins, or spin density. More formally, the signal detected from an element of volume, $\mathrm{d}V$, at position $\mathbf{r}$ and with spin density $\rho(\mathbf{r})$, is given by

$$\mathrm{d}S(\mathbf{G}, t) \propto \rho(\mathbf{r}) \exp[\mathrm{i}\omega(\mathbf{r})\, t]\, \mathrm{d}V, \tag{2.17}$$

where t represents the duration of $\mathbf{G}$. The quantification of $\rho(\mathbf{r})$ requires the constant of proportionality in Eq. (2.17) to be determined. Although the constant of proportionality will subsequently be neglected, determination of this constant may be achieved by investigating a known volume of sample. In the rotating frame of reference, where the signal is heterodyned at a frequency of ω_0, $\omega(\mathbf{r})$ reduces to $\gamma\mathbf{G}\cdot\mathbf{r}$ with the integration

of Eq. (2.17) over the sample volume, V, given by

$$S(\mathbf{G}, t) = \iiint \rho(\mathbf{r}) \exp[\mathrm{i}\gamma \mathbf{G} \cdot \mathbf{r} t] \, \mathrm{d}\mathbf{r}. \tag{2.18}$$

Mansfield and Grannell [12] recognised Eq. (2.18) has the form of a Fourier transform and introduced the concept of **k**-space. The reciprocal space vector, **k**, is defined as

$$\mathbf{k} = \frac{\gamma \mathbf{G} t}{2\pi}. \tag{2.19}$$

The substitution of Eq. (2.19) into Eq. (2.18) gives

$$S(\mathbf{k}) = \iiint \rho(\mathbf{r}) \exp[\mathrm{i}2\pi \mathbf{k} \cdot \mathbf{r}] \, \mathrm{d}\mathbf{r}, \tag{2.20}$$

which is the Fourier conjugate of

$$\rho(\mathbf{r}) = \iiint S(\mathbf{k}) \exp[-\mathrm{i}2\pi \mathbf{k} \cdot \mathbf{r}] \, \mathrm{d}\mathbf{k}, \tag{2.21}$$

such that sampling of the signal in **k**-space enables $\rho(\mathbf{r})$, *i.e.* an image, to be produced by the Fourier transformation of $S(\mathbf{k})$. From Eq. (2.19), the traversal of **k**-space necessary to sample $S(\mathbf{k})$ can be achieved by varying either t or **G** in processes known as frequency and phase encoding. Note that as the units of **k** are reciprocal space units, the field-of-view (FOV) of an image is defined by the sampling resolution in **k**-space, whilst the spatial resolution is defined by the range of **k**-space sampled. Relaxation is neglected in Eq. (2.20), with dephasing due only to the magnetic field gradient.

Frequency encoding

The process during which $S(\mathbf{k})$ is sampled continuously in the presence of a constant magnetic field gradient, known as a read gradient and denoted G_r, is called frequency encoding. In accordance with Eq. (2.16), G_r is responsible for a spatially-dependent Larmor frequency enabling the position of the emitting nuclei to be determined. Using frequency encoding an entire line of **k**-space may be sampled per excitation, with the

FOV in the read direction, $\mathrm{FOV_r}$, given by

$$\mathrm{FOV_r} = \frac{2\pi}{\gamma G_\mathrm{r} t_\mathrm{d}}, \tag{2.22}$$

with t_d, the dwell time, as defined in Section 2.1.2.

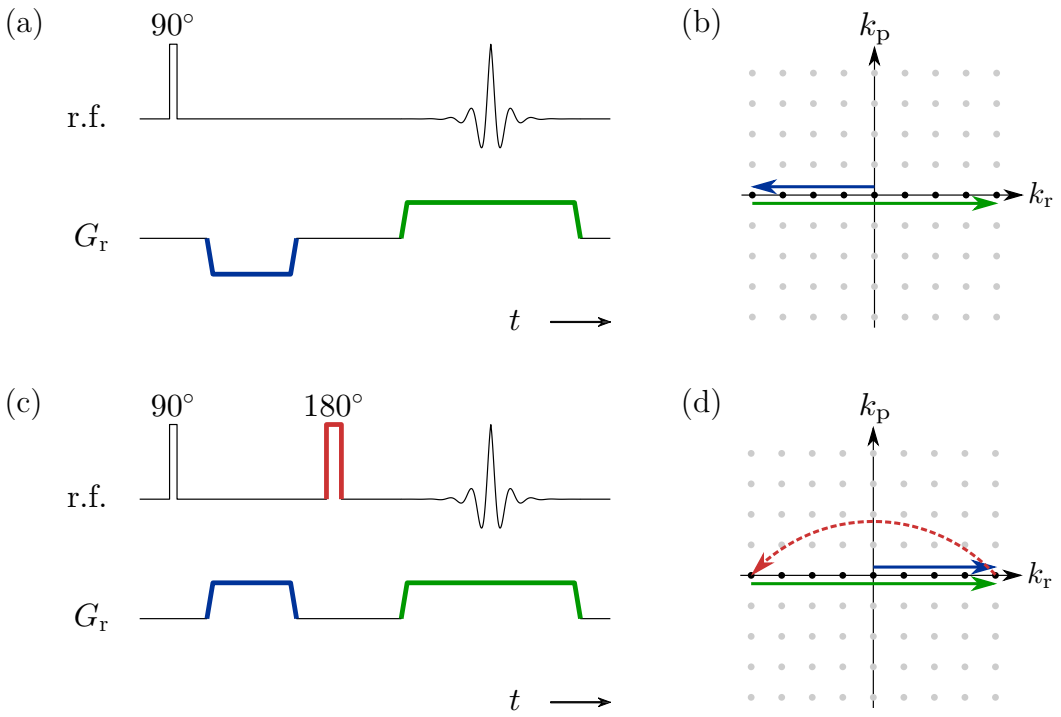

Fig. 2.10: (a) A gradient echo pulse sequence and (b) the corresponding **k**-space raster: (●) the initial read gradient traverses to $-k_\mathrm{r}$ max and (●) the second read gradient traverses k_r whilst (●) $S(\mathbf{k})$ is sampled. (c) A spin echo pulse sequence and (d) the corresponding **k**-space raster: (●) the initial read gradient traverses to $+k_\mathrm{r}$ max, which is then inverted by (●) a 180° refocusing pulse; now at $-k_\mathrm{r}$ max, (●) the second read gradient is applied to traverse k_r whilst (●) $S(\mathbf{k})$ is sampled. Note that $k = (1/2\pi)\,\gamma G t$.

Figure 2.10(a) shows a gradient echo pulse sequence, used for the acquisition of a one-dimensional (1D) image, utilising read gradients applied in opposite directions. Following the 90° excitation pulse, a read gradient is applied in the negative direction for a fixed duration to impart a spatially-dependent phase shift on the spin ensemble. This is equivalent to traversing to $-k_\mathrm{r}$ max. A second read gradient is applied in the positive direction to traverse from $-k_\mathrm{r}$ max to $+k_\mathrm{r}$ max whilst $S(\mathbf{k})$ is sampled at a rate defined by t_d. Assuming no molecular displacement, the spin ensemble is completely

rephased at the centre of **k**-space. In practice, spin ensemble dephasing due to apparent spin-spin relaxation restricts the time available for frequency encoding, as defined by T_2^*. Gradient echo imaging is, for this reason, far less robust than spin and stimulated echo methods. For example, Fig. 2.10(c) shows a spin echo pulse sequence [13] which utilises read gradients of equal direction positioned about a 180° refocusing pulse; the additional phase shifts accrued due to B_0 field inhomogeneities are rephased by the 180° refocusing pulse, as described in Section 2.1.4. The centre of **k**-space is timed to coincide with the centre of the spin echo to maximise SNR and reduce phase artefacts.

Phase encoding

The application of a constant magnetic field gradient for a fixed duration imparts a spatially-dependent phase shift on the emitting nuclei. Using this process, known as phase encoding, a single point in **k**-space is sampled per excitation. Successive points in **k**-space are sampled by incrementing the strength of the magnetic field gradient, known as the phase gradient and denoted G_p, or incrementing the gradient duration, t_p. For a fixed t_p, the FOV in the phase direction, $\mathrm{FOV_p}$, is given by

$$\mathrm{FOV_p} = \frac{2\pi}{\gamma G_{\mathrm{p,inc}} t_\mathrm{p}}, \tag{2.23}$$

where $G_{\mathrm{p,inc}}$ is the increment in G_p. The sampling of **k**-space using phase encoding is time-consuming when compared to frequency encoding as the experimental acquisition time is proportional to the number of excitations. Whilst frequency and phase encoding traverse **k**-space in 1D, the two are often combined to traverse **k**-space in 2D, with G_p applied perpendicular to G_r. An example of combined frequency and phase encoding, enabling a 2D image to be obtained, is provided in Section 2.2.2. Note that a second phase encoding gradient may be applied perpendicular to both G_r and G_p to traverse **k**-space in 3D and obtain a 3D image.

2.2.2 Slice selection

The r.f. pulses introduced in Section 2.1.2 were assumed to act upon the spin ensemble equally. In practice, this is achieved by application of a short duration, high power, wide bandwidth r.f. pulse known as a hard pulse. However, in many cases, it is necessary to

investigate only a reduced range of spectral frequencies. This is achieved by the use of a long duration, low power, narrow bandwidth r.f. pulse known as a soft pulse. In the simplest case, a soft pulse may be used to excite a narrow range of spectral frequencies, or chemical shift, a process termed chemically-selective excitation. Alternatively, soft pulses may be applied in conjunction with a magnetic field gradient, known as a slice gradient and denoted G_s. In accordance with Eq. (2.16), ω during the application of G_s along the z-axis is dependent on z. Therefore, a soft pulse with a narrow bandwidth, $\Delta\omega_\mathrm{s}$, will excite a slice within the sample. The slice thickness, Δz, is given by

$$\Delta z = \frac{\Delta\omega_\mathrm{s}}{\gamma G_\mathrm{s}}, \tag{2.24}$$

whilst the slice shape in the direction of G_s is controlled by the shape of the soft pulse applied. The slice shape and pulse shape represent Fourier transform pairs; in practice, a Gaussian shaped soft pulse is used most frequently, exciting a Gaussian shaped slice. Note that Δz may be increased either by increasing $\Delta\omega_\mathrm{s}$ or decreasing G_s, and a soft pulse may be calibrated to provide any desired rotation of $\mathbf{M}$ in the region of interest, most often 90 or 180°.

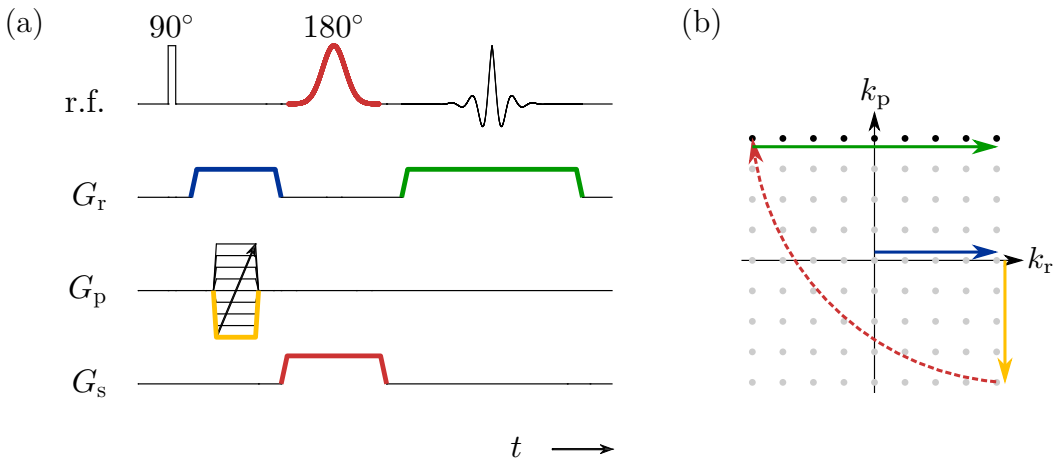

Fig. 2.11: (a) A spin echo pulse sequence and (b) the corresponding **k**-space raster: (●) the initial read gradient traverses to $+k_\mathrm{r}$ max whilst (●) the phase gradient traverses to $-k_\mathrm{p}$ max; this is inverted by (●) a soft 180° refocusing pulse, here shown coupled with a slice gradient for slice selection; now at $-k_\mathrm{r}$ max and $+k_\mathrm{p}$ max, (●) a second read gradient is applied to traverse k_r whilst (●) $S(\mathbf{k})$ is sampled. This is repeated for N increments in G_p to sample a full 2D **k**-space raster.

Figure 2.11 shows a slice selective, spin echo pulse sequence using both frequency and phase encoding to traverse **k**-space in 2D and obtain a 2D image. Following a 90° excitation pulse, a read gradient traverses to $+k_{\mathrm{r}}$ max whilst a phase gradient simultaneously traverses k_{p}, as described in Section 2.2.1, such that a spatially-dependent phase shift is imparted on the spin ensemble. A soft 180° refocusing pulse is applied in combination with a slice gradient to invert the accrued phase shifts within a slice of thickness Δz. The second read gradient traverses k_{r} whilst $S(\mathbf{k})$ is sampled. This procedure is repeated for N increments in G_{p} to sample a full 2D **k**-space raster.

2.3 Dynamics and MR

The study of flow using MR may be performed using one of two approaches; namely time-of-flight (TOF) or phase encoding methods. Phase encoding methods will now be introduced, with the interested reader directed towards the review article of Mantle and Sederman [14] for an introduction to TOF methods.

2.3.1 Displacement encoding and q-space

Phase encoding pulsed field gradient (PFG) MR methods are widely considered to be the most robust and quantitative way of measuring flow [2]. From Eq. (2.16), the phase shift accrued in the rotating frame of reference during application of a time-dependent magnetic field gradient, known as the flow gradient and denoted $\mathbf{g}(t)$, is given by

$$\phi(t) = \gamma \int_0^t \mathbf{g}(t)\,\mathbf{r}(t)\ \mathrm{d}t, \tag{2.25}$$

where $\phi(t)$ and $\mathbf{r}(t)$ represent the time-dependent phase, ϕ, and position, respectively. For a molecule initially at $\mathbf{r}$, the phase shift accrued during the application of a bipolar magnetic field gradient pair, as shown in Fig. 2.12 with g the strength of $\mathbf{g}$, equals

$$\phi = \gamma \mathbf{g} \cdot (\mathbf{r}' - \mathbf{r})\,\delta, \tag{2.26}$$

where δ is the flow gradient duration and $\mathbf{r}'$ is the position of the molecule at time Δ, with Δ the flow gradient separation time. Note that Δ is also known as the observation

or contrast time. The corresponding signal may be described using

$$S(\mathbf{g},\delta) = \int \rho(\mathbf{r}) \int p(\mathbf{r}' - \mathbf{r}, \Delta) \exp\left[\mathrm{i}\gamma \mathbf{g} \cdot (\mathbf{r}' - \mathbf{r})\,\delta\right] \mathrm{d}\mathbf{r}'\,\mathrm{d}\mathbf{r}, \tag{2.27}$$

where $p(\mathbf{r}' - \mathbf{r}, \Delta)$ denotes the probability that a molecule initially at $\mathbf{r}$ has migrated to $\mathbf{r}'$ during Δ. Kärger and Heink [15] recognised Eq. (2.27) has the form of a Fourier transform and introduced the concept of $\mathbf{q}$-space. The reciprocal displacement vector, $\mathbf{q}$, is defined as

$$\mathbf{q} = \frac{\gamma \mathbf{g} \delta}{2\pi}. \tag{2.28}$$

The substitution of Eq. (2.28) into Eq. (2.27) gives

$$S(\mathbf{q}) = \int \bar{p}(\mathbf{R}, \Delta) \exp\left[\mathrm{i}2\pi \mathbf{q} \cdot \mathbf{R}\right] \mathrm{d}\mathbf{R}, \tag{2.29}$$

where $\mathbf{R} = \mathbf{r}' - \mathbf{r}$ and $\bar{p}(\mathbf{R}, \Delta)$, the volume-averaged flow propagator, is equal to

$$\bar{p}(\mathbf{R}, \Delta) = \int \rho(\mathbf{r})\, p(\mathbf{R}, \Delta)\ \mathrm{d}\mathbf{r}. \tag{2.30}$$

The volume-averaged flow propagator completely characterises the molecular displacements of the sample under study [16].

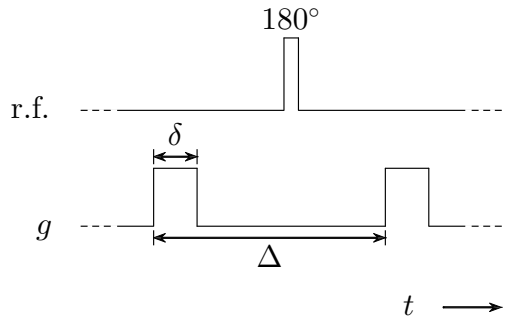

Fig. 2.12: A bipolar magnetic field gradient pair, showing flow gradients of magnitude g, duration δ, and separation Δ, centred about a 180° refocusing pulse.

In the absence of molecular displacement, the accrued phase shift is zero; the spin ensemble is completely rephased following the application of the second flow gradient. In the presence of molecular displacement, the accrued phase shift is non-zero. The study of incoherent and coherent motion using phase encoding will now be described.

Incoherent motion

In the presence of molecular self-diffusion, the flow propagator is a zero-mean Gaussian distribution. The resulting Gaussian distribution of phase shifts causes the dephasing of the spin ensemble and the attenuation of $S(\mathbf{q})$. In practice, the extent of attenuation is characterised by sampling $S(\mathbf{q})$ whilst traversing $\mathbf{q}$ by varying $\mathbf{g}$ or δ. Stejskal and Tanner [17] derived an expression, now called the Stejskal–Tanner equation, to describe the attenuation of the magnitude of $S(\mathbf{q})$, given by

$$\frac{|S(\mathbf{q})|}{|S(0)|} = \exp\left[-4\pi^2\mathbf{q}^2 \cdot \mathbf{D}\left(\Delta - \frac{\delta}{3}\right)\right], \tag{2.31}$$

with $\mathbf{D}$ the diffusion tensor and $|S(0)|$ the magnitude of $S(\mathbf{q})$ at the centre of $\mathbf{q}$-space. For unrestricted diffusion, the diffusion coefficient, D, in the direction of $\mathbf{g}$ is estimated by using a plot of $\ln(|S(q)| / |S(0)|)$ versus $4\pi^2 q^2(\Delta - \delta/3)$, with $q = (1/2\pi)\gamma g\delta$ and $-D$ given by the gradient of the straight line. Although the pulsed gradient spin echo (PGSE) pulse sequence depicted in Fig. 2.13 is often used to study molecular displacements, the pulsed gradient stimulated echo (PGSTE) pulse sequence is preferred when $T_1 \gg T_2$, whilst the alternating PGSTE (APGSTE) pulse sequence [11] is used when removal of background magnetic field gradients is necessary.

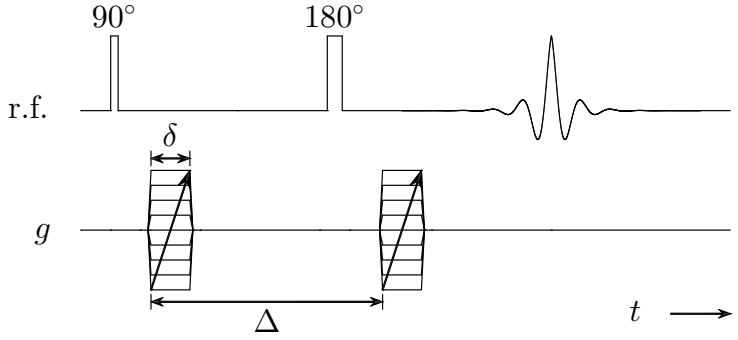

Fig. 2.13: A PGSE pulse sequence [17] used for the study of molecular displacement.

Coherent motion

The flow propagator in the presence of flow is non-Gaussian and characteristic of the flow under study. Equation (2.29) is the Fourier conjugate of

$$\bar{p}\left(\mathbf{R},\Delta\right)=\int S\left(\mathbf{q}\right)\exp\left[-\mathrm{i}2\pi\mathbf{q}\cdot\mathbf{R}\right]\mathrm{d}\mathbf{q} \tag{2.32}$$

such that sampling of the signal in **q**-space enables $\bar{p}\left(\mathbf{R},\Delta\right)$, *i.e.* the flow propagator, to be produced by the Fourier transformation of $S\left(\mathbf{q}\right)$. Note that since the units of **q** are reciprocal displacement units, the field-of-flow (FOF) of a flow propagator is defined by the sampling resolution in **q**-space, whilst displacement resolution is defined by the range of **q**-space sampled. Successive points in **q**-space are sampled by incrementing **g** or δ. For a fixed δ, the FOF is given by

$$\mathrm{FOF}=\frac{2\pi}{\gamma g_{\mathrm{inc}}\delta}, \tag{2.33}$$

where g_{inc} is the increment in g. In practice, coherent and incoherent motion occur simultaneously, with incoherent motion causing the broadening of $\bar{p}\left(\mathbf{R},\Delta\right)$ and limiting the displacement resolution of the flow propagator. The flow propagator is produced by sampling $S\left(\mathbf{q}\right)$ at N increments in **q** using the PGSE, PGSTE, or APGSTE pulse sequences. Since only a single point in **q**-space is sampled per excitation, the sampling of $S\left(\mathbf{q}\right)$ is time-consuming.

2.3.2 Imaging k-space and q-space

Measurements of flow propagators may be spatially-resolved using methods outlined in Section 2.2, with the signal in **k**- and **q**-space, $S\left(\mathbf{k},\mathbf{q}\right)$, described by

$$S\left(\mathbf{k},\mathbf{q}\right)=\iiint\rho\left(\mathbf{r}\right)\exp\left[\mathrm{i}2\pi\mathbf{k}\cdot\mathbf{r}\right]\int\bar{p}\left(\mathbf{R},\Delta\right)\exp\left[\mathrm{i}2\pi\mathbf{q}\cdot\mathbf{R}\right]\mathrm{d}\mathbf{R}\,\mathrm{d}\mathbf{r}, \tag{2.34}$$

with $S\left(\mathbf{k},\mathbf{q}\right)$ sampled whilst independently traversing **k**- and **q**-space. The spatially-resolved flow propagators are produced by Fourier transformation of $S\left(\mathbf{k},\mathbf{q}\right)$ initially in **k**-space and then in **q**-space following normalisation with respect to $\rho\left(\mathbf{r}\right)$. However,

the acquisition of spatially-resolved flow propagators is time-consuming, particularly in 2D due to the requirement of phase encoding.

Equation (2.25) implies that the phase shift accrued in the rotating frame of reference during the presence of a time-dependent flow gradient, $\mathbf{g}(t)$, is proportional to $\mathbf{r}(t)$. Using Newton kinematics, it is known that

$$\mathbf{r}(t) = \mathbf{r}(0) + \mathbf{v}t + \frac{1}{2}\mathbf{a}t^2 + ..., \tag{2.35}$$

where $\mathbf{v}$ and $\mathbf{a}$ represent velocity and acceleration, respectively, and $\mathbf{r}(0)$ is the initial position. The substitution of Eq. (2.35) into Eq. (2.25) provides the moments of the magnetic field gradient, $\mathbf{g}$, where

$$\mu_0 = \mathbf{r}(0) \int_0^t \mathbf{g}(t)\ \mathrm{d}t, \tag{2.36}$$

$$\mu_1 = \mathbf{v} \int_0^t \mathbf{g}(t)\, t\, \mathrm{d}t, \tag{2.37}$$

$$\mu_2 = \frac{1}{2}\mathbf{a} \int_0^t \mathbf{g}(t)\, t^2\, \mathrm{d}t, \tag{2.38}$$

are the zeroth, first, and second moments, respectively. For the bipolar magnetic field gradient pair shown in Fig. 2.12, μ_0 is zero, with the accrued phase shift proportional to μ_1, *i.e.* velocity, where

$$\phi = \gamma\delta\mathbf{g} \cdot \mathbf{v}\Delta. \tag{2.39}$$

Note that the accrued phase shift due to μ_2, *i.e.* acceleration, is non-zero but negligible when compared to that accrued due to velocity. The application of a pair of bipolar magnetic field gradient pairs may be used to reduce μ_1 to zero and study acceleration. Additional phase shifts accrued due to B_0 field inhomogeneities and background magnetic field gradients are removed by utilising two increments in $\mathbf{g}$ and determining the net phase shift accrued. To prevent phase wrapping, $\mathbf{g}$, δ, and Δ are often calibrated based on an initial estimate of $\mathbf{v}$ to provide a maximum phase shift of 2π.

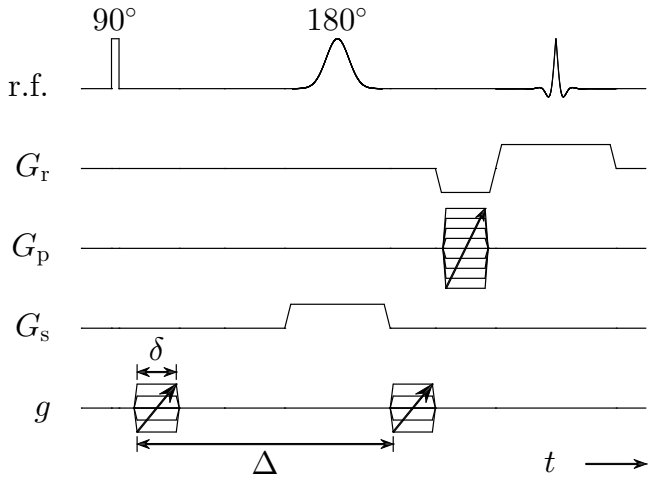

Fig. 2.14: A spin echo MR flow imaging pulse sequence used for the imaging of velocity.

The spin echo MR flow imaging pulse sequence shown in Fig. 2.14 combines image and displacement encoding to enable the imaging of velocity in 2D. It is interesting to note that, in accordance with Eqs. (2.36) to (2.38), any magnetic field gradient may be responsible for displacement encoding and (often undesirable) phase shifts due to a non-zero μ_1. For example, with reference to Fig. 2.14, phase shifts may also be accrued due to the read, phase, and slice gradients. The process during which μ_1 of a magnetic field gradient is reduced to zero is known as velocity compensation. A more complete introduction to velocity compensation can be found in the journal article of Pope and Yao [18].

2.4 Application of MR to complex fluids

In this Section, an introduction to the application of MR to rheological characterisation and colloidal dispersions is discussed. A more complete discussion can be found in the references therein.

2.4.1 Rheological characterisation

Rheological characterisation was introduced in Section 1.2 as the study of a fluid subjected to deformational, or shear, flow. Such characterisation is often performed using conventional, benchtop rheometry techniques. Conventional rheometry techniques can be divided into two main categories; namely drag force and pressure-driven flows [19].

In drag force flows, rotational geometries such as the Couette cell and cone-and-plate are used to generate shear in a narrow gap between stationary and rotating surfaces. In contrast, shear is induced by a pressure gradient in the case of pressure-driven flows such as the capillary or pipe flow geometry. Conventional rheometry techniques provide only one shear viscosity-shear rate data point in a single measurement and hence characterisation of the flow curve over a range of shear rates is time-consuming, requiring an increase in rotational speed in the case of rotational geometries or pressure gradient in pressure-driven geometries. Furthermore, such techniques can probe only bulk fluid behaviour and, whilst this is satisfactory for simple fluids, it is unsatisfactory for many of the complex process fluids encountered in industry. Process fluids may exhibit both solid- and liquid-like behaviour and a number of complex flow phenomena, including wall slip, shear banding, particle migration and fracture. For this reason, there exists a need to obtain detailed information about the flow field generated in the geometry to enable the observation and quantification of such phenomena [20]. Whilst conventional rheometry is unable to provide detailed information about the flow field, many techniques—including neutron [21], light [22], and X-ray [23] scattering, optical birefringence studies [24], and laser Doppler [25], ultrasound [26], and particle image [27] velocimetry—are capable of providing such information. For example, Doppler optical coherence tomography has successfully been applied to study the rheology of complex fluids in capillary [28] and rotational [29] rheometer geometries. However, Doppler optical coherence tomography and the alternatives listed all suffer some limitation, either in the flow geometry that can be used, the optical opacity demands of the fluid under study, or the requirement of tracer particles. The interested reader is directed towards the recent review articles of Haavisto *et al.* [30] and Harvey *et al.* [31] for more detailed discussions of Doppler and ultrasound methods, respectively.

Perhaps the most versatile technique for the rheological characterisation of process fluids is MR; it is non-invasive and without limitation on optical opacity. Furthermore, an additional advantage of MR when compared with other techniques is its ability to probe a variety of different length and time scales, as was discussed in Section 1.1. For example, MR spectroscopy was used by Martins *et al.* [32] to investigate molecular reorientation in a polymer fluid following a sample rotation within a fixed magnetic field, and later to study polymer fluids under shear conditions in cone-and-plate [33] and Couette cell [34] geometries. In contrast, Xia and Callaghan [35] used MR flow imaging to spatially-resolve measurements of velocity in 2D to investigate the transition of a polymer solution from Newtonian to non-Newtonian rheology, with increasing

polymer concentration, in a capillary geometry. Since these early days, MR rheometry has developed into a highly versatile technique applicable to a large number of flow geometries [36]. In this Section, a number of applications of MR to study the rheology of complex fluids, in several rheometer geometries, are described, with a particular focus on spatially-resolved measurements of velocity obtained using MR flow imaging. For a more complete introduction to MR rheometry, the interested reader is directed towards the review articles of Callaghan [37] and Bonn *et al.* [38].

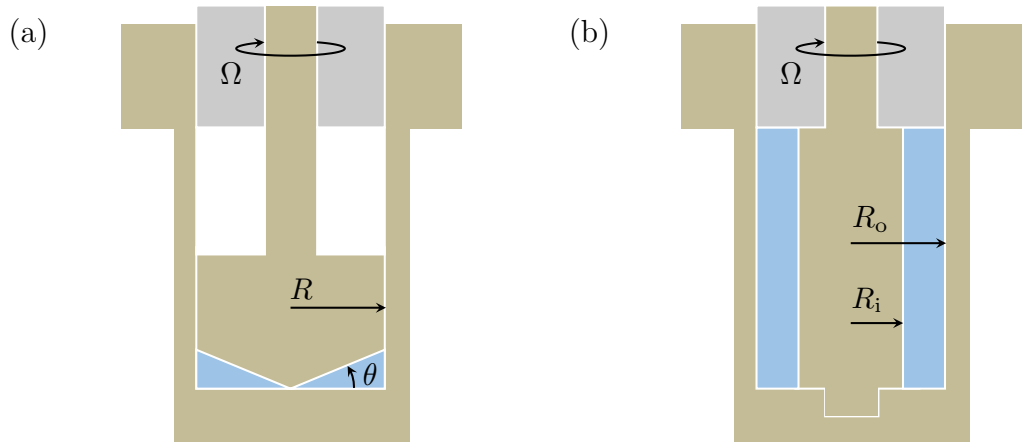

Fig. 2.15: A schematic representation of the (●) liquid-filled (a) cone-and-plate and (b) wide gap Couette cell geometries, often constructed using (●) poly(ether etherketone), in which the cone and inner cylinder are rotated at a constant angular frequency, Ω, respectively.

The most commonly used geometries for MR rheometry are the cone-and-plate and wide gap Couette cell shown in Fig. 2.15. For a cone-and-plate geometry, comprising of a stationary flat plate and rotating cone, the shear stress across the gap for a fixed angular frequency, Ω, and small gap angle, θ, is almost constant, with a single shear rate expected. However, Britton and Callaghan [39] observed wall slip and shear rate heterogeneity for tomato ketchup, using a cone-and-plate geometry with $\theta = 7°$, and later observed the shear banding of a surfactant solution [40,41]. These observations further demonstrate the need for detailed information about the flow field under study. Since the shear stress is constant for a given Ω and θ, investigation of a range of shear stresses using a cone-and-plate geometry can be time-consuming. In contrast, the shear stress, τ, across a wide gap Couette cell, comprising of concentric cylinders in which the inner cylinder is rotated and the outer cylinder held stationary, is given as a function

of radial position, r, by

$$\tau\left(r\right) = \tau_{\mathrm{i}}\left(\frac{R_{\mathrm{i}}}{r}\right)^{2}, \tag{2.40}$$

as determined using a momentum balance, where τ_{i} is the shear stress at the wall of the inner cylinder of radius R_{i}. In accordance with Eq. (2.40), τ decreases from a maximum at the wall of the inner cylinder to a minimum at the wall of the outer cylinder [38]. Therefore, a range of shear stresses can be probed in only a single measurement using a wide gap Couette cell geometry. In 1994, Rofe *et al.* [42] used MR flow imaging to obtain velocity profiles of a polymer solution demonstrating power-law rheology under shear, for which the tangential velocity, v, can be described as a function of r using

$$v\left(r\right) = \Omega R_{\mathrm{i}}\frac{\Xi\left(1-\Xi^{-\frac{2}{n}}\right)}{\Upsilon\left(1-\Upsilon^{-\frac{2}{n}}\right)}, \tag{2.41}$$

where Ξ and Υ are the ratios of r to R_{o}, the radius of the outer cylinder, and R_{i} to R_{o}, respectively, and n is the flow behaviour index [43]. The shear rate, $\dot{\gamma}$, is given by

$$\dot{\gamma}\left(r\right) = 2\Omega\frac{\Xi^{-\frac{2}{n}}}{n\left(1-\Upsilon^{-\frac{2}{n}}\right)}. \tag{2.42}$$

Figure 2.16(a) shows velocity profiles obtained using Eq. (2.41) for three example fluids demonstrating power-law rheology and depicts a change in velocity profile shape as n is decreased. A non-linear least squares (NLLS) regression of Eq. (2.41) to the velocity profiles was therefore used by Rofe *et al.* [42] to provide an estimate of n describing the rheology of the polymer solution under study. Since those early days, this approach has successfully been applied to characterise n describing a variety of foodstuffs—including cream, butter, egg white, tomato ketchup, and cornflour-in-water solutions [39]—and apparent wall slip in xanthan gum-in-water solutions [44], foams, and emulsions [45,46]. Shear banding [40,47–50] and particle migration have also been investigated [51–53]. This approach is not limited to fluids demonstrating power-law rheology, but has also successfully been applied to Herschel–Bulkley fluids. For Herschel–Bulkley fluids there

exists a critical r, denoted r_0, at which τ is equal to the yield stress of the fluid, τ_0; in the region bounded by r_0 and R_o, $\tau \leq \tau_0$ and $\dot{\gamma} = 0\,\mathrm{s}^{-1}$. Since r_0 is dependent upon τ_i, and therefore Ω, an increase in r_0 with an increase in Ω, for xanthan gum-in-water solutions and mayonnaise, was observed by Hollingsworth and Johns [46]. An identical trend was also demonstrated by Drappier *et al.* [54] for a semi-dilute wormlike micellar system. Dilute wormlike micellar systems have previously been shown to demonstrate shear-thickening and fracture behaviour [55,56]. Furthermore, the evaluation of Eq. (2.40) at $r = r_0$ can be used to provide an estimate of τ_0 if τ_i is known. Unfortunately, since measurement of τ_i requires a non-trivial measurement of torque, the flow curve cannot be characterised using this approach.

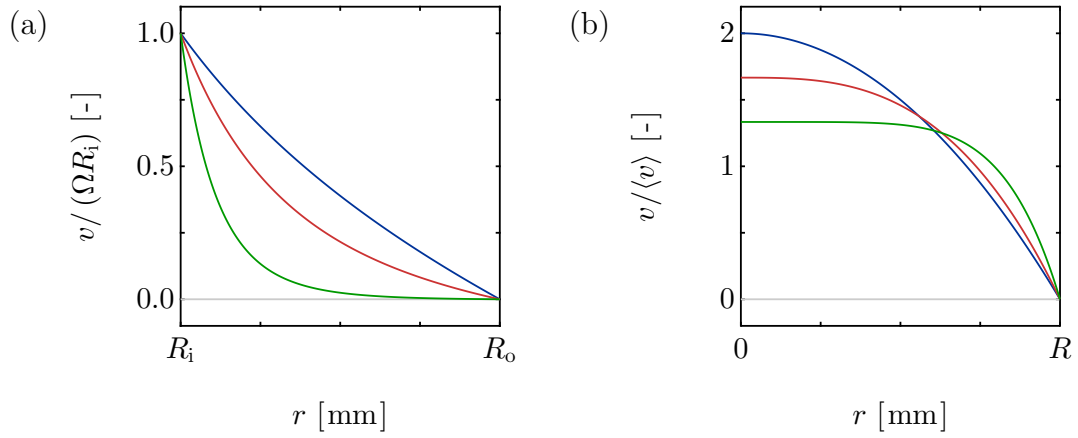

Fig. 2.16: (a) Couette cell velocity profiles (represented as a fraction of ΩR_i) calculated using Eq. (2.41) for three example fluids; (—) $n = 1.0$, (—) $n = 0.5$, and (—) $n = 0.2$. (b) Corresponding pipe flow velocity profiles (represented as a fraction of $\langle v \rangle$) obtained using Eq. (2.44).

Despite the success of the cone-and-plate and Couette cell geometries for the study of fluids demonstrating power-law and Herschel–Bulkley rheology, these operate only in offline configuration, with an online, or inline, geometry required for process control and optimisation. The pressure-driven pipe flow geometry offers one such alternative, with τ given as a function of r by

$$\tau\,(r) = \frac{\mathrm{d}P}{\mathrm{d}L}\frac{r}{2}, \tag{2.43}$$

as determined from a force balance, where $\mathrm{d}P/\mathrm{d}L$ is the pressure drop per unit length.

In accordance with Eq. (2.43), τ decreases linearly from a maximum at the pipe wall to zero at the pipe centre. Therefore, a range of shear stresses can be probed in only a single measurement using a pipe flow geometry. In 1991, Xia and Callaghan [35] used MR flow imaging to obtain velocity profiles of polymer solutions demonstrating power-law rheology at different concentrations and volumetric flow rates, $\dot{V}$. For power-law fluids, v may be described as a function of r using

$$v\left(r\right) = \langle v \rangle \left(\frac{3n+1}{n+1}\right)\left(1 - \left(\frac{r}{R}\right)^{\frac{n+1}{n}}\right), \tag{2.44}$$

where $\langle v \rangle$ is the mean fluid velocity and R the pipe radius. Figure 2.16(b) demonstrates velocity profiles simulated using Eq. (2.44) for the three example fluids considered in Fig. 2.16(a) and shows a change in the shape of the velocity profile as n is decreased and a reduction in the maximum velocity. For this reason, a NLLS regression of Eq. (2.44) was employed by Xia and Callaghan [35] to estimate n describing the rheology of the polymer solution under study over a shear rate range, depending on $\dot{V}$, of up to $70\,\mathrm{s}^{-1}$. Since those early days, this approach has successfully been applied and extended to estimate n describing the rheology of a number of fluids demonstrating power-law and Herschel–Bulkley rheology [44,57–60]. Note that for Herschel–Bulkley fluids, $\dot{\gamma} = 0\,\mathrm{s}^{-1}$ within a region bounded by 0 and r_0. Wall slip was also investigated by Rofe *et al.* [44] for xanthan gum-in-water solutions, with the results obtained in agreement with those determined using a wide gap Couette cell geometry. Unlike the Couette cell geometry, however, characterisation of the flow curve is possible using a pipe flow geometry by measurement of $\mathrm{d}P/\mathrm{d}L$. Using a measurement of $\mathrm{d}P/\mathrm{d}L$ and r_0, Arola *et al.* [60] were able to evaluate Eq. (2.43) at r_0 and provide an estimate of τ_0. The τ_0 values obtained were accurate to within $< 2\%$ of those τ_0 values determined using conventional rheometry. This suggests that MR flow imaging can be used, together with complementary $\mathrm{d}P/\mathrm{d}L$ data, for the accurate rheological characterisation of non-Newtonian fluids in a pipe flow geometry. The rheological characterisation of model fluids exhibiting power-law and Herschel–Bulkley rheology using this approach is described in Chapters 3 and 5, respectively. Note that a consideration of the different MR flow imaging techniques was not provided here, with the interested reader directed towards Section 3.1.

2.4.2 Colloidal dispersions

Colloidal dispersions, introduced in Section 1.1.2 and comprising of a dispersed phase sized between 10 nm and 1 µm distributed throughout a dispersion medium, have been the subject of many studies using MR. Since the prediction of the rheology of colloidal dispersions is difficult [61], many studies have used MR rheometry methods outlined in Section 2.4.1 to provide insights into the rheology of such dispersions. This has successfully been applied to a variety of colloidal dispersions, including emulsions [46,62]. Most recently, Novak and Britton [63] used MR flow imaging to characterise the rheology of ionic liquids, liquid ionic salts with chemical and physical properties suited to a wide range of industrial applications, in cone-and-plate and Couette cell geometries. The application of MR to colloidal dispersions is, however, not limited to rheological characterisation, with further applications of MR to colloidal dispersions including the study of concentrated [64] and multiple emulsions [65] and freezing [66]. These applications have also been extended in recent years, with MR used to characterise surface chemistry [67] and probe interparticle interactions [68].

Since colloidal dispersions are thermodynamically unstable, with collisions between colloids occurring due to both thermal and gravitational motion, products formulated as colloidal dispersions typically exhibit a limited shelf-life. To this end, many studies using MR have investigated colloidal stability. For example, MR imaging and dynamic MR have successfully been applied to investigate the stability of emulsions [65,69–72], suspensions [68], and foams [73] through measurement of concentration and emulsion droplet size distributions. Emulsions have also been studied in the presence of emulsifiers [71] and demulsifiers [74] using these techniques. Most recently, dynamic MR was used to determine the ideal emulsifier for use in the oilfield industry [75]. In Chapters 7 and 8, the study of colloidal stability using MR is extended to provide greater insight into the transient gelation of otherwise stable colloidal dispersions [76]. The interested reader is directed towards Section 1.1.2 for a more complete introduction to colloidal dispersions and discussion of colloidal stability.

2.5 References

[1] Gladden, L.F., 1994, Nuclear magnetic resonance in chemical engineering: principles and applications. *Chem. Eng. Sci.*, **49**, 3339–3408.

[2] Callaghan, P.T., *Principles of Nuclear Magnetic Resonance Microscopy*, Clarendon Press, Oxford, GB, 1993.

[3] Bloch, F., 1946, Nuclear induction. *Phys. Rev.*, **70**, 460–474.

[4] Shannon, C.E., 1949, Communication in the presence of noise. *Proc. Inst. Radio Eng.*, **37**, 10–21.

[5] Levitt, M.H., *Spin Dynamics: Basics of Nuclear Magnetic Resonance*, John Wiley & Sons, Chichester, GB, 2008.

[6] Keeler, J., *Understanding NMR Spectroscopy*, John Wiley & Sons, Chichester, GB, 2010.

[7] Vold, R.L., Waugh, J.S., Klein, M.P. and Phelps, D.E., 1968, Measurement of spin relaxation in complex systems. *J. Chem. Phys.*, **48**, 3831–3832.

[8] Hahn, E.L., 1950, Spin echoes. *Phys. Rev.*, **80**, 580–594.

[9] Carr, H.Y. and Purcell, E.M., 1954, Effects of diffusion on free precession in nuclear magnetic resonance experiments. *Phys. Rev.*, **94**, 630–638.

[10] Meiboom, S. and Gill, D., 1958, Modified spin-echo method for measuring nuclear relaxation times. *Rev. Sci. Instrum.*, **29**, 688–691.

[11] Cotts, R.M., Hoch, M.J.R., Sun, T. and Markert, J.T., 1989, Pulsed field gradient stimulated echo methods for improved NMR diffusion measurements in heterogeneous systems. *J. Magn. Reson.*, **83**, 252–266.

[12] Mansfield, P. and Grannell, P.K., 1973, NMR 'diffraction' in solids? *J. Phys. C: Solid State Phys.*, **6**, L422–L426.

[13] Edelstein, W.A., Hutchison, J.M.S., Johnson, G. and Redpath, T., 1980, Spin warp NMR imaging and applications to human whole-body imaging. *Phys. Med. Biol.*, **25**, 751–756.

[14] Mantle, M.D. and Sederman, A.J., 2003, Dynamic MRI in chemical process and reaction engineering. *Prog. Nucl. Magn. Reson. Spectrosc.*, **43**, 3–60.

[15] Kärger, J. and Heink, W., 1983, The propagator representation of molecular transport in microporous crystallites. *J. Magn. Reson.*, **51**, 1–7.

[16] Maneval, J.E., Powell, R.L., McCarthy, M.J. and McCarthy, K.L., in *Particulate Two-phase Flow*, Butterworth-Heinemann, Boston, US, 1993, pp. 127–140.

[17] Stejskal, E.O. and Tanner, J.E., 1965, Spin diffusion measurements: spin echoes in the presence of a time-dependent field gradient. *J. Chem. Phys.*, **42**, 288–292.

[18] Pope, J.M. and Yao, S., 1993, Quantitative NMR imaging of flow. *Concepts Magn. Reson.*, **5**, 281–302.

[19] Macosko, C.W., *Rheology: Principles, Measurements, and Applications*, John Wiley & Sons, New York, US, 1994.

[20] Callaghan, P.T., 2006, Rheo-NMR and velocity imaging. *Curr. Opin. Colloid Interface Sci.*, **11**, 13–18.

[21] Kalus, J., Neubauer, G. and Schmelzer, U., 1990, A new shear apparatus for small angle neutron scattering (SANS) measurements. *Rev. Sci. Instrum.*, **61**, 3384–3389.

[22] Nakatani, A.I., Waldow, D.A. and Han, C.C., 1992, A rheometer with two-dimensional area detection for light scattering studies of polymer melts and solutions. *Rev. Sci. Instrum.*, **63**, 3590–3598.

[23] Plano, R.J., Safinya, C.R., Sirota, E.B. and Wenzel, L.J., 1993, X-ray Couette shear cell for nonequilibrium structural studies of complex fluids under flow. *Rev. Sci. Instrum.*, **64**, 1309–1318.

[24] Fuller, G.G., *Optical Rheometry of Complex Fluids*, Oxford University Press, New York, US, 1995.

[25] Shapley, N.C., Brown, R.A. and Armstrong, R.C., 2004, Evaluation of particle migration models based on laser Doppler velocimetry measurements in concentrated suspensions. *J. Rheol.*, **48**, 255–279.

[26] Manneville, S., Bécu, L. and Colin, A., 2004, High-frequency ultrasonic speckle velocimetry in sheared complex fluids. *Eur. Phys. J. Appl. Phys.*, **28**, 361–373.

[27] Miller, E. and Rothstein, J.P., 2007, Transient evolution of shear-banding wormlike micellar solutions. *J. Non-Newton. Fluid Mech.*, **143**, 22–37.

[28] Lauri, J., Bykov, A.V. and Myllylä, R., 2011, Determination of suspension viscosity from the flow velocity profile measured by doppler optical coherence tomography. *Photonics Lett. Pol.*, **3**, 82–84.

[29] Harvey, M. and Waigh, T.A., 2011, Optical coherence tomography velocimetry in controlled shear flow. *Phys. Rev. E*, **83**, 1–5.

[30] Haavisto, S., Koponen, A.I. and Salmela, J., 2014, New insight into rheology and flow properties of complex fluids with Doppler optical coherence tomography. *Front. Chem.*, **2**, 27.

[31] Harvey, G., Gachagan, A. and Mutasa, T., 2014, Review of high-power ultrasound—industrial applications and measurement methods. *IEEE Trans. Ultrason. Ferroelectr. Freq. Control*, **61**, 481–495.

[32] Martins, A.F., Esnault, P. and Volino, F., 1986, Measurement of the viscoelastic coefficients of main-chain nematic polymers by an NMR technique. *Phys. Rev. Lett.*, **57**, 1745–1748.

[33] Nakatani, A.I., Poliks, D. and Samulski, E.T., 1990, NMR investigation of chain deformation in sheared polymer fluids. *Macromolecules*, **23**, 2686–2692.

[34] Callaghan, P.T. and Gil, A.M., 1999, ^{1}H NMR spectroscopy of polymers under shear and extensional flow. *Rheol. Acta*, **38**, 528–536.

[35] Xia, Y. and Callaghan, P.T., 1991, Study of shear thinning on high polymer solution using dynamic NMR microscopy. *Macromolecules*, **24**, 4777–4786.

[36] Britton, M.M., Callaghan, P.T., Kilfoil, M.L., Mair, R.W. and Owens, K.M., 1998, NMR velocimetry and spectroscopy at microscopic resolution in small rheometric devices. *Appl. Magn. Reson.*, **15**, 287–301.

[37] Callaghan, P.T., 1999, Rheo-NMR: nuclear magnetic resonance and the rheology of complex fluids. *Rep. Prog. Phys.*, **62**, 599–670.

[38] Bonn, D., Rodts, S., Groenink, M., Rafaï, S., Shahidzadeh-Bonn, N. and Coussot, P., 2008, Some applications of magnetic resonance imaging in fluid mechanics: complex flows and complex fluids. *Annu. Rev. Fluid Mech.*, **40**, 209–233.

[39] Britton, M.M. and Callaghan, P.T., 1997, NMR microscopy and the nonlinear rheology of food materials. *Magn. Reson. Chem.*, **35**, S37–S46.

[40] Britton, M.M. and Callaghan, P.T., 1997, Two-phase shear band structures at uniform stress. *Phys. Rev. Lett.*, **78**, 4930–4933.

[41] Callaghan, P.T., 2008, Rheo NMR and shear banding. *Rheol. Acta*, **47**, 243–255.

[42] Rofe, C.J., Lambert, R.K. and Callaghan, P.T., 1994, Nuclear magnetic resonance imaging of flow for a shear-thinning polymer in cylindrical Couette geometry. *J. Rheol.*, **38**, 875–887.

[43] McKelvey, J.M., *Polymer Processing*, John Wiley & Sons, New York, US, 1962.

[44] Rofe, C.J., Vargas, L. de, Perez-González, J., Lambert, R.K. and Callaghan, P.T., 1996, Nuclear magnetic resonance imaging of apparent slip effects in xanthan solutions. *J. Rheol.*, **40**, 1115–1128.

[45] Bertola, V., Bertrand, F., Tabuteau, H., Bonn, D. and Coussot, P., 2003, Wall slip and yielding in pasty materials. *J. Rheol.*, **47**, 1211–1226.

[46] Hollingsworth, K.G. and Johns, M.L., 2004, Rheo-nuclear magnetic resonance of emulsion systems. *J. Rheol.*, **48**, 787–803.

[47] Mair, R.W. and Callaghan, P.T., 1997, Shear flow of wormlike micelles in pipe and cylindrical Couette geometries as studied by nuclear magnetic resonance microscopy. *J. Rheol.*, **41**, 901–924.

[48] Britton, M.M. and Callaghan, P.T., 1999, Shear banding instability in wormlike micellar solutions. *Eur. Phys. J. B*, **7**, 237–249.

[49] Fischer, E. and Callaghan, P.T., 2001, Shear banding and the isotropic-to-nematic transition in wormlike micelles. *Phys. Rev. E*, **64**, 011501.

[50] López-González, M.R., Holmes, W.M., Callaghan, P.T. and Photinos, P.J., 2004, Shear banding fluctuations and nematic order in wormlike micelles. *Phys. Rev. Lett.*, **93**, 268302.

[51] Graham, A.L., Altobelli, S.A., Fukushima, E., Mondy, L.A. and Stephens, T.S., 1991, Note: NMR imaging of shear-induced diffusion and structure in concentrated suspensions undergoing Couette flow. *J. Rheol.*, **35**, 191–201.

[52] Altobelli, S.A., Givler, R.C. and Fukushima, E., 1991, Velocity and concentration measurements of suspensions by nuclear magnetic resonance imaging. *J. Rheol.*, **35**, 721–734.

[53] Abbott, J.R., Tetlow, N., Graham, A.L., Altobelli, S.A. and Fukushima, E., 1991, Experimental observations of particle migration in concentrated suspensions: Couette flow. *J. Rheol.*, **35**, 773–795.

[54] Drappier, J., Bonn, D., Meunier, J., Lerouge, S., Decruppe, J.-P. and Bertrand, F., 2006, Correlation between birefringent bands and shear bands in surfactant solutions. *J. Stat. Mech.*, **2006**, P04003.

[55] Hu, Y.T., Boltenhagen, P. and Pine, D.J., 1998, Shear thickening in low-concentration solutions of wormlike micelles. I. Direct visualization of transient behavior and phase transitions. *J. Rheol.*, **42**, 1185–1208.

[56] Hu, Y.T., Boltenhagen, P., Matthys, E. and Pine, D.J., 1998, Shear thickening in low-concentration solutions of wormlike micelles. II. Slip, fracture, and stability of the shear-induced phase. *J. Rheol.*, **42**, 1209–1226.

[57] Seymour, J.D., Maneval, J.E., McCarthy, K.L., Powell, R.L. and McCarthy, M.J., 1995, Rheological characterization of fluids using NMR velocity spectrum measurements. *J. Texture Stud.*, **26**, 89–101.

[58] Arola, D.F., Barrall, G.A., Powell, R.L., McCarthy, K.L. and McCarthy, M.J., 1997, Use of nuclear magnetic resonance imaging as a viscometer for process monitoring. *Chem. Eng. Sci.*, **52**, 2049–2057.

[59] Arola, D.F., Powell, R.L., Barrall, G.A. and McCarthy, M.J., 1998, A simplified method for accuracy estimation of nuclear magnetic resonant imaging. *Rev. Sci. Instrum.*, **69**, 3300–3307.

[60] Arola, D.F., Powell, R.L., Barrall, G.A. and McCarthy, M.J., 1999, Pointwise observations for rheological characterization using nuclear magnetic resonance imaging. *J. Rheol.*, **43**, 9–30.

[61] Bergenholtz, J., 2001, Theory of rheology of colloidal dispersions. *Curr. Opin. Colloid Interface Sci.*, **6**, 484–488.

[62] Johns, M.L., 2009, NMR studies of emulsions. *Curr. Opin. Colloid Interface Sci.*, **14**, 178–183.

[63] Novak, J. and Britton, M.M., 2013, Magnetic resonance imaging of the rheology of ionic liquid colloidal suspensions. *Soft Matter*, **9**, 2730–2737.

[64] Balinov, B., Söderman, O. and Ravey, J.C., 1994, Diffraction-like effects observed in the PGSE experiment when applied to a highly concentrated water/oil emulsion. *J. Phys. Chem.*, **98**, 393–395.

[65] Lönnqvist, I., Håkansson, B., Balinov, B. and Söderman, O., 1997, NMR self-diffusion studies of the water and the oil components in a W/O/W emulsion. *J. Colloid Interf. Sci.*, **192**, 66–73.

[66] Hindmarsh, J.P., Hollingsworth, K.G., Wilson, D.I. and Johns, M.L., 2004, An NMR study of the freezing of emulsion-containing drops. *J. Colloid Interf. Sci.*, **275**, 165–171.

[67] Hens, Z. and Martins, J.C., 2013, A solution NMR toolbox for characterizing the surface chemistry of colloidal nanocrystals. *Chem. Mater.*, **25**, 1211–1221.

[68] Cooper, C.L., Cosgrove, T., Duijneveldt, J.S. van, Murray, M. and Prescott, S.W., 2013, The use of solvent relaxation NMR to study colloidal suspensions. *Soft Matter*, **9**, 7211–7228.

[69] Kauten, R.J., Maneval, J.E. and McCarthy, M.J., 1991, Fast determination of spatially localized volume fractions in emulsions. *J. Food Sci.*, **56**, 799–801.

[70] Pilhofer, G.M., McCarthy, M.J., German, J.B. and Kauten, R.J., 1993, Phase separation in optically opaque emulsions. *J. Food Eng.*, **20**, 369–380.

[71] Balinov, B., Urdahl, O., Söderman, O. and Sjöblom, J., 1994, Characterization of water-in-crude oil emulsions by the NMR self-diffusion technique. *Colloids Surf. A: Physicochem. Eng. Aspects*, **82**, 173–181.

[72] Johns, M.L. and Hollingsworth, K.G., 2007, Characterisation of emulsion systems using NMR and MRI. *Prog. Nucl. Magn. Reson. Spectrosc.*, **50**, 51–70.

[73] Smith, K., Burbidge, A., Apperley, D., Hodgkinson, P., Markwell, F.A., Topgaard, D. and Hughes, E., 2016, Stray-field NMR diffusion q-space diffraction imaging of monodisperse coarsening foams. *J. Colloid Interf. Sci.*, **476**, 1–27.

[74] Peña, A.A., Hirasaki, G.J. and Miller, C.A., 2005, Chemically induced destabilization of water-in-crude oil emulsions. *Ind. Eng. Chem. Res.*, **44**, 1139–1149.

[75] Carneiro, G.F., Silva, R.C., Barbosa, L.L., Freitas, J.C.C., Sad, C.M.S., Tose, L.V., Vaz, B.G., Romão, W., De Castro, E.V.R., Neto, A.C. and Lacerda, V., 2015, Characterisation and selection of demulsifiers for water-in-crude oil emulsions using low-field ^{1}H NMR and ESI-FT-ICR MS. *Fuel*, **140**, 762–769.

[76] Bergenholtz, J., Poon, W.C.K. and Fuchs, M., 2003, Gelation in model colloid-polymer mixtures. *Langmuir*, **19**, 4493–4503.

Chapter 3

Characterising power-law fluids using cumulant analysis

Rheology plays an important role in many industrial processes; from baking to catalyst preparation. The characterisation of process fluid rheology is typically performed using conventional benchtop rheometers operating offline. An online, or inline, technique is therefore sought for real-time characterisation, as is required for the optimisation of product properties through careful process control. Until recently, magnetic resonance (MR) was, perhaps, an unlikely choice for this application due to the requirement of high field strength, expensive, superconducting magnet technology. However, recent developments in low field strength, inexpensive, permanent magnet technology have made MR an attractive alternative; it is non-invasive and without limitation on optical opacity.

Rheological characterisation using MR, or MR rheometry, typically uses spatially-resolved measurements of velocity in a method termed MR flow imaging. However, this method is unsuitable for online, real-time application due to the long acquisition times and/or the requirement of high field strengths. Pulsed field gradient (PFG) MR offers an alternative method that extends MR rheometry to low field strengths and single-axis gradient hardware. In this Chapter, a model-dependent approach is developed to enable the rheological characterisation of fluids demonstrating non-Newtonian power-law rheology through a cumulant analysis of the PFG MR data directly. The sensitivity of this approach to noisy data and reduced sampling is investigated using numerical simulations, with validation of the simulated results provided by an experimental case study on aqueous xanthan gum solutions demonstrating power-law rheology.

3.1 Introduction

In Section 1.1.2, the importance of rheology in the manufacture of a catalysed diesel particulate filter (cDPF) was described. However, such importance is not limited to the manufacture of emission control technologies, such as cDPFs, by Johnson Matthey, but realised in a large number of industrial applications, with those involving flow—such as coating, mixing, and spraying—particularly sensitive to rheology [1]. Constitutive equations, introduced in Section 1.2, offer a convenient way for engineers to describe (or model) the rheology of process fluids using only rheological parameters appropriate to that equation. Whilst fluids with increasingly complex rheology require increasingly complex constitutive equations, the rheology of many process fluids can be accurately described, over a suitable range of shear rates, using the Ostwald–de Waele [2] constitutive equation, or power-law model, given by

$$\tau\left(\dot{\gamma}\right) = K\dot{\gamma}^{n}, \tag{3.1}$$

with τ and $\dot{\gamma}$ the shear stress and shear rate, respectively, n the flow behaviour index, and K the consistency factor. As discussed in Section 1.2, the smaller the value of n, the greater the degree of shear-thinning behaviour. Perturbations in n are, therefore, responsible for considerable changes in rheology, with the control and optimisation of n critical to many industrial processes. The rheological characterisation of process fluids is typically performed using benchtop rheometers operating in an offline configuration. An online, or inline, technique is therefore sought for the real-time rheological characterisation of process fluids, as is required for the optimisation of product properties through process control.

Rheological characterisation using magnetic resonance (MR) often utilises spatially-resolved measurements of velocity, obtained using MR flow imaging, to characterise local shear rates [3]. Although this approach may be applied to any flow geometry—including Couette cell, cone-and-plate, and parallel plate geometries [4]—only flow in a cylindrical pipe is suitable for online, or inline, application. Therefore, only a pipe flow geometry is considered in this Chapter, with the interested reader directed towards Section 2.4.1 for a general review of so-called MR rheometry. In a pipe flow geometry, a corresponding measurement of the pressure drop may be used to quantify local shear stresses and, when combined with local shear rates, the flow curve of the fluid under

study. This approach was used by Arola *et al.* [5–7] to characterise the flow curve of various non-Newtonian fluids. A regression of a constitutive equation to the flow curve may then be performed, if required, to estimate the rheological parameters. However, the accurate estimation of the rheological parameters using this approach requires an accurate measurement of velocity and pressure drop, with the range of shear rates that the flow curve is accurate over sensitive to a combination of velocity resolution, number of spatially-resolved data points, and flow properties [6]. The accuracy of the measured velocity data is sensitive to a combination of the signal-to-noise ratio (SNR) and the number of spatially-resolved data points. For a given accrued phase shift, ϕ, resulting from coherent motion, the SNR defines the velocity-to-noise ratio (VNR) [8], where

$$\mathrm{VNR} = \frac{|\phi|}{\sqrt{2}}\mathrm{SNR} \tag{3.2}$$

and $|...|$ represents the magnitude of the data, with VNR therefore directly proportional to the SNR of the MR experiment and $|\phi|$. For these reasons, depending on the system under study, more than 100 spatially-resolved velocity data points might be required to ensure accurate rheological characterisation [5]. Whilst conventional MR flow imaging techniques, *i.e.* single spin echo pulse sequences, limit the temporal resolution of this approach, these are, perhaps, the most robust way of measuring velocity. Although a comprehensive comparison of fast MR flow imaging techniques is beyond the scope of this thesis, a summary of such techniques is provided in Table 3.1.

Table 3.1: Comparison of MR flow imaging pulse sequences, where all values reported are approximate and system-dependent. Adapted from Gladden and Sederman [9].

pulse sequence	acquisition time	velocity measured	spatial resolution
spin echo	1–100 min	$\leq 5\,\mathrm{m\,s^{-1}}$	$< 50\,\mu\mathrm{m}$
EPI	20–100 ms	$1–100\,\mathrm{cm\,s^{-1}}$	50–500 µm
spiral	3–25 ms	$\leq 5\,\mathrm{m\,s^{-1}}$	50–500 µm
RARE	2–10 s	$\leq 10\,\mathrm{cm\,s^{-1}}$	$< 50\,\mu\mathrm{m}$
FLASH	> 150 ms	$50\,\mathrm{cm\,s^{-1}}$	$> 50\,\mu\mathrm{m}$
SPI (SPRITE)	seconds to hours	$0.5–50\,\mathrm{m\,s^{-1}}$	$< 50\,\mu\mathrm{m}$

The ideal technique for online, or inline, monitoring of industrial processes in real-time must be robust; that is, suitable for application to all process fluids and flows [10]. Spiral [11] and EPI (echo planar imaging) [12] techniques offer the fastest image acquisition times but are, perhaps, the least robust of those techniques listed in Table 3.1, with both techniques requiring long T_2 and T_2^* due to the long spatial encoding times. Furthermore, the spiral technique is sensitive to background magnetic field gradients and requires complex image reconstruction. Although the RARE (rapid imaging with refocused echoes) [13] technique is robust to short T_2^*, it requires long T_2 and can measure only a limited range of velocities. The FLASH (fast low angle shot) [14] technique is robust to short T_2 and short T_2^*, however, the low SNR associated with FLASH is often unable to provide the spatial resolution required. Spin echo and SPI (single point imaging) or SPRITE (single point ramped imaging with T_1 enhancement) techniques offer the slowest acquisition times but are the most robust of those techniques listed in Table 3.1, with both techniques robust to short T_2 and T_2^* and capable of providing the spatial resolution and measuring the range of velocities required. The robust rheological characterisation of process fluids in real-time using MR flow imaging is, therefore, experimentally challenging. Furthermore, the requirement of expensive spatial encoding gradient hardware, coupled with the need for high SNR, makes the implementation of these pulse sequences problematic using low-field MR hardware since a reduction in the external magnetic field strength, B_0, is responsible for a reduction in SNR. A transition to low-field MR hardware is necessary for online, or inline, rheological characterisation due to a reduction in cost, increase in portability, and reduction in safety concerns when compared with high-field MR hardware.

To this end, recent research has focused on the development of new acquisition and analysis strategies enabling flow and rheological characterisation at low field strengths and in real-time. For example, Osán *et al.* [15] exploited the sensitivity of the Carr–Purcell Meiboom–Gill (CPMG) pulse sequence [16,17], as introduced in Section 2.1.4, to molecular displacement to estimate the mean fluid displacement in a measurement lasting only 2 s. During the train of 180° refocusing pulses, the outflow of spins from the excitation region is responsible for a loss of signal, with the loss of signal proportional to the mean fluid displacement. Although this represents a volume-averaged method, requiring no spatial encoding gradient hardware and offering an increase in SNR when compared with spatially-resolved methods, this approach is an indirect measurement of velocity. In contrast, phase encoding MR techniques offer a direct measurement of velocity and are, perhaps, the most robust and quantitative way of measuring flow [18].

Pulsed field gradient (PFG) MR is a phase encoding technique involving the application of a bipolar magnetic field gradient pair, in conjunction with spin echoes [19] or stimulated echoes [20]. Molecules experiencing coherent motion, *i.e.* flow, will accrue a phase shift that is proportional to their displacement, $\mathbf{R}$, over a flow contrast time, Δ, with the accrued ϕ equal to $\gamma\delta\mathbf{g}\cdot\mathbf{R}$, where γ is the gyromagnetic ratio of the nucleus under study and δ is the duration of the flow encoding gradient, $\mathbf{g}$. For simplicity, vector notation will be dropped with ζ the molecular displacement in the direction of the flow gradient, applied with magnitude g in a direction perpendicular to the flow. Note that ζ and velocity, v, may be used interchangeably, where $\zeta = v\Delta$. The signal is sampled in q-space, defined as $q = (1/2\pi)\,\gamma g\delta$, with q-space traversed by varying either g or δ.

Early work by Packer [21] theoretically investigated the effect of coherent motion on the signal in q-space for a fixed flow gradient, *i.e.* with Δ equal to δ and $\phi = \gamma v g \delta^2$. This was validated experimentally to characterise a single-velocity flow system. For multiple-velocity flow systems, the acquired signal in q-space, $S(q)$, is a superposition of signals from individual isochromats, each possessing a different phase shift. Fourier transformation of $S(q)$ yields a volume-averaged displacement probability distribution, or flow propagator [22], that completely characterises the flow under study [23]. The signal acquired in q-space in the absence of molecular self-diffusion, which is responsible for broadening of the flow propagator and an attenuation of the signal due to dephasing of the spin ensemble [19], is given by

$$S(q) = \int p(\zeta) \exp\left[\mathrm{i}2\pi q\zeta\right] \mathrm{d}\zeta, \tag{3.3}$$

where $p(\zeta)$ represents the flow propagator and the signal in q-space and the flow propagator represent mutually conjugate Fourier pairs. It is interesting to note that, as the units of q are reciprocal displacement units, the field-of-flow (FOF) of $p(\zeta)$ is defined by the sampling density of the signal in q-space and displacement resolution is defined by the range of q-space sampled. Flow propagators were used by Grover and Singer [24] to characterise flow through a human finger, and later by Garroway [25] for Newtonian flow through a cylindrical pipe. More recent developments in this area have also been made [26]. The use of flow propagators for rheological characterisation was theoretically described by McCarthy *et al.* [27], and qualitative experimental agreement was later demonstrated for a range of Newtonian and non-Newtonian fluids [28]. Despite

recent efforts [29], the quantitative use of flow propagators remains challenging. In this Chapter, a new approach utilising PFG MR and cumulant analysis is introduced to enable the estimation of n describing the non-linear contribution to the stress response of a fluid demonstrating power-law rheology, during flow, using only single-axis gradient hardware. The removal of expensive three-axis spatial encoding gradient hardware increases the SNR associated with the MR measurement and facilitates a transition to low-field MR hardware. A more general introduction to MR flow imaging and PFG MR can be found in Section 2.3.

Using simple fluid mechanics it can be shown that, for the flow of a fluid demonstrating power-law rheology through a cylindrical pipe, the fluid displacement at radial position r is given by

$$\zeta(r) = \langle\zeta\rangle \left(\frac{3n+1}{n+1}\right)\left(1 - \left(\frac{r}{R}\right)^{\frac{n+1}{n}}\right), \tag{3.4}$$

where $\langle\zeta\rangle$ is the mean fluid displacement and R is the pipe radius. Figure 3.1 shows displacement profiles for three example fluids and demonstrates a reduction in the maximum displacement as n is reduced. It follows that perturbations in n will, therefore, be expected to induce changes in $p(\zeta)$. However, the use of $p(\zeta)$ for the rheological characterisation of non-Newtonian fluids is problematic due to the strict sampling requirements imposed to prevent the introduction of artefacts during Fourier transform. Firstly, $S(q)$ is required to be sampled at adequate density, as defined by the FOF, to prevent fold-over. Secondly, $S(q)$ is required to be sampled over a sufficient range of q-space, such that $S(q)$ approaches zero, to prevent truncation artefacts. The introduction of truncation artefacts during Fourier transform may, however, be experimentally unavoidable due to gradient strength limitations and spin-spin relaxation times which restrict the range of q-space accessible. Furthermore, the long acquisition times associated with such sampling requirements, dependent on spin-lattice relaxation times but typically several tens of minutes, prevent the real-time rheological characterisation of non-Newtonian fluids using this approach. To this end, an alternative approach is developed in this Chapter which eliminates the need for Fourier transform and enables the estimation of n for fluids demonstrating power-law rheology from $S(q)$ directly. The principles outlining this approach, involving a cumulant analysis of the signal in q-space, are now introduced.

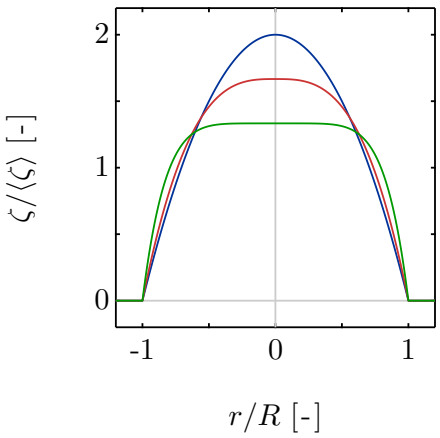

Fig. 3.1: Fluid displacement (represented as a fraction of the mean fluid displacement) plotted as a function of radial position (represented as a fraction of the pipe radius) for three example fluids demonstrating power-law rheology; (—) $n = 1.0$, (—) $n = 0.5$, and (—) $n = 0.2$. The displacement data were generated using Eq. (3.4).

Probability distributions, such as $p(\zeta)$, can be specified using moments. Changes in $p(\zeta)$ due to perturbations in n are expected to induce changes in the moments of $p(\zeta)$. Moments of a probability distribution may be taken about 0, known as raw moments, or about the mean, known as central moments. For example, the raw moments of $p(\zeta)$ are given by

$$\mu'_j = \sum \zeta^j p(\zeta), \tag{3.5}$$

where μ'_j is the j^{th} raw moment of $p(\zeta)$. Note that the first raw moment, μ'_1, is known as the mean and denoted μ. The central moments of $p(\zeta)$ are then given by

$$\mu_j = \sum (\zeta - \mu)^j p(\zeta), \tag{3.6}$$

where μ_j is the j^{th} central moment of $p(\zeta)$. Whilst Eqs. (3.5) and (3.6) are unsuitable for the real-time estimation of the moments of $p(\zeta)$, due to the long acquisition times associated with the measurement of $p(\zeta)$, moments may also be estimated using the characteristic function of $p(\zeta)$. The characteristic function of a probability distribution is defined as the Fourier transform of the distribution. It is known, from Eq. (3.3), that

$S(q)$ and $p(\zeta)$ represent mutually conjugate Fourier pairs, with $S(q)$ the characteristic function of $p(\zeta)$. The raw moments of $p(\zeta)$ are then given by

$$S(q) = \sum_{j=0}^{\infty} \frac{(\mathrm{i}2\pi q)^j}{j!} \mu'_j, \tag{3.7}$$

where $p(\zeta)$ is uniquely specified by $S(q)$ [30]. Using Eq. (3.7), the raw moments of $p(\zeta)$ may be determined from $S(q)$ directly, eliminating the need for Fourier transform and the associated strict sampling requirements and long acquisition times. However, cumulants are often preferred for simplicity; only two cumulants are required to specify a Gaussian probability distribution, with cumulants above second order equal to zero, compared to an infinite number of moments [31,32]. The cumulant generating function is given by the natural logarithm of the characteristic function and defined as

$$\ln S(q) = \sum_{j=1}^{\infty} \frac{(\mathrm{i}2\pi q)^j}{j!} \kappa_j, \tag{3.8}$$

where κ_j corresponds to the j^{th} cumulant. From the expansion of Eq. (3.8) it is noted that the log-magnitude of $S(q)$ is defined by even powers of q, whilst odd powers of q give the phase of $S(q)$. It can be shown that the first four cumulants have the form

$$\kappa_1 = \mu, \tag{3.9}$$

$$\kappa_2 = \mu_2, \tag{3.10}$$

$$\kappa_3 = \mu_3, \tag{3.11}$$

$$\kappa_4 = \mu_4 - 3\mu_2^2, \tag{3.12}$$

with κ_1, κ_2, κ_3, and κ_4 known as mean, variance, skewness, and kurtosis, respectively. Linear least squares (LLS) regression of Eq. (3.8) to the experimental dataset provides a measure of the cumulants specifying $p(\zeta)$. Note that $p(\zeta)$ and $S(q)$ are non-uniquely specified by their cumulants (or their moments).

Cumulant analysis, therefore, offers a simple approach which eliminates strict sampling requirements and removes prohibitively long acquisition times. This approach, which has previously been used in the MR community to analyse the flow of Newtonian and non-Newtonian fluids at low SNR [33,34], is here developed to enable the estimation of n for fluids demonstrating power-law rheology. The flow propagator is non-Gaussian and so cumulants above second order can be extracted. If cumulants are known for a suitable range of n, with given experimental parameters, the estimation of n is possible through comparison of the experimental cumulants with those obtained numerically. Furthermore, the error associated with a cumulant may be determined by performing a LLS regression across an increasing range of q-space, as outlined by Scheven *et al.* [34], with the standard deviation of the cumulants providing a measure of the error. The robustness of cumulant analysis to SNR is here exploited to determine the minimum data needed to estimate n with reasonable accuracy, here defined as $\pm 5\%$, this error being typical of conventional rheometry methods [35]. Several variables may contribute to the accuracy of the characterisation; namely SNR, number of sampled q-space data points, and n characterising the fluid under study. These three variables are investigated systematically using simulated MR data. The relative contributions of each variable to the accuracy of the rheological characterisation are also considered. Validation of the numerical simulations is provided through an experimental study on model fluids demonstrating Newtonian and power-law rheology, namely water and xanthan gum-in-water solutions, using MR and conventional rheometry.

The proposed cumulant MR approach is model-dependent and so caution must be taken to ensure that the rheology of the fluid under study can be accurately described using the power-law model over the shear rate range of the experiment. Any deviation from power-law rheology may be responsible for an increase in the error associated with the estimation of n, however, the accuracy of this approach is independent of the shear rate range if power-law rheology is maintained. By comparison, MR flow imaging and conventional rheometry provide model-independent data, with a non-linear least squares (NLLS) regression of Eq. (3.1) to the flow curve performed at a later time.

3.2 Model development

The cumulant MR approach developed here, as summarised in Fig. 3.2, first requires the numerical simulation of $S(q)$ for a suitable range of n. Previous work by Kaiser

et al. [36] generated $S(q)$ numerically using Eq. (3.3) for a finite spin ensemble of 10^4 nuclear spins. In this work, an analytical expression derived by McCarthy *et al.* [27] is used to describe $p(\zeta)$, and generate $S(q)$ numerically, as a function of n. The details of the derivation are shown below.

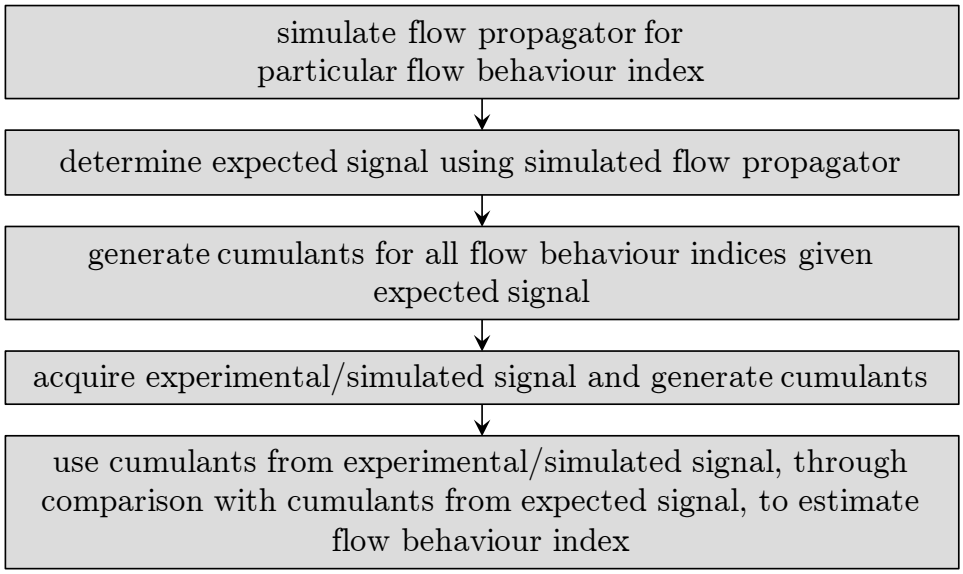

Fig. 3.2: A block diagram outlining the five key stages in the proposed cumulant MR approach.

From Eq. (3.4), ζ can be correlated with radial position, r, for a fluid demonstrating power-law rheology using

$$r(\zeta) = R\left(1 - \frac{\zeta}{\zeta_{\max}}\right)^{\frac{n}{n+1}}, \tag{3.13}$$

where $\zeta_{\max}$ is the maximum fluid displacement for a given n and is found by evaluating Eq. (3.4) at $r = 0\,\mathrm{mm}$. If a homogeneous spin density is assumed, $p(\zeta)$ per unit length is proportional to the area of the flow field associated with ζ, given by the differential of $A(\zeta)$ and denoted $\mathrm{d}A$, with $A(\zeta) = \pi r(\zeta)^2$. In the absence of self-diffusion, $p(\zeta)$ can be described as

$$p(\zeta) \propto \frac{\mathrm{d}}{\mathrm{d}\zeta}\left(\pi R^2\left(1 - \frac{\zeta}{\zeta_{\max}}\right)^{\frac{2n}{n+1}}\right). \tag{3.14}$$

We now drop the constant πR^2 for convenience and evaluate the differential in Eq. (3.14) to obtain an analytical expression describing $p(\zeta)$ as a function of n, given by

$$p(\zeta, n) = \begin{cases} \dfrac{1}{\zeta_{\max}} \left(\dfrac{2n}{n+1} \right) \left(1 - \dfrac{\zeta}{\zeta_{\max}} \right)^{\frac{n-1}{n+1}}, & 0 < \zeta < \zeta_{\max}, \\ 0, & \zeta_{\max} \leq \zeta. \end{cases} \tag{3.15}$$

Similar expressions describing $p(\zeta)$ for fluids demonstrating Newtonian and Bingham rheology may be found in the literature [27,28]. Figure 3.3(a) shows $p(\zeta)$ for the three examples of n considered in Fig. 3.1; it is seen that a reduction in n is responsible for a reduction in $\zeta_{\max}$ and an increase in the maximum probability. These changes are due to a flattening of the displacement profile with decreasing n, as shown in Fig. 3.1. When the constitutive equation describing the rheological behaviour of the fluid under study does not allow the differentiation of Eq. (3.14), $p(\zeta)$ can be determined numerically.

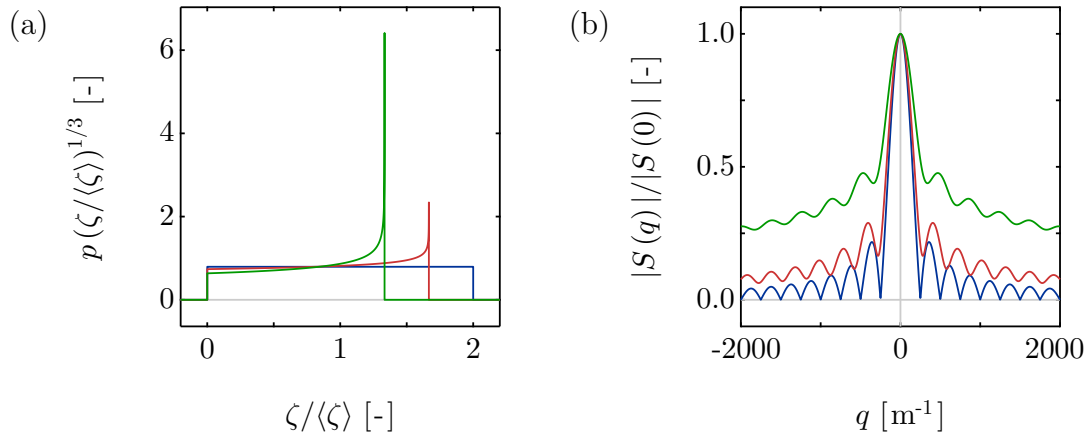

Fig. 3.3: (a) Flow propagators and (b) the corresponding magnitude of $S(q)$ across a range of $\pm 2000\,\mathrm{m}^{-1}$ for three example fluids; where (—) $n = 1.0$, (—) $n = 0.5$, and (—) $n = 0.2$. The expected $S(q)$ data were simulated with $\langle\zeta\rangle = 2\,\mathrm{mm}$ in the absence of self-diffusion and the outflow of spins. The flow propagators have been scaled to the power of the third root for clarity.

Experimentally, an outflow of spins will lead to some loss of signal, with the amount lost proportional to the local displacement. To account for this, a correction is applied

to $p(\zeta, n)$ given by

$$p'(\zeta, n) = (1 - \Lambda)\, p(\zeta, n), \tag{3.16}$$

where $p'(\zeta, n)$ represents the experimentally-acquired flow propagator and Λ is given by ζ/L, with L the length of the excitation region as determined by the experimental set-up. Alternatively, Eq. (3.16) may be applied to $p'(\zeta, n)$ to recover $p(\zeta, n)$. Further, self-diffusion is responsible for the Gaussian broadening of $p'(\zeta)$ such that the expected complex signal in q-space, as a function of n, becomes

$$\frac{S(q, n)}{|S(0)|} = \int p'(\zeta, n) \exp\left[\mathrm{i}2\pi q\zeta - 4\pi^2 D\left(\Delta - \frac{\delta}{3}\right) q^2\right] \mathrm{d}\zeta, \tag{3.17}$$

where D is the self-diffusion coefficient. Changes in the flow propagators caused by a reduction in n, as observed in Fig. 3.3(a), are shown in Fig. 3.3(b) to cause a decrease in the frequency of the oscillations in $S(q)$ and also an increase in $|S(q)|$ at the limits of q-space sampled. The existence of a relationship between $S(q)$ and n makes PFG MR an ideal tool for the estimation of n; it is non-invasive and not limited by optical opacity, offering advantages over alternative imaging and sensor techniques. This is a model-dependent approach, so holds true only for those instances where the rheology of a fluid may be accurately described by the power-law model over the range of shear rates investigated.

The log-magnitude and phase of $S(q)$ can be accurately approximated using the cumulant generating function given by Eq. (3.8). For a Gaussian probability distribution, a truncated cumulant expansion may be used with cumulants above second order zero. In the present application, non-Gaussian probability distributions such as those shown in Fig. 3.3(a) are expected with cumulants above second order non-zero; systematic residuals may be introduced if the log-magnitude and phase of $S(q)$ cannot be accurately represented by a truncated cumulant expansion. To reduce the introduction of systematic residuals during the LLS regression of Eq. (3.8) to the log-magnitude and phase of $S(q)$, a maximum fit range is evaluated using the goodness-of-fit parameter, Q. In the absence of systematic residuals and in the presence of Gaussian noise, the probability of the sum of squared residuals obtained, χ^2, is described using a Gaussian

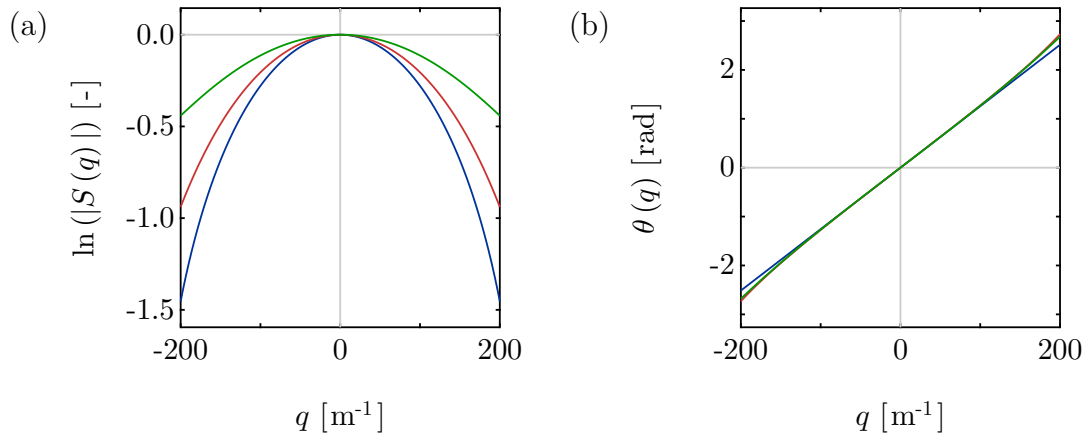

Fig. 3.4: The evolution of the (a) log-magnitude and (b) phase of $S\,(q)$ over low-q for three example fluids; where (—) $n = 1.0$, (—) $n = 0.5$, and (—) $n = 0.2$. The expected $S\,(q)$ data were simulated with $\langle\zeta\rangle = 2\,\text{mm}$ in the absence of self-diffusion and the outflow of spins.

distribution. The goodness-of-fit parameter estimates the likelihood that χ^2 occurred due to Gaussian noise; if χ^2 is less than expected, $Q = 1$ and systematic residuals are unlikely, whilst if χ^2 is greater than expected, $Q = 0$ with systematic residuals likely. Note that Q is given by the incomplete gamma function,

$$Q \equiv \frac{1}{\Gamma\,(\upsilon/2)} \int_{\chi^2/(2\sigma^2)}^{\infty} s^{\frac{\upsilon}{2}-1} \exp\left[-s\right] \mathrm{d}s, \tag{3.18}$$

where Γ is a gamma function, σ the standard deviation of the noise, and υ the number of data points minus the number of unknown fitting parameters, *i.e.* the degrees of freedom. Using Eq. (3.18), Q is evaluated across an increasing range of q-space, with a critical Q defined, Q_c, below which the fit is considered unacceptable. The maximum fit range, $|q_\text{max}|$, is the maximum range of q for which $Q > Q_\text{c}$. Although Q_c may vary between 10^{-3} and 10^{-1}, a value of $Q_\text{c} = 0.05$ is selected based on previous work [34]. For a more complete introduction to fit quality, and general least squares regression, the interested reader is directed towards the textbooks of Bevington and Robinson [37] and Press *et al.* [38].

In the present application, the requirement of higher-order cumulants necessary to specify the oscillations observed in Fig. 3.3(b) is removed by considering $S\,(q)$ over a low-q range. Figure 3.4 shows the (a) log-magnitude and (b) phase of $S\,(q)$ over a low-q

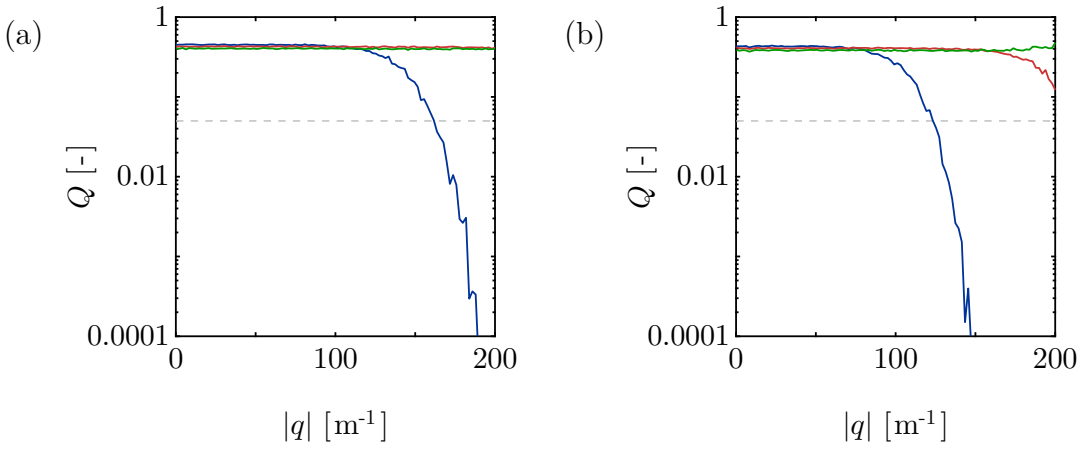

Fig. 3.5: The evolution of Q following the regression of a truncated cumulant expansion to the (a) log-magnitude and (b) phase of $S(q)$ over a low-q range for $n = 1.0$, with the inclusion of cumulants up to (—) second, (—) fourth, and (—) sixth order. The expected $S(q)$ data were simulated with 128 sampled q-space data points, SNR = 100, and $\langle\zeta\rangle = 2\,\text{mm}$ in the absence of self-diffusion and the outflow of spins.

range for three examples of n, with θ observed in Fig. 3.4(b) to increase approximately linearly with q. Such data, in the presence of pseudo-random Gaussian noise, were used to quantify Q across an increasing range of q and following the inclusion of higher-order cumulants. The values of Q obtained are summarised in Fig. 3.5 for the (a) log-magnitude and (b) phase of $S(q)$. As expected, Q decreases with an increasing range of q, whilst the inclusion of higher-order cumulants is responsible for an increase in Q. However, for $Q_\text{c} = 0.05$ and over a low-q range of $\pm 0.4\langle\zeta\rangle^{-1}\,\text{m}^{-1}$, only cumulants up to fourth order need be considered when $n \leq 1.0$ and SNR $< 10\,000$. Note that $|q_\text{max}|$ increases with decreasing SNR. The log-magnitude and phase of $S(q)$ can, therefore, be accurately represented over a low-q range using

$$\ln\left(|S(q)|\right) = -\frac{1}{2}\kappa_2\left(2\pi q\right)^2 + \frac{1}{24}\kappa_4\left(2\pi q\right)^4, \tag{3.19}$$

$$\theta(q) = \kappa_1\left(2\pi q\right) - \frac{1}{6}\kappa_3\left(2\pi q\right)^3, \tag{3.20}$$

if free of systematic residuals, as can arise from broken Hermitian symmetry due to experimental artefacts. If the non-Hermitian component is a small fraction of $S(q)$, then $S(q)$ may be symmetrised using a method outlined by Scheven *et al.* [34].

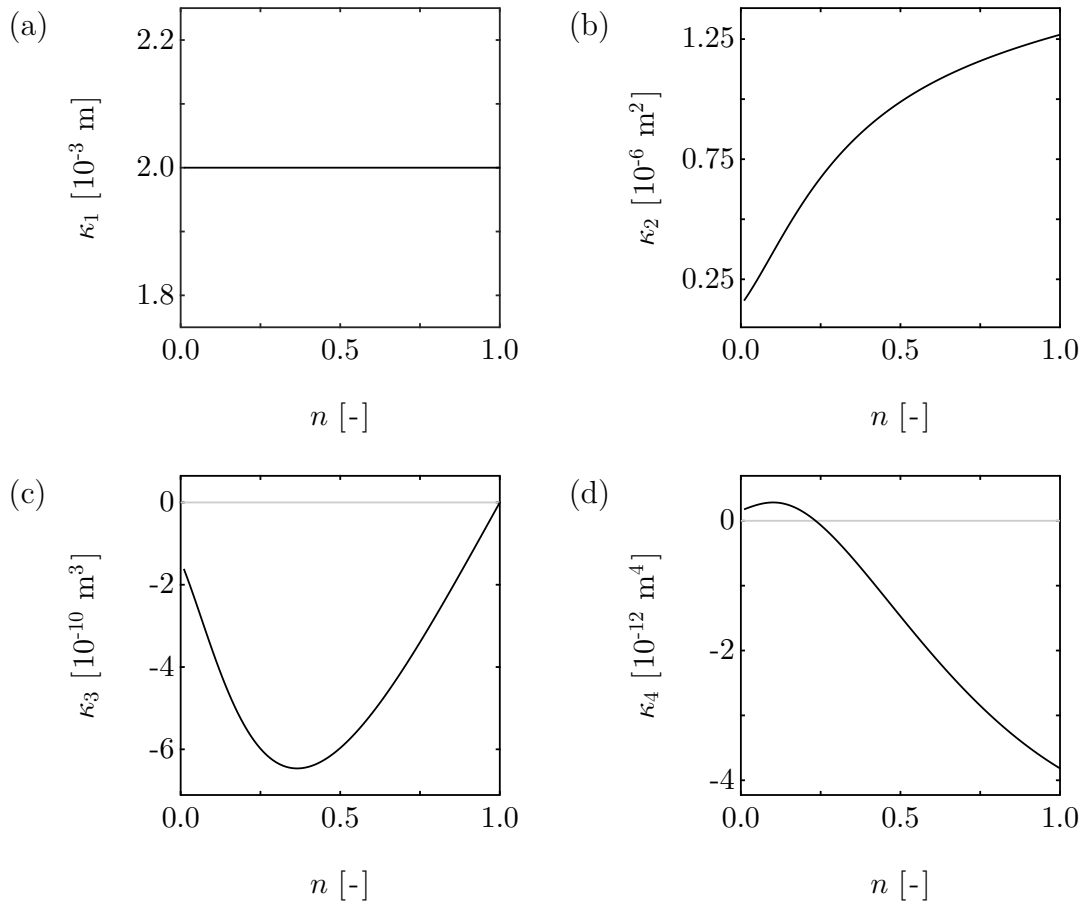

Fig. 3.6: (a) First, (b) second, (c) third, and (d) fourth cumulants plotted as a function of n. The expected $S(q)$ data were simulated with $\langle\zeta\rangle = 2\,\text{mm}$ in the absence of self-diffusion and the outflow of spins.

A LLS regression of Eqs. (3.19) and (3.20) is performed across an increasing range of q, to the upper limit of $|q_{\max}|$, to obtain multiple cumulants. Note that lower limits on the fit range, defined as $2^{-1/4}\,|q_{\max}|$ for the log-magnitude and $2^{-1/3}\,|q_{\max}|$ for the phase of $S(q)$, are imposed, as outlined in the literature [34]. The cumulants reported in this Chapter are the Q-weighted mean cumulant values and the errors are equal to the standard deviation of the cumulants. If the limit of $|q_{\max}|$ is not reached, then $|q_{\max}|$ can be assumed to equal the maximum value of q-space sampled. Equations (3.15) to (3.17) can then be used to generate the expected $S(q)$ data for a suitable range of n and with typical experimental parameters. Due to the relationship between $S(q)$ and ζ, as explained by Eq. (3.17), the numerical simulation of $S(q)$ requires prior knowledge of $\langle\zeta\rangle$. Fortunately, $\langle\zeta\rangle$ can be obtained using Eq. (3.20), where $\langle\zeta\rangle = \kappa_1$, with $\theta(q)$ data acquired experimentally. Using the methods outlined previously, cumulants for all n

were then obtained from the expected $S(q)$ data. The relationship between cumulants and n is shown in Fig. 3.6 for (a) κ_1, (b) κ_2, (c) κ_3, and (d) κ_4, where κ_2 is observed to be unique in its solution of n. If we assume a Gaussian distribution of cumulants corresponding to the increasing fit range, due to random Gaussian noise, a probability distribution of n can be produced for each cumulant above first order using the mean cumulant value and the standard deviation of the cumulants. The product of the three distributions, denoted $p(n)$ and given by $p(n,\kappa_2)\,p(n,\kappa_3)\,p(n,\kappa_4)$, gives the overall distribution. The n values reported in this Chapter correspond to the mean n values calculated from $p(n)$, with the standard deviations a measure of the uncertainty.

3.3 Materials and methods

3.3.1 Simulations

Numerical simulations were performed in MATLAB 2012b, operating under Windows 7, to examine the sensitivity of the proposed cumulant MR approach to important experimental parameters. The simulated data were generated by the addition of pseudo-random Gaussian noise in quadrature, with zero mean and standard deviation σ, to noise-free data obtained using Eq. (3.17), with

$$\frac{S(q,n)}{|S(0)|} = \int p'(\zeta,n)\exp\left[\mathrm{i}2\pi q\zeta - 4\pi^2 D\left(\Delta - \frac{\delta}{3}\right)q^2\right]\mathrm{d}\zeta + e(q) \tag{3.21}$$

and where $e(q)$ represents noise. SNR is defined as the ratio of the signal intensity at the centre of q-space to σ. Simulation parameters, including flow gradient timings and magnitudes, were identical to those experimental parameters outlined in Section 3.3.2 for the acquisition of low-q data. Remaining parameters are defined as follows:

- The value of $\zeta_{\max}$ was determined by evaluating Eq. (3.4) at $r = 0\,\mathrm{mm}$ for each value of n, and $p'(\zeta,n)$ was determined for 2^{15} linear increments in ζ between zero and $\zeta_{\max}$, with $\langle\zeta\rangle = 3.57\,\mathrm{mm}$, equal to that used experimentally.
- n was increased linearly between 0.1 and 1.0 in 10 steps.
- q-space was sampled linearly over a low-q range of $\pm 0.4\langle\zeta\rangle^{-1}\,\mathrm{m}^{-1}$ using 2^A points, with A taking integer values between 1 and 10 to sample 2–1024 points.

- Noise, *i.e.* the noise-to-signal ratio represented as a percentage, was incremented linearly between 0 and 10% in 11 steps, corresponding to an SNR range of 10–∞. Note that SNR = 100 is equal to 1% noise.

Simulations were repeated 10^2 times, each with pseudo-random Gaussian noise, for all combinations of experimental parameters. Mean cumulants and mean n were determined for each repetition using the methods outlined in Section 3.2, and the simulation values reported are the mean and standard deviation, *i.e.* the uncertainty, of the mean cumulants and mean n, respectively. To generate cumulant data for comparison with experimental data, 150 increments in n were utilised evenly spaced between 0.01 and 1.50 to provide a resolution in n of 0.01.

3.3.2 Experimental

Materials and experimental set-up

Aqueous solutions of xanthan gum (Sigma Aldrich, GB), a polysaccharide commonly used for rheology modification, were prepared at concentrations of 0.0, 0.2, 0.4, and 0.6 wt% using deionised water (ELGA Purelab Option). Dilute solutions of xanthan gum-in-water have previously been shown to demonstrate shear-thinning behaviour [39], with power-law rheology expected across a suitable range of shear rates [40]. Complete dissolution of xanthan gum was achieved by stirring for 8 h using an overhead stirrer (Ika–Werke RW20); care was taken to prevent air entrapment during stirring.

A schematic representation of the experimental set-up is shown in Fig. 3.7. The flow system, comprising of a 14 mm inner diameter (i.d.) acrylic pipe of length 2.0 m and a total loop volume of 1.5 L, was operated in a closed loop configuration. A peristaltic pump (MasterFlex Console Drive) capable of delivering volumetric flow rates, $\dot{V}$, of up to 50 mL s^{-1} was used and steady flow was ensured through use of a flow pulsation dampener. To ensure developed flow in the region of pipe under study, it was necessary to consider the hydrodynamic entrance length, l, given by

$$\frac{l}{d} = 0.05\mathrm{Re} \tag{3.22}$$

for the laminar flow of a Newtonian fluid, where d is the pipe diameter and Re is the

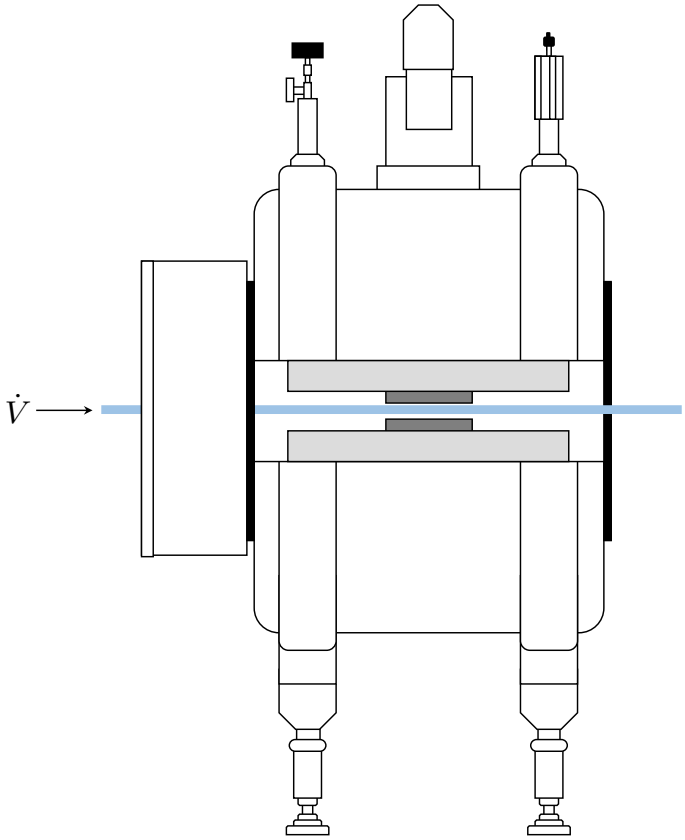

Fig. 3.7: A schematic of the experimental set-up, showing a 2 T horizontal-bore superconducting magnet, equipped with (●) three-axis gradient hardware and (●) r.f. coil, and (●) flow system.

Reynolds number, defined as

$$\mathrm{Re} = \frac{\rho \langle v \rangle d}{\eta}, \tag{3.23}$$

with ρ the fluid density, $\langle v \rangle$ the mean fluid velocity, equal to $\langle \zeta \rangle \Delta^{-1}$, and η the shear viscosity. Laminar flow is typically observed for Reynolds numbers up to 2000 [41], such that an entrance length of up to 100 times the pipe i.d. is necessary to ensure developed flow; in this work, the radiofrequency (r.f.) coil was positioned 1.5 m downstream of the pipe inlet. The experiments were performed at a single, fixed $\dot{V} = 11.5 \pm 0.5\,\mathrm{mL\,s^{-1}}$, measured gravimetrically, with $\langle v \rangle = 75 \pm 4\,\mathrm{mm\,s^{-1}}$ and a shear rate range of $1\text{–}100\,\mathrm{s^{-1}}$, as determined from the MR flow imaging data. This is within the laminar flow regime.

Magnetic resonance

All experiments were performed on a Bruker AV85 spectrometer operating with a 2 T horizontal-bore superconducting magnet, shown schematically in Fig. 3.7. The magnet was fitted with a 60 mm i.d. birdcage r.f. coil tuned to a frequency of 85.2 MHz for the ^{1}H resonance. A three-axis gradient system with a maximum gradient strength of 10.7 G cm^{-1} was used for spatial and flow encoding.

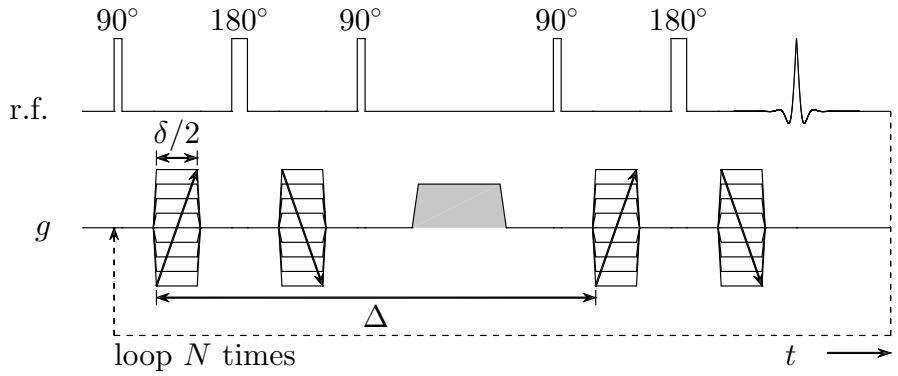

Fig. 3.8: A schematic of the 13-interval APGSTE sequence used for the acquisition of the flow propagator and low-q data for cumulant analysis, complete with (●) homospoil.

The 13-interval alternating pulsed field gradient stimulated echo (APGSTE) pulse sequence [42] shown in Fig. 3.8 was used to sample the high-q data required to obtain a flow propagator and the low-q data required for cumulant analysis. These two sets of data are not acquired simultaneously due to the sampling requirements associated with the use of a Fourier transform, as outlined in Section 3.1. To sample the high-q data required to obtain a flow propagator, flow gradients were applied with a duration (δ) of 2 ms and a flow contrast time (Δ) of 40 ms. The flow gradient magnitude (g) was incremented linearly between ± 6.0 G cm^{-1} in 128 steps (N) to sample a q-space range of ± 5100 m^{-1} and provide a FOF of 310 mm s^{-1}. This FOF being sufficient to exceed the maximum expected velocity of 150 ± 8 mm s^{-1} and satisfy one requirement of the Fourier transform. Parameters were held constant for each concentration of xanthan gum-in-water solution investigated. A recycle time of 10 s, equal to $\sim$4 times T_1 (2.6 s), was utilised with 4 signal averages to give a total acquisition time of 85 min. To obtain the low-q data in the range ± 106 m^{-1} for cumulant analysis, approximately equal to $\pm 0.4 \langle \zeta \rangle^{-1}$ m^{-1}, flow gradients were applied with $\delta = 0.5$ ms and $\Delta = 50$ ms. The flow gradient magnitude was incremented linearly in 128 steps between ± 0.5 G cm^{-1} to give

an acquisition time of 85 min with a recycle time of 10 s and 4 signal averages. These acquisition parameters were used for all samples. Much shorter acquisition times can be achieved when fewer flow gradient increments are required for cumulant analysis, as shown in Section 3.4, or by using fast flow encoding techniques [24–26].

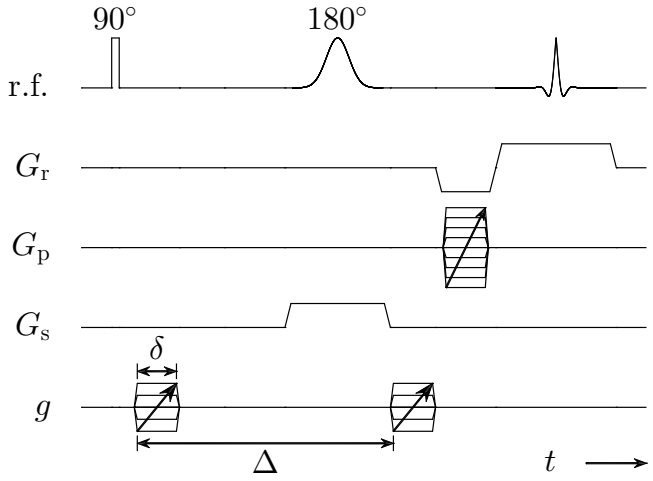

Fig. 3.9: A schematic of the spin echo MR flow imaging sequence used for the imaging of velocity.

To validate the accuracy of the PFG MR measurements, spatially-resolved velocity images were acquired for each concentration of xanthan gum-in-water solution investigated using the simple slice selective spin echo MR flow imaging sequence [9] shown in Fig. 3.9. Data were acquired with a slice thickness of 10 mm and SNR = 100. A field-of-view (FOV) of 18 mm was selected in the read and phase directions with 128 phase increments and 128 read points to give a resolution of 141 µm × 141 µm. Flow gradients were applied with $\delta = 2$ ms and $\Delta = 20$ ms, and two increments in flow gradient magnitude were utilised with the magnitude calibrated for each sample to ensure a maximum phase shift of 2π. The acquisition time of a single MR flow image was 45 min with a recycle time of 2.6 s and four signal averages. For quantification of the velocity data, a zero velocity MR flow image was acquired for each concentration of xanthan gum-in-water solution investigated. All experiments were performed at 19.0±0.5 °C.

Conventional rheometry

Estimates of n determined using the proposed cumulant MR approach and MR flow imaging were validated using a Rheometric Scientific ARES 320 rheometer. A smooth-

walled concentric cylinder Couette cell geometry, with inner cylinder of outer diameter 32 mm and length 34 mm, was used for each concentration of xanthan gum-in-water solution investigated. The wall gap was 1 mm and the temperature was 19.0±1.0 °C. The rheometer was operated in controlled-rate mode, with apparent shear stress measured during a two-way shear rate sweep of 0.01–500 s^{-1}. A correction is required to be applied to the apparent (measured) flow curve to obtain the true flow curve [43], as given by

$$\eta_a(\dot{\gamma}_a) = \left(\frac{4}{3+n}\right) K \dot{\gamma}_a^{n-1} \tag{3.24}$$

for the case of a Couette cell geometry, where η_a is the apparent shear viscosity, defined as the shear stress to shear rate ratio, and τ_a and $\dot{\gamma}_a$ represent the apparent shear stress and shear rates, respectively.

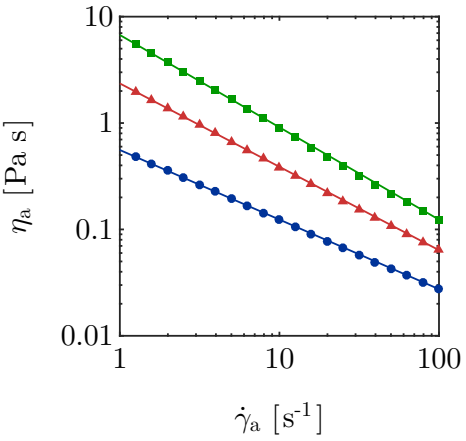

Fig. 3.10: Apparent shear viscosity, η_a, against apparent shear rate, $\dot{\gamma}_a$, for the (●) 0.2, (▲) 0.4, and (■) 0.6 wt% xanthan gum-in-water solutions plotted across the shear rate range of the MR experiments. The data were acquired using conventional rheometry methods with a shear rate sweep of 0.01–500 s^{-1}. Solid lines represent the NLLS regression of Eq. (3.24) to the experimental data, fitted across 1–100 s^{-1}, with K values of 0.560±0.002, 2.36±0.01, and 6.73±0.03 Pa s^n for the 0.2, 0.4, and 0.6 wt% xanthan gum-in-water solutions, respectively, and n values as described in Table 3.2.

Measured apparent shear viscosity-shear rate curves for 0.2, 0.4, and 0.6 wt% xanthan gum-in-water solutions are shown in Fig. 3.10 across the shear rate range of the MR experiments. At very low shear rates, a plateau is observed as the shear viscosity

approaches the low-shear viscosity, η_0, which increases with the xanthan gum concentration. All concentrations of xanthan gum-in-water solution investigated demonstrate shear-thinning behaviour; for 0.6 wt% xanthan gum-in-water solution, shear viscosity decreases by almost two orders of magnitude as the shear rate is increased from 1 to $100\,\mathrm{s}^{-1}$. Similar trends are observed at lower concentrations of xanthan gum-in-water solution. The NLLS regression of Eq. (3.24) to the apparent shear viscosity-shear rate curves, across the shear rate range of the MR experiments, was used to provide estimates of n describing the xanthan gum-in-water solutions under study. This regression is shown in Fig. 3.10, with the regression data observed to be accurate to within the scatter of the experimental data, confirming power-law rheology across the shear rate range of the MR experiments. As summarised in Table 3.2, n obtained using this approach were 1.00±0.01, 0.37±0.01, 0.24±0.01, and 0.15±0.01 for the 0.0, 0.2, 0.4, and 0.6 wt% xanthan gum-in-water solutions, respectively, with the error representative of a 95% confidence interval in the individual fit. There was no evidence of wall slip in the shear viscosity-shear rate data obtained.

3.4 Results and discussion

3.4.1 Sensitivity to the flow behaviour index

The proposed cumulant MR approach was used to quantify $p(n)$ and provide an estimate of n for all combinations of experimental parameters described in Section 3.3.1. Simulation experiments were repeated 10^2 times, each with pseudo-random Gaussian noise, to investigate the accuracy and error associated with the estimate of n obtained using the proposed cumulant MR approach. Figure 3.11 shows $p(\kappa_2, n)$, $p(\kappa_3, n)$, and $p(\kappa_4, n)$ obtained for a single simulation experiment with an input n of 0.5, 128 sampled q-space data points and SNR = 100. It is observed that the maximum probability decreases and the width of the distribution increases for higher-order cumulants due to the greater uncertainty associated with these cumulants, as obtained through LLS regression of Eqs. (3.19) and (3.20) to the log-magnitude and phase of the simulated $S(q)$ data, respectively. The distribution of $p(n)$, given by $p(\kappa_2, n)\,p(\kappa_3, n)\,p(\kappa_4, n)$, is strongly influence by κ_2. For the example shown, $p(n)$ gives an output n of 0.51±0.02, accurate to within less than 2% of the input n, where the uncertainty represents the standard deviation of $p(n)$. The robustness of the proposed cumulant MR approach to changes in n will now be described.

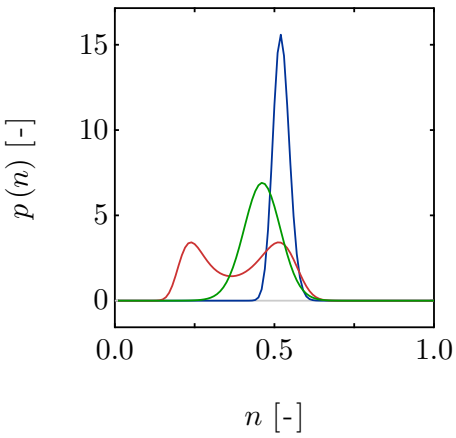

Fig. 3.11: A probability distribution showing the probability of n, given (—) κ_2, (—) κ_3, and (—) κ_4, obtained using the proposed cumulant MR approach with simulated data. The data were generated with 128 sampled q-space data points and SNR = 100 for an input of $n = 0.5$.

Figure 3.12 demonstrates the robustness of the proposed cumulant MR approach to changes in n by showing the mean and uncertainty of κ_2 as n is increased from 0.1 to 1.0 for (a) 256 and (b) 16 sampled q-space data points with SNR of ∞, 100, and 50. Note that q-space was sampled linearly between $\pm 106\,\mathrm{m}^{-1}$. The scaled mean κ_2 is shown in Fig. 3.12 to remain approximately constant, deviating from unity by less than $\pm 1\%$, thus indicating an absence of systematic error and robustness to changes in experimental parameters, as well as n. In contrast, the uncertainty associated with κ_2 increases with a reduction in n, reduction in SNR, and reduction in the number of sampled q-space data points; for 16 sampled q-space data points and SNR = 50, the uncertainty in the measurement of κ_2 decreases from 7 to 4% as n increases from 0.1 to 1.0. Similar trends are observed for higher-order cumulants.

Using methods described in Section 3.2, the mean and standard deviation of the 10^2 mean n values estimated using the proposed cumulant MR approach were calculated. Figure 3.13 compares the input n to output n predicted using cumulant analysis for (a) 256 and (b) 16 sampled q-space data points, sampled linearly between $\pm 106\,\mathrm{m}^{-1}$, and SNR of ∞, 100, and 50, with the error bars equal to the standard deviation. The output n deviates from the input n by less than $\pm 2\%$, with the highest errors associated with 16 sampled q-space data points and SNR = 50. However, the uncertainty associated with the estimate of n changes considerably across the range of parameters investigated, increasing with a reduction in SNR and reduction in the number of sam-

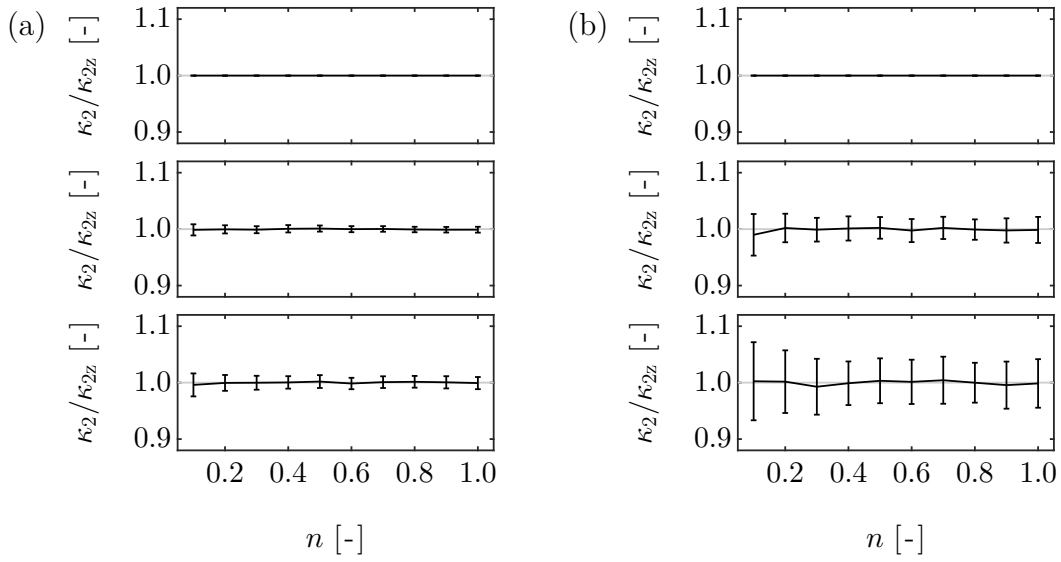

Fig. 3.12: Plots to demonstrate the relationship between the mean κ_2 (represented as a fraction of the noise-free mean κ_2, κ_{2z}) and n. Data are plotted for (a) 256 and (b) 16 sampled q-space data points, with SNR of (top to bottom) ∞, 100, and 50. Error bars represent the standard deviation of κ_2 generated from 10^2 repeats.

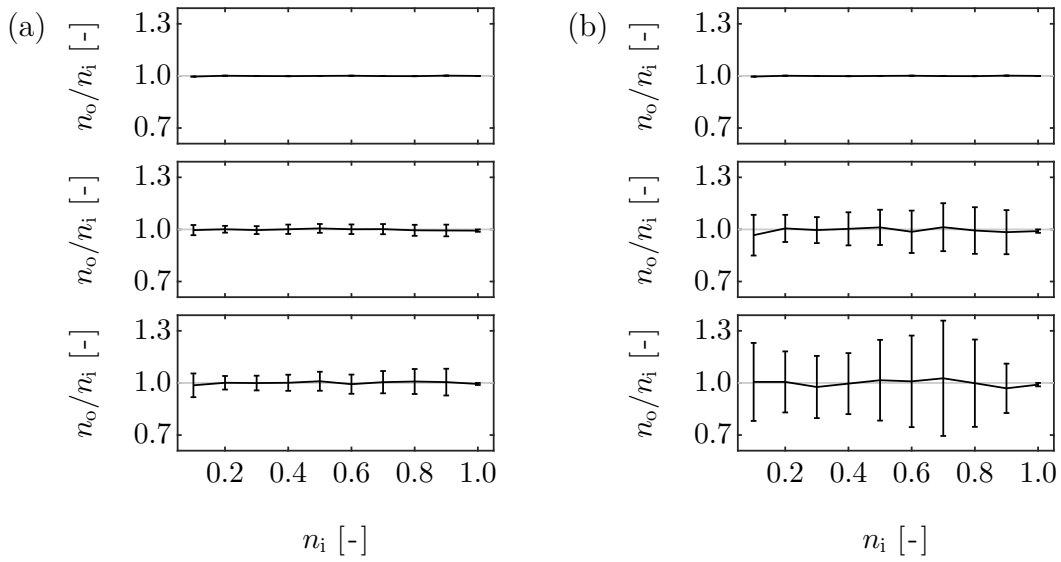

Fig. 3.13: Plots to compare the expected (or input) n, n_i, and recovered (or output) n, n_o, obtained using cumulant analysis for a range of n for (a) 256 and (b) 16 sampled q-space data points and SNR of (top to bottom) ∞, 100, and 50. Error bars represent uncertainties in n_o due to uncertainties in the measured cumulants.

pled q-space data points. Fluctuations in the uncertainty of the output n are observed as the input n varies, but these fluctuations are small when compared to those induced due to changes in SNR and the number of sampled q-space data points. The accuracy of the proposed cumulant MR approach is, therefore, largely insensitive to n.

3.4.2 Sensitivity to noisy data and reduced sampling

The mean n obtained from the 10^2 repeat simulations was used to quantify the error associated with the estimation of n. Figure 3.14 shows the error associated with the estimation of n, as a function of both noise and the number of sampled q-space data points, for (a) $n = 0.1$ and (b) $n = 1.0$. It is observed that the sampling requirement is highly dependent upon the noise for a given error in n, as expected. For the MR experiments reported here, which utilised a 2 T magnet, an SNR of > 1000 was typical. Under these conditions, only 4 points are required to be sampled in q-space to provide an error in n of $< 5\%$. This represents a 94% reduction in the acquisition time using the proposed cumulant MR approach to estimate n when compared to the acquisition of an MR flow image with 128 phase encoding steps.

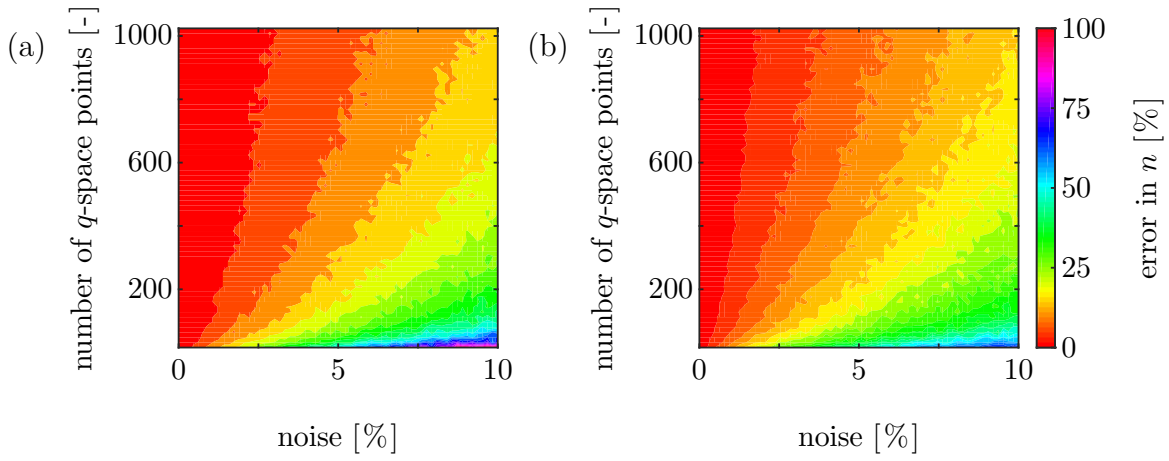

Fig. 3.14: Two-dimensional contour plots demonstrating the error associated with the estimate of n for the range of SNR and number of sampled q-space data points investigated, for n of (a) 0.1 and (b) 1.0, using 64 increments in both noise and number of sampled q-space data points.

As the noise increases, an increasing number of q-space data points are required to be sampled to achieve the same error; for a noise level of 2%, 128 q-space data points are required to provide an error in the estimate of n of less than 5%. The results are

in good agreement with previous work [34] and further demonstrate the robustness of cumulant analysis to noisy data, where the degree of robustness is dependent upon the number of sampled q-space data points. For a noise level of $< 1\%$, typical of low-field MR, only 8 points are required to be sampled in q-space if an error of less than 5% is required in the estimation of n and $n = 0.1$. These results are significant as they imply that the proposed cumulant MR approach can be used to determine quantitative rheological parameters on low-field, maybe even Earth's field, MR hardware. On such hardware, the low SNR associated with spatially-resolved measurements may render MR flow imaging inaccurate and/or impractical for the estimation of n.

3.4.3 Experimental validation using MR

Cumulant MR methods

The signal in q-space was sampled over a low-q range for the purpose of cumulant analysis. Following symmetrisation of $S(q)$ using methods outlined in the literature [34], LLS regression of Eqs. (3.19) and (3.20) to the symmetrised log-magnitude and phase of $S(q)$, respectively, was used to obtain cumulants that varied with n, as was shown in Fig. 3.6. Note that analysis of Q across an increasing range of q-space, as described in Section 3.2, indicated that $|q_{\max}|$ was not exceeded for any sample investigated, with LLS regression performed across the entire range of $\pm 106\,\mathrm{m}^{-1}$. Cumulants were generated, using the method outlined in Section 3.2, and compared with those determined experimentally. Using this approach, $p(n)$ was obtained for each concentration of xanthan gum-in-water solution investigated, with the mean of $p(n)$ providing an estimate of n. All samples indicated shear-thinning behaviour; across the shear rate range of the MR experiments (1–$100\,\mathrm{s}^{-1}$), n was estimated as 1.01 ± 0.03, 0.39 ± 0.01, 0.23 ± 0.01, and 0.15 ± 0.01 for the 0.0, 0.2, 0.4, and 0.6 wt% xanthan gum-in-water solutions, respectively. The uncertainties represent the standard deviations of the respective probability distributions. An increase in xanthan gum concentration is, therefore, responsible for a decrease in n. This trend is in agreement with literature [44]. Furthermore, the estimate of n obtained for the 0.0 wt% xanthan gum-in-water solution is in agreement to within 1% of that expected for a Newtonian fluid (where $n = 1.00$). These results are summarised in Table 3.2.

A comparison of the experimental and LLS regression data is shown in Fig. 3.15 for each concentration of xanthan gum-in-water solution investigated, with the individual

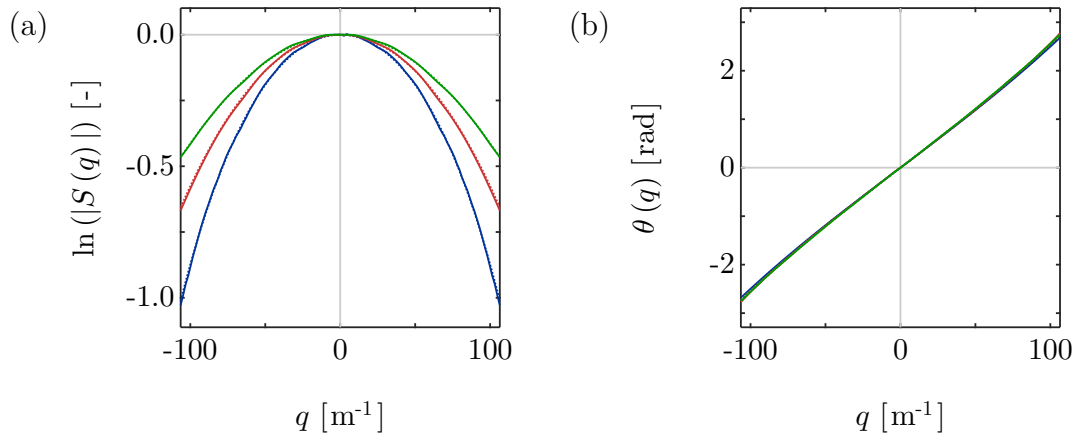

Fig. 3.15: Plots to show the (a) log-magnitude and (b) phase of $S\,(q)$ for the (—) 0.2, (—) 0.4, and (—) 0.6 wt% xanthan gum-in-water solutions. The solid and dashed lines show the experimentally-acquired and regression data, respectively; the two datasets overlap.

fits accurate to within the accuracy of the experimental data. Note that an increase in xanthan gum concentration is responsible for an increase in the signal at the limits of q-space sampled, in agreement with trends observed in Fig. 3.4(a) and indicative of increasing shear-thinning behaviour. These results are consistent with those observed using conventional rheometry, as described in Section 3.3.2.

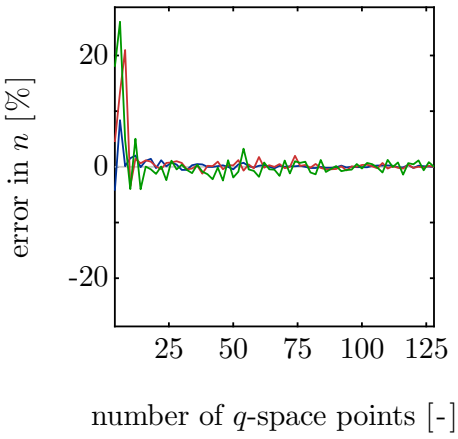

Fig. 3.16: A plot to show the error associated with the estimate of n for the (—) 0.2, (—) 0.4, and (—) 0.6 wt% xanthan gum-in-water solutions, when compared with n determined using 128 points, as the number of sampled q-space data points is increased. Note that n was calculated using cumulants determined from a single LLS regression to the experimental $S\,(q)$ data.

Figure 3.16 demonstrates the sensitivity of the number of sampled q-space data points on the error associated with the estimate of n, when compared with the estimate of n obtained using 128 sampled q-space data points, for each concentration of xanthan gum-in-water solution investigated. It is observed that the error is largely independent of xanthan gum concentration, *i.e.* n of the fluid under study. This further validates the results of the simulation experiments reported in Section 3.4.2. In all cases, the number of sampled q-space data points can be reduced to less than 40 without increasing the error in n, thus suggesting that the acquisition of 128 points is unnecessary. Furthermore, the error associated with the proposed cumulant MR approach with only 4 sampled q-space data points is $< 5\%$, demonstrating that a reduction in acquisition time from 45 min to 3 min is possible using the proposed approach when compared to the acquisition of an MR flow image using a single spin echo sequence with 128 phase encoding steps. This represents a reduction in acquisition time of 94%.

Comparison with non-cumulant MR methods

Changes in the flow distribution were investigated through acquisition of flow propagators for each concentration of xanthan gum-in-water solution investigated. A correction was applied to the experimentally-acquired flow propagators, in the form of Eq. (3.16), to recover $p(\zeta)$. Shown in Fig. 3.17 are $p(\zeta)$ obtained for the (a) 0.0, (b) 0.2, (c) 0.4, and (d) 0.6 wt% xanthan gum-in-water solutions. An increase in xanthan gum concentration from 0.0 to 0.6 wt% is shown in Fig. 3.17 to be responsible for a reduction in $\zeta_{\max}$ from 6.2 to 4.0 mm, corresponding to a reduction in the maximum velocity from 155 to 100 mm s^{-1}. Furthermore, an increase in the maximum probability is observed as the concentration of xanthan gum is increased, thus indicating a reduction in n describing the fluid under study, *i.e.* an increase in shear-thinning behaviour. Note that $\dot{V}$ calculated from the flow propagators was 12.8 ± 0.5 mL s^{-1}, with the error a result of Gibbs ringing due to the truncation of $S(q)$. These artefacts are more pronounced with a reduction in n due to the emergence of a dominant spike in the flow propagator. This dominant spike, which approaches a shifted delta function as n approaches zero, is responsible for a constant amplitude signal with oscillating phase, and so the truncation of $S(q)$ is inevitable at low values of n. Truncation artefacts could be minimised through apodisation of $S(q)$ before Fourier transform, however, this would reduce the velocity resolution of the flow propagator and make the quantitative or qualitative use of flow propagators in this application challenging.

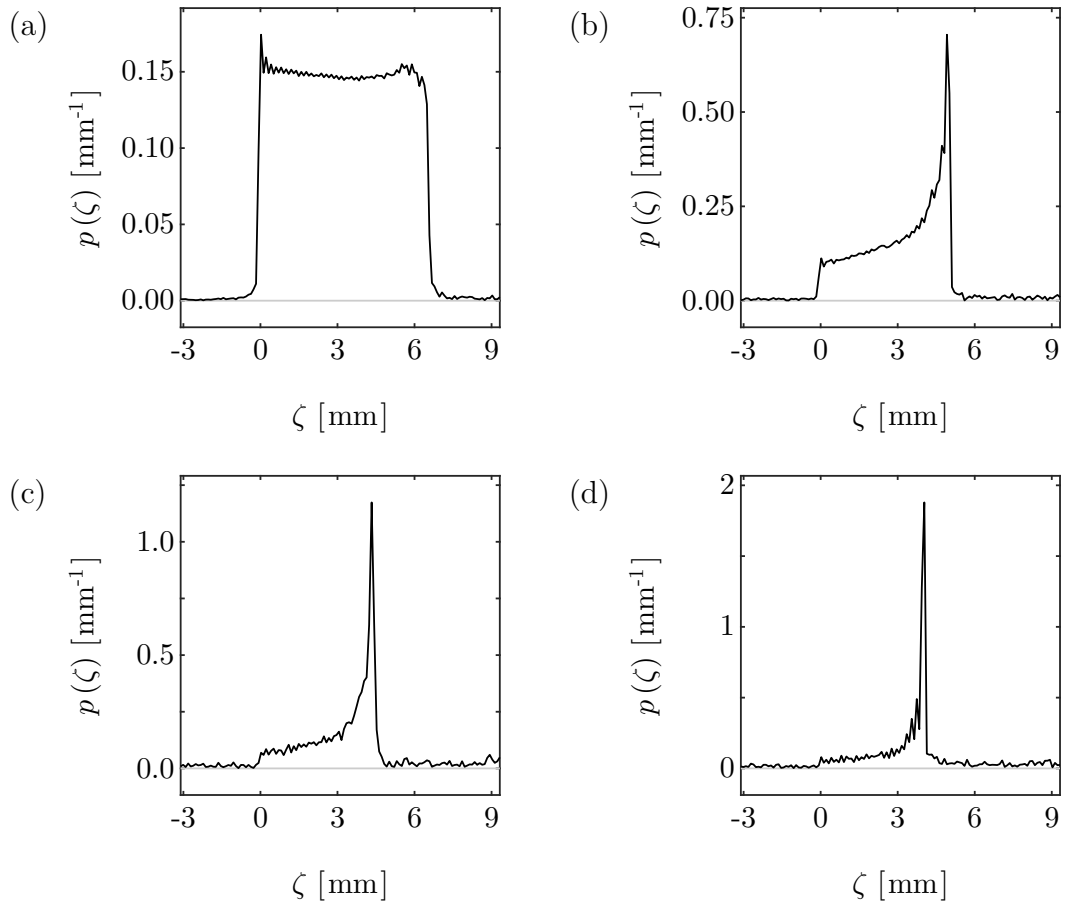

Fig. 3.17: Plots to show the experimentally-acquired $p(\zeta)$ data for the (a) 0.0, (b) 0.2, (c) 0.4, and (d) 0.6 wt% xanthan gum-in-water solutions.

Two-dimensional (2D) MR flow images were acquired for each concentration of xanthan gum-in-water solution investigated with a spatial resolution of 141 µm × 141 µm, sufficient to provide ∼100 spatially-resolved velocity data points across the geometry under study. Figure 3.18 shows MR flow images for the (a) 0.0, (b) 0.2, (c) 0.4, and (d) 0.6 wt% xanthan gum-in-water solutions, where the velocity represents axial velocity, *i.e.* z-velocity. The SNR in the images is 100. Flow rates calculated from the MR flow images (11.6±0.4 mL s^{-1}) suggest that this technique is accurate to within the limits of the error of the gravimetric flow measurement (11.5±0.5 mL s^{-1}). The maximum velocity of the 0.0 wt% xanthan gum-in-water solution was 154 mm s^{-1}, also within the experimental error assuming a parabolic velocity profile (150±8 mm s^{-1}). This corresponds to a Reynolds number of ∼1100. A transition to the turbulent flow regime is typically observed between Reynolds numbers of 2000–4000 [41]. As expected, the MR

flow images show radial symmetry typical of laminar flow and do not show any of the features attributed to turbulent flow.

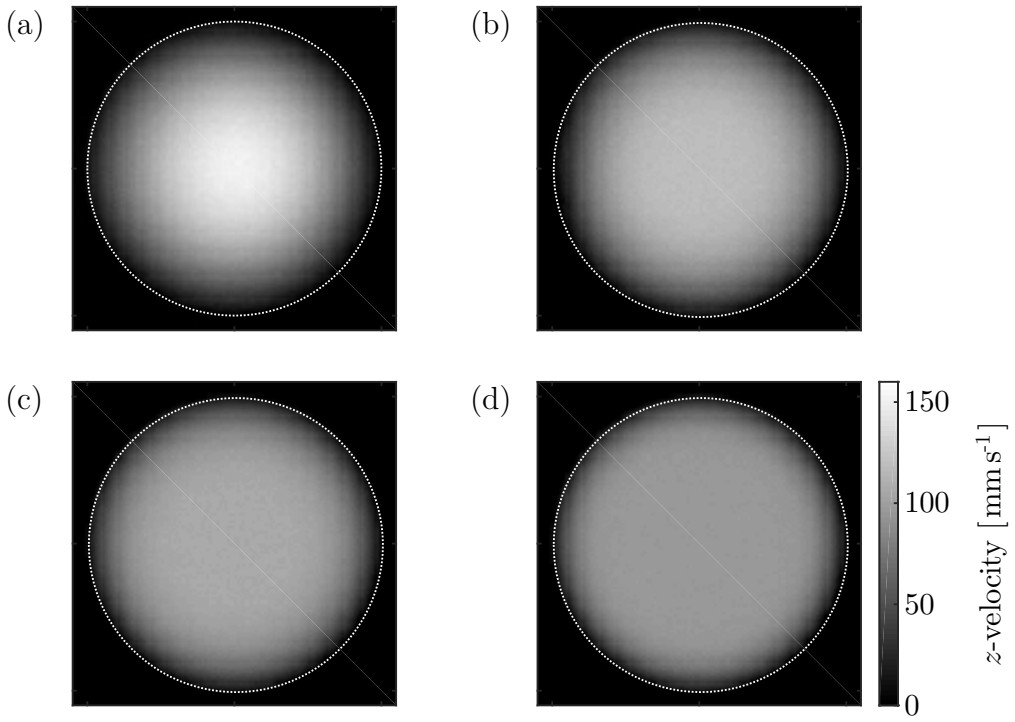

Fig. 3.18: MR flow images acquired for the (a) 0.0, (b) 0.2, (c) 0.4, and (d) 0.6 wt% xanthan gum-in-water solutions with $\dot{V} = 11.5 \pm 0.5\,\mathrm{mL\,s^{-1}}$. The MR flow images have a spatial resolution of 141 µm × 141 µm, an FOV of 18 mm × 18 mm, and were acquired in 90 min. The SNR in the corresponding intensity images is 100.

An estimate of n was obtained for each concentration of xanthan gum-in-water solution investigated by performing a 2D NLLS regression of $\Delta^{-1}\zeta\,(r)$ to the respective MR flow image, with $\zeta\,(r)$ given by Eq. (3.4). This 2D NLLS regression is depicted in Fig. 3.19 by means of velocity profiles generated using radially-averaged MR flow image and regression data; these two sets of data are shown in Fig. 3.19 to be in agreement to within the accuracy of the experimental data, confirming power-law rheology over the shear rate range of the MR experiments (1–100 s^{-1}). Using this method, n was estimated as 0.99±0.04, 0.39±0.02, 0.25±0.01, and 0.15±0.01 for the 0.0, 0.2, 0.4, and 0.6 wt% xanthan gum-in-water solutions, respectively, where the error is representative of a 95% confidence interval in the individual fit. The results from MR flow imaging are summarised in Table 3.2, with the result for 0.0 wt% xanthan gum-in-water solution accurate to within 1% of that expected for a Newtonian fluid (where $n = 1.00$).

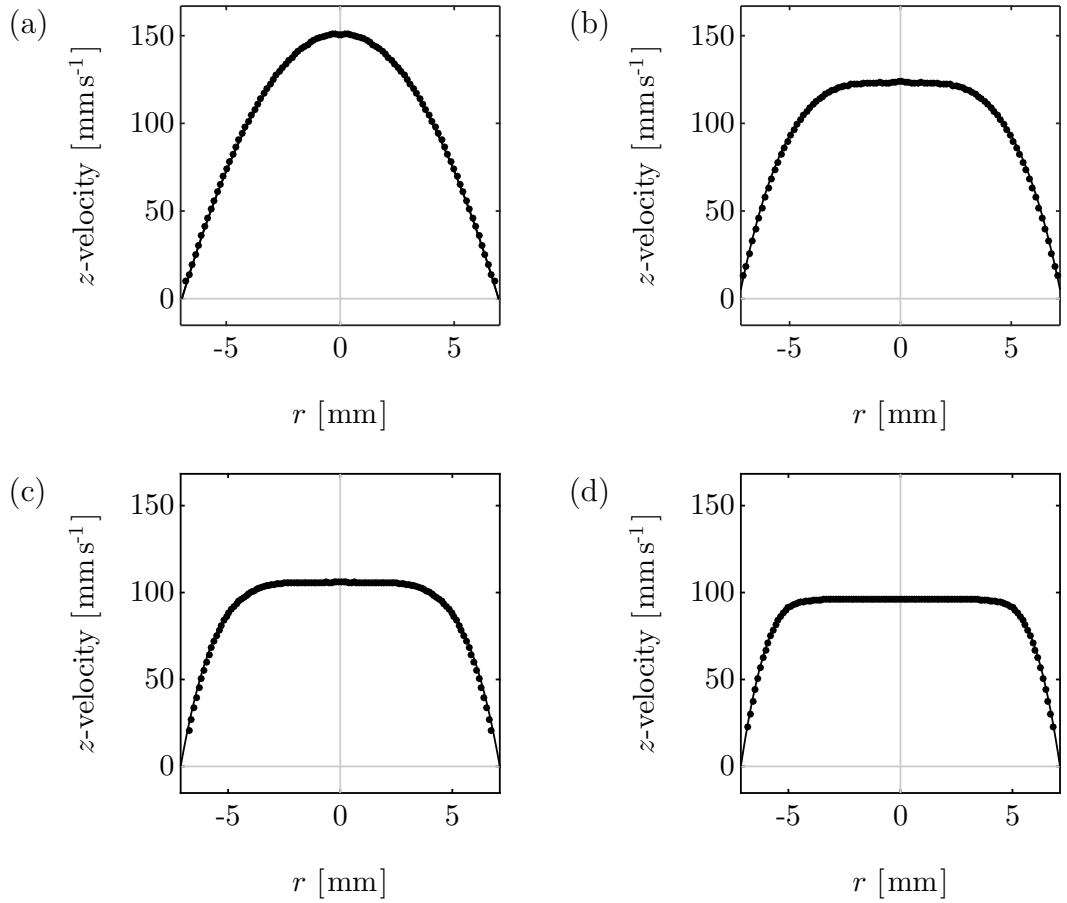

Fig. 3.19: Velocity profiles for the (a) 0.0, (b) 0.2, (c) 0.4, and (d) 0.6 wt% xanthan gum-in-water solutions showing the (●) radially-averaged MR flow images. The solid lines correspond to the radially-averaged 2D regression data obtained by performing a 2D NLLS regression of $\Delta^{-1}\zeta(r)$ to the MR flow images, with $\zeta(r)$ given by Eq. (3.4). The error in the fit is within the accuracy of the experimental data.

Table 3.2 compares n determined using the proposed cumulant MR approach with those obtained using MR flow imaging and conventional rheometry. In all cases, the results from the three methods are observed to be in agreement to within 5%, comparable with the accuracy of conventional rheometry. Furthermore, those calculated using MR flow imaging are accurate to within 8% of those found using the proposed cumulant MR approach. Cumulant MR therefore offers a new approach to rheological characterisation using MR, with the potential increase in temporal resolution enabling temporal changes in n over time scales of 3 min to be identified. The acquisition time may be reduced further with a reduction in T_1, decreasing to only 16 s for $T_1 = 260$ ms. Moreover, the requirement of more expensive gradient hardware is negated, extending

Table 3.2: A comparison of n estimated for the 0.0, 0.2, 0.4, and 0.6 wt% xanthan gum-in-water solutions using conventional rheometry, MR flow imaging, and cumulant MR methods, evaluated across a shear rate range of 1–100 s^{-1}.

method	n [-]			
	0.0 wt%	0.2 wt%	0.4 wt%	0.6 wt%
conventional rheometry	1.00±0.01	0.37±0.01	0.24±0.01	0.15±0.01
MR flow imaging	0.99±0.04	0.39±0.02	0.25±0.01	0.15±0.01
cumulant MR	1.01±0.03	0.39±0.01	0.23±0.01	0.15±0.01

MR rheometry to single-axis, low-power gradient systems. This approach could also be applied on low-field, portable MR hardware due to the robustness demonstrated by cumulant analysis to noisy data. Furthermore, such an approach could be combined with a corresponding measurement of pressure drop to characterise the flow curve.

3.5 Conclusions

In this Chapter, a PFG MR and cumulant analysis approach was proposed enabling the estimation of n describing fluids demonstrating power-law rheology. An expression describing $S(q)$ in terms of n was used to systematically investigate the parameters of interest; including SNR, number of sampled q-space data points, and n. It was shown that the proposed cumulant MR approach is robust to reductions in both the number of sampled q-space data points and SNR. An increase in the temporal resolution of this proposed approach is possible through a reduction in the number of sampled data points, with the reduction limited by the SNR of the system under study. To validate the proposed cumulant MR approach, an experimental case study on xanthan gum-in-water solutions demonstrating power-law rheology was performed. Estimates of n obtained using the proposed cumulant MR approach were accurate to within 8% of those obtained using MR flow imaging, with all n accurate to within 5% of the same quantities determined using conventional rheometry. All n were characterised across a shear rate range of 1–100 s^{-1}.

Using this approach it has been shown that with SNR as low as 50, quantitative results can be acquired to within 5% of the expected value when 128 q-space points are sampled. This can be reduced to 8 q-space points for SNR = 100 to obtain results of the same accuracy, and only 4 points with SNR >1000. An obvious implication of

this is that the requirement of only a single-axis, low-power gradient system removes the need for more expensive hardware for the MR characterisation of non-Newtonian fluids. Furthermore, the robustness of this approach to SNR < 100 opens up new and exciting opportunities for portable, low-field MR hardware.

3.6 References

[1] Collyer, A.A. and Clegg, D.W., *Rheological Measurement*, Springer, Dordrecht, NL, 1998.

[2] Ostwald, W., 1929, Ueber die rechnerische darstellung des strukturgebietes der viskosität. *Kolloid-Z.*, **47**, 176–187.

[3] Callaghan, P.T., 2006, Rheo-NMR and velocity imaging. *Curr. Opin. Colloid Interface Sci.*, **11**, 13–18.

[4] Britton, M.M., Callaghan, P.T., Kilfoil, M.L., Mair, R.W. and Owens, K.M., 1998, NMR velocimetry and spectroscopy at microscopic resolution in small rheometric devices. *Appl. Magn. Reson.*, **15**, 287–301.

[5] Arola, D.F., Barrall, G.A., Powell, R.L., McCarthy, K.L. and McCarthy, M.J., 1997, Use of nuclear magnetic resonance imaging as a viscometer for process monitoring. *Chem. Eng. Sci.*, **52**, 2049–2057.

[6] Arola, D.F., Powell, R.L., Barrall, G.A. and McCarthy, M.J., 1998, A simplified method for accuracy estimation of nuclear magnetic resonant imaging. *Rev. Sci. Instrum.*, **69**, 3300–3307.

[7] Arola, D.F., Powell, R.L., Barrall, G.A. and McCarthy, M.J., 1999, Pointwise observations for rheological characterization using nuclear magnetic resonance imaging. *J. Rheol.*, **43**, 9–30.

[8] Papaharilaou, Y., Doorly, D.J. and Sherwin, S.J., 2001, Assessing the accuracy of two-dimensional phase-contrast MRI measurements of complex unsteady flows. *J. Magn. Reson. Imaging*, **14**, 714–723.

[9] Gladden, L.F. and Sederman, A.J., 2013, Recent advances in flow MRI. *J. Magn. Reson.*, **229**, 2–11.

[10] Dalitz, F., Cudaj, M., Maiwald, M. and Guthausen, G., 2012, Process and reaction monitoring by low-field NMR spectroscopy. *Prog. Nucl. Magn. Reson. Spectrosc.*, **60**, 52–70.

[11] Ahn, C.B., Kim, J.H. and Cho, Z.H., 1986, High-speed spiral-scan echo planar NMR imaging–I. *IEEE Trans. Med. Imaging*, **5**, 2–7.

[12] Mansfield, P., 1977, Multi-planar image formation using. *J. Phys. C: Solid State Phys.*, **10**, L55–L58.

[13] Hennig, J., Nauerth, A. and Friedburg, H., 1986, RARE imaging: a fast imaging method for clinical MR. *Magn. Reson. Med.*, **3**, 823–833.

[14] Haase, A., Frahm, J., Matthaei, D., Hanicke, W. and Merboldt, K.D., 1986, FLASH imaging. Rapid NMR imaging using low flip-angle pulses. *J. Magn. Reson.*, **67**, 258–266.

[15] Osán, T.M., Ollé, J.M., Carpinella, M., Cerioni, L.M.C., Pusiol, D.J., Appel, M., Freeman, J. and Espejo, I., 2011, Fast measurements of average flow velocity by low-field ^{1}H NMR. *J. Magn. Reson.*, **209**, 116–122.

[16] Carr, H.Y. and Purcell, E.M., 1954, Effects of diffusion on free precession in nuclear magnetic resonance experiments. *Phys. Rev.*, **94**, 630–638.

[17] Meiboom, S. and Gill, D., 1958, Modified spin-echo method for measuring nuclear relaxation times. *Rev. Sci. Instrum.*, **29**, 688–691.

[18] Callaghan, P.T., *Principles of Nuclear Magnetic Resonance Microscopy*, Clarendon Press, Oxford, GB, 1993.

[19] Stejskal, E.O. and Tanner, J.E., 1965, Spin diffusion measurements: spin echoes in the presence of a time-dependent field gradient. *J. Chem. Phys.*, **42**, 288–292.

[20] Tanner, J.E., 1970, Use of the stimulated echo in NMR diffusion studies. *J. Chem. Phys.*, **52**, 2523–2526.

[21] Packer, K.J., 1969, The study of slow coherent molecular motion by pulsed nuclear magnetic resonance. *Mol. Phys.*, **17**, 355–368.

[22] Kärger, J. and Heink, W., 1983, The propagator representation of molecular transport in microporous crystallites. *J. Magn. Reson.*, **51**, 1–7.

[23] Maneval, J.E., Powell, R.L., McCarthy, M.J. and McCarthy, K.L., in *Particulate Two-phase Flow*, Butterworth-Heinemann, Boston, US, 1993, pp. 127–140.

[24] Grover, T. and Singer, J.R., 1971, NMR spin-echo flow measurements. *J. Appl. Phys.*, **42**, 938–940.

[25] Garroway, A.N., 1974, Velocity measurements in flowing fluids by MNR. *J. Phys. D: Appl. Phys.*, **7**, L159–L163.

[26] Stamps, J.P., Ottink, B., Visser, J.M., Duynhoven, J.P.M. van and Hulst, R., 2001, Difftrain: a novel approach to a true spectroscopic single-scan diffusion measurement. *J. Magn. Reson.*, **151**, 28–31.

[27] McCarthy, M.J., Maneval, J.E. and Powell, R.L., in *Advances in Food Engineering*, CRC Press, Boca Raton, US, 1992, pp. 87–97.

[28] Seymour, J.D., Maneval, J.E., McCarthy, K.L., Powell, R.L. and McCarthy, M.J., 1995, Rheological characterization of fluids using NMR velocity spectrum measurements. *J. Texture Stud.*, **26**, 89–101.

[29] Chevalier, T., Rodts, S., Chevalier, C. and Coussot, P., 2014, Quantitative exploitation of PFG NMR and MRI velocimetry data for the rheological study of yield stress fluid flows at macro- and micro-scales in complex geometries. *Exp. Fluids*, **56**, 1868.

[30] Zelen, M. and Severo, N.C., in *Handbook of Mathematical Functions: With Formulas, Graphs, and Mathematical Tables*, Dover Publications, New York, US, 10th, 1972, pp. 925–997.

[31] Thiele, T.N., *Theory of Observations*, Charles and Edward Layton, London, GB, 1903.

[32] Speed, T.P., 1983, Cumulants and partition lattices. *Aust. J. Stat.*, **25**, 378–388.

[33] Scheven, U.M., Verganelakis, D., Harris, R., Johns, M.L. and Gladden, L.F., 2005, Quantitative nuclear magnetic resonance measurements of preasymptotic dispersion in flow through porous media. *Phys. Fluids*, **17**, 1–7.

[34] Scheven, U.M., Crawshaw, J.P., Anderson, V.J., Harris, R., Johns, M.L. and Gladden, L.F., 2007, A cumulant analysis for non-Gaussian displacement distributions in Newtonian and non-Newtonian flows through porous media. *Magn. Reson. Imaging*, **25**, 513–516.

[35] Barnes, H.A., Hutton, J.F. and Walters, K., *An Introduction to Rheology*, Elsevier, Amsterdam, NL, 1989.

[36] Kaiser, L.G., Logan, J.W., Meersmann, T. and Pines, A., 2001, Dynamic NMR microscopy of gas phase Poiseuille flow. *J. Magn. Reson.*, **149**, 144–148.

[37] Bevington, P.R. and Robinson, D.K., *Data Reduction and Error Analysis for the Physical Sciences*, McGraw-Hill, New York, US, Third, 2003.

[38] Press, W.H., Teukolsky, S.A., Vetterling, W.T. and Flannery, B.P., *Numerical Recipes in C: The Art of Scientific Computing*, Cambridge University Press, Cambridge, GB, Second, 2007.

[39] Benmouffok-Benbelkacem, G., Caton, F., Baravian, C. and Skali-Lami, S., 2010, Non-linear viscoelasticity and temporal behavior of typical yield stress fluids: Carbopol, xanthan and ketchup. *Rheol. Acta*, **49**, 305–314.

[40] Hollingsworth, K.G. and Johns, M.L., 2004, Rheo-nuclear magnetic resonance of emulsion systems. *J. Rheol.*, **48**, 787–803.

[41] Coulson, J.M., Richardson, J.F., Backhurst, J.R. and Harker, J.H., *Coulson & Richardson's Chemical Engineering: Fluid flow, heat transfer, and mass transfer*, Butterworth-Heinemann, Oxford, GB, 1999.

[42] Cotts, R.M., Hoch, M.J.R., Sun, T. and Markert, J.T., 1989, Pulsed field gradient stimulated echo methods for improved NMR diffusion measurements in heterogeneous systems. *J. Magn. Reson.*, **83**, 252–266.

[43] Brunn, P.O. and Asoud, H., 2002, Analysis of shear rheometry of yield stress materials and apparent yield stress materials. *Rheol. Acta*, **41**, 524–531.

[44] Bandulasena, H.C.H., Zimmerman, W.B. and Rees, J.M., 2011, An inverse method for rheometry of power-law fluids. *Meas. Sci. Technol.*, **22**, 125402.

Chapter 4

Extension to Herschel–Bulkley fluids

In Chapter 3, a cumulant analysis of the signal in q-space, $S(q)$, was used to estimate the flow behaviour index of fluids demonstrating non-Newtonian, power-law rheology. A corresponding measurement of pressure drop would enable the estimation of the consistency factor and thus the characterisation of the flow curve. However, the power-law constitutive equation is insufficient to accurately describe the rheology of process fluids (and products) demonstrating both solid- and liquid-like behaviour. This non-Newtonian behaviour may be explained by considering the concept of yield stress, a parameter introduced in Section 1.2 that quantifies the minimum shear stress required to be applied to a fluid before deformational flow can begin to occur. The rheology of such non-Newtonian fluids may be accurately described using the Herschel–Bulkley constitutive equation.

In this Chapter, the model-dependent approach developed in Chapter 3 is extended to enable the pipe-flow characterisation of fluids demonstrating Herschel–Bulkley rheology. However, using numerical simulations it is shown that the proposed cumulant MR approach is unsuitable for use with the Herschel–Bulkley constitutive equation due to interdependence between the rheological parameters. To this end, this Chapter also outlines the development of a model-dependent Bayesian MR approach to enable estimation of the rheological parameters of fluids demonstrating Herschel–Bulkley rheology. The robustness of the proposed Bayesian MR approach to reduced sampling and noisy data is investigated in Chapter 5 using numerical simulations and applied experimentally to a model fluid demonstrating Herschel–Bulkley rheology.

4.1 Introduction

Many fluids encountered in everyday life—including mayonnaise, shaving foam, and toothpaste—exhibit both solid- and liquid-like behaviour. Such non-Newtonian behaviour may be explained simply by considering the concept of yield stress, a parameter introduced in Section 1.2 that quantifies the minimum shear stress that is required to be applied to a fluid before deformational flow can begin to occur. Fluids exhibiting yield stress behaviour demonstrate solid-like behaviour at low applied stresses, below the yield stress, but liquid-like behaviour at high applied stresses [1]. Although the existence of yield stress has been questioned [2,3], it does nevertheless provide a convenient way for engineers to describe (or quantify) rheology. For example, the rheology of many fluids can be accurately described by using the Herschel–Bulkley constitutive equation [4], or model, introduced in Section 1.2 as

$$\tau\left(\dot{\gamma}\right) = \tau_0 + K\dot{\gamma}^n, \tag{4.1}$$

with τ the shear stress, $\dot{\gamma}$ the shear rate, and where τ_0, K, and n represent the yield stress, consistency factor, and flow behaviour index, respectively. The relationship between τ and $\dot{\gamma}$, often referred to as the flow curve and denoted $\tau\left(\dot{\gamma}\right)$, can be described conveniently using rheological parameters appropriate to the Herschel–Bulkley model. Note that a major weakness of the Herschel–Bulkley model is its inability to unambiguously establish the rheological parameters, since different sets of these parameters can provide equivalent fits to the experimental flow curve [5].

Yield stress behaviour can be affected by changes in the sample pH and concentration [6], with such properties responsible for changes in the flow curve. These changes can be detrimental to many industrial processes, particularly those involving flow [7]. The characterisation and monitoring of the flow curve of fluids in these applications is therefore critical for process control and optimisation. In some cases, however, the flow curve is no longer a measure of the material properties of the fluid but depends on the shear history [1,8,9]. For this reason, rheological characterisation should be performed online, or inline, and in real-time, with the use of offline techniques, *e.g.* conventional, benchtop rheometry methods [10], unsuitable for this application. Furthermore, as described in Section 2.4.1, there exists a need to obtain detailed information about the flow field generated by the device inducing deformational flow [11] to enable the ob-

servation and quantification of flow phenomena, including (apparent) wall slip [10,12]. Whilst optical methods such as laser Doppler [13] and ultrasound velocimetry [14] enable the visualisation of the flow field, both involve tracer particles and are limited in the sample geometries that can be used. Light scattering techniques are also limited to optically transparent or semi-transparent fluid flows. In contrast, magnetic resonance (MR) enables the non-invasive study of translational motion without any limitation on optical opacity.

As introduced in Section 2.3, the study of translational motion using MR was first realised by Carr and Purcell [15] through the exploitation of spin-spin relaxation times. This has since developed, with phase encoding MR techniques widely considered to be the most robust and quantitative way of measuring flow [16]. Such techniques are often coupled with MR imaging hardware, in a method termed MR flow imaging [17], to perform spatially-resolved measurements of velocity in one, two, or three dimensions. For example, Arola *et al.* [18–20] used one-dimensional (1D) measurements of velocity to quantify fluid displacement as a function of radial position in a pipe flow geometry for non-Newtonian fluids demonstrating power-law [18,19] and Herschel–Bulkley [20] rheology. A pipe flow geometry is ideally suited to online, or inline, application. Shear rate data were evaluated through the linear least squares (LLS) regression of an even-order polynomial to the displacement data, followed by differentiation of the regression data. Measurements of pressure drop per unit length, $\mathrm{d}P/\mathrm{d}L$, were then used to quantify the shear stress at the wall, τ_w, using

$$\tau_\mathrm{w} = \frac{\mathrm{d}P}{\mathrm{d}L}\frac{R}{2}, \tag{4.2}$$

which is derived from a force balance and where R represents the pipe radius. From Eq. (4.2) it can be shown that

$$\tau = \frac{r}{R}\tau_\mathrm{w}, \tag{4.3}$$

where r is the radial position. Note that τ increases linearly from 0 at the centre of the pipe to τ_w at the wall and is independent of the rheological behaviour of the fluid under study. Using this approach, it is possible to characterise $\tau\left(\dot{\gamma}\right)$ over a range of shear

rates in only a single measurement lasting several minutes, with the regression of a constitutive equation, such as Eq. (4.1), to the experimental $\tau\left(\dot{\gamma}\right)$ data then performed to provide estimates of the rheological parameters. The accuracy of this approach is sensitive to the accuracy of both the pressure drop and displacement data obtained, therefore demanding adequate spatial and velocity resolution [18–20]. Arola *et al.* [20] suggest that over 100 spatially-resolved velocity data points may be required to achieve an error in τ_0 of less than 2% when compared to conventional rheometry methods. Although a number of fast imaging techniques exist [21–23], as reviewed in Section 3.1, many of these are unable to provide the spatial and/or temporal resolution required to ensure accurate rheological characterisation in real-time, and so the online, or inline, use of MR flow imaging in this application is challenging. By using the pulsed field gradient (PFG) MR method introduced in this work, MR rheometry is extended to single-axis gradient hardware, thereby eliminating the requirement of spatial encoding and enabling a substantial reduction in data acquisition times such that online, or inline, measurements are now possible. This has potential for use in process control and optimisation. The principles underlying the developments presented in this Chapter are now introduced; to avoid confusion, notation as used in Chapter 3 is adopted.

For fluids demonstrating Herschel–Bulkley rheology, Eqs. (4.1) and (4.3) can be used to show that fluid displacement, ζ, in a cylindrical pipe flow geometry is described as a function of r by

$$\zeta\left(r, n, r_0\right) = \begin{cases} \zeta_{\max}, & 0 \leq r < r_0, \\ \zeta_{\max}\left(1 - \left(\dfrac{r - r_0}{R - r_0}\right)^{\frac{n+1}{n}}\right), & r_0 \leq r \leq R, \end{cases} \tag{4.4}$$

where $\zeta_{\max}$ is the maximum fluid displacement. Figure 4.1 shows displacement profiles obtained using Eq. (4.4) for three example fluids demonstrating Newtonian and non-Newtonian behaviour; $n = 1.0$ and $r_0/R = 0.0$, $n = 0.5$ and $r_0/R = 0.5$, and $n = 0.5$ and $r_0/R = 0.8$. It is seen in Fig. 4.1 that, for a fluid demonstrating Herschel–Bulkley rheology, there exists a plug flow region at the centre of the pipe bounded by r_0 and determined by evaluating Eq. (4.3) at $\tau = \tau_0$; within this plug flow region, $\tau \leq \tau_0$ and $\dot{\gamma} = 0\,\mathrm{s}^{-1}$. Fluid displacement within the region bounded by r_0 and R increases from 0 at R to $\zeta_{\max}$ at r_0, with an increase in r_0/R and a decrease in n responsible for an

increase in the width of the plug flow region, a flattening of the displacement profile, and a reduction in ζ_{max}. Note that, in accordance with Eq. (4.3), τ_0/τ_w and r_0/R are interchangeable, thus enabling the estimation of τ_0 if τ_w is known. Changes in the rheological parameters of the fluid under study are, therefore, expected to induce changes in the displacement profiles and associated volume-averaged displacement probability distributions, or flow propagators [24]. Flow propagators completely characterise the flow under study [25] and are obtained through the Fourier transform of the PFG MR signal sampled in q-space, $S(q)$, as given by

$$S(q) = \int p(\zeta) \exp[i2\pi q\zeta] \, d\zeta, \tag{4.5}$$

where $p(\zeta)$ defines the flow propagator and $q = (1/2\pi)\gamma g\delta$, with γ the gyromagnetic ratio of the nucleus under study and g and δ the magnitude and duration of the flow encoding gradient, respectively [26]. By controlling g it is possible to traverse q-space whilst sampling $S(q)$. In accordance with Eq. (4.5), $S(q)$ and $p(\zeta)$ represent mutually conjugate Fourier pairs; Fourier transformation of $S(q)$ provides a flow propagator, representative of the flow under study, with a field-of-flow (FOF) equal to the reciprocal of the sampling resolution in q-space and a displacement resolution given by the reciprocal of the range of q-space sampled.

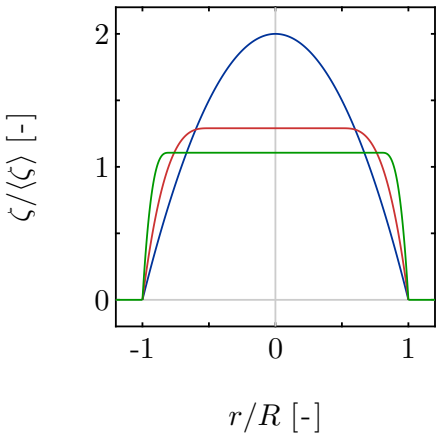

Fig. 4.1: Fluid displacement (represented as a fraction of the mean fluid displacement) plotted as a function of radial position (represented as a fraction of the pipe radius) for three example fluids demonstrating Herschel–Bulkley rheology; where (—) $n = 1.0$ and $r_0/R = 0.0$, (—) $n = 0.5$ and $r_0/R = 0.5$, and (—) $n = 0.5$ and $r_0/R = 0.8$. The displacement data were generated using Eq. (4.4).

The use of flow propagators for rheological characterisation was first proposed theoretically by McCarthy *et al.* [27], with $p(\zeta)$ known to be sensitive to the rheological parameters of the fluid under study. Whilst differences in the shape of the flow propagators have been reported for a range of Newtonian and non-Newtonian fluids [28], the quantitative use of flow propagators remains challenging due to hardware limitations, *i.e.* gradient hardware, and practical constraints, such as data acquisition times, that limit the range of q-space accessible. The signal at the limits of q-space sampled will often not approach zero, and so the introduction of truncation artefacts during Fourier transform may be experimentally unavoidable. To this end, the sensitivity of $S(q)$ to changes in $p(\zeta)$ was exploited in Chapter 3 to enable the rheological characterisation of power-law fluids using the acquisition data directly, thus removing the need for Fourier transform and preventing the introduction of truncation artefacts. Furthermore, strict sampling requirements were removed, allowing considerable reductions in acquisition times; for the model fluids investigated, an accurate estimate of n was achieved when sampling only 4 points in q-space. This represented a reduction in acquisition time of 94% when compared with the acquisition of an MR flow image.

In this Chapter, the methodology developed in Chapter 3 is extended to Herschel–Bulkley fluids. Using numerical simulations, it is shown that the proposed cumulant MR approach is unable to unambiguously determine the Herschel–Bulkley rheological parameters due to the known interdependence that exists between n, τ_0, and K [29]. To this end, an alternative approach is developed utilising Bayesian analysis that does enable the unambiguous determination of n, τ_0, and K.

4.2 Cumulant analysis

4.2.1 Model development

In Chapter 3 it was shown that the natural logarithm of $S(q)$ can be described using

$$\ln S(q) = \sum_{j=1}^{\infty} \frac{(\mathrm{i}2\pi q)^j}{j!} \kappa_j, \tag{4.6}$$

known as the cumulant generating function, where κ_j corresponds to the j^{th} cumulant. The cumulant MR approach developed here, enabling the estimation of the Herschel–

Bulkley rheological parameters, is summarised in Fig. 4.2, with a more complete introduction to cumulant analysis included in Section 3.1. The generation of cumulants requires the numerical simulation of $S(q)$ for a suitable range of n and r_0/R. In this work, an analytical expression derived by Chevalier *et al.* [30] is used to describe $p(\zeta)$, and generate $S(q)$ numerically, as a function of both n and r_0/R. The details of the derivation are shown below.

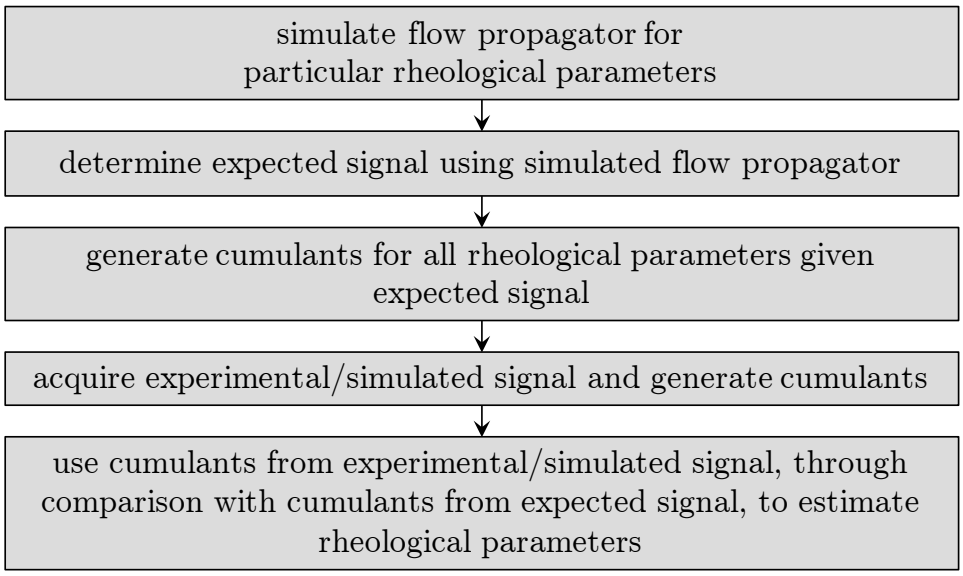

Fig. 4.2: A block diagram outlining the five key stages in the proposed cumulant MR approach.

From Eq. (4.4), ζ can be correlated with radial position, r, for a fluid demonstrating Herschel–Bulkley rheology using

$$r(\zeta) = r_0 + (R - r_0)\left(1 - \frac{\zeta}{\zeta_{\max}}\right)^{\frac{n}{n+1}}. \tag{4.7}$$

If a homogeneous spin density is assumed, $p(\zeta)$ per unit length is proportional to the area of the flow field associated with ζ, given by the differential of $A(\zeta)$ and denoted $\mathrm{d}A$, with $A(\zeta) = \pi r(\zeta)^2$. In the absence of self-diffusion, $p(\zeta)$ can be described as

$$p(\zeta) \propto \frac{\mathrm{d}}{\mathrm{d}\zeta}\left(\pi\left(r_0 + (R - r_0)\left(1 - \frac{\zeta}{\zeta_{\max}}\right)^{\frac{n}{n+1}}\right)^2\right). \tag{4.8}$$

We now drop the constant πR^2 for convenience and evaluate the differential in Eq. (4.8) to obtain an analytical expression describing $p(\zeta)$, as a function of n and r_0/R, given by

$$p(\zeta, n, r_0) = \begin{cases} \dfrac{2}{\zeta_{\max}} \dfrac{R - r_0}{R^2} \dfrac{n}{n+1} \left(1 - \dfrac{\zeta}{\zeta_{\max}}\right)^{\frac{-1}{n+1}} \\ \quad \times \left(r_0 + (R - r_0)\left(1 - \dfrac{\zeta}{\zeta_{\max}}\right)^{\frac{n}{n+1}}\right), & 0 < \zeta < \zeta_{\max}, \\ \left(\dfrac{r_0}{R}\right)^2 \delta_{\zeta - \zeta_{\max}}, & \zeta = \zeta_{\max}, \end{cases} \tag{4.9}$$

where $\delta_{\zeta-\zeta_{\max}}$ is a Dirac delta function with respect to ζ. Figure 4.3 shows $p(\zeta)$ for the three example fluids considered in Fig. 4.1. It is seen that a decrease in n and an increase in r_0/R, *i.e.* an increase in τ_0/τ_w, causes a decrease in $\zeta_{\max}$ and an increase in the maximum probability. The changes in $p(\zeta)$ due to changes in n and r_0/R are, therefore, expected to induce measurable changes in $S(q)$.

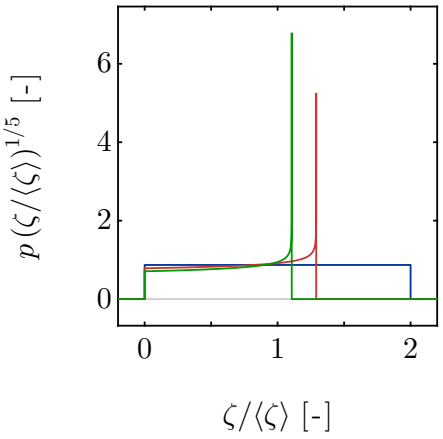

Fig. 4.3: Simulated flow propagators for three example fluids; where (—) $n = 1.0$ and $r_0/R = 0.0$, (—) $n = 0.5$ and $r_0/R = 0.5$, and (—) $n = 0.5$ and $r_0/R = 0.8$. The flow propagators have been scaled to the power of the fifth root for clarity.

Experimentally, an outflow of spins will lead to some loss of signal, with the amount lost proportional to the local displacement. To account for this, a correction is applied

to $p(\zeta, n, r_0)$ calculated using Eq. (4.9) with the form

$$p'(\zeta, n, r_0) = (1 - \Lambda)\, p(\zeta, n, r_0), \tag{4.10}$$

where $p'(\zeta, n, r_0)$ is the experimentally-acquired flow propagator and $\Lambda = \zeta/L$, with L the length of the excitation region as determined by the experimental set-up. Furthermore, self-diffusion is responsible for the Gaussian broadening of $p'(\zeta, n, r_0)$ such that the expected complex signal in q-space becomes

$$\frac{S(q, n, r_0)}{|S(0)|} = \int p'(\zeta, n, r_0) \exp\left[\mathrm{i}2\pi q\zeta - 4\pi^2 D\left(\Delta - \frac{\delta}{3}\right) q^2\right] \mathrm{d}\zeta, \tag{4.11}$$

with D the self-diffusion coefficient and Δ the flow contrast time. Sampling $S(q)$ over a low-q range negates the requirement of higher-order cumulants, with the optimum sampling range found in Section 3.2 to be $\pm 0.4\langle\zeta\rangle^{-1}\,\mathrm{m}^{-1}$, where $\langle\zeta\rangle$ is the mean fluid displacement. For the calculation of $\langle\zeta\rangle$, the integration of Eq. (4.4) with respect to the cross-sectional area of the pipe, and between the limits of 0 and R, gives

$$\langle\zeta\rangle = \zeta_{\max}\left(\frac{n+1}{3n+1} + \frac{2r_0 n\,(n+1)}{R\,(3n+1)\,(2n+1)} + \frac{2n^2 r_0^2}{R^2\,(3n+1)\,(2n+1)}\right). \tag{4.12}$$

If $\langle\zeta\rangle$ is known, the expected $S(q)$ can be determined for particular n and r_0/R using Eq. (4.11). Figure 4.4 shows the (a) log-magnitude and (b) phase of $S(q)$ over a low-q range for the three example fluids considered in Fig. 4.1. A decrease in n and increase in r_0/R is responsible for an increase in $\ln(|S(q)|)$ at the limits of q-space sampled. Over a low-q-range, the log-magnitude and phase of $S(q)$ can be described using

$$\ln(|S(q)|) = -\frac{1}{2}\kappa_2 (2\pi q)^2 + \frac{1}{24}\kappa_4 (2\pi q)^4, \tag{4.13}$$

$$\theta(q) = \kappa_1 (2\pi q) - \frac{1}{6}\kappa_3 (2\pi q)^3, \tag{4.14}$$

with κ_1, κ_2, κ_3, and κ_4 known as mean, variance, skewness, and kurtosis, respectively.

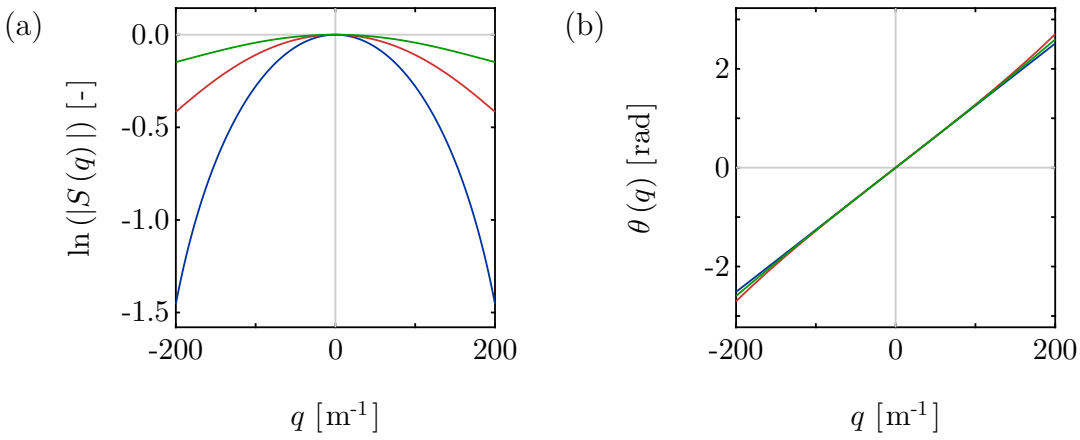

Fig. 4.4: The evolution of the (a) log-magnitude and (b) phase of $S(q)$ over a low-q range for three example fluids; where (—) $n = 1.0$ and $r_0/R = 0.0$, (—) $n = 0.5$ and $r_0/R = 0.5$, and (—) $n = 0.5$ and $r_0/R = 0.8$. The expected $S(q)$ data were simulated with $\langle \zeta \rangle = 2\,\text{mm}$ in the absence of self-diffusion and the outflow of spins.

Using Eqs. (4.9) to (4.12), expected $S(q)$ data were simulated for a suitable range of rheological parameters. The LLS regression of Eqs. (4.13) and (4.14) to the expected $S(q)$ data was performed across an increasing range of q, to the upper limit of q-space sampled, $|q_{\text{max}}|$, to generate multiple cumulants. Note that lower limits on the fit range defined as $2^{-1/4}\,|q_{\text{max}}|$ for the log-magnitude and $2^{-1/3}\,|q_{\text{max}}|$ for the phase of $S(q)$ are imposed, as outlined in the literature [31]. The cumulants reported are the Q-weighted mean cumulant values, with the errors representative of the standard deviation of the cumulants. Using methods outlined previously, cumulants for all n and r_0/R were then obtained from the expected $S(q)$ data. The relationship between the cumulants and n and r_0/R is shown in Fig. 4.5 for (a) κ_1, (b) κ_2, (c) κ_3, and (d) κ_4. It is interesting to note that, as $\ln S(q)$ is non-uniquely specified by its cumulants and/or due to the known interdependence that exists between n and r_0/R [29], all cumulants are seen in Fig. 4.5 to be non-unique in their solution of both n and r_0/R. The significance of this is investigated in Section 4.2.3, where numerical simulations are used to study the sensitivity of the proposed cumulant MR approach to changes in the Herschel–Bulkley rheological parameters for a fixed signal-to-noise ratio (SNR).

If we assume a Gaussian distribution of cumulants corresponding to the increasing fit range, due to random Gaussian noise, a probability distribution of n and r_0/R can be produced for each cumulant (above first order) using the mean cumulant value and the standard deviation of the cumulants. The product of the three distributions, denoted

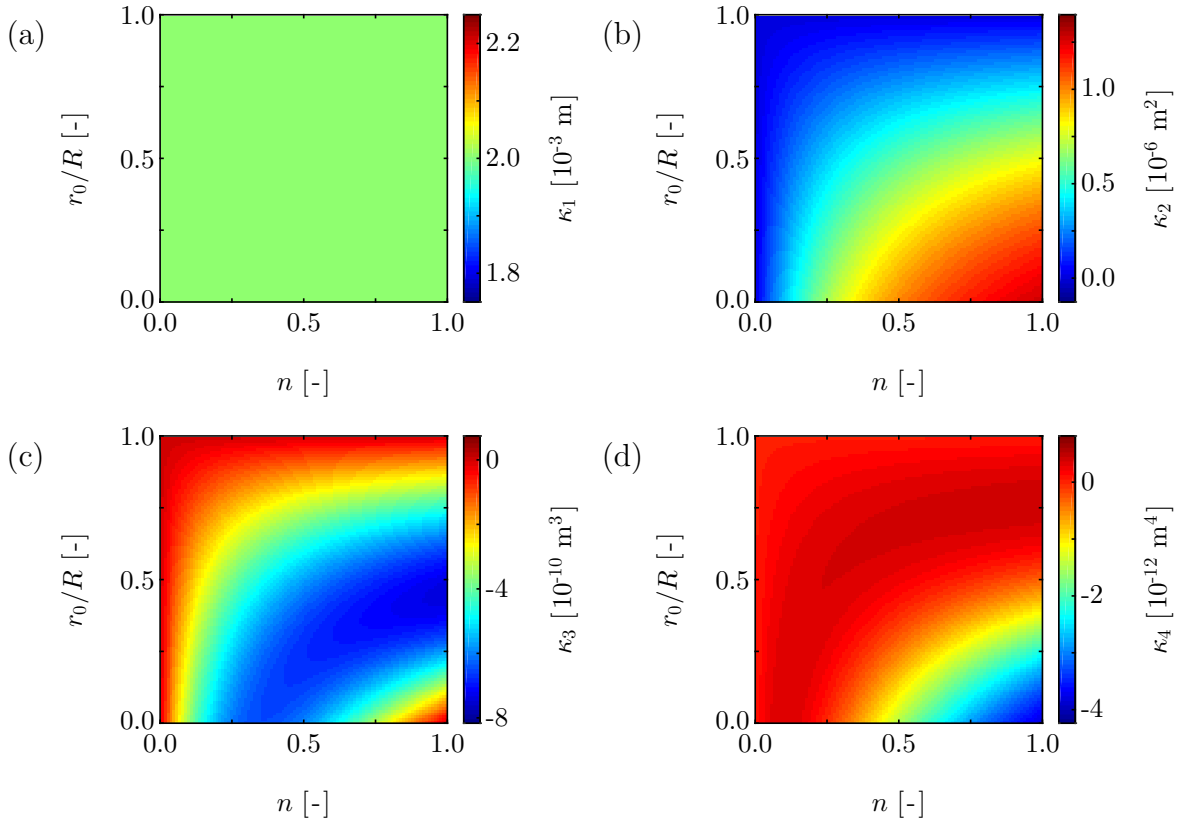

Fig. 4.5: (a) First, (b) second, (c) third, and (d) fourth cumulants plotted as a function of n and r_0/R. The expected $S(q)$ data were simulated with $\langle\zeta\rangle = 2\,\text{mm}$ in the absence of self-diffusion and the outflow of spins.

$p(n, r_0)$ and given by $p(n, r_0, \kappa_2)\, p(n, r_0, \kappa_3)\, p(n, r_0, \kappa_4)$, gives the overall distribution; n and r_0/R values reported correspond to the mean n and r_0/R values, respectively, calculated from $p(n, r_0)$, with the standard deviations a measure of the uncertainty.

4.2.2 Simulations

Numerical simulations were performed in MATLAB 2012b, operating under Windows 7, to examine the sensitivity of the proposed cumulant MR approach to changes in the Herschel–Bulkley rheological parameters. Simulated data were generated by the addition of pseudo-random Gaussian noise in quadrature, with zero mean and standard deviation σ, to noise-free data obtained using Eq. (4.11), such that

$$\frac{S(q, n, r_0)}{|S(0)|} = \int p'(\zeta, n, r_0) \exp\left[\mathrm{i}2\pi q\zeta - 4\pi^2 D\left(\Delta - \frac{\delta}{3}\right) q^2\right] \mathrm{d}\zeta + e(q)\,, \qquad (4.15)$$

where $e(q)$ represents the added pseudo-random Gaussian noise. Note that SNR is here defined as the ratio of the signal intensity at the centre of q-space to σ. Experimental variables were selected as follows:

- $\langle\zeta\rangle = 2\,\mathrm{mm}$, with the value of $\zeta_{\max}$ determined for each combination of n and r_0 considered using Eq. (4.12), and $p'(\zeta, n, r_0)$ determined for 2^{15} linear increments in ζ between zero and $\zeta_{\max}$.
- n was increased linearly between 0.1 and 1.0 in 10 steps.
- r_0/R, corresponding to τ_0/τ_{w}, was incremented linearly in 10 steps between 0.0 and 0.9.
- The signal in q-space was sampled linearly at 128 points in q-space over a low-q range of $\pm 0.4\langle\zeta\rangle^{-1}\,\mathrm{m}^{-1}$.
- Noise, *i.e.* the noise-to-signal ratio represented as a percentage, was fixed at 0.01, corresponding to SNR = 100.

Simulations were performed 10^2 times, each with pseudo-random Gaussian noise, for all combinations of experimental parameters. Mean n and r_0/R were determined for each repetition using the methods outlined in Section 4.2.1, and the simulation values reported in Section 4.2.3 are the mean and standard deviation of the 100 mean n and r_0/R values. To generate the cumulant data for comparison with experimental data, 100 increments in n and r_0/R were used evenly spaced between 0.01 and 1.00 and 0.00 and 0.99, respectively, to provide a resolution of 0.01.

4.2.3 Results and discussion

Figure 4.6 shows $p(n, r_0)$ obtained using the proposed cumulant MR approach for a single simulation experiment with 128 sampled q-space data points and SNR = 100. An increase in the estimate of n is seen to cause an increase in r_0/R; this interdependence was previously observed using conventional rheometry [29] and makes the unambiguous determination of n and r_0/R difficult [5]. From $p(n, r_0)$ shown in Fig. 4.6, estimates of $n = 0.38\pm0.18$ and $r_0/R = 0.34\pm0.18$ were obtained, where the uncertainties represent the standard deviation of n and r_0/R, accurate to within 32% of the input n and r_0/R of 0.50.

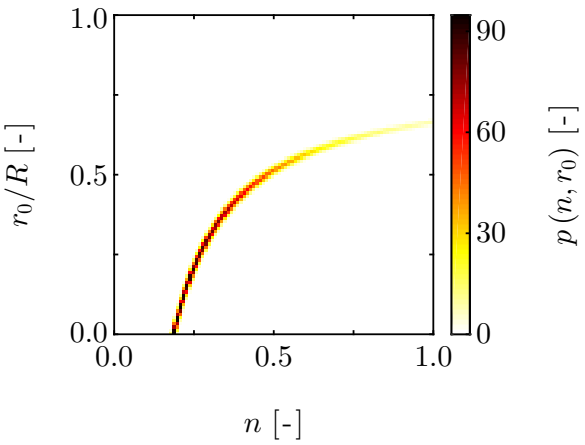

Fig. 4.6: A 2D probability distribution showing the probability of n and r_0/R obtained using the proposed cumulant MR approach with simulated data. The data were generated with 128 sampled q-space data points and SNR = 100 for an input n and r_0/R of 0.5.

Simulation experiments were repeated 10^2 times for all combinations of input n and r_0/R, each with pseudo-random Gaussian noise. The mean and standard deviation of the 100 mean n and r_0/R values were used to quantify the accuracy and uncertainty associated with the proposed cumulant MR approach. Figure 4.7 shows the mean and uncertainty of (a) n for r_0/R of 0.0, 0.2, and 0.5, and (b) r_0/R for n of 1.0, 0.8, and 0.5 with 128 sampled q-space data points and fixed SNR = 100. Although Fig. 4.7(a) shows the expected trend, *i.e.* an increase in the output n with an increase in the input n, the proposed cumulant MR approach is responsible for both random and systematic error. Across all r_0/R, a decrease in the input n from 1.0 to 0.1 was responsible for an increase in the mean absolute error in the output n from 25 to 240% and an increase in the mean uncertainty from 9.0 to 120%. In contrast, the accuracy of the output n was almost independent of the input r_0/R, with a mean absolute error (for all input n considered) of 50% and a mean uncertainty of 37%. Considering r_0/R, it is observed in Fig. 4.7(b) that the mean absolute error in the output r_0/R was dependent upon the input r_0/R; across all n, an increase in the input r_0/R from 0.1 to 0.9 was responsible for a decrease in the mean absolute error from 130 to 17% and a decrease in the mean uncertainty from 59 to 7.6%. In addition, the mean absolute error associated with the output r_0/R (for an input r_0/R in the range 0.1–0.9) increased from 25 to 93% for a decrease in the input n from 1.0 to 0.1, with an increase in the mean uncertainty from 75 to 190%. Across all rheological parameters, the mean absolute error in the output n and r_0/R was 50 and 33%, respectively, with mean uncertainties of 37 and 110%.

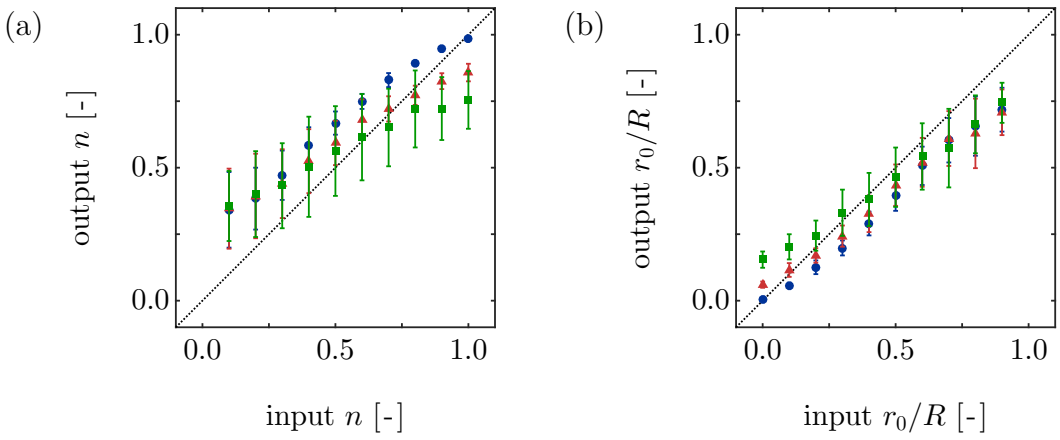

Fig. 4.7: (a) A comparison between the input n, *i.e.* the ground truth, and output n, *i.e.* the estimate, using the proposed cumulant MR approach with 128 sampled q-space data points and SNR = 100, plotted for r_0/R equal to (●) 0.0, (▲) 0.2, and (■) 0.5. (b) Corresponding data plotted for the estimate of r_0/R with n equal to (●) 1.0, (▲) 0.8, and (■) 0.5. The diagonal line (·····) represents the expected result, *i.e.* input = output.

These results are important as they imply that the accuracy of the estimation of n and r_0/R increases as both n and r_0/R tend to 1.0. Furthermore, the results suggest that, for 128 sampled q-space data points and with SNR = 100, the proposed cumulant MR approach is unable to unambiguously determine n and r_0/R and is unsuitable for the rheological characterisation of Herschel–Bulkley fluids. This finding is most likely due to the known interdependence that exists between n and r_0/R, with an alternative approach sought that is suitable for use with such fluids.

4.2.4 Conclusions

A cumulant MR approach was developed to enable numerical simulation of the signal in q-space and rheological characterisation of Herschel–Bulkley fluids using cumulant analysis. However, due to the known interdependence between Herschel–Bulkley rheological parameters, the proposed cumulant MR approach is unable to unambiguously determine n and r_0/R and is thus unsuitable for use with Herschel–Bulkley fluids; for 128 sampled q-space data points and SNR = 100, mean absolute errors of 50 and 33% were typical for n and r_0/R, respectively, with mean uncertainties of 37 and 110%. Therefore, an alternative approach is sought that overcomes the interdependence between the Herschel–Bulkley rheological parameters and does enable the unambiguous determination of n and r_0/R.

4.3 Bayesian analysis

4.3.1 Model development

Bayesian analysis is a probabilistic approach that has previously been applied in a variety of MR applications [32–38]; it has been shown to improve the accuracy of flow measurements by the use of reduced sampling [33], and to enable the recovery of MR spectra [32] and particle size distributions [37] from noisy data. In Bayesian analysis, the state of the system, Θ, is inferred from a set of experimental observations, $\hat{y}$, using the posterior probability density function, $p(\Theta|\hat{y})$, given by

$$p(\Theta|\hat{y}) \propto p(\hat{y}|\Theta)\, p(\Theta)\,, \tag{4.16}$$

where $p(\hat{y}|\Theta)$ is the likelihood function and $p(\Theta)$ incorporates prior knowledge.

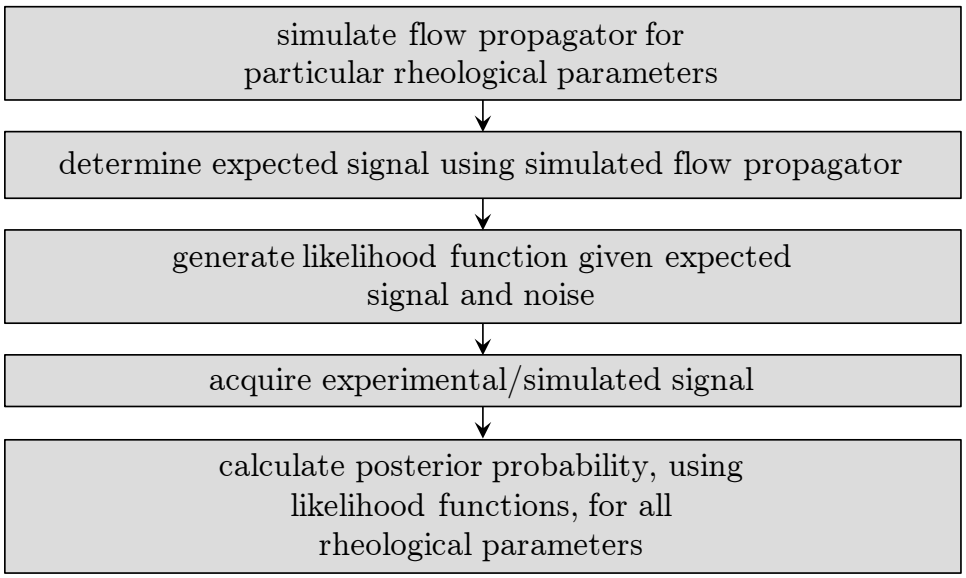

Fig. 4.8: A block diagram outlining the five key stages in the proposed Bayesian MR approach.

In this Chapter, a Bayesian MR approach is developed to enable the estimation of Herschel–Bulkley rheological parameters using PFG MR, where $\hat{y}$ corresponds to $S(q)$ and Θ corresponds to n and r_0/R describing the rheology of the fluid under study. The likelihood function then describes the variation of $S(q)$ for a particular combination

of n and r_0/R, and the prior describes what is already known about the probabilities of the values of n and r_0/R. A prior in which the probabilities within a specified range are identical is known as a simple uninformative prior. The development of a Bayesian MR approach enabling the estimation of these parameters is illustrated in Fig. 4.8 and will now be outlined.

The signal in q-space is sampled in quadrature across a high-q range in the presence of Gaussian noise. Therefore, the likelihood function utilising the complex $S(q)$ data takes the form

$$p(S(q)|n, r_0) = \frac{1}{\sigma\sqrt{2\pi}} \exp\left[-\frac{|S(q) - \lambda|^2}{2\sigma^2}\right] \tag{4.17}$$

for flow that is stable over the experimental duration, *i.e.* laminar flow, where λ is the expected complex signal in q-space for a particular q, n, and r_0/R, denoted $\mathbb{E}[S(q)]$. For simplicity, $\mathbb{E}[S(q)]$ will be referred to as $f(q, n, r_0)$. In addition to the variation of the phase of $S(q)$ and $f(q, n, r_0)$ with q, $S(q)$ may also possess an additional phase offset due to the receiver. A comparison between $S(q)$ and $f(q, n, r_0)$ data requires the removal of this phase offset through phase correction of the $S(q)$ data such that the phase of the signal at $q = 0\,\mathrm{m}^{-1}$ is zero. Alternatively, the need for phase correction is removed by considering the magnitude of $S(q)$. For complex data with random phase, a Rayleigh distribution may be used to describe the likelihood function [39]. However, the phase associated with $S(q)$ is not random and so the likelihood function is instead described using

$$p(S(q)|n, r_0) = \frac{|S(q)|}{\sigma^2} \exp\left[-\frac{|S(q)|^2 + |\lambda|^2}{2\sigma^2}\right] J_0\left(\frac{|S(q)|\,|\lambda|}{\sigma^2}\right), \tag{4.18}$$

known as a Rician distribution [40], where J_0 is a modified zeroth order Bessel function of the first kind. Figure 4.9 shows (a) Gaussian and (b) Rician distributions at three values of SNR, with a Rician distribution shown to tend to a Rayleigh distribution at low SNR and a Gaussian distribution at high SNR. The choice of likelihood function, *i.e.* a Gaussian likelihood function describing complex $S(q)$ data or a Rician likelihood function describing $|S(q)|$, is investigated in Section 4.3.2 by considering the accuracy associated with the estimation of n and r_0/R using numerical simulations.

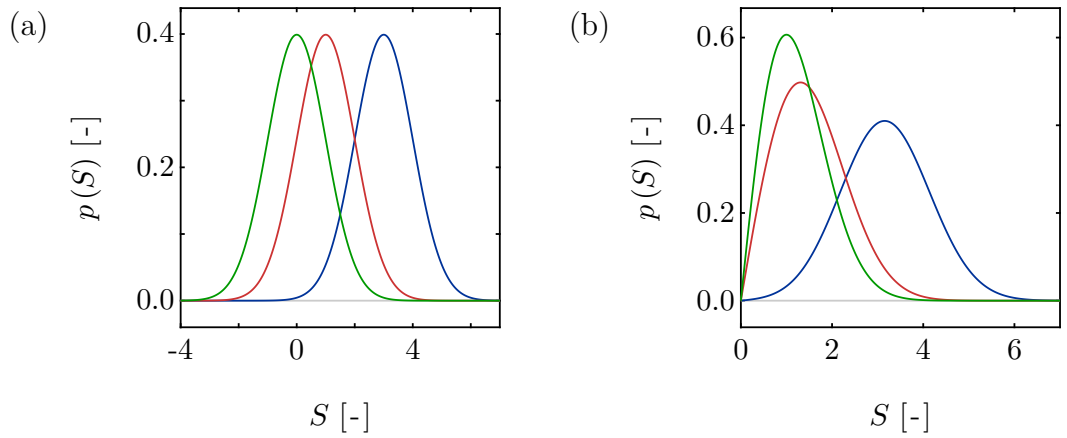

Fig. 4.9: Plots to show (a) Gaussian and (b) Rician distributions with $\sigma = 1$ and SNR of (—) 3, (—) 1, and (—) 0.

In order to determine $p\left(S\left(q\right)|n, r_0\right)$, $f\left(q, n, r_0\right)$ must first be obtained numerically using the methodology developed in Section 4.2.1, where

$$\frac{f\left(q, n, r_0\right)}{\left|f\left(0\right)\right|} = \int p'\left(\zeta, n, r_0\right) \exp\left[\mathrm{i}2\pi q\zeta - 4\pi^2 D\left(\Delta - \frac{\delta}{3}\right) q^2\right] \mathrm{d}\zeta \tag{4.19}$$

and $p'\left(\zeta, n, r_0\right)$ is determined using Eqs. (4.9) and (4.10), requiring $\zeta_{\max}$ be calculated using Eq. (4.12). Figure 4.10 shows the (a) real component, (b) imaginary component, and (c) magnitude of $f\left(q\right)$ over a high-q range of $\pm 10\langle\zeta\rangle^{-1}\,\mathrm{m}^{-1}$ for the three example fluids considered in Fig. 4.1. A decrease in n and an increase in r_0/R is observed to cause both a decrease in the frequency of oscillations in $f\left(q\right)$ and an increase in $\left|f\left(q\right)\right|$ at the limits of q-space sampled. It is interesting to note that, as follows from simple Fourier theory, the size of the plug flow region can be obtained from $\left|S\left(q\right)\right|$ at high-q (if the diffusion coefficient is known), and its displacement can be obtained from the frequency of the oscillations in q-space. Experimentally, gradient hardware limitations and spin relaxation times limit the range of q-space accessible. Therefore, an optimum q-space sampling range is required to be defined that minimises the gradient hardware requirements whilst enabling the accurate estimation of n and r_0/R. In Chapter 3, the optimum range of q-space required to be sampled for cumulant analysis was determined to be $\pm 0.4\langle\zeta\rangle^{-1}\,\mathrm{m}^{-1}$ through measurement of the goodness-of-fit parameter across an increasing range of q-space. For the case of Bayesian analysis, an alternative approach was employed in which the variability of $f\left(q\right)$ with both n and r_0/R was determined.

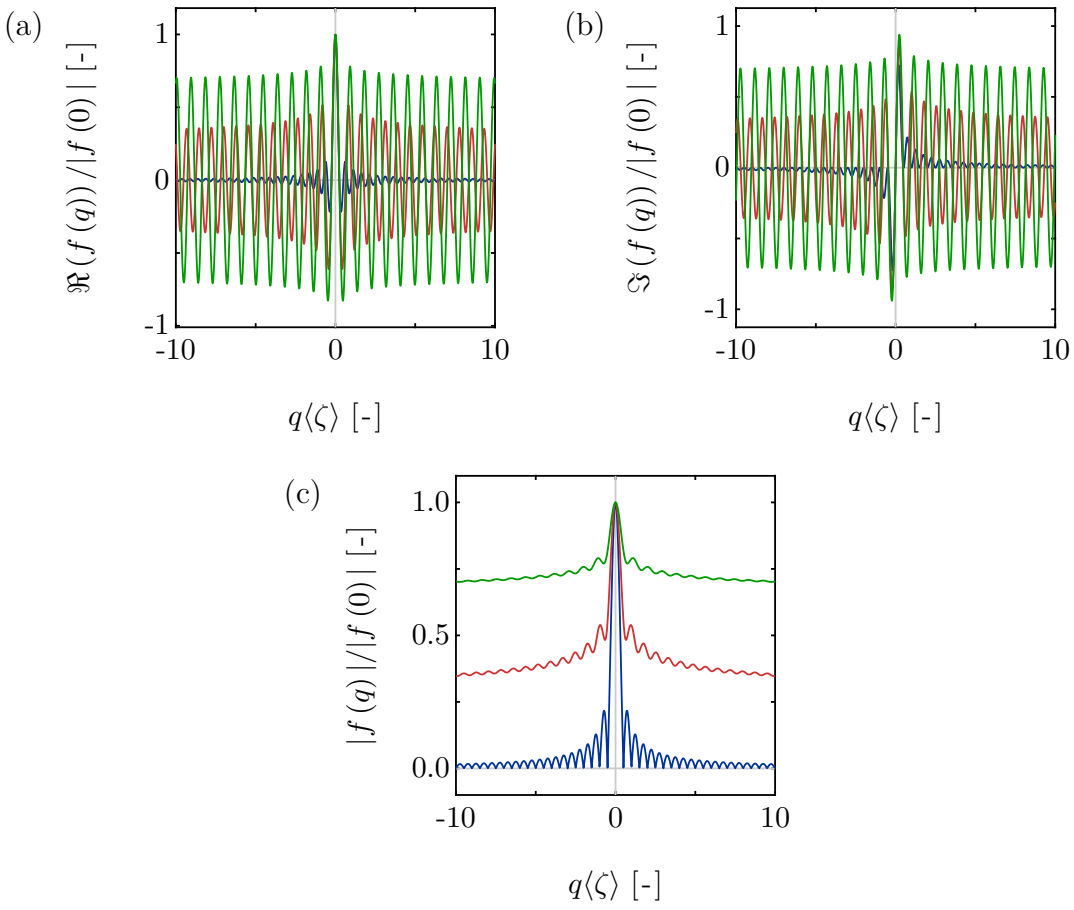

Fig. 4.10: Evolution of the (a) real component, (b) imaginary component, and (c) magnitude of $f(q)$ over a high-q range for three example fluids; where (—) $n = 1.0$ and $r_0/R = 0.0$, (—) $n = 0.5$ and $r_0/R = 0.5$, and (—) $n = 0.5$ and $r_0/R = 0.8$. The expected $f(q)$ data were simulated with $\langle\zeta\rangle = 2\,\text{mm}$ in the absence of self-diffusion and the outflow of spins.

It follows, from simple Fourier theory and in the absence of self-diffusion, that the shifted delta function arising in $p'(\zeta)$ due to an increase in r_0/R, as shown in Fig. 4.3, is responsible for a constant magnitude signal with oscillating phase. A reduction in n, however, is responsible for a signal with both oscillating magnitude and phase. To this end, the determination of the optimum sampling range for Bayesian analysis requires careful consideration of the variability of both of these components of $f(q)$ with q and the determination of those regions in q-space that are most sensitive to n and r_0/R. This variability was quantified, for a particular q and across a suitable range of n and r_0/R, using two metrics; namely the range and standard deviation of $f(q)$. Note that Herschel–Bulkley rheology was assumed.

Using methodology developed in Section 4.2.1, $f(q)$ was simulated for 100 linear increments in n and r_0/R between 0.01 and 1.00 and 0.00 and 0.99, respectively, and across a q-space range of $\pm 10\langle\zeta\rangle^{-1}\,\mathrm{m}^{-1}$. Figure 4.11 shows the mean contributions of n and r_0/R to the (a) real component, (c) imaginary component, and (e) magnitude of $f(q)$. The standard deviations of the (b) real component, (d) imaginary component, and (f) magnitude of $f(q)$ are also presented. It is demonstrated in Fig. 4.11(e) that $\langle|f(q)|\rangle$ associated with n is 0.67 at the centre of q-space, compared with 0.33 for that arising due to r_0/R. However, $\langle|f(q)|\rangle$ arising due to r_0/R remains independent of q whilst that associated with n decreases with increasing $|q|$; $\langle|f(q)|\rangle$ associated with n decreases from 0.67 to 0.14 as $|q|$ is increased from $0\,\mathrm{m}^{-1}$ to $10\langle\zeta\rangle^{-1}\,\mathrm{m}^{-1}$, corresponding to a reduction of $< 80\%$. Note that the contributions to $\langle|f(q)|\rangle$ from n and r_0/R are identical at $\pm 0.5\langle\zeta\rangle^{-1}\,\mathrm{m}^{-1}$. Similar trends are also observed in Figs. 4.11(a) and (c) for the real and imaginary components of $f(q)$, respectively. Considering the standard deviation of the contributions of n and r_0/R to $f(q)$, it is shown in Figs. 4.11(b) and (d) that the standard deviation of the real and imaginary components first increases with an increase in $|q|$, to a maximum at $\pm 2\langle\zeta\rangle^{-1}\,\mathrm{m}^{-1}$, before then decreasing. This indicates that a sampling range of at least $\pm 2\langle\zeta\rangle^{-1}\,\mathrm{m}^{-1}$ is required to maximise the sensitivity of the proposed Bayesian MR approaches to changes in the Herschel–Bulkley rheological parameters of the fluid under study, with a maximum variability in $f(q)$ with both n and r_0/R expected across this region.

A reduction in SNR with an increase in $|q|$, due to a reduction in $\langle|f(q)|\rangle$ associated with n, and flow encoding gradient strength limitations restrict the range of q-space accessible, particularly for small molecular displacements and at low field strengths. In addition, further reductions in SNR with an increase in $|q|$ result from self-diffusion, which is responsible for the Gaussian broadening of $p'(\zeta)$ and the attenuation of $|f(q)|$, the extent of which depends upon $|q|$, D, and Δ [26]. For these reasons, an optimum q-space sampling range of $\pm 4\langle\zeta\rangle^{-1}\,\mathrm{m}^{-1}$ is proposed; at $\pm 4\langle\zeta\rangle^{-1}\,\mathrm{m}^{-1}$, the mean signal associated with r_0/R is seen in Fig. 4.11(e) to be approximately twice the mean signal that arises due to n, with the opposite true in the centre of q-space. Whilst the sampling of a q-space range greater than $\pm 4\langle\zeta\rangle^{-1}\,\mathrm{m}^{-1}$ will not negatively affect the estimation of Herschel–Bulkley rheological parameters using the proposed Bayesian MR approaches, a suitable sampling density across the proposed range of $\pm 4\langle\zeta\rangle^{-1}\,\mathrm{m}^{-1}$ is advised to ensure maximum sensitivity to changes in both n and r_0/R, as described above. The number of q-space data points required to be sampled over this range is investigated and discussed in detail in Chapter 5.

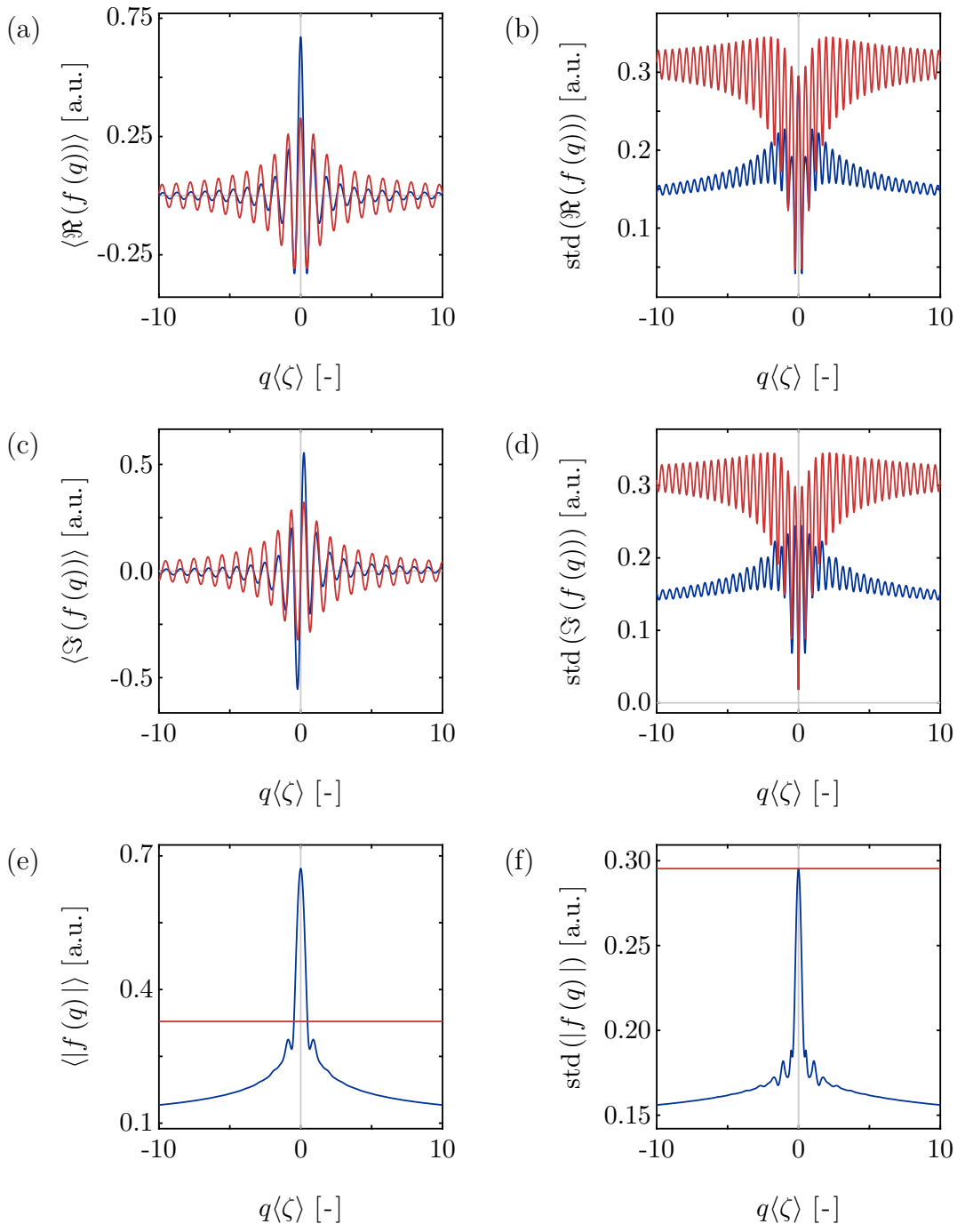

Fig. 4.11: The evolution of the mean (a) real components, (c) imaginary components, and (e) magnitudes of the (—) n and (—) r_0/R contributions to $f(q)$ and (b,d,f) corresponding standard deviations. Expected $f(q)$ data were simulated with $\langle\zeta\rangle = 2\,\text{mm}$ and $|f(0)| = 0$ a.u. in the absence of self-diffusion and outflow of spins for 100 increments in n and r_0/R evenly spaced between 0.01–1.00 and 0.00–0.99, respectively.

Flow propagators generated using Eqs. (4.9) and (4.10) can be used with Eq. (4.19) to generate $f(q, n, r_0)$ for any combination of n and r_0/R. A 3D dictionary is then constructed for all required n, r_0/R, and q, with the posterior probability of a particular n and r_0/R obtained from a set of experimental measurements of $S(q)$ by calculating the probability of each measurement using Eqs. (4.17) and (4.18). The product of the individual probabilities gives the posterior probability, as described by

$$p(n, r_0|\hat{y}) = \prod_{i=1}^{N} \frac{1}{\sigma\sqrt{2\pi}} \exp\left[-\frac{|S(q_i) - \lambda|^2}{2\sigma^2}\right] \tag{4.20}$$

and

$$p(n, r_0|\hat{y}) = \prod_{i=1}^{N} \frac{|S(q_i)|}{\sigma^2} \exp\left[-\frac{|S(q_i)|^2 + |\lambda|^2}{2\sigma^2}\right] J_0\left(\frac{|S(q_i)|\,|\lambda|}{\sigma^2}\right) \tag{4.21}$$

for the Gaussian and Rician likelihood functions, respectively, where N is the number of sampled q-space data points. This is repeated for all combinations of n and r_0/R to quantify the full 2D posterior probability distribution, $p(\Theta|\hat{y})$, where $\hat{y} = S(q)$ and $\Theta = \{n, r_0\}$. A summation along the n and r_0 axes may be used to characterise $p(n|\hat{y})$ and $p(r_0|\hat{y})$, respectively, with estimates of n and r_0/R given by the means of these distributions and the standard deviations a measure of the uncertainty.

4.3.2 Simulations

The sensitivity of the proposed Bayesian MR approaches, utilising the Gaussian and Rician likelihood functions, to changes in the Herschel–Bulkley rheological parameters was investigated with 128 sampled q-space data points and a fixed SNR = 100 using the experimental parameters reported in Section 4.2.2 but instead over a high-q range of $\pm 4\langle\zeta\rangle^{-1}\,\mathrm{m}^{-1}$. For Bayesian analysis of the $S(q, n, r_0)$ data simulated using Eq. (4.15), a simple uninformative prior ($p(\Theta)$ in Eq. (4.16)) was used such that the probability of each of the parameter values considered was assumed to be identical. In particular, the range of priors comprised of a set of 501 values evenly spaced between 0 and 1 for both n and r_0/R, corresponding to a resolution of 0.002. Using Eq. (4.19), $f(q, n, r_0)$ was simulated for all n and r_0 values and $p(\Theta|\hat{y})$ obtained using Eqs. (4.20) and (4.21) for

the Gaussian and Rician likelihood functions, respectively; the means extracted from $p(\Theta|\hat{y})$ provide an estimate of n and r_0/R, with the standard deviations a measure of the uncertainty. Simulation experiments were repeated 10^2 times, each with pseudo-random Gaussian noise, for all combinations of parameters identified previously. Values reported, unless otherwise stated, correspond to the mean of the 100 means, with the standard deviation of the 100 means a measure of the uncertainty.

4.3.3 Results and discussion

The robustness of the proposed Bayesian MR approaches to changes in n and r_0/R was investigated with 128 sampled q-space data points at a single, fixed SNR = 100. Figure 4.12 shows $p(\Theta|\hat{y})$ obtained using the (a) Gaussian and (b) Rician likelihood functions with the same dataset for an input n and r_0/R of 0.50. It is seen that both Bayesian MR approaches enable the accurate estimation of n and r_0/R; from $p(\Theta|\hat{y})$, $n = 0.50\pm0.01$ and $r_0/R = 0.50\pm0.01$ are obtained using the Gaussian likelihood function, and $n = 0.49\pm0.02$ and $r_0/R = 0.50\pm0.01$ using the Rician likelihood function. The estimated parameters are, therefore, accurate to within 1% of the input n and r_0/R using the Gaussian likelihood function, compared with 2% when using the Rician likelihood function. Note that due to the interdependence between the Herschel–Bulkley rheological parameters, both $p(\Theta|\hat{y})$ demonstrate an identical trend.

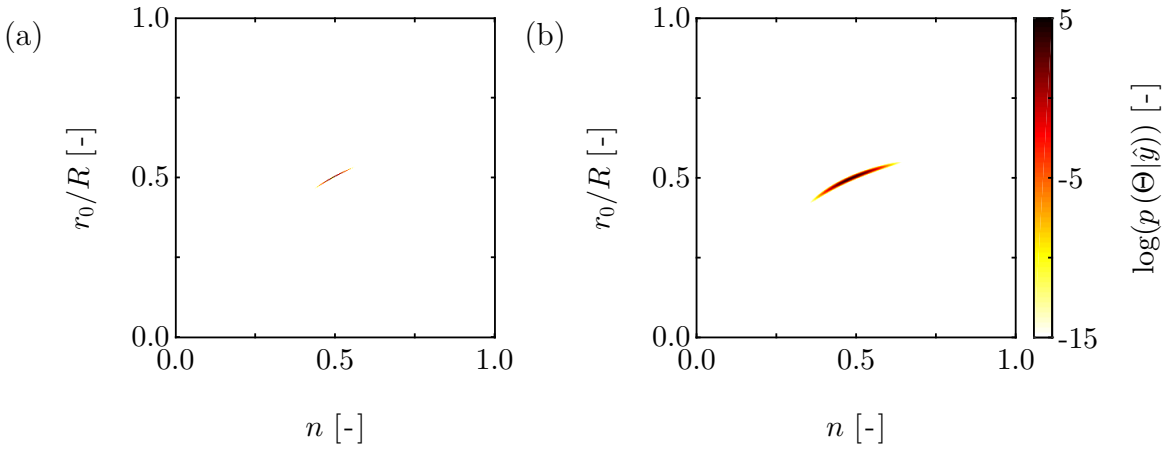

Fig. 4.12: A 2D probability distribution, plotted on a log scale, showing the probability of n and r_0/R obtained using the proposed Bayesian MR approaches, utilising the (a) Gaussian and (b) Rician likelihood functions, with simulated data. The data were generated with 128 sampled q-space data points and SNR = 100 for an input of $n = 0.5$ and $r_0/R = 0.5$.

Simulation experiments were repeated 10^2 times for all combinations of input n and r_0/R described in Section 4.2.2, each with pseudo-random Gaussian noise. The mean and standard deviation of the 100 mean n and r_0/R values were used to quantify the accuracy and uncertainty associated with the proposed Bayesian MR approaches. Figure 4.13 shows the mean and uncertainty of n for r_0/R of 0.0, 0.2, and 0.5 using the (a) Gaussian and (b) Rician likelihood functions with 128 sampled q-space data points and a fixed SNR = 100. Unlike when using the proposed cumulant MR approach, the mean output n show the expected trend and are absent of systematic error.

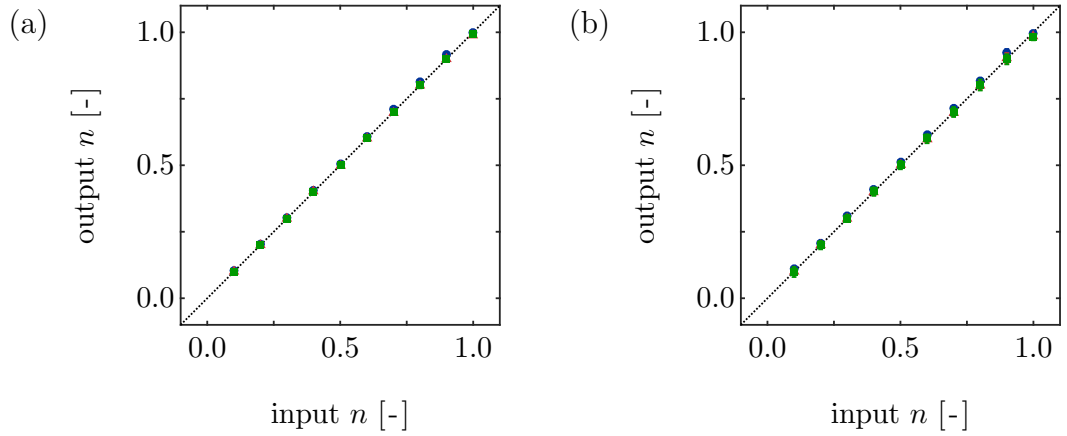

Fig. 4.13: A comparison between the input n, *i.e.* the ground truth, and output n, *i.e.* the estimate, using the proposed Bayesian MR approaches with 128 sampled q-space data points and SNR = 100, plotted for r_0/R equal to (●) 0.0, (▲) 0.2, and (■) 0.5. Data were obtained using the (a) Gaussian and (b) Rician likelihood functions, and the diagonal line (·····) represents the expected result, *i.e.* input = output.

Considering the Bayesian MR approach utilising the Gaussian likelihood function, the mean absolute error in the output n for all input r_0/R considered was $< 1.1\%$ and almost independent of the input n. In contrast, the mean uncertainty was dependent upon the input n, increasing from 0.74 to 9.8% as the input n decreased from 1.0 to 0.1. The accuracy of the output n was also independent of the input r_0/R, with a mean absolute error across all n of 0.50%, however, the mean uncertainty across this range increased from 0.90 to 8.5% as the input r_0/R increased from 0.0 to 0.9. Considering the Bayesian MR approach utilising the Rician likelihood function, the mean absolute error in the output n (across all r_0/R) was $< 4.1\%$, almost 4 times greater than the mean absolute error associated with using the Gaussian likelihood function, and again independent of the input n. Likewise, the mean uncertainty associated with the output

n as the input n decreased from 1.0 to 0.1 also compares unfavourably, increasing from 1.3 to 23%. The accuracy of the output n was independent of the input r_0/R, with a mean absolute error across all n of 1.2%, whilst the mean uncertainty over this range increased from 1.5 to 21% as the input r_0/R increased from 0.0 to 0.9.

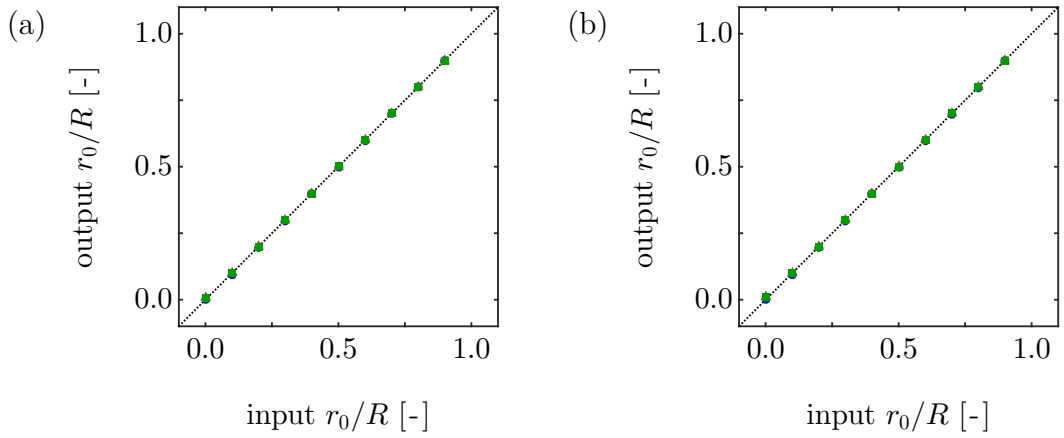

Fig. 4.14: A comparison between the input r_0/R, *i.e.* the ground truth, and output r_0/R, *i.e.* the estimate, using the proposed Bayesian MR approaches with 128 sampled q-space data points and SNR = 100, plotted for n equal to (●) 1.0, (▲) 0.8, and (■) 0.5. Data were obtained using the (a) Gaussian and (b) Rician likelihood functions, and the diagonal line (·····) represents the expected result, *i.e.* input = output.

Figure 4.14 shows the mean and uncertainty of r_0/R for n of 1.0, 0.8, and 0.5 using the (a) Gaussian and (b) Rician likelihood functions. Note the absence of systematic error in the output r_0/R. Considering the Bayesian MR approach utilising the Gaussian likelihood function, the mean absolute error in the output r_0/R was dependent upon the input r_0/R; across all n, an increase in the input r_0/R from 0.1 to 0.9 caused a decrease in both the mean absolute error, from 1.6 to 0.45%, and mean uncertainty, from 10 to 1.0%. In addition, the mean absolute error associated with the output r_0/R (for input r_0/R in the range 0.1–0.9) increased from 1.0 to 2.5% for a decrease in the input n from 1.0 to 0.1, with an increase in the mean uncertainty from 0.6 to 10%. For the Bayesian MR approach utilising the Rician likelihood function, the mean absolute error in the output r_0/R was again dependent upon the input r_0/R, decreasing from 3.2 to 1.7% as the input r_0/R increased from 0.1 to 0.9. The mean uncertainty across this range decreased from 15 to 2.0%. Similarly, a decrease in the input n from 1.0 to 0.1 caused an increase in both the mean absolute error associated with the output r_0/R, from 1.3 to 9.3%, and the mean uncertainty, from 0.8 to 21%.

In summary, the mean absolute error associated with the estimates of n and r_0/R obtained using the proposed Bayesian MR approaches (for all n and r_0/R considered) was 0.50 and 0.49%, respectively, when utilising the Gaussian likelihood function, and 1.2 and 1.3% utilising the Rician likelihood function. The mean uncertainty was 2.7 and 2.6% for n and r_0/R, respectively, when utilising the Gaussian likelihood function, and 6.5 and 4.9% utilising the Rician likelihood function. Therefore, whilst both proposed Bayesian MR approaches enable the unambiguous determination of n and r_0/R, the Gaussian likelihood function appears the obvious choice for future studies due to the increased accuracy and decreased uncertainty when compared to the Rician likelihood function.

4.3.4 Conclusions

The sensitivity of the proposed Bayesian MR approaches was investigated using numerical simulations with 128 sampled q-space data points and SNR = 100. Although both approaches enabled the unambiguous determination of the Herschel–Bulkley rheological parameters, therefore overcoming the known interdependence between n and r_0/R, less good agreement between the estimates of n and r_0/R and the ground truths was observed when utilising a Rician likelihood function. Analysis of the accuracy and uncertainty associated with the estimation of n and r_0/R suggested the Bayesian MR approach utilising the Gaussian likelihood function to be accurate to within 0.50 and 0.49% of the expected n and r_0/R, respectively, with mean uncertainties of 2.7 and 2.6%. In contrast, the mean accuracy of the estimates of n and r_0/R when utilising the Rician likelihood function was 1.2 and 1.3%, respectively, with mean uncertainties of 6.5 and 4.9%. Although both approaches are accurate to within that of conventional rheometry [10], over the optimum sampling range for Bayesian analysis determined in this Chapter to equal $\pm 4\langle\zeta\rangle^{-1}\,\mathrm{m}^{-1}$, a Gaussian likelihood function is shown to be more appropriate for use in the characterisation of Herschel–Bulkley fluids than a Rician likelihood function.

4.4 Conclusions

In this Chapter, two MR rheometry approaches have been developed using cumulant and Bayesian analysis. The robustness and sensitivity of the proposed cumulant and Bayesian MR approaches to changes in the Herschel–Bulkley rheological parameters

was investigated using numerical simulations. It has been demonstrated that the proposed cumulant MR approach is unsuitable for use with Herschel–Bulkley fluids, with random and systematic errors in the estimates of n and r_0/R caused by interdependence between the Herschel–Bulkley rheological parameters. For this reason, with 128 sampled q-space data points and SNR = 100, errors in the estimates of n and r_0/R of 50 and 33% were typical.

The numerical simulations performed using the proposed Bayesian MR approaches, utilising Rician and Gaussian likelihood functions, provided estimates of n and r_0/R absent of systematic errors. Random errors in n and r_0/R of 1.2 and 1.3%, respectively, were observed utilising the Rician likelihood function, compared with 0.50 and 0.49% when utilising the Gaussian likelihood function. Therefore, the errors associated with the estimates of n and r_0/R are decreased by an order of magnitude using the proposed Bayesian MR approach utilising the Rician likelihood function, and by two orders of magnitude utilising the Gaussian likelihood function, when compared with those n and r_0/R obtained using the proposed cumulant MR approach. In both cases, the random errors are less than the 5% error typical of conventional rheometry. This suggests that both proposed Bayesian MR approaches are suitable for use with Herschel–Bulkley fluids, with a Gaussian likelihood function selected for future work due to the increase in accuracy and decrease in uncertainty. The sensitivity of the proposed Bayesian MR approach utilising the Gaussian likelihood function to noisy data and reduced sampling is investigated in Chapter 5.

4.5 References

[1] Møller, P.C.F., Mewis, J. and Bonn, D., 2006, Yield stress and thixotropy: on the difficulty of measuring yield stresses in practice. *Soft Matter*, **2**, 274–283.

[2] Barnes, H.A. and Walters, K., 1985, The yield stress myth? *Rheol. Acta*, **24**, 323–326.

[3] Barnes, H.A., 1999, The yield stress—a review or '$\pi\alpha\nu\tau\alpha\ \rho\epsilon\iota$'—everything flows? *J. Non-Newton. Fluid Mech.*, **81**, 133–178.

[4] Herschel, W.H. and Bulkley, R., 1926, Konsistenzmessungen von gummi-benz-ollösungen. *Kolloid-Z.*, **39**, 291–300.

[5] Turian, R.M., Ma, T.W., Hsu, F.L.G. and Sung, D.J., 1997, Characterization, settling, and rheology of concentrated fine particulate mineral slurries. *Powder Technol.*, **93**, 219–233.

[6] Benna, M., Kbir-Ariguib, N., Magnin, A. and Bergaya, F., 1999, Effect of pH on rheological properties of purified sodium bentonite suspensions. *J. Colloid Interf. Sci.*, **218**, 442–455.

[7] Collyer, A.A. and Clegg, D.W., *Rheological Measurement*, Springer, Dordrecht, NL, 1998.

[8] Caton, F. and Baravian, C., 2008, Plastic behavior of some yield stress fluids: from creep to long-time yield. *Rheol. Acta*, **47**, 601–607.

[9] Benmouffok-Benbelkacem, G., Caton, F., Baravian, C. and Skali-Lami, S., 2010, Non-linear viscoelasticity and temporal behavior of typical yield stress fluids: Carbopol, xanthan and ketchup. *Rheol. Acta*, **49**, 305–314.

[10] Barnes, H.A., Hutton, J.F. and Walters, K., *An Introduction to Rheology*, Elsevier, Amsterdam, NL, 1989.

[11] Callaghan, P.T., 2006, Rheo-NMR and velocity imaging. *Curr. Opin. Colloid Interface Sci.*, **11**, 13–18.

[12] Barnes, H.A., 1995, A review of the slip (wall depletion) of polymer solutions, emulsions and particle suspensions in viscometers: its cause, character, and cure. *J. Non-Newton. Fluid Mech.*, **56**, 221–251.

[13] Manneville, S., Bécu, L. and Colin, A., 2004, High-frequency ultrasonic speckle velocimetry in sheared complex fluids. *Eur. Phys. J. Appl. Phys.*, **28**, 361–373.

[14] Shapley, N.C., Brown, R.A. and Armstrong, R.C., 2004, Evaluation of particle migration models based on laser Doppler velocimetry measurements in concentrated suspensions. *J. Rheol.*, **48**, 255–279.

[15] Carr, H.Y. and Purcell, E.M., 1954, Effects of diffusion on free precession in nuclear magnetic resonance experiments. *Phys. Rev.*, **94**, 630–638.

[16] Callaghan, P.T., *Principles of Nuclear Magnetic Resonance Microscopy*, Clarendon Press, Oxford, GB, 1993.

[17] Gladden, L.F. and Sederman, A.J., 2013, Recent advances in flow MRI. *J. Magn. Reson.*, **229**, 2–11.

[18] Arola, D.F., Barrall, G.A., Powell, R.L., McCarthy, K.L. and McCarthy, M.J., 1997, Use of nuclear magnetic resonance imaging as a viscometer for process monitoring. *Chem. Eng. Sci.*, **52**, 2049–2057.

[19] Arola, D.F., Powell, R.L., Barrall, G.A. and McCarthy, M.J., 1998, A simplified method for accuracy estimation of nuclear magnetic resonant imaging. *Rev. Sci. Instrum.*, **69**, 3300–3307.

[20] Arola, D.F., Powell, R.L., Barrall, G.A. and McCarthy, M.J., 1999, Pointwise observations for rheological characterization using nuclear magnetic resonance imaging. *J. Rheol.*, **43**, 9–30.

[21] Sederman, A.J., Mantle, M.D., Buckley, C. and Gladden, L.F., 2004, MRI technique for measurement of velocity vectors, acceleration, and autocorrelation functions in turbulent flow. *J. Magn. Reson.*, **166**, 182–189.

[22] Galvosas, P. and Callaghan, P.T., 2006, Fast magnetic resonance imaging and velocimetry for liquids under high flow rates. *J. Magn. Reson.*, **181**, 119–125.

[23] Tayler, A.B., Holland, D.J., Sederman, A.J. and Gladden, L.F., 2011, Time resolved velocity measurements of unsteady systems using spiral imaging. *J. Magn. Reson.*, **211**, 1–10.

[24] Kärger, J. and Heink, W., 1983, The propagator representation of molecular transport in microporous crystallites. *J. Magn. Reson.*, **51**, 1–7.

[25] Maneval, J.E., Powell, R.L., McCarthy, M.J. and McCarthy, K.L., in *Particulate Two-phase Flow*, Butterworth-Heinemann, Boston, US, 1993, pp. 127–140.

[26] Stejskal, E.O. and Tanner, J.E., 1965, Spin diffusion measurements: spin echoes in the presence of a time-dependent field gradient. *J. Chem. Phys.*, **42**, 288–292.

[27] McCarthy, M.J., Maneval, J.E. and Powell, R.L., in *Advances in Food Engineering*, CRC Press, Boca Raton, US, 1992, pp. 87–97.

[28] Seymour, J.D., Maneval, J.E., McCarthy, K.L., Powell, R.L. and McCarthy, M.J., 1995, Rheological characterization of fluids using NMR velocity spectrum measurements. *J. Texture Stud.*, **26**, 89–101.

[29] Mullineux, G., 2008, Non-linear least squares fitting of coefficients in the Herschel–Bulkley model. *Appl. Math. Model.*, **32**, 2538–2551.

[30] Chevalier, T., Rodts, S., Chevalier, C. and Coussot, P., 2014, Quantitative exploitation of PFG NMR and MRI velocimetry data for the rheological study of yield stress fluid flows at macro- and micro-scales in complex geometries. *Exp. Fluids*, **56**, 1868.

[31] Scheven, U.M., Crawshaw, J.P., Anderson, V.J., Harris, R., Johns, M.L. and Gladden, L.F., 2007, A cumulant analysis for non-Gaussian displacement distributions in Newtonian and non-Newtonian flows through porous media. *Magn. Reson. Imaging*, **25**, 513–516.

[32] Bretthorst, G.L., Hung, C.-C., D'Avignon, D.A. and Ackerman, J.J.H., 1988, Bayesian analysis of time-domain magnetic resonance signals. *J. Magn. Reson.*, **79**, 369–376.

[33] Xing, D., Gibbs, S.J., Derbyshire, J.A., Fordham, E.J., Carpenter, T.A. and Hall, L.D., 1995, Bayesian analysis for quantitative NMR flow and diffusion imaging. *J. Magn. Reson., Ser. B*, **106**, 1–9.

[34] Wise, R.G., Newling, B., Gates, A.R.C., Xing, D., Carpenter, T.A. and Hall, L.D., 1996, Measurement of pulsatile flow using MRI and a Bayesian technique of probability analysis. *Magn. Reson. Imaging*, **14**, 173–185.

[35] Bretthorst, G.L., Hutton, W.C., Garbow, J.R. and Ackerman, J.J.H., 2005, Exponential parameter estimation (in NMR) using Bayesian probability theory. *Concepts Magn. Reson. Part A*, **27A**, 55–63.

[36] Holland, D.J., Blake, A., Tayler, A.B., Sederman, A.J. and Gladden, L.F., 2011, A Bayesian approach to characterising multi-phase flows using magnetic resonance: application to bubble flows. *J. Magn. Reson.*, **209**, 83–87.

[37] Ross, J.G., Holland, D.J., Blake, A., Sederman, A.J. and Gladden, L.F., 2012, Extending the use of Earth's field NMR using Bayesian methodology: application to particle sizing. *J. Magn. Reson.*, **222**, 44–52.

[38] Ziovas, K., Sederman, A.J., Gehin-Delval, C., Gunes, D.Z., Hughes, E. and Mantle, M.D., 2016, Rapid sphere sizing using a Bayesian analysis of reciprocal space imaging data. *J. Colloid Interf. Sci.*, **462**, 110–122.

[39] Cárdenas-Blanco, A., Tejos, C., Irarrazaval, P. and Cameron, I., 2008, Noise in magnitude magnetic resonance images. *Concepts Magn. Reson. Part A*, **32A**, 409–416.

[40] Gudbjartsson, H. and Patz, S., 1995, The Rician distribution of noisy MRI data. *Magn. Reson. Med.*, **34**, 910–914.

Chapter 5

Characterising Herschel–Bulkley fluids using Bayesian analysis

Since many industrial processes are known to be sensitive to the rheology of process fluids, there exists a need for methods that provide online, or inline, rheological characterisation necessary for process control (and optimisation) over time scales of minutes or less. To this end, a new approach to magnetic resonance (MR) rheometry was developed in Chapter 4 utilising pulsed field gradient (PFG) MR and Bayesian analysis to enable estimation of the Herschel–Bulkley rheological parameters, eliminating the requirement of velocity image acquisition and expensive gradient hardware. Note that MR offers a non-invasive technique that is without limitation on optical opacity. These measurements cannot be achieved using a cumulant analysis of the signal in q-space due to interdependence between the rheological parameters.

In this Chapter, the robustness of the proposed Bayesian MR approach utilising a Gaussian likelihood function to noisy data and reduced sampling is investigated using numerical simulations, and it is shown that with a signal-to-noise ratio (SNR) of 100, typical of low-field MR, only 16 data points are required to be sampled in q-space. Experimental validation of the simulations is performed on a model Herschel–Bulkley fluid using PFG MR, with rheological parameters obtained using Bayesian MR and compared with those parameters estimated using MR flow imaging and conventional rheometry methods. It is shown experimentally, with SNR > 1000, that only 8 points are required to be sampled in q-space to achieve this measurement. This corresponds to an acquisition time of $< 60\,\mathrm{s}$ and represents an 88% reduction in acquisition time when compared to MR flow imaging.

5.1 Introduction

The flow curve of many process fluids may be accurately described using

$$\tau\left(\dot{\gamma}\right) = \tau_0 + K\dot{\gamma}^n, \tag{5.1}$$

known as the Herschel–Bulkley model [1], with τ the shear stress, $\dot{\gamma}$ the shear rate, and where τ_0, K, and n represent the yield stress, consistency factor and flow behaviour index of the fluid, respectively. Rheological characterisation involves the estimation of τ_0, K, and n describing the rheology of the fluid under study. Such characterisation is necessary for process control and optimisation, with changes in process fluid rheology due to fluctuations in sample pH and concentration [2] detrimental to many industrial processes, particularly those involving flow [3]. The estimation of the Herschel–Bulkley parameters is typically achieved using conventional rheometry methods [4] operating in an offline configuration, however, there exists a need for online, or inline, rheological characterisation in real-time due to the shear history-dependent nature of the rheology of many process fluids [5–7] and/or the presence of flow phenomena, including (apparent) wall slip [4,8]. Whilst alternative methods have been investigated [9,10], magnetic resonance (MR) enables the non-invasive study of translational motion without limitation on optical opacity.

Over recent years, a number of MR rheometry techniques have developed for this application, including those using MR relaxometry [11,12] and flow imaging [13–15]. Although phase encoding MR techniques are widely considered to be the most robust and quantitative way of measuring flow [16], the accuracy of MR rheometry utilising MR flow imaging is sensitive to the accuracy of the pressure drop and velocity data obtained, therefore demanding adequate spatial and velocity resolution. In some cases, over 100 spatially-resolved velocity data points may be required to achieve an error in τ_0 of less than 2% when compared to conventional rheometry [15]. Also, conventional MR flow imaging techniques limit the temporal resolution of this approach, with fast MR flow imaging techniques [17–19] often unable to provide the spatial and/or temporal resolution required to ensure accurate rheological characterisation in real-time. The use of MR flow imaging in this application is, therefore, challenging. To this end, a pulsed field gradient (PFG) MR approach was developed in Chapter 4 to enable the rheological characterisation of Herschel–Bulkley fluids, in a pipe flow geometry, utilis-

ing Bayesian analysis. This extends MR rheometry to single-axis gradient hardware, thereby eliminating the requirement of spatial encoding. Bayesian analysis is a probabilistic approach that has been applied to a large number of MR applications [20–26]. For example, it has been demonstrated to improve the accuracy of flow measurements by the use of reduced sampling [21], and to enable the recovery of MR spectra [20] and particle size distributions [25] from noisy data. In Bayesian analysis, the state of the system, Θ, is inferred from a set of experimental observations, $\hat{y}$, using the posterior probability density function, $p(\Theta|\hat{y})$, given by

$$p(\Theta|\hat{y}) \propto p(\hat{y}|\Theta)\, p(\Theta)\,, \tag{5.2}$$

where $p(\hat{y}|\Theta)$ is the likelihood function and $p(\Theta)$ incorporates prior knowledge. In this work, rheological characterisation is achieved through Bayesian analysis of the PFG MR signal, $S(q)$, described by

$$S(q) = \int p'(\zeta) \exp\left[\mathrm{i}2\pi q\zeta\right] \mathrm{d}\zeta, \tag{5.3}$$

with $p'(\zeta)$ the experimentally-acquired flow propagator in terms of the displacement, ζ, and $q = (1/2\pi)\,\gamma g\delta$, where γ is the gyromagnetic ratio of the nucleus under study and g and δ represent the magnitude and duration of the flow gradient, respectively [27]. Therefore, $\hat{y}$ and Θ correspond to $S(q)$ and the Herschel–Bulkley rheological parameters, *i.e.* n and r_0, respectively, where r_0 is the radial position corresponding to τ_0. In this application, $p(S(q)|n, r_0)$ describes the variation of $S(q)$ for a particular combination of n and r_0, and $p(\Theta)$ describes what is already known about the probabilities of these parameters. In Chapter 4 it was shown that

$$p(S(q)|n, r_0) = \frac{1}{\sigma\sqrt{2\pi}} \exp\left[-\frac{|S(q) - f(q, n, r_0)|^2}{2\sigma^2}\right] \tag{5.4}$$

for flow that is stable over the experimental duration, *i.e.* laminar flow, and where σ is the standard deviation of the Gaussian noise in the real and imaginary channels of $S(q)$, $f(q, n, r_0)$ is the expected signal in q-space for a particular n and r_0, and $|...|$ is

the magnitude of the data. Furthermore,

$$\frac{f\left(q,n,r_0\right)}{\left|f\left(0\right)\right|}=\int p'\left(\zeta,n,r_0\right)\exp\left[\mathrm{i}2\pi q\zeta-4\pi^2D\left(\Delta-\frac{\delta}{3}\right)q^2\right]\mathrm{d}\zeta, \tag{5.5}$$

where D is the self-diffusion coefficient and Δ is the flow contrast time, and

$$p\left(n,r_0|\hat{y}\right)=\prod_{i=1}^{N}\frac{1}{\sigma\sqrt{2\pi}}\exp\left[-\frac{\left|S\left(q_i\right)-f\left(q,n,r_0\right)\right|^2}{2\sigma^2}\right], \tag{5.6}$$

where N is the number of sampled q-space data points, *i.e.* the number of experimental measurements. Here, σ is obtained from the experimental dataset. The simulation of $p'\left(\zeta,n,r_0\right)$ using Eqs. (4.9), (4.10) and (4.12) requires knowledge of the maximum fluid displacement, $\zeta_{\max}$, which can only be determined if the mean fluid displacement, $\langle\zeta\rangle$, is known. For Bayesian analysis of experimental data, an accurate estimate of $\langle\zeta\rangle$ may be obtained by measuring the evolution of the phase of $S\left(q\right)$ at low values of q, where the measured phase shift is directly proportional to $\langle\zeta\rangle$. A summary of the Bayesian MR approach is illustrated in Fig. 5.1. The interested reader is directed towards Chapter 4 for a more comprehensive description of the Bayesian MR approach.

A three-dimensional (3D) dictionary of f may then be constructed for all required n, r_0/R, and q, with R the pipe radius, and the posterior probability of a particular n and r_0/R obtained from a set of experimental measurements of $S\left(q\right)$ using Eq. (5.6). This process is repeated for all combinations of n and r_0/R to quantify the full two-dimensional (2D) $p\left(\Theta|\hat{y}\right)$, where $\hat{y}=S\left(q\right)$ and $\Theta=\{n,r_0\}$, as summarised in Fig. 5.1. The summation of $p\left(\Theta|\hat{y}\right)$ along the r_0 and n axes may be used to characterise $p\left(n|\hat{y}\right)$ and $p\left(r_0|\hat{y}\right)$, respectively, with estimates of n and r_0 given by the distribution means and the standard deviations a measure of the uncertainty. A measurement of pressure drop per unit length, $\mathrm{d}P/\mathrm{d}L$, can then be used with Eqs. (4.2) and (4.3) to estimate τ_0, with an estimate of K determined using an expression previously derived by Chilton and Stainsby [28] and given by

$$\frac{\mathrm{d}P}{\mathrm{d}L}=\frac{2K}{R}\left(\frac{4\langle\zeta\rangle}{\Delta R}\right)^n\left(\frac{3n+1}{4n}\right)^n\frac{1}{1-\iota}\left(\frac{1}{1-X\iota-Y\iota^2-Z\iota^3}\right)^n, \tag{5.7}$$

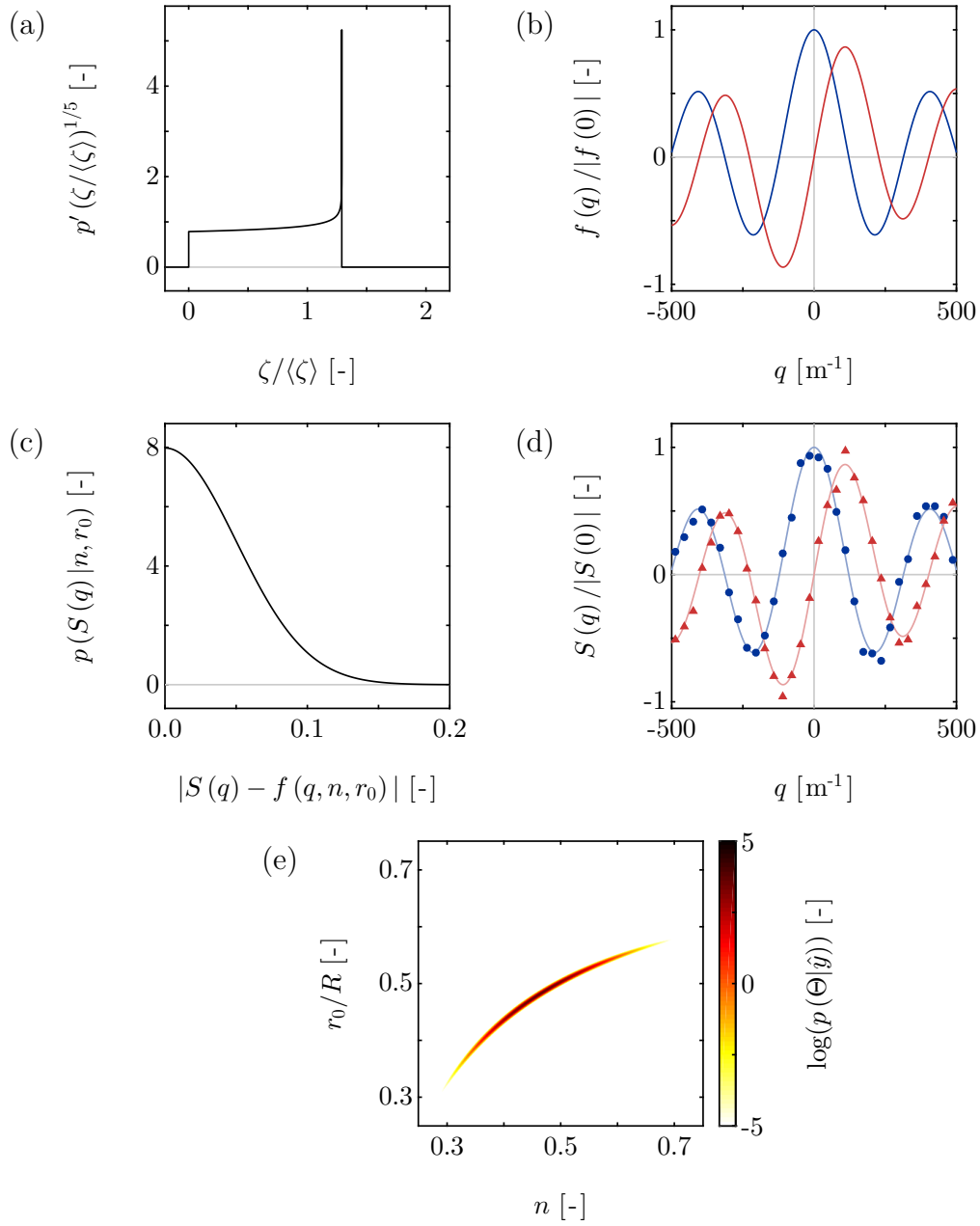

Fig. 5.1: A schematic to show the Bayesian MR approach: (a) $p'(\zeta)$ is simulated for a particular combination of n of r_0/R using Eqs. (4.9), (4.10), and (4.12); (b) Eq. (5.5) is used to calculate the (—) real and (—) imaginary components of $f(q)$; (c) a likelihood function is generated using Eq. (5.4); (d) the (●) real and (▲) imaginary components of $S(q)$ are sampled; (e) the posterior probability for n and r_0/R is given by Eq. (5.6) and repeated for all combinations of n and r_0/R to quantify $p(\Theta|\hat{y})$. Data shown were simulated for $\langle\zeta\rangle = 2\,\text{mm}$ in the absence of self-diffusion and an outflow of spins, with an input n and r_0/R of 0.5, 128 sampled q-space data points, and SNR = 20.

where

$$\iota = \frac{r_0}{R}, \tag{5.8}$$

$$X = \frac{1}{(2n+1)}, \tag{5.9}$$

$$Y = \frac{2n}{(n+1)\,(2n+1)}, \tag{5.10}$$

$$Z = \frac{2n^2}{(n+1)\,(2n+1)}. \tag{5.11}$$

Alternatively, Eqs. (5.7) to (5.11) may be used with a 2D posterior probability distribution and corresponding measurement of $\mathrm{d}P/\mathrm{d}L$ (or distribution thereof) to quantify a full 3D $p\,(\Theta|\hat{y})$, where $\Theta = \{n, \tau_0, K\}$. Complete rheological characterisation is therefore possible, enabling quantification of the flow curve over a range of shear rates in only a single measurement. Furthermore, MR rheometry is extended to single-axis gradient hardware and eliminates the need for Fourier transform, offering advantages over alternative methods for the estimation of the rheological parameters. The robustness of Bayesian analysis to noisy data also implies that this technique may be applied on inexpensive, low-field MR hardware.

In this Chapter, it is shown that an accurate measurement of the flow curve can be achieved in as little as 60 s. The robustness of the Bayesian MR approach to reduced sampling and noisy data is systematically investigated using data generated through numerical simulations to determine the minimum number of data points needed to characterise the rheological parameters with reasonable accuracy, here defined as $\pm 5\%$, this error being typical of conventional rheometry methods [4]. Also considered is the sensitivity of the Bayesian MR approach to changes in n and r_0/R of the fluid under study. The results of the simulations are validated through experimental study of model Herschel–Bulkley fluids, namely Carbopol 940 solutions [29,30], using the Bayesian MR approach described here. Carbopol belongs to a class of materials known as carbomers, which are cross-linked polyacrylic-based polymers [31]. The rheological parameters and flow curves obtained using the Bayesian MR approach are also compared with the same data obtained using MR flow imaging and conventional rheometry methods.

5.2 Materials and methods

5.2.1 Simulations

The sensitivity of the Bayesian MR approach to relevant experimental variables was investigated using numerical simulation experiments. All simulations were performed in MATLAB 2012b, operating under Windows 7. A modified version of Eq. (5.5) was used for the simulation of complex $S(q, n, r_0)$ data, given by

$$\frac{S(q, n, r_0)}{|S(0)|} = \int p'(\zeta, n, r_0) \exp\left[\mathrm{i}2\pi q\zeta - 4\pi^2 D\left(\Delta - \frac{\delta}{3}\right)q^2\right] \mathrm{d}\zeta + e(q), \qquad (5.12)$$

where $e(q)$ represents the addition of pseudo-random Gaussian noise, with zero mean and standard deviation σ, in quadrature. Using Eq. (5.12), simulated $S(q, n, r_0)$ data were generated with the following parameters:

- n was increased linearly between 0.1 and 1.0 in 10 steps.
- r_0/R was incremented linearly in 10 steps between 0.0 and 0.9, with R equal to 7 mm, consistent with that used experimentally.
- q-space was sampled linearly between $\pm|q_{\max}|$, defined by the gradient timings and magnitude but approximately equal to $\pm 4\langle\zeta\rangle^{-1}\,\mathrm{m}^{-1}$, using 2^A points, with A taking integer values between 1 and 10 to sample 2–1024 points.
- Noise was incremented linearly between 0 and 10% in 11 steps, corresponding to SNR in the range 10–∞.

In all cases, SNR is defined as the ratio of the signal intensity at the centre of q-space to the standard deviation of the noise. The mean fluid displacement was 2 mm corresponding to an optimum q-space range of $\pm 2000\,\mathrm{m}^{-1}$, as determined in Section 4.3.1. For Bayesian analysis of the simulated $S(q, n, r_0)$ data, and also that acquired experimentally, a simple uninformative prior (see $p(\Theta)$ in Eq. (5.2)) was used such that the probability of each of the parameter values considered was assumed to be identical. In particular, the range of priors comprised of a set of 501 values evenly spaced between 0 and 1 for both n and r_0/R, corresponding to a resolution of 0.002. Using the method outlined in Section 5.1, $f(q, n, r_0)$ was simulated for all n and r_0/R values and $p(\Theta|\hat{y})$

obtained; the means extracted from $p(\Theta|\hat{y})$ provide an estimate of n and r_0/R, with the standard deviations a measure of the uncertainty. The numerical simulation experiments were repeated 10^2 times, each with pseudo-random Gaussian noise. Rheological parameters reported in Section 5.3 correspond to the mean of the 100 means, with the standard deviation of the 100 means a measure of the uncertainty.

5.2.2 Experimental

Materials and experimental set-up

Aqueous solutions of Carbopol 940 (B.F. Goodrich, US) were prepared at concentrations of 0.1 and 0.2 wt% using deionised water (ELGA Purelab Option). The complete dissolution of Carbopol 940 was achieved by stirring for 18 h using an overhead stirrer (Ika–Werke RW20); care was taken to prevent the entrapment of air during the stirring process. The pH was measured (Corning 240 pH meter) and adjusted to 4.5 and 5.0 for 0.1 and 0.2 wt% Carbopol 940-in-water solutions, respectively, using sodium hydroxide (Fisher Scientific, GB); these combinations of concentration and pH having previously demonstrated Herschel–Bulkley rheology [29]. Whilst Carbopol 940-in-water solutions are generally considered to exhibit little or no thixotropy [30], shear history-dependent behaviour at concentrations of ≥ 0.2 wt% has been observed [6,7].

The flow system comprised an acrylic pipe of inner diameter (i.d.) 14 mm and length 2.0 m, with a total loop volume of 1.5 L, operating in a closed loop configuration. A peristaltic pump (MasterFlex Console Drive) capable of delivering flow rates of up to 50 mL s^{-1} was selected, and steady flow was ensured through coupling of the pump with a flow pulsation dampener. Flow rates, $\dot{V}$, were determined gravimetrically. The radiofrequency (r.f.) coil was situated 1.5 m downstream of the pipe inlet, exceeding an inlet length of 100 times pipe i.d. which is recommended to ensure developed flow [32]. Pressure drop was measured across a length of 1.6 m using a differential pressure gauge (Digitron 2002P). For the 0.1 wt% Carbopol 940-in-water solution, a pressure drop of 827 ± 41 Pa m^{-1} was measured with $\dot{V} = 16.3\pm0.8$ mL s^{-1}. Note that the uncertainties represent the standard deviation of five repeated measurements. A pressure drop of 3190 ± 190 Pa m^{-1} was measured for the 0.2 wt% Carbopol 940-in-water solution, with $\dot{V} = 3.00\pm0.07$ mL s^{-1}. These operating parameters correspond to shear rate ranges of over two orders of magnitude; 0.1–63 and 0.1–22 s^{-1} for the 0.1 and 0.2 wt% Carbopol 940-in-water solutions, respectively, as determined from MR flow imaging.

Magnetic resonance

All MR experiments were performed on a Bruker AV85 spectrometer operating with a 2 T horizontal-bore superconducting magnet. The magnet was fitted with a 60 mm birdcage r.f. coil tuned to a frequency of 85.2 MHz for the ^{1}H resonance. A three-axis gradient system with a maximum gradient strength of 10.7 G cm^{-1} was used for spatial and flow encoding.

A 13-interval alternating pulsed field gradient stimulated echo (APGSTE) pulse sequence [33] was used to sample q-space data in the range of $\pm 4\langle\zeta\rangle^{-1}$ m^{-1} for Bayesian analysis. Flow gradients were applied with a duration (δ) of 2 ms and flow contrast time (Δ) equal to 40 ms. The maximum gradient strength was varied between ± 1.3 and ± 9.0 G cm^{-1} for the 0.1 and 0.2 wt% Carbopol 940-in-water solutions, respectively, to sample q-space ranges of up to ± 1080 and ± 7660 m^{-1}. In both cases, q-space was sampled linearly in 128 steps (N). A total of 4 signal averages were acquired with a recycle time of 1.7 s, equal to 5 times T_1 (340 ms), giving a total data acquisition time of 15 min. This is equivalent to 7 s per data point acquired. Flow rates quantified through measurement of the evolution of the phase at low values of q, as described in Section 5.1, were 15.8 ± 0.5 and 3.16 ± 0.09 mL s^{-1} for the 0.1 and 0.2 wt% Carbopol 940-in-water solutions, respectively, in agreement with gravimetric measurements to within the experimental uncertainty. Flow propagators were also acquired to demonstrate changes in the flow distribution at the two concentrations of Carbopol 940-in-water solution investigated using the same APGSTE pulse sequence that was used for the Bayesian MR approach but with a different range of q-space data points. Flow gradient timings and magnitudes were concentration specific. For the 0.1 wt% Carbopol 940-in-water solution, $\delta = 3$ ms and $\Delta = 60$ ms with a maximum gradient strength of ± 2.3 G cm^{-1} to provide a field-of-flow of $4\langle\zeta\rangle$ mm and sample a q-space range of up to ± 2870 m^{-1}. For the 0.2 wt% Carbopol 940-in-water solution, flow gradients were applied with $\delta = 2$ ms and a maximum gradient strength of ± 9.5 G cm^{-1}, with $\Delta = 100$ ms. This corresponds to a q-space range of up to ± 8090 m^{-1}. In all cases, $N = 128$ steps. A total of 4 signal averages were acquired with a recycle time of 1.7 s, giving a total data acquisition time of approximately 15 min.

In addition, spatially-resolved 2D MR flow images were acquired for each Carbopol 940-in-water solution investigated using a slice selective, spin echo MR flow imaging sequence with a slice thickness of 10 mm. A field-of-view of 18 mm was selected in both the read and phase directions, with 128 phase increments and 128 read points, to give

a resolution of 141 µm × 141 µm. Data were acquired such that the SNR within each liquid-filled voxel was 100. Flow gradients were applied with $\delta = 2\,\text{ms}$ and $\Delta = 10\,\text{ms}$ and $\delta = 2\,\text{ms}$ and $\Delta = 40\,\text{ms}$ for the 0.1 and 0.2 wt% Carbopol 940-in-water solutions, respectively. Two increments in g were utilised with the gradient strength calibrated for each concentration to ensure a maximum phase shift of 2π. Images were acquired in 8 min with a recycle time of 450 ms and 4 signal averages. The non-linear least squares (NLLS) regression of

$$\zeta\left(r, n, r_0\right) = \begin{cases} \zeta_{\max}, & 0 \leq r < r_0, \\ \zeta_{\max}\left(1 - \left(\dfrac{r - r_0}{R - r_0}\right)^{\frac{n+1}{n}}\right), & r_0 \leq r \leq R, \end{cases} \tag{5.13}$$

to the 2D velocity (or displacement) image was used to estimate rheological parameters n and r_0, with the 95% confidence interval in the individual fit a measure of uncertainty and the corresponding pressure drop data providing τ_0 and K. All MR experiments were performed at 19.0±0.5 °C. Flow rates calculated from the MR flow images were 15.8±0.8 and 2.92±0.15 $\text{mL}\,\text{s}^{-1}$ for the 0.1 and 0.2 wt% Carbopol 940-in-water solutions, respectively, in agreement with those flow rates obtained from the gravimetric measurements and low q-space analysis to within the experimental uncertainty.

Conventional rheometry

Benchtop measurements of the rheology of the Carbopol 940-in-water solutions investigated were performed using a Bohlin Instruments CVO-120 HR rheometer equipped with a Peltier plate to control the temperature to 19.0±1.0 °C. The rheometer was operated in controlled-stress mode. In this mode of operation, the yield stress is obtained without the need for extrapolation, as is required when operating in controlled-rate mode [34]. A smooth-walled, 40 mm diameter parallel plate geometry was used with a plate separation of 0.75 mm; apparent shear rate was measured across a shear stress sweep of 0.01–100 Pa in 4 min. A correction is required to be applied to the apparent (measured) flow curve to obtain the true flow curve [34], as given by

$$\tau_{\text{a}}\left(\dot{\gamma}_{\text{a}}\right) = \frac{4}{3}\tau_0 + \left(\frac{4}{3+n}\right) K \dot{\gamma}_{\text{a}}^{n} \tag{5.14}$$

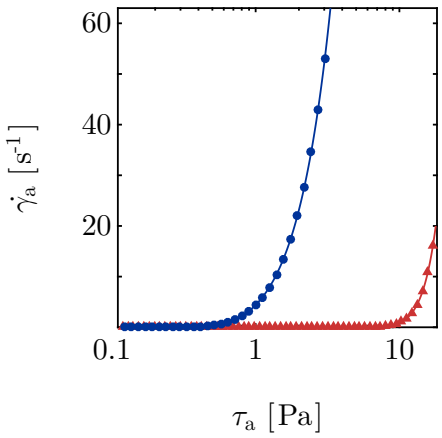

Fig. 5.2: Apparent shear rate-shear stress data for the (●) 0.1 and (▲) 0.2 wt% Carbopol 940-in-water solutions obtained using conventional rheometry. The symbols show the experimentally-acquired data and the solid lines show the regression data obtained by NLLS regression of Eq. (5.14) over the shear rate ranges of the MR experiments.

for the case of a parallel plate geometry, where τ_a and $\dot{\gamma}_a$ are the apparent shear stress and shear rate, respectively. The NLLS regression of Eq. (5.14) to the apparent flow curves, across the same shear rate ranges as the MR experiments, was used to provide estimates of the rheological parameters. This regression is depicted in Fig. 5.2 for the 0.1 and 0.2 wt% Carbopol 940-in-water solutions, with the regression data accurate to within the scatter of the experimental data, confirming Herschel–Bulkley rheology. The rheological parameters obtained across the range of shear rates investigated are summarised in Table 5.1, where the uncertainty represents the 95% confidence interval in the individual fit. It is seen that an increase in concentration of Carbopol 940 from 0.1 to 0.2 wt% is responsible for a reduction in n from 0.60±0.02 to 0.28±0.01. There is also an increase in both τ_0 and K, from 0.31±0.01 to 3.3±0.1 Pa and 0.22±0.01 and 4.8±0.1 Pa s^n, respectively, with these trends in agreement with those observed in the literature [29]. There was no evidence of wall slip in the data obtained.

5.3 Results and discussion

5.3.1 Sensitivity to the Herschel–Bulkley parameters

The results of the numerical simulations described in Section 5.2.1 are now presented and discussed. A 2D posterior probability distribution, $p(\Theta|\hat{y})$, generated using simu-

lated data with 128 sampled q-space data points and SNR = 100 is shown in Fig. 5.3. An SNR of 100 is typical of low-field MR. From $p(\Theta|\hat{y})$, estimates of $n = 0.51 \pm 0.02$ and $r_0/R = 0.50 \pm 0.02$ were obtained, where the uncertainties represent the standard deviation of n and r_0/R, accurate to within 2% of the ground truth of $n = 0.50$ and $r_0/R = 0.50$. With reference to Fig. 5.1(e), an increase in the noise level is observed to cause a broadening of the posterior distribution and a decrease in maximum probability. The sensitivity to noise is investigated in Section 5.3.2.

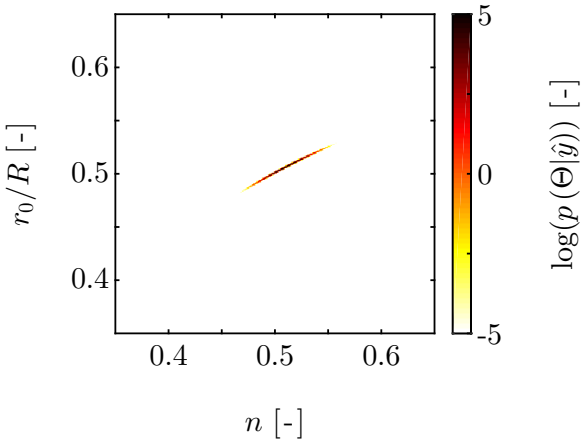

Fig. 5.3: A 2D posterior probability distribution, plotted on a log scale, showing the probability of n and r_0/R given the experimental observations $\hat{y}$ obtained using simulated data. Data were generated with 128 sampled q-space data points and SNR = 100 for a ground truth of $n = 0.5$ and $r_0/R = 0.5$.

Considering only the data corresponding to 16 sampled q-space data points with SNR = 100, the sensitivity of the accuracy of the Bayesian MR approach for estimation of the Herschel–Bulkley rheological parameters can be investigated. Figure 5.4(a) shows the estimate of n, given by the mean of the 100 repeat simulation experiments, compared with the ground truth for three values of r_0/R. The accuracy of the estimate of n increases with an increase in r_0/R, however, the mean error in n remains $< 2\%$ with a mean uncertainty (defined as the standard deviation of the 100 repeat simulation experiments) of 7%. Corresponding data for r_0/R at the three values of n reported in Fig. 5.4(b) indicate that the accuracy of the estimate of r_0/R is independent of the ground truth. Across the range of rheological parameters investigated, the mean error in r_0/R was $< 2\%$ and the mean uncertainty was $< 7\%$. These results imply that the accuracy of the Bayesian MR approach is largely insensitive to changes in the rheology of the fluid under study, and therefore ideally suited to Herschel–Bulkley, power-law,

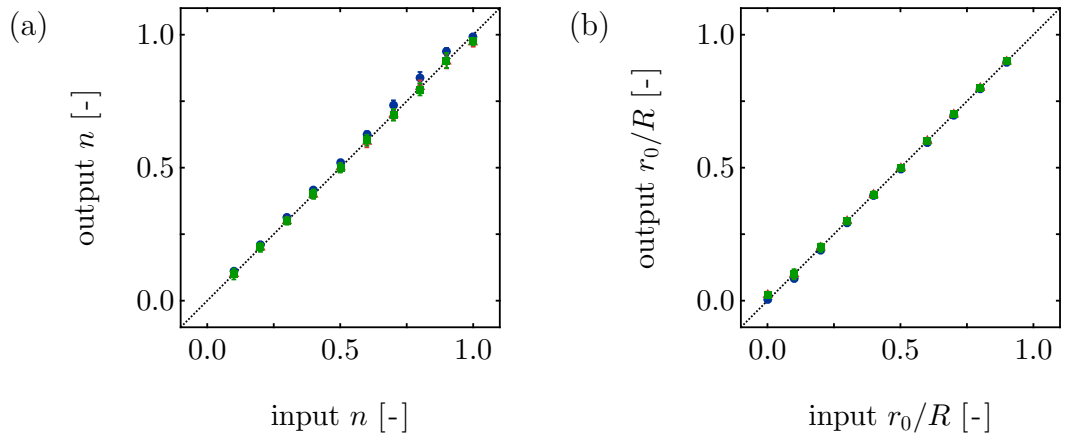

Fig. 5.4: (a) A comparison between the input n, *i.e.* the ground truth, and output n, *i.e.* the estimate, using the Bayesian MR approach with 16 sampled q-space data points and SNR = 100, plotted for r_0/R equals (●) 0.0, (▲) 0.2, and (■) 0.5. (b) Corresponding data plotted for the estimate of r_0/R with n equal to (●) 1.0, (▲) 0.8, and (■) 0.5. Error bars represent the standard deviation of the 100 repeat simulation experiments, *i.e.* the uncertainty. The diagonal line (·····) represents the expected result.

and Newtonian fluids. Further, only 16 points are required to be sampled in q-space with SNR = 100 if an accuracy of within 2% of the ground truth is acceptable for n and r_0/R, with an uncertainty of 7%.

5.3.2 Sensitivity to noisy data and reduced sampling

As a technique, Bayesian analysis has previously demonstrated an excellent robustness to noisy data [20,25] and reduced sampling [21]. Here, this robustness was investigated for noise levels of up to 10%, corresponding to SNR of ≥ 10, with as few as 2 sampled q-space data points. Figure 5.5 shows the relationship between the estimate of n and the ground truth using simulated data with $r_0/R = 0.5$ and (a) 16 q-space data points and SNR of ∞, 100, and 50, and (b) fixed SNR = 100 with 4, 16, and 64 sampled q-space data points. The estimate of n is given by the mean of the 100 repeat simulation experiments. It is shown in Fig. 5.5(a) that the accuracy of the estimation of n utilising 16 sampled q-space data points is insensitive to a reduction in SNR from ∞ to 50, with all results accurate to within $< 2\%$ of the ground truth and absent of systematic error. As expected, the mean uncertainty associated with the estimation of n increases with a reduction in SNR, from 0% at an SNR = ∞ up to 9% at an SNR = 50. Despite the reduction in SNR, the accuracy of the estimation of n remains comparable to that

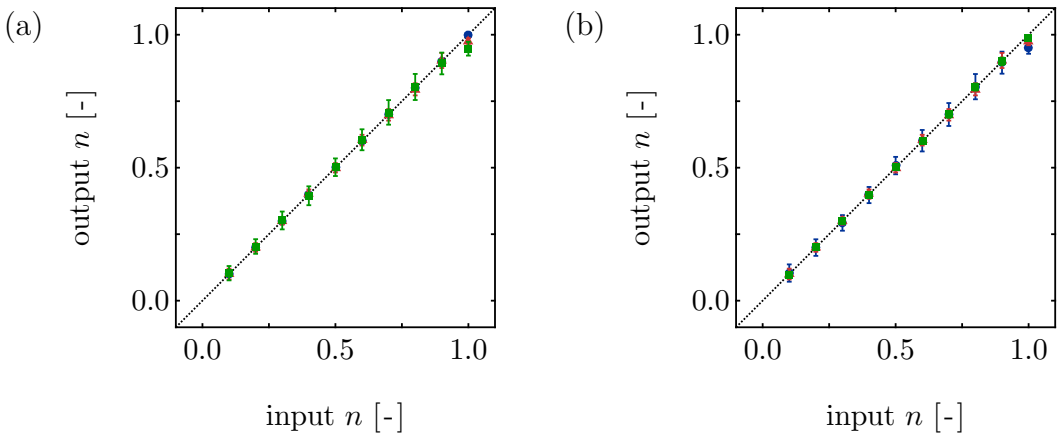

Fig. 5.5: (a) A comparison between the input n, *i.e.* the ground truth, and output n, *i.e.* the estimate, using the Bayesian MR approach with $r_0/R = 0.5$ and 16 sampled q-space data points, plotted for SNR equal to (●) ∞, (▲) 100, and (■) 50. (b) The same data plotted for SNR = 100 and (●) 4, (▲) 16, and (■) 64 sampled q-space data points. Error bars represent the standard deviation of the 100 repeat simulation experiments, *i.e.* the uncertainty. The diagonal line (·····) represents the expected result.

of conventional rheometry techniques [4], suggesting that the Bayesian MR approach is robust to noisy data. Considering the number of sampled q-space data points, for a fixed SNR = 100, it is observed in Fig. 5.5(b) that the accuracy of the estimation of n is increased as the number of data points is increased. For example, an increase from 4 to 64 q-space data points, representing a sixteen-fold increase in the experimental acquisition time, is responsible for a reduction in the mean error from 2 to $< 1\%$ and mean uncertainty from 10 to $< 3\%$. Similar trends were observed for the estimation of r_0/R. The Bayesian MR approach has, therefore, demonstrated an excellent robustness to noisy data and reduced sampling. For SNR = 100, only 16 q-space data points are required to be sampled for accurate estimation of the rheological parameters. For cases where SNR > 100, this requirement can be reduced further.

5.3.3 Experimental validation using MR

Bayesian MR methods

For validation of the results of the numerical simulations, Bayesian MR experiments were performed on Carbopol 940-in-water solutions demonstrating Herschel–Bulkley rheology. Figure 5.6 shows the (a) real and (b) imaginary components of the q-space

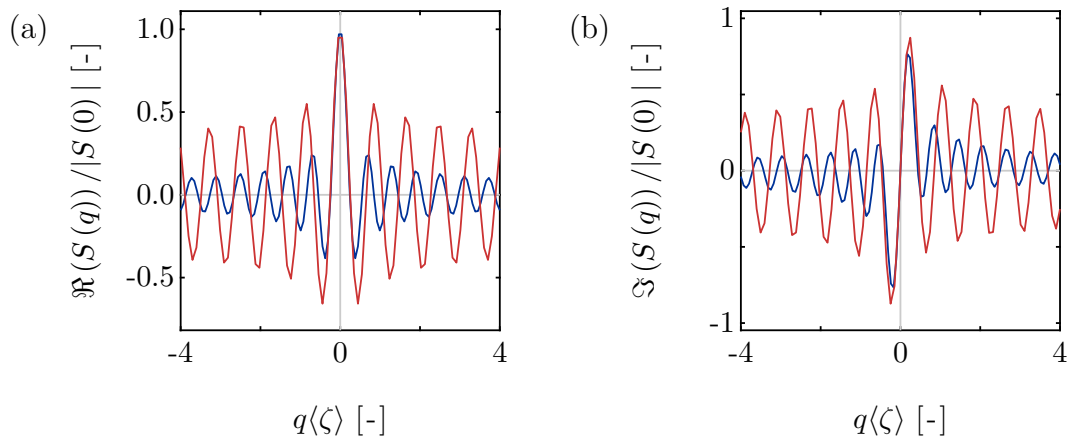

Fig. 5.6: The evolution of the normalised (a) real and (b) imaginary components of the experimentally-acquired $S\left(q\right)$, plotted across a q-space range of $\pm 4\langle\zeta\rangle^{-1}\,\mathrm{m}^{-1}$ for the (—) 0.1 and (—) 0.2 wt% Carbopol 940-in-water solutions; SNR > 1000.

signal sampled at 128 points for the 0.1 and 0.2 wt% Carbopol 940-in-water solutions. An increase in Carbopol 940 concentration from 0.1 to 0.2 wt% is observed to cause an increase in the magnitude of the signal at the limits of q-space sampled and a decrease in the frequency of the oscillations in q-space. For completeness, it is noted that these changes are consistent with the flow propagators shown in Fig. 5.7, in which it is seen that an increase in concentration of Carbopol 940 causes a reduction in ζ_{max} and an increase in the maximum probability (due to an increase in r_0/R). All flow propagators demonstrate a broadening due to self-diffusion and an absence of wall slip.

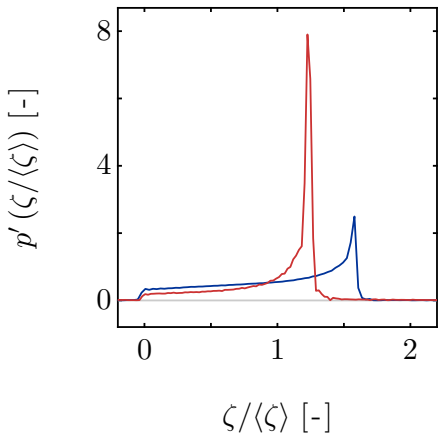

Fig. 5.7: The experimentally-acquired $p'\left(\zeta\right)$ for the (—) 0.1 and (—) 0.2 wt% Carbopol 940-in-water solutions.

Using methods outlined in Section 5.1, $p(\Theta|\hat{y})$ was determined for each Carbopol 940-in-water solution investigated, with the means and standard deviations of $p(\Theta|\hat{y})$ providing estimates of n and τ_0 (since $\mathrm{d}P/\mathrm{d}L$ was measured). Equations (5.7) to (5.11) were then used to estimate K and recover the flow curve. Generated $p(\Theta|\hat{y})$ are shown in Fig. 5.8 for the (a) 0.1 and (b) 0.2 wt% Carbopol 940-in-water solutions. For the 0.1 wt% Carbopol 940-in-water solution, $p(\Theta|\hat{y})$ provided n and τ_0 of 0.54±0.01 and 0.32±0.02 Pa, respectively, with the uncertainties reported equal to the standard deviation of the distributions, and K was estimated to equal 0.24±0.01 Pa s^n. Rheological parameters estimated for the 0.2 wt% Carbopol 940-in-water solution were 0.30±0.01, 4.6±0.1 Pa, and 2.4±0.1 Pa s^n for n, τ_0, and K, respectively.

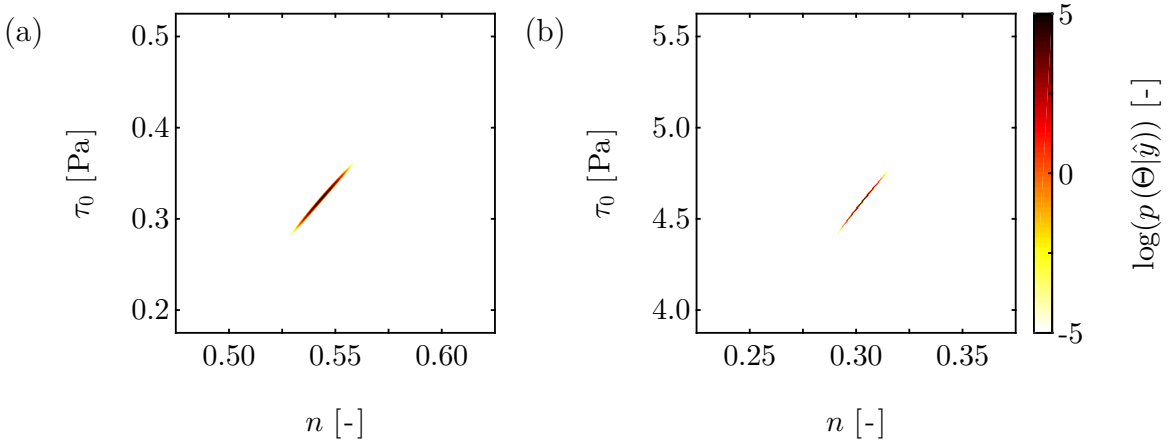

Fig. 5.8: 2D posterior probability distributions, plotted on a log scale, showing the probability of n and τ_0 given $\hat{y}$ for the (a) 0.1 and (b) 0.2 wt% Carbopol 940-in-water solutions. The SNR (at $q = 0\,\mathrm{m}^{-1}$) is > 1000, with the 128 points in q-space sampled using the experimental procedure outlined in Section 5.2.2.

The robustness of the Bayesian MR approach to reduced sampling was investigated by the successive elimination of q-space data points, between the maximum ranges of q-space sampled, with estimates of n and τ_0 determined. Figure 5.9 shows estimates of (a) n and (b) τ_0 for the 0.1 and 0.2 wt% Carbopol 940-in-water solutions as the number of sampled q-space data points is decreased. It is shown that the estimates of n and τ_0 are insensitive to the number of sampled q-space data points up to reduced sampling in excess of 80% (corresponding to a reduction from 128 to 20 sampled q-space data points). Whilst the error increases at a higher level of reduced sampling, Fig. 5.9 shows that an accurate estimate of n (with an error of $< 5\%$) can still be obtained when only 2 q-space data points are sampled, with up to 8 q-space data points required for the

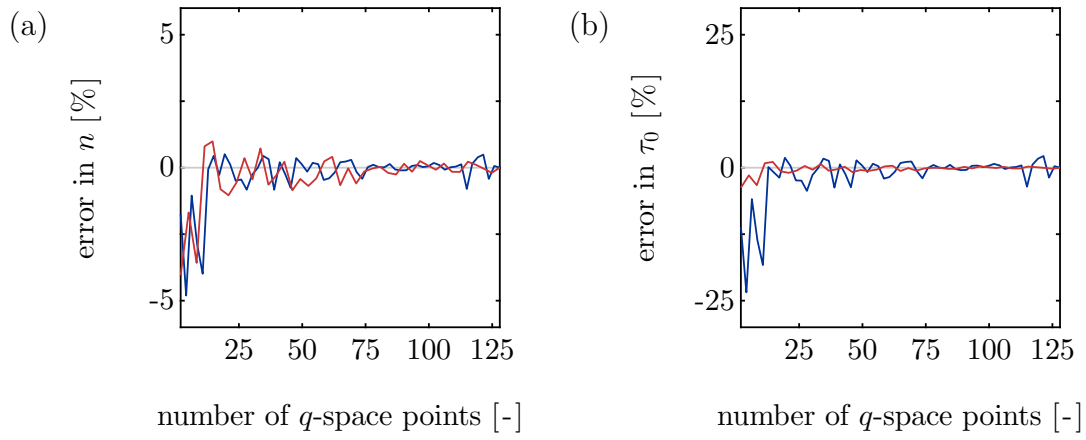

Fig. 5.9: Plots to demonstrate the relationship between the number of points sampled in q-space and the error associated with the estimate of (a) n and (b) τ_0, obtained for the (—) 0.1 and (—) 0.2 wt% Carbopol 940-in-water solutions, when compared with parameters obtained using 128 sampled q-space data points.

accurate estimation of τ_0. The acquisition of 8 q-space data points would correspond to a total data acquisition time of < 60 s, for four signal averages and a recycle time of 1.7 s, and represent a reduction in acquisition time of 88% when compared with the acquisition time of an MR flow image. Although a simple linear sampling scheme has been applied, it may be possible to further reduce the number of required q-space data points by choosing a non-linear sampling scheme.

Comparison with non-Bayesian MR methods

The rheological parameters estimated using the Bayesian MR, MR flow imaging, and conventional rheometry methods are summarised in Table 5.1. Before comparing these data, the results of the MR flow imaging method are presented.

Two-dimensional (2D) MR flow images were acquired for each concentration of Carbopol 940-in-water solution investigated with a spatial resolution of 141 µm × 141 µm, sufficient to provide ∼100 spatially-resolved velocity data points across the geometry under study. Figure 5.10 shows MR flow images for the (a) 0.1 and (b) 0.2 wt% Carbopol 940-in-water solutions, where the displacement represents axial displacement, *i.e.* z-displacement. The SNR in the corresponding intensity images is 100. It is seen that an increase in Carbopol 940 concentration from 0.1 to 0.2 wt% is responsible for a decrease in the maximum scaled displacement and an increase in r_0/R. As expected, the MR flow images do not demonstrate any of the features attributed to turbulent

flow, with both images showing radial symmetry typical of laminar flow. A 2D NLLS regression of $\Delta^{-1}\zeta(r)$ was performed to the MR flow image for each concentration of Carbopol 940-in-water solution investigated to quantify n and r_0/R, with $\zeta(r)$ given by Eq. (5.13). Figure 5.11 depicts the radially-averaged MR flow images, or displacement profiles, and regression data, with the displacement profiles and regression data in agreement to within experimental error. Note that estimates of τ_0 and K can then be extracted using Eqs. (4.2) and (4.3) and Eqs. (5.7) to (5.11), respectively. For the 0.1 wt% Carbopol 940-in-water solution, this approach provided estimates of n and τ_0 of 0.55±0.01 and 0.34±0.04 Pa, respectively, where the uncertainty is equal to the 95% confidence interval in the individual fit, with $K = 0.25 \pm 0.01\,\mathrm{Pa\,s}^n$. Rheological parameters obtained for the 0.2 wt% Carbopol 940-in-water solution using this approach were 0.22±0.01, 3.4±0.5 Pa, and 4.0±0.1 $\mathrm{Pa\,s}^n$ for n, τ_0, and K, respectively.

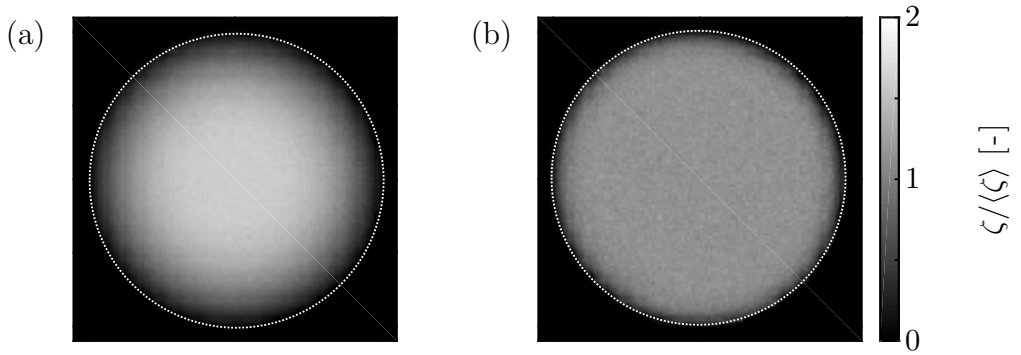

Fig. 5.10: MR flow images acquired for the (a) 0.1 and (b) 0.2 wt% Carbopol 940-in-water solutions. The MR flow images have a spatial resolution of 141 µm × 141 µm, for a field-of-view of 18 mm × 18 mm, and were acquired in 8 min. The SNR in the corresponding intensity images is 100.

Considering Table 5.1, results from the Bayesian MR and MR flow imaging methods can be compared with those from conventional rheometry. Figure 5.12 shows the corresponding flow curves for (a) 0.1 and (b) 0.2 wt% Carbopol 940-in-water solutions, calculated using Eq. (5.1) with the parameters reported in Table 5.1. From Table 5.1, it is clearly seen that the values of n, τ_0, and K determined for 0.1 wt% Carbopol 940-in-water solution using the three different methods are consistent, with the numerical values of the parameters obtained using the two MR rheometry methods consistent to within the experimental errors. Furthermore, as shown in Fig. 5.12(a), the flow curves obtained from the three methods are almost identical. The flow curves in Fig. 5.12 are plotted across the shear rate ranges of the MR experiments.

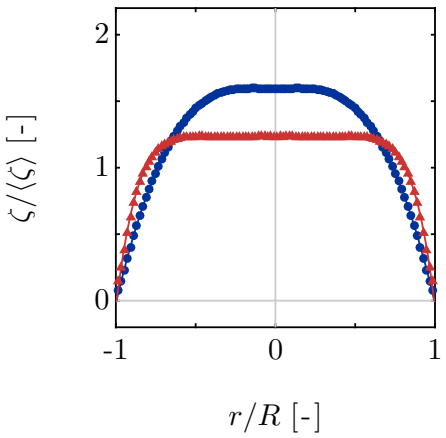

Fig. 5.11: Displacement profiles for the (●) 0.1 and (▲) 0.2 wt% Carbopol 940-in-water solutions showing the radially-averaged MR flow images. The solid lines correspond to the radially-averaged 2D regression data obtained by performing a 2D NLLS regression of $\Delta^{-1}\zeta(r)$ to the MR flow images, with $\zeta(r)$ given by Eq. (5.13). The error in the fit is within the accuracy of the experimental data.

In contrast, with reference to Table 5.1, the rheological parameters determined for the 0.2 wt% Carbopol 940-in-water solution using the three different methods show less good agreement. However, despite differences in the numerical values of the parameters determined using the two MR rheometry methods, their respective flow curves are almost indistinguishable from one another. This highlights a weakness of the Herschel–Bulkley constitutive equation, namely an inability to unambiguously establish the rhe-

Table 5.1: A comparison of the rheological parameters of the 0.1 and 0.2 wt% Carbopol 940-in-water solutions obtained using Bayesian MR, MR flow imaging, and conventional rheometry methods, evaluated across shear rate ranges of 0.1–63 and 0.1–22 s^{-1}, respectively.

concentration [wt%]	method	rheological parameters		
		n [-]	τ_0 [Pa]	K [Pa s^n]
0.1	Bayesian MR	0.54±0.01	0.32±0.02	0.24±0.01
	MR flow imaging	0.55±0.01	0.34±0.04	0.25±0.01
	conventional rheometry	0.60±0.02	0.31±0.01	0.22±0.01
0.2	Bayesian MR	0.30±0.01	4.6±0.1	2.4±0.1
	MR flow imaging	0.22±0.01	3.4±0.5	4.0±0.1
	conventional rheometry	0.28±0.01	3.3±0.1	4.8±0.1

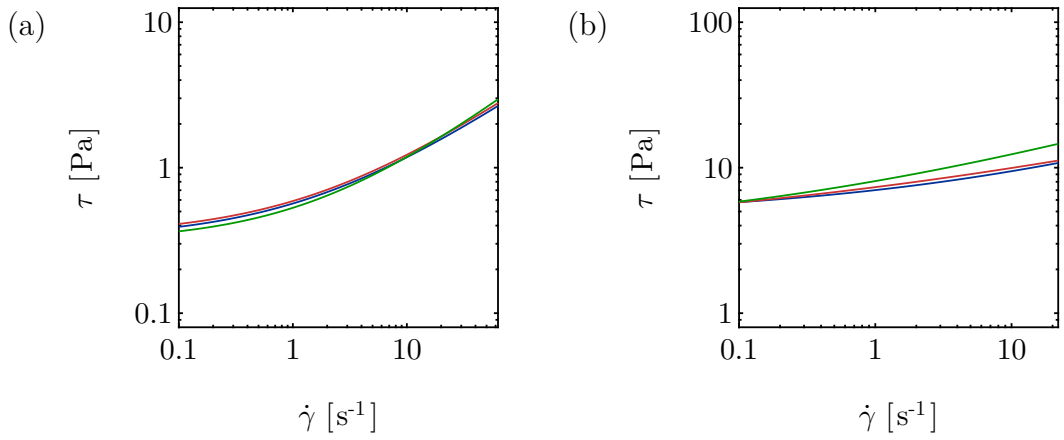

Fig. 5.12: Shear stress-shear rate data for the (a) 0.1 and (b) 0.2 wt% Carbopol 940-in-water solutions obtained using (—) Bayesian MR, (—) MR flow imaging, and (—) conventional rheometry, plotted across the shear rate ranges of the MR experiments (0.1–63 and 0.1–22 s^{-1}, respectively, as determined from MR flow imaging).

ological parameters, since different sets of rheological parameters can provide equivalent fits to the experimental data [35]. This ambiguity arises due to the known interdependence between the Herschel–Bulkley rheological parameters, as demonstrated by Fig. 5.1(e). With reference to Fig. 5.12(b), it is observed that the flow curve determined using conventional rheometry is significantly different from those determined using MR rheometry. This is most likely explained by the shear history-dependent behaviour of the 0.2 wt% Carbopol 940-in-water solution, with differences of up to 40% in τ_0 of ≥ 0.2 wt% Carbopol 940-in-water solutions previously reported [6,7], and the different flow geometries used. Since, in an industrial process, the history-dependent behaviour of a process fluid is important, the capacity of the Bayesian MR approach to provide accurate measurements of rheological parameters online, or inline, and in acquisition times of < 60 s is of great value. It is interesting to note that, although not shown in Fig. 5.12, the uncertainty in the flow curves is small despite the magnitude of the uncertainties in the individual rheological parameters.

5.4 Conclusions

In this Chapter, an MR rheometry approach utilising Bayesian analysis has been used for the rheological characterisation of fluids demonstrating Herschel–Bulkley rheology in a pipe flow geometry using PFG MR, requiring single-axis gradient hardware. The

approach analyses acquisition data directly, removing the need for Fourier transform, negating strict sampling requirements and hence permitting significant reductions in acquisition times.

The Bayesian MR approach was used to obtain a posterior probability distribution, through comparison with the experimentally-acquired PFG MR signal, enabling parameter estimation for n, with the pressure drop being used to estimate τ_0 and K. Numerical simulation experiments performed indicated the Bayesian MR approach to be robust to noisy data and reduced sampling, with only 16 data points required to be sampled in q-space at SNR = 100. These simulation studies were validated using experimentally-acquired Bayesian MR datasets for 0.1 and 0.2 wt% Carbopol 940-in-water solutions. It was found that the Bayesian MR approach provided estimates of the rheological parameters describing the Herschel–Bulkley fluids in < 60 s. The estimates of the rheological parameters determined using the Bayesian MR approach were then compared with the same values determined using MR flow imaging and conventional rheometry. Whilst the rheological parameters, and hence flow curves, provided by all three methods for the 0.1 wt% Carbopol 940-in-water solution were consistent, those for 0.2 wt% were inconsistent. Both MR rheometry methods gave similar flow curves, however, the flow curve measured using conventional rheometry differed significantly; this is most likely due to the shear history-dependent nature of the rheology of the 0.2 wt% Carbopol 940-in-water solution and the different flow geometries used. The results presented are significant and imply that the Bayesian MR approach not only offers the convenience of fast parameter estimation, but that this may offer new opportunities for the study and characterisation of history-dependent behaviour. It is also noted that the Bayesian MR approach is robust to relatively low SNR, and therefore offers opportunities for transfer to low-field (and intermediate-field) MR hardware [36] for online, or inline, process monitoring.

Whilst this measurement has been demonstrated in application to Herschel–Bulkley fluids, it is readily applied to power-law fluids without further modification and could easily be adapted for other rheological models.

5.5 References

[1] Herschel, W.H. and Bulkley, R., 1926, Konsistenzmessungen von gummi-benz-ollösungen. *Kolloid-Z.*, **39**, 291–300.

[2] Benna, M., Kbir-Ariguib, N., Magnin, A. and Bergaya, F., 1999, Effect of pH on rheological properties of purified sodium bentonite suspensions. *J. Colloid Interf. Sci.*, **218**, 442–455.

[3] Collyer, A.A. and Clegg, D.W., *Rheological Measurement*, Springer, Dordrecht, NL, 1998.

[4] Barnes, H.A., Hutton, J.F. and Walters, K., *An Introduction to Rheology*, Elsevier, Amsterdam, NL, 1989.

[5] Møller, P.C.F., Mewis, J. and Bonn, D., 2006, Yield stress and thixotropy: on the difficulty of measuring yield stresses in practice. *Soft Matter*, **2**, 274–283.

[6] Caton, F. and Baravian, C., 2008, Plastic behavior of some yield stress fluids: from creep to long-time yield. *Rheol. Acta*, **47**, 601–607.

[7] Benmouffok-Benbelkacem, G., Caton, F., Baravian, C. and Skali-Lami, S., 2010, Non-linear viscoelasticity and temporal behavior of typical yield stress fluids: Carbopol, xanthan and ketchup. *Rheol. Acta*, **49**, 305–314.

[8] Barnes, H.A., 1995, A review of the slip (wall depletion) of polymer solutions, emulsions and particle suspensions in viscometers: its cause, character, and cure. *J. Non-Newton. Fluid Mech.*, **56**, 221–251.

[9] Manneville, S., Bécu, L. and Colin, A., 2004, High-frequency ultrasonic speckle velocimetry in sheared complex fluids. *Eur. Phys. J. Appl. Phys.*, **28**, 361–373.

[10] Shapley, N.C., Brown, R.A. and Armstrong, R.C., 2004, Evaluation of particle migration models based on laser Doppler velocimetry measurements in concentrated suspensions. *J. Rheol.*, **48**, 255–279.

[11] Osán, T.M., Ollé, J.M., Carpinella, M., Cerioni, L.M.C., Pusiol, D.J., Appel, M., Freeman, J. and Espejo, I., 2011, Fast measurements of average flow velocity by low-field ^{1}H NMR. *J. Magn. Reson.*, **209**, 116–122.

[12] Herold, H., Hardy, E.H., Ranft, M., Wassmer, K.H. and Nestle, N., 2013, Online rheo-TD NMR for analysing batch polymerisation processes. *Microporous Mesoporous Mater.*, **178**, 74–78.

[13] Arola, D.F., Barrall, G.A., Powell, R.L., McCarthy, K.L. and McCarthy, M.J., 1997, Use of nuclear magnetic resonance imaging as a viscometer for process monitoring. *Chem. Eng. Sci.*, **52**, 2049–2057.

[14] Arola, D.F., Powell, R.L., Barrall, G.A. and McCarthy, M.J., 1998, A simplified method for accuracy estimation of nuclear magnetic resonant imaging. *Rev. Sci. Instrum.*, **69**, 3300–3307.

[15] Arola, D.F., Powell, R.L., Barrall, G.A. and McCarthy, M.J., 1999, Pointwise observations for rheological characterization using nuclear magnetic resonance imaging. *J. Rheol.*, **43**, 9–30.

[16] Callaghan, P.T., *Principles of Nuclear Magnetic Resonance Microscopy*, Clarendon Press, Oxford, GB, 1993.

[17] Sederman, A.J., Mantle, M.D., Buckley, C. and Gladden, L.F., 2004, MRI technique for measurement of velocity vectors, acceleration, and autocorrelation functions in turbulent flow. *J. Magn. Reson.*, **166**, 182–189.

[18] Galvosas, P. and Callaghan, P.T., 2006, Fast magnetic resonance imaging and velocimetry for liquids under high flow rates. *J. Magn. Reson.*, **181**, 119–125.

[19] Tayler, A.B., Holland, D.J., Sederman, A.J. and Gladden, L.F., 2011, Time resolved velocity measurements of unsteady systems using spiral imaging. *J. Magn. Reson.*, **211**, 1–10.

[20] Bretthorst, G.L., Hung, C.-C., D'Avignon, D.A. and Ackerman, J.J.H., 1988, Bayesian analysis of time-domain magnetic resonance signals. *J. Magn. Reson.*, **79**, 369–376.

[21] Xing, D., Gibbs, S.J., Derbyshire, J.A., Fordham, E.J., Carpenter, T.A. and Hall, L.D., 1995, Bayesian analysis for quantitative NMR flow and diffusion imaging. *J. Magn. Reson., Ser. B*, **106**, 1–9.

[22] Wise, R.G., Newling, B., Gates, A.R.C., Xing, D., Carpenter, T.A. and Hall, L.D., 1996, Measurement of pulsatile flow using MRI and a Bayesian technique of probability analysis. *Magn. Reson. Imaging*, **14**, 173–185.

[23] Bretthorst, G.L., Hutton, W.C., Garbow, J.R. and Ackerman, J.J.H., 2005, Exponential parameter estimation (in NMR) using Bayesian probability theory. *Concepts Magn. Reson. Part A*, **27A**, 55–63.

[24] Holland, D.J., Blake, A., Tayler, A.B., Sederman, A.J. and Gladden, L.F., 2011, A Bayesian approach to characterising multi-phase flows using magnetic resonance: application to bubble flows. *J. Magn. Reson.*, **209**, 83–87.

[25] Ross, J.G., Holland, D.J., Blake, A., Sederman, A.J. and Gladden, L.F., 2012, Extending the use of Earth's field NMR using Bayesian methodology: application to particle sizing. *J. Magn. Reson.*, **222**, 44–52.

[26] Ziovas, K., Sederman, A.J., Gehin-Delval, C., Gunes, D.Z., Hughes, E. and Mantle, M.D., 2016, Rapid sphere sizing using a Bayesian analysis of reciprocal space imaging data. *J. Colloid Interf. Sci.*, **462**, 110–122.

[27] Stejskal, E.O. and Tanner, J.E., 1965, Spin diffusion measurements: spin echoes in the presence of a time-dependent field gradient. *J. Chem. Phys.*, **42**, 288–292.

[28] Chilton, R.A. and Stainsby, R., 1998, Pressure loss equations for laminar and turbulent non-Newtonian pipe flow. *J. Hydraul. Eng.*, **124**, 522–529.

[29] Alberini, F., Simmons, M.J.H., Ingram, A. and Stitt, E.H., 2014, Use of an areal distribution of mixing intensity to describe blending of non-Newtonian fluids in a kenics KM static mixer using PLIF. *AIChE J.*, **60**, 332–342.

[30] *Flow and Suspension Properties of Carbopol® Polymers*, The Lubrizol Corp., Cleveland, US, 2002.

[31] Curran, S.J., Hayes, R.E., Afacan, A., Williams, M.C. and Tanguy, P.A., 2002, Properties of Carbopol solutions as models for yield-stress fluids. *J. Food Sci.*, **67**, 176–180.

[32] Coulson, J.M., Richardson, J.F., Backhurst, J.R. and Harker, J.H., *Coulson & Richardson's Chemical Engineering: Fluid flow, heat transfer, and mass transfer*, Butterworth-Heinemann, Oxford, GB, 1999.

[33] Cotts, R.M., Hoch, M.J.R., Sun, T. and Markert, J.T., 1989, Pulsed field gradient stimulated echo methods for improved NMR diffusion measurements in heterogeneous systems. *J. Magn. Reson.*, **83**, 252–266.

[34] Brunn, P.O. and Asoud, H., 2002, Analysis of shear rheometry of yield stress materials and apparent yield stress materials. *Rheol. Acta*, **41**, 524–531.

[35] Turian, R.M., Ma, T.W., Hsu, F.L.G. and Sung, D.J., 1997, Characterization, settling, and rheology of concentrated fine particulate mineral slurries. *Powder Technol.*, **93**, 219–233.

[36] Mitchell, J., Chandrasekera, T.C., Holland, D.J., Gladden, L.F. and Fordham, E.J., 2013, Magnetic resonance imaging in laboratory petrophysical core analysis. *Phys. Rep.*, **526**, 165–225.

Chapter 6

Case study: washcoating slurry

A Bayesian analysis of the pulsed field gradient (PFG) magnetic resonance (MR) signal was used in Chapter 4 to characterise the rheology of Herschel–Bulkley fluids in a pipe flow geometry. The robustness of the Bayesian MR approach to both reduced sampling and noisy data was later investigated in Chapter 5 using numerical simulations, with experimental validation provided using model Herschel–Bulkley fluids. It was observed, where the signal-to-noise ratio (SNR) was > 1000, that only 8 points need be sampled to estimate the flow curve.

In this Chapter, the Bayesian MR approach is applied to characterise the rheology of an aluminium oxide, with chemical formula Al_2O_3 and often referred to as alumina, in acetic acid slurry. Such slurries are of significant importance in industry where they are widely used in the washcoating process required in the manufacture of catalysed diesel particulate filters (cDPFs). As was previously described in Chapter 1, cDPFs are autocatalysts used in the automotive industry for the abatement of harmful species and to ensure compliance with increasingly stringent emission limit legislation. It is known that the performance of the resulting cDPF is sensitive to the catalyst thickness, with this governed by the slurry rheology. The rheology of such slurries is sensitive to pH, solids concentration, and particle size. To this end, the suitability of MR rheometry, namely Bayesian MR and MR flow imaging, to detect a deviation from specification is here investigated; changes in the rheology of alumina-in-acetic acid slurry following the addition of acetic acid are successfully detected using Bayesian MR, with the estimates of the rheological parameters in agreement to within the experimental uncertainty of conventional rheometry. Bayesian MR is therefore ideally suited to the online, or inline, rheological characterisation of process fluids.

6.1 Introduction

Over recent years, the demand for improved emission control technology has increased due to increasingly stringent emission limit legislation in both the developed and developing countries [1]. Today, the exhaust gases of gasoline engines are typically treated using a three-way catalytic converter to convert harmful pollutants, including carbon monoxide (CO), nitrogen oxides (NO_x), and hydrocarbons (HC), to harmless products. However, an increase in demand for more economical vehicles due to rising fuel prices has seen a recent increase in the popularity of light duty diesel engines. Such diesel engines, which made up 55% of the European passenger vehicle market in 2012 compared with just 31% in 2000 [2], are capable of offering improved fuel economy and reduced greenhouse gas emissions but require an alternative aftertreatment system due to the lean operating conditions, *i.e.* high air-to-fuel ratio. Aftertreatment systems developed for use with diesel engines include diesel oxidation catalysts (DOCs), diesel particulate filters (DPFs), catalysed DPFs (cDPFs), selective catalytic reduction (SCR), and lean NO_x traps (LNTs). Although a discussion of these systems is beyond the scope of this thesis, with the interested reader instead directed towards Ahmadinejad *et al.* [3] and Johnson [4], Fig. 6.1 shows some common combinations of these systems used to meet current emission limit legislation.

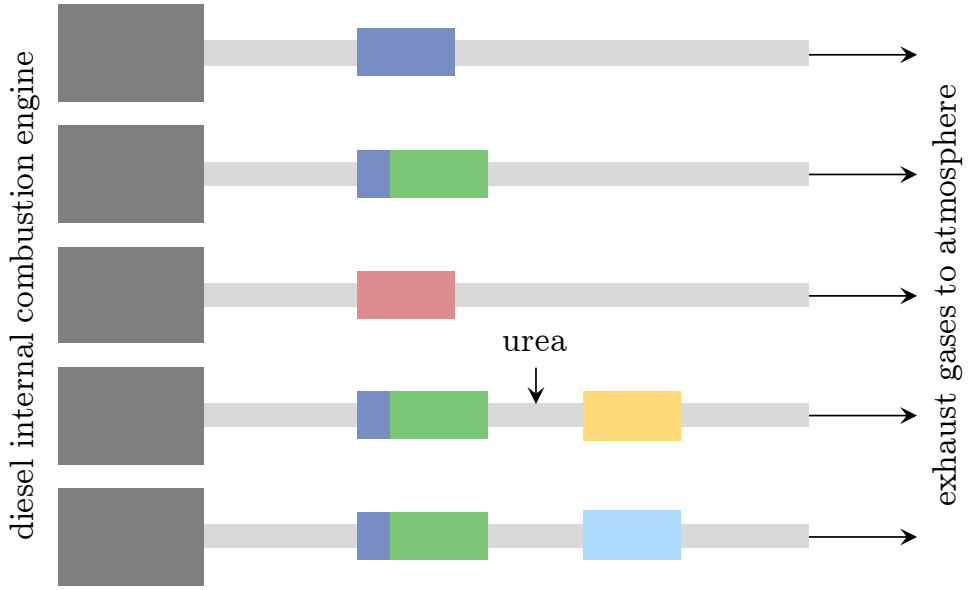

Fig. 6.1: A schematic of the systems (and combinations thereof) used for the treatment of the exhaust gases of diesel engines, showing (●) DOC, (●) DPF, (●) cDPF, (●) SCR, and (●) LNT. Adapted from Ramskill [5].

For example, with reference to Fig. 6.1, a continuously regenerating trap (CRT®) consists of a DOC located upstream of a DPF. At the DOC, CO and HC are oxidised to produce carbon dioxide (CO_2) and water (H_2O), with nitrogen oxide (NO) oxidised to produce nitrogen dioxide (NO_2). The NO_2 then reacts with particulate matter (PM), which accumulates at the DPF, to continuously regenerate the DPF at a temperature of 250 °C [3,6]. Note that the temperature requirements can be reduced through the use of a catalysed CRT® (cCRT®). Due to the space requirements of the combined DOC and DPF systems, these are typically restricted to a position located under the floor of the vehicle where the exhaust gas temperatures are low. Alternatively, multifunctional emissions abatement systems (such as cDPFs) offer a reduction in packaging volume, space requirements, and cost [7]. Such systems are manufactured by Johnson Matthey (JM).

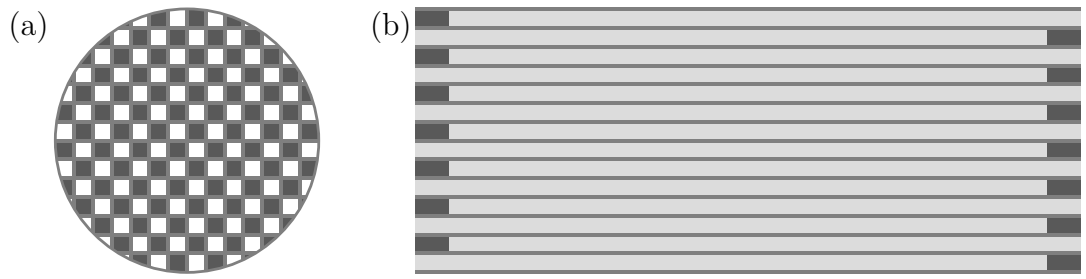

Fig. 6.2: Schematic representations of the (a) end and (b) side views of a DPF, showing the alternate plugged channels of the wall-flow monolith which force the exhaust gases to flow through the permeable wall.

At their simplest level, DPFs are a porous ceramic substrate made from cordierite, silicon carbide, or aluminium titanate using extrusion [8]. These materials have been selected due to their high mechanical strengths and robustness to high temperatures and severe mechanical vibrations [6]. DPFs consist of alternate, permeable channels plugged at opposite ends, as depicted in Fig. 6.2, and are now fitted on all new diesel-powered vehicles [3]. The exhaust gas enters the inlet channels where, unable to pass through the impermeable plugs, it is forced through the permeable walls of the wall-flow monolith and PM is deposited. However, recent developments in filter technologies and catalyst formulations mean that DPFs are now routinely combined with catalytic material. A catalysed soot filter (CSF®) [9], for example, has been developed which incorporates catalytic material into the DPF such that the requirement of a separate DOC is negated; the CSF® will oxidise the CO, HC, and NO whilst simultaneously

removing PM. The reduced space requirements of the CSF® mean that this system can be located at a position nearer to the diesel engine, where the exhaust gas temperatures are greater thus further improving the conversion of CO, HC, and NO. More recently, a selective catalytic reducing filter (SCRF®) [10] incorporating a DPF and SCR has been developed for the simultaneous abatement of NO_x and removal of PM.

During the manufacture of a cDPF, the raw catalyst material is first milled. Milling is a mechanical process during which the size of the catalyst particles is reduced, with finer particles known to demonstrate a better adhesion with the wall-flow monolith [11]. Through careful selection of the mill type—for example stirred media [12], ball [13] or jet [14] mills—and control of the mill conditions, the desired particle size distribution (PSD) may be achieved [15]. After milling, a washcoating slurry containing the milled catalyst material is applied to the surface of the wall-flow monolith, in a process called washcoating, and subsequently dried. The optimisation of cDPF properties, needed to ensure the abatement of harmful species and compliance with emission limit legislation, requires the control of two main factors:

- **Distribution uniformity.** The presence of catalyst on the surface of the wall-flow monolith is known to cause a decrease in permeability, with a non-uniform catalyst thickness responsible for non-uniform flow distribution; higher gas flow rates and greater through-wall velocities are expected in the regions where there is an absence of catalyst [5,16]. Previous studies have indicated that non-ideal drying is responsible for a non-uniform distribution of catalyst [17,18]. Therefore, careful control and optimisation during the drying process is required. Whilst a detailed discussion of the drying process will not be provided here, the interested reader is directed towards Chapter 1.

- **Catalyst thickness.** Careful control and optimisation of catalyst thickness is required due to the decrease in permeability associated with the presence of catalyst on the surface of the wall-flow monolith. The catalyst thickness is known to be sensitive to the rheology of the washcoating slurry, which may be affected by pH value, catalyst concentration and PSD, and/or binder concentration [15,19–21]. The optimisation of catalyst thickness, therefore, requires an accurate measurement of rheology.

The washcoating slurry under study is prepared by milling alumina in the presence of deionised water. After milling, acetic acid is added to the milled alumina-in-deionised

water to cause a change in rheology. Due to the aforementioned reasons, careful control of the so-called alumina-in-acetic acid slurry rheology is necessary to ensure optimum cDPF performance after drying. To this end, JM require a technique that enables the online, or inline, rheological characterisation of process fluids such that deviations from specification, due to unexpected changes in process conditions, can be detected. The alumina-in-acetic acid slurry under study has previously been shown to demonstrate power-law rheology up to concentrations of 45 wt% [22], given by

$$\tau\left(\dot{\gamma}\right) = K\dot{\gamma}^{n}, \tag{6.1}$$

where τ and $\dot{\gamma}$ represent the shear stress and shear rate, respectively, K is the consistency factor and n the flow behaviour index [23]. However, a yield stress is observed in this work at higher concentrations, with the rheology of the 55 wt% alumina-in-acetic acid slurry characterised using

$$\tau\left(\dot{\gamma}\right) = \tau_0 + K\dot{\gamma}^{n}, \tag{6.2}$$

known as the Herschel–Bulkley model [24], where τ_0 is the yield stress. The sensitivity of the catalyst thickness to rheology is not unique to the manufacture of cDPFs, but has been observed in a large number of washcoating applications [21,25]. Therefore, an ability to measure the rheology of washcoating slurries online, or inline, has potential for use in a large number of industrial applications.

The suitability of magnetic resonance (MR) rheometry for this application is here investigated by experimental study on an alumina-in-acetic acid slurry before and after the addition of acetic acid. In particular, the signal in q-space, denoted $S\left(q\right)$ and given by

$$S\left(q\right) = \int p\left(\zeta\right) \exp\left[\mathrm{i}2\pi q\zeta\right] \mathrm{d}\zeta, \tag{6.3}$$

is sampled using pulsed field gradient (PFG) MR to investigate changes in the volume-averaged displacement probability distribution, $p\left(\zeta\right)$, where $q = \left(1/2\pi\right)\gamma g\delta$, with γ the gyromagnetic ratio of the nucleus under study and g and δ the magnitude and duration

of the flow gradient, respectively [26]. Therefore, q-space is traversed by varying g or δ and $S(q)$ is sampled. Since $S(q)$ and $p(\zeta)$ represent mutually conjugate Fourier pairs, Fourier transformation of $S(q)$ provides a volume-averaged displacement probability distribution, or flow propagator [27], characteristic of the flow under study [28]; the field-of-flow (FOF) of $p(\zeta)$ is defined by the reciprocal of the sampling resolution in q-space, whilst the displacement resolution of $p(\zeta)$ is equal to the reciprocal of the range of q-space sampled. The signal in q-space is also sampled over a range of $\pm 4\langle\zeta\rangle^{-1}\,\mathrm{m}^{-1}$ for Bayesian analysis using the method developed in Chapter 4. In Bayesian analysis, the state of the system, Θ, is inferred from a set of experimental observations, $\hat{y}$, using the posterior probability density function, $p(\Theta|\hat{y})$, given by

$$p(\Theta|\hat{y}) \propto p(\hat{y}|\Theta)\, p(\Theta)\,, \tag{6.4}$$

where $p(\hat{y}|\Theta)$ is the likelihood function and $p(\Theta)$ incorporates prior knowledge. In this work, rheological characterisation is performed using a Bayesian analysis of the PFG MR signal, such that $\hat{y}$ corresponds to $S(q)$ and Θ corresponds to the Herschel–Bulkley rheological parameters describing the rheology of the fluid under study. The likelihood function then describes the variation of $S(q)$ for a given combination of rheological parameters, and the prior describes what is already known about the probabilities of these parameters. A complete introduction to the Bayesian MR approach is included in Chapter 5.

In addition to the acquisition of flow propagators and the data required for use with the Bayesian MR approach, the flow field was also resolved spatially using 2D MR flow imaging. It is observed that changes in the flow field induced by the addition of acetic acid, *i.e.* changes in the rheology of the alumina-in-acetic acid slurry under study, can be detected online using MR rheometry. In particular, a decrease in K and τ_0 is seen as the pH value is decreased from 6.0 to 5.0, whilst n remains approximately constant. These changes are in agreement with previous work [22] and consistent with those observed offline using conventional rheometry. The difficulties associated with the study of process fluids, when compared with model fluids, are also outlined using 2D MR imaging. It is important to note that rheology is paramount in a wide range of industrial processes, from spraying and mixing to drying and coating [29]. Furthermore, the Bayesian MR approach can be adapted to enable the online, or inline, rheological characterisation of a large number of process fluids.

6.2 Materials and methods

6.2.1 Simulations

For Bayesian analysis, an uninformative prior ($p(\Theta)$ in Eq. (6.4)) was used such that the probability of each of the parameters values considered was assumed to be identical. In particular, the range of priors comprised of a set of 501 values evenly spaced between 0 and 1 for both n and r_0/R, where r_0 is the radial position corresponding to τ_0 and R is the pipe radius, with a resolution of 0.002. Using the method outlined in Chapter 5, the expected signal in q-space, $f(q, n, r_0)$, was simulated numerically across all n and r_0/R described and $p(\Theta|\hat{y})$ obtained; the means extracted from $p(\Theta|\hat{y})$ then provide an estimate of n and r_0/R, with the standard deviations a measure of the uncertainty and r_0/R later used to calculate τ_0.

6.2.2 Experimental

Materials and experimental set-up

The alumina-in-acetic acid slurry used in this study was prepared by JM at a concentration of 55 wt% using PURALOX® SCFa-140 (Sasol, DE), with 98% purity [30,31], suspended in distilled water. Milling was performed to reduce the size of the alumina particles, with the particle sizes pre- and post-milling summarised in Table 6.1. After milling, 20 mL of acetic acid (Fisher Scientific, GB) was added to 3 L of 55 wt% milled alumina-in-deionised water slurry using a pipette (Eppendorf, DE). An overhead stirrer (Ika–Werke RW20) was used to mix the resulting alumina-in-acetic acid slurry for several hours to prevent sedimentation and ensure a homogeneous mixture. The pH of the milled alumina-in-acetic acid slurry was measured (Corning 240 pH meter), with an initial pH of 6.0. After the addition of a further 10 mL of acetic acid during flow, the final pH of the slurry was 5.0.

Table 6.1: A comparison of pre- and post-milling alumina particle sizes, where d_{50} and d_{90} represent the particle diameters, d, containing 50 and 90% of particles, respectively.

size [µm]	pre-milling	post-milling
d_{50}	21	4.0
d_{90}	43	17

The flow loop, comprising a 3.0 m length of polyvinyl chloride (PVC) pipe of inner diameter (i.d.) 13 mm, was operated in a closed loop configuration. Flow rates of up to 50 mL s^{-1} were provided using a peristaltic pump (MasterFlex Console Drive), and steady flow was ensured using a flow pulsation dampener. Note that an overhead stirrer was used to prevent sedimentation, and aid with mixing, following the addition of acetic acid. Flow rates, $\dot{V}$, were determined gravimetrically. The radiofrequency (r.f.) coil was situated 2.0 m downstream of the pipe inlet, exceeding the inlet length of 100 times pipe i.d. recommended to ensure developed flow [32]. Pressure drop was measured across a length of 2.4 m using a differential pressure gauge (Digitron 2002P). A pressure drop of 2530±150 Pa m^{-1} was measured before the addition of acetic acid, with $\dot{V}$ = 1.21±0.09 mL s^{-1}, decreasing to 1530±120 Pa m^{-1}, with $\dot{V}$ = 2.39±0.21 mL s^{-1}, following the addition of acetic acid. This corresponds to shear rate ranges of almost an order of magnitude; 1.0–5.0 and 1.0–9.9 s^{-1} for the initial and final milled alumina-in-acetic acid slurries, respectively, as determined from MR flow imaging.

Magnetic resonance

MR experiments were performed using a Bruker AV85 spectrometer operating with a 2 T horizontal-bore superconducting magnet. The magnet was fitted with a 60 mm birdcage r.f. coil tuned to a frequency of 85.2 MHz for the ^{1}H resonance. A three-axis gradient system with a maximum gradient strength of 10.7 G cm^{-1} was used for spatial and flow encoding.

Table 6.2: A comparison of flow gradient parameters and ranges of q-space sampled for the acquisition of flow propagators, and the data required for use with Bayesian MR, of the alumina-in-acetic acid slurry before and after the addition of acetic acid. Corresponding parameters used for MR flow imaging are also reported.

	method	flow gradient parameters			$\lvert q_{\max}\rvert$
		δ [ms]	Δ [ms]	$\lvert g_{\max}\rvert$ [G cm^{-1}]	[m^{-1}]
before	Bayesian MR	3.0	50	1.2	1500
	flow propagators	3.5	150	9.5	14 200
	MR flow imaging	2.0	10	-	-
after	Bayesian MR	3.0	50	0.59	750
	flow propagators	3.0	65	9.5	12 100
	MR flow imaging	2.0	10	-	-

A 13-interval alternating pulsed field gradient stimulated echo (APGSTE) pulse sequence [33] was used to sample $S(q)$ over a q-space range of $\pm 4\langle\zeta\rangle^{-1}\,\mathrm{m}^{-1}$ for Bayesian analysis and over high-q for the acquisition of flow propagators; the two datasets cannot be sampled simultaneously due to the requirement of Fourier transform. Flow gradient parameters used before and after the addition of acetic acid—including the duration, flow contrast time, Δ, and maximum gradient magnitude, $|g_{\max}|$—are summarised in Table 6.2. The range of q-space sampled, $|q_{\max}|$, is also reported. In all cases, q-space was sampled linearly between $\pm|q_{\max}|$ in 128 steps. Four signal averages were acquired with a recycle time of 1 s, equal to 5 times T_1 (200 ms), and a data acquisition time of 8 min 40 s. This is equivalent to 4 s per data point acquired. Flow rates quantified through measurement of the evolution of the phase at low values of q were 1.13±0.03 and 2.24±0.06 mL s^{-1} before and after the addition of acetic acid, respectively, and in agreement to within the experimental uncertainty of gravimetric measurements.

In addition, spatially-resolved 2D MR flow images were acquired for the alumina-in-acetic acid slurry before and after the addition of acetic acid using a slice selective, spin echo MR flow imaging sequence [34]. A field-of-view of 18 mm was used in the read and phase directions, with 128 read points and phase increments, to give a resolution of 141 µm × 141 µm. The data were acquired with a slice thickness of 10 mm and an SNR within each liquid-filled voxel of 100. Flow gradient parameters are summarised in Table 6.2, with Δ limited by T_2 and g selected in each case to ensure the maximum phase shift did not exceed 2π. Images were acquired in 4 min 20 s, with a recycle time of 260 ms and 4 signal averages, and non-linear least squares (NLLS) regression of

$$\zeta(r, n, r_0) = \begin{cases} \zeta_{\max}, & 0 \leq r < r_0, \\ \zeta_{\max}\left(1 - \left(\dfrac{r - r_0}{R - r_0}\right)^{\frac{n+1}{n}}\right), & r_0 \leq r \leq R, \end{cases} \tag{6.5}$$

used to estimate n and r_0, where $\zeta_{\max}$ is the maximum fluid displacement, with the 95% confidence interval in the individual fit a measure of the uncertainty and pressure drop providing τ_0 and K. MR experiments were performed at 19.0±0.5 °C. The flow rates calculated from MR flow images were 1.14±0.04 mL s^{-1} before the addition of acetic acid and 2.30±0.10 mL s^{-1} after, in agreement to within the experimental uncertainty of gravimetric measurements and low q-space analysis.

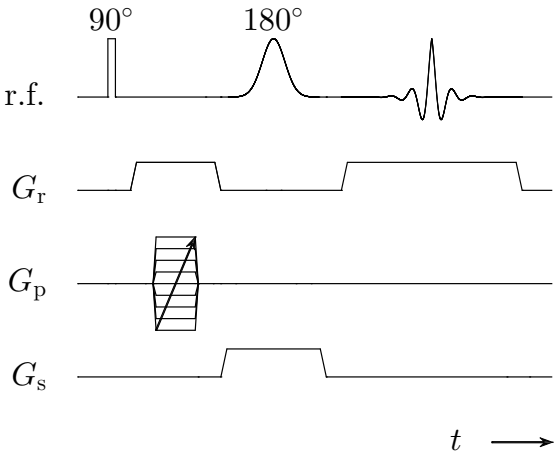

Fig. 6.3: The slice selective spin echo MR imaging pulse sequence used for the imaging of intensity.

Figure 6.3 shows a 2D slice selective spin echo MR imaging pulse sequence used for the acquisition of 2D images during flow to test for sedimentation, creaming, and/or shear induced migration. Acquisition parameters were identical to those described for MR flow imaging, with SNR = 100. A total of 4 signal averages were acquired with a recycle time of 260 ms to give an acquisition time of 2 min 10 s.

Conventional rheometry

Benchtop measurements of the rheology of the initial and final alumina-in-acetic acid slurries were performed using a Malvern Instruments Kinexus Lab+ controlled-stress rheometer. The controlled-stress mode of operation enables τ_0 to be estimated without the need for extrapolation [35]. A Peltier plate was used to control the temperature at 19.0±1.0 °C. Rough-walled parallel plates were used to eliminate wall slip behaviour, with 40 mm diameter and a plate separation of 1 mm. Shear rate was measured across a shear stress sweep of 0.01–100 Pa in 5 min. A correction was applied to the apparent (measured) flow curve to obtain the true flow curve [35], as given by

$$\tau_a\left(\dot{\gamma}_a\right) = \frac{4}{3}\tau_0 + \left(\frac{4}{3+n}\right) K \dot{\gamma}_a^n \tag{6.6}$$

for the case of a parallel plate geometry, where τ_a and $\dot{\gamma}_a$ represent the apparent shear stress and shear rate, respectively.

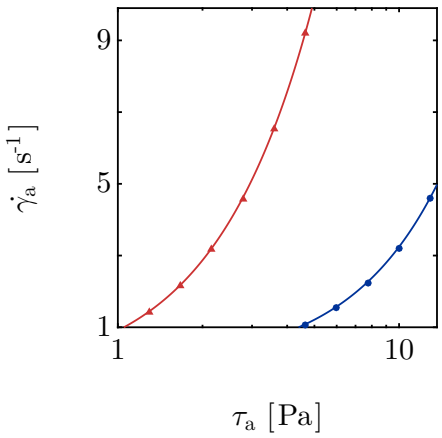

Fig. 6.4: Apparent shear rate-shear stress data for the (●) initial and (▲) final alumina-in-acetic acid slurries. Symbols show the experimentally-acquired data and the solid lines show the regression data; the NLLS regression was performed over the same shear rate ranges as the MR experiments using Eq. (6.6).

The NLLS regression of Eq. (6.6) to the apparent flow curve, across the same ranges of shear rate as probed in the Bayesian MR and MR flow imaging experiments, was used to provide estimates of the rheological parameters. The regression data is shown in Fig. 6.4 for the initial and final alumina-in-acetic acid slurries, with the regression data accurate to within the scatter of the experimental data, confirming Herschel–Bulkley rheology over the shear rate ranges of the MR experiments. The rheological parameters obtained across the shear rate ranges investigated are summarised in Table 6.3, where the uncertainty represents the 95% confidence interval in the individual fit.

6.3 Results and discussion

6.3.1 Bayesian MR methods

The signal in q-space was sampled over a q-space range of $\pm 4\langle\zeta\rangle^{-1}\,\mathrm{m}^{-1}$ for Bayesian analysis using the method developed in Chapter 4 and extended in Chapter 5. Using the Bayesian MR approach, $p\left(\Theta|\hat{y}\right)$ was quantified, where $\hat{y} = S\left(q\right)$ and $\Theta = \{n, r_0\}$, with the means and standard deviations of $p\left(\Theta|\hat{y}\right)$ providing an estimate of n and τ_0 (since pressure drop was measured). The value of K was estimated using the method described in Chapter 5. Figure 6.5 shows $p\left(\Theta|\hat{y}\right)$ quantified for the alumina-in-acetic acid slurry (a) before and (b) after the addition of acetic acid.

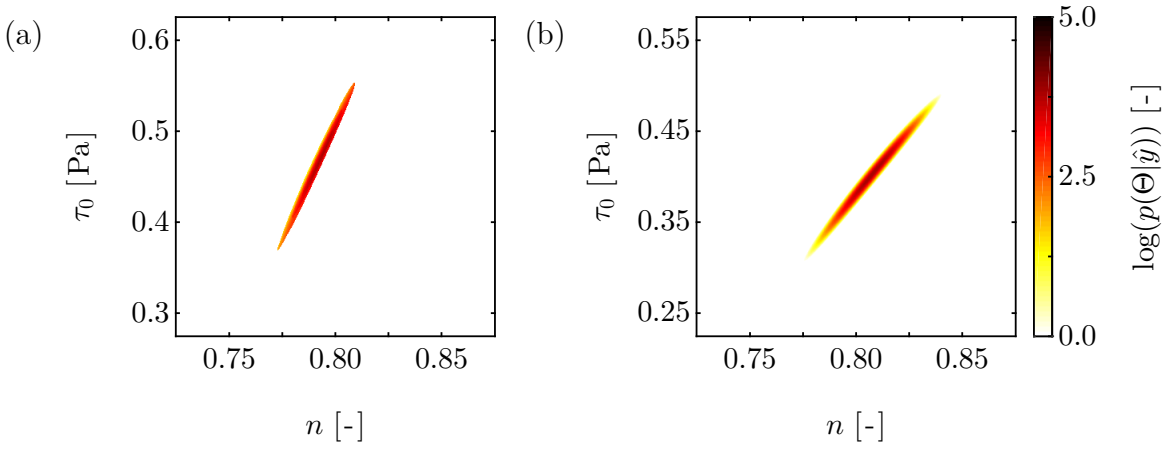

Fig. 6.5: 2D posterior probability distributions, plotted on a log scale, showing the probability of n and τ_0 given $\hat{y}$ for the alumina-in-acetic acid slurry (a) before and (b) after the addition of acetic acid. The SNR (at $q = 0\,\mathrm{m}^{-1}$) is > 1000, with the 128 points in q-space sampled using the experimental procedure outlined in Section 6.2.2.

Using the Bayesian MR approach, only small changes in n and τ_0 were observed following the addition of acetic acid; n was seen to increase from 0.79±0.02 to 0.81±0.02, whilst τ_0 decreased from 0.47±0.04 to 0.40±0.03 Pa. Changes in K were considerable, decreasing from 3.9±0.1 to 1.3±0.1 $\mathrm{Pa\,s}^n$ following the addition of acetic acid. These changes, summarised in Table 6.3, are consistent with previous work [22] in which only small changes in n were observed as the pH value was decreased from 7.0 to 2.0.

6.3.2 Comparison with non-Bayesian MR methods

Flow propagators were acquired to investigate changes in the flow distribution with an increase in acetic acid concentration. Figure 6.6 shows $p'(\zeta)$ of the alumina-in-acetic acid slurry (a) before and (b) after the addition of acetic acid, with a dominant spike in $p'(\zeta)$ at the maximum displacement indicative of yield stress behaviour. It is also interesting to note that only minimal changes in $p'(\zeta)$ can be observed following the addition of acetic acid, suggesting that n and r_0/R do not change considerably. These results agree qualitatively with the rheological parameters determined using conventional rheometry and Bayesian MR. For validation of the Bayesian MR approach, MR flow imaging was also used to characterise the rheology of the alumina-in-acetic acid slurries. Figure 6.7 shows MR flow images of the alumina-in-acetic acid slurry (a) before and (b) after the addition of acetic acid, where the displacement represents axial displacement, *i.e.* z-displacement.

The images have SNR = 100 and spatial resolution of 141 µm × 141 µm, sufficient to provide ∼90 spatially-resolved velocity data points across the pipe. The addition of acetic acid is observed to cause only small changes in the flow field, consistent with conventional rheometry. As expected, the MR flow images do not demonstrate any of the features attributed to turbulent flow, although a slight disturbance can be observed at the bottom of the flow field, particularly following the addition of acetic acid. These changes are shown in Fig. 6.7(d) to result from sedimentation. This occurs following the addition of acetic acid, perhaps due to the decrease in shear viscosity and increase in settling velocity according to Stokes' law [36], and highlights a challenge associated with the study of real, particle-laden process fluids.

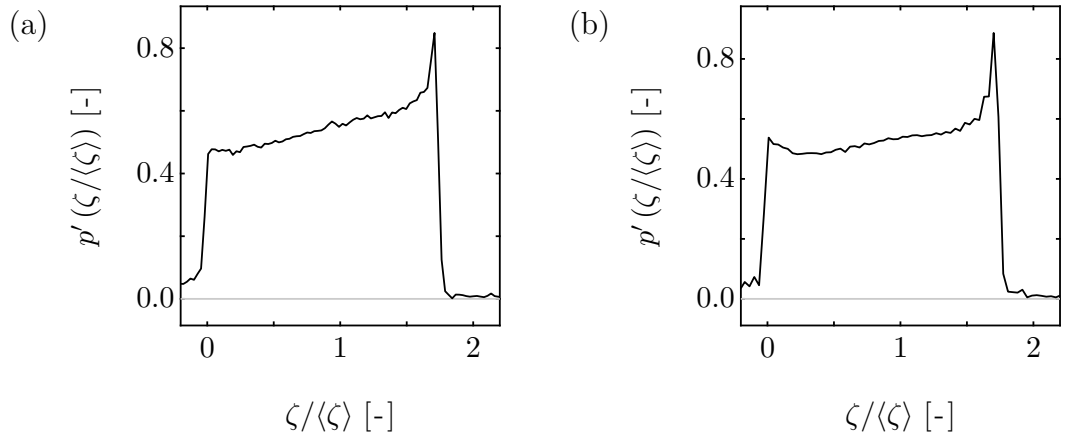

Fig. 6.6: The experimentally-acquired $p'(\zeta)$ for the alumina-in-acetic acid slurry (a) before and (b) after the addition of acetic acid.

A 2D NLLS regression of $\Delta^{-1}\zeta(r)$ was performed to the MR flow images to quantify n and r_0/R before and after the addition of acetic acid, with $\zeta(r)$ given by Eq. (6.5). Figure 6.8 shows radially-averaged displacement profiles and corresponding regression data; the displacement profiles and regression data are in agreement to within experimental error. From these, τ_0 and K can be estimated using the methodology described in Chapter 5. Before the addition of acetic acid, this approach provided n and τ_0 estimates of 0.75±0.04 and 0.50±0.04 Pa, respectively, where the uncertainty is equal to the 95% confidence interval in the individual fit, with $K = 4.1 \pm 0.1\,\mathrm{Pa\,s}^n$. Rheological parameters obtained after the addition of acetic acid were 0.79±0.02, 0.45±0.02 Pa, and $1.3 \pm 0.1\,\mathrm{Pa\,s}^n$ for n, τ_0, and K, respectively. These parameters are summarised in Table 6.3.

Whilst n and τ_0 have remained approximately constant following the addition of acetic acid, and a decrease in pH from 6.0 to 5.0, K has decreased considerably. These observations are consistent with the Bayesian MR approach discussed in Section 6.3.1 and parameters reported in previous work using conventional rheometry [22]. For the sample under study, fortunately, the sedimentation observed does not appear to negatively affect the accuracy of the rheological characterisation using either the Bayesian MR approach or MR flow imaging. This is most likely due to the small proportion of flow field affected by the sediment and/or the volume-averaged nature of the Bayesian MR approach. That said, the Bayesian MR approach can be readily adapted to account for and overcome such issues.

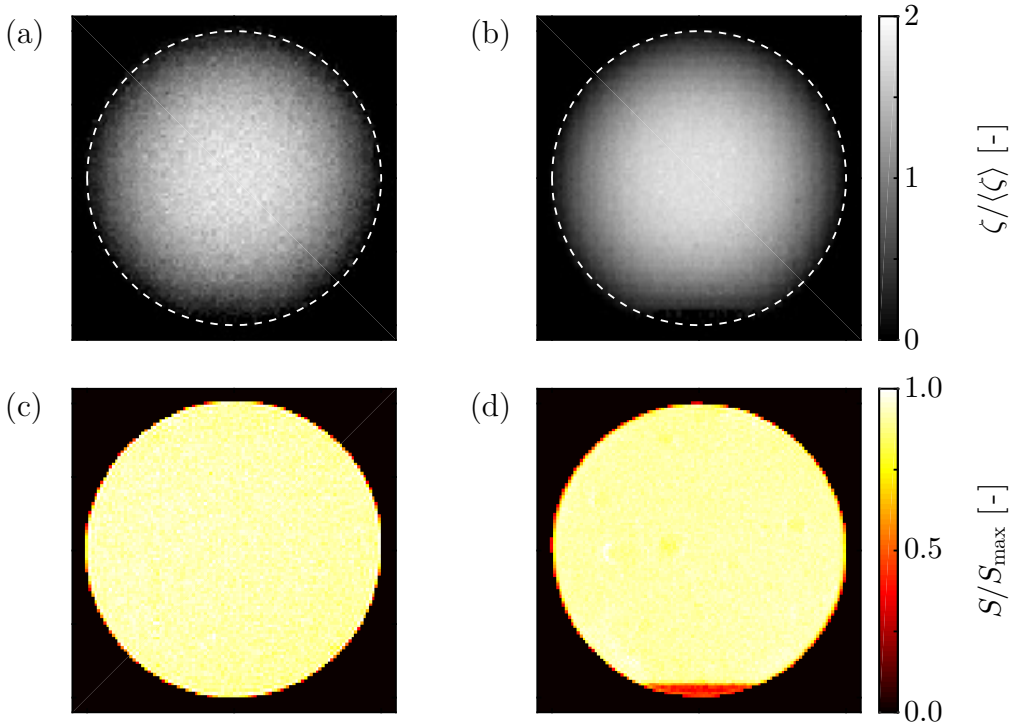

Fig. 6.7: MR flow images acquired for the alumina-in-acetic acid slurry (a) before and (b) after the addition of acetic acid, represented as a fraction of $\langle\zeta\rangle$. Also shown are the corresponding MR images (c) before and (d) after the addition of acetic acid, with sedimentation observed, represented as a fraction of maximum signal intensity, $S_{\max}$. All images have a spatial resolution of 141 µm × 141 µm and SNR = 100.

With reference to Table 6.3, it is observed that the two MR rheometry methods are self-consistent and consistent with conventional rheometry for the alumina-in-acetic acid slurry under study both before and after the addition of acetic acid. In particular,

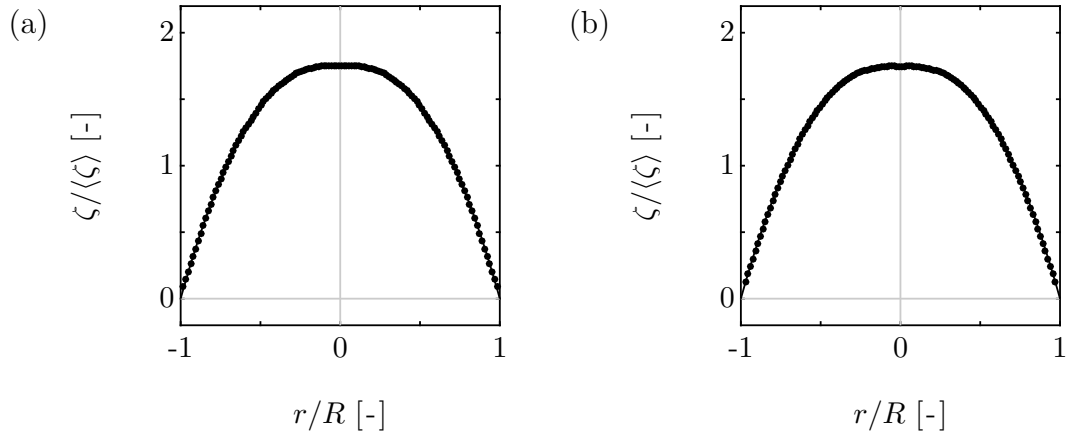

Fig. 6.8: Displacement profiles of the alumina-in-acetic acid slurry (a) before and (b) after the addition of acetic acid showing the radially-averaged (●) MR flow images and (—) regression data, obtained by performing a 2D NLLS regression of $\Delta^{-1}\zeta(r)$ to the MR flow images with $\zeta(r)$ given by Eq. (6.5). The error in the regression data is within the accuracy of the experimental data.

estimates of n obtained using the Bayesian MR approach are accurate to within 5% of those n determined using MR flow imaging and 4% of those values determined using conventional rheometry. These results are significant and imply that the Bayesian MR approach may be used online, or inline, to provide accurate estimates of the rheological parameters describing the rheology of the process fluid under study. Furthermore, this has potential for use on low-field MR hardware.

Table 6.3: A comparison of the rheological parameters of the alumina-in-acetic acid slurry before and after the addition of acetic acid obtained using Bayesian MR, MR flow imaging, and conventional rheometry methods, evaluated across shear rate ranges of 1.0–5.0 and 1.0–9.9 s^{-1}, respectively.

	method	rheological parameters		
		n [-]	τ_0 [Pa]	K [Pa s^n]
before	Bayesian MR	0.79±0.02	0.47±0.04	3.9±0.1
	MR flow imaging	0.75±0.04	0.50±0.04	4.1±0.1
	conventional rheometry	0.76±0.01	0.49±0.09	3.6±0.1
after	Bayesian MR	0.81±0.02	0.40±0.03	1.3±0.1
	MR flow imaging	0.79±0.02	0.45±0.02	1.3±0.1
	conventional rheometry	0.82±0.02	0.37±0.03	0.63±0.02

6.4 Conclusions

In this Chapter, the application of the Bayesian MR approach developed in Chapter 4 to a real process fluid, namely an alumina-in-acetic acid slurry, has been investigated. The rheology of such slurries, used by JM in the manufacture of cDPFs, is known to be sensitive to the pH value, solids concentration, and PSD of the milled alumina. To this end, the Bayesian MR approach was applied online and used to observe changes in rheological behaviour following the addition of acetic acid. The pH value decreased from 6.0 to 5.0, hence mimicking the deviation of a process fluid from specification. Alumina-in-acetic acid slurry is observed to demonstrate Herschel–Bulkley rheological behaviour, as characterised by n, K, and τ_0.

Following the addition of acetic acid, changes in n, K, and τ_0 were detected using three different methods; namely Bayesian MR, MR flow imaging, and conventional rheometry. The estimates of n, K, and τ_0 obtained using the two MR rheometry methods are self-consistent, to within 13%, and also consistent to within 8% of conventional rheometry. Whilst this has successfully confirmed the suitability of the Bayesian MR approach for the online, or inline, rheological characterisation of process fluids, further work is required to examine the applicability of this approach on low-field MR hardware. Note that the numerical simulation results reported in Chapter 5 at SNR = 100 suggest that an extension to low-field MR should be straightforward.

6.5 References

[1] Twigg, M.V., 2006, Roles of catalytic oxidation in control of vehicle exhaust emissions. *Catal. Today*, **117**, 407–418.

[2] Hansen, S., *European experience shows that cars and trucks powered by clean diesel key to meeting CO_2 emissions reduction targets*, 2013.

[3] Ahmadinejad, M., Desai, M.R., Watling, T.C. and York, A.P.E., in *Adv. Chem. Eng.* Elsevier, 2007, vol. 33, pp. 47–101.

[4] Johnson, T., 2008, Diesel engine emissions and their control: an overview. *Platin. Met. Rev.*, **52**, 23–37.

[5] Ramskill, N.P., Ph.D. Thesis, University of Cambridge, GB, 2014.

[6] Twigg, M.V., 2007, Progress and future challenges in controlling automotive exhaust gas emissions. *Appl. Catal., B*, **70**, 2–15.

[7] Ramskill, N.P., Gladden, L.F., York, A.P.E., Sederman, A.J., Mitchell, J. and Hardstone, K.A., 2013, Understanding the operation and preparation of diesel particulate filters using a multi-faceted nuclear magnetic resonance approach. *Catal. Today*, **216**, 104–110.

[8] Benbow, J. and Bridgwater, J., *Paste Flow and Extrusion*, Oxford University Press, Oxford, GB, 1993.

[9] Twigg, M.V. and Phillips, P.R., 2009, Cleaning the air we breathe—controlling diesel particulate emissions from passenger cars. *Platin. Met. Rev.*, **53**, 27–34.

[10] Watling, T.C., Ravenscroft, M.R. and Avery, G., 2012, Development, validation and application of a model for an SCR catalyst coated diesel particulate filter. *Catal. Today*, **188**, 32–41.

[11] Germani, G., Stefanescu, A., Schuurman, Y. and Veen, A.C. van, 2007, Preparation and characterization of porous alumina-based catalyst coatings in microchannels. *Chem. Eng. Sci.*, **62**, 5084–5091.

[12] Bel Fadhel, H. and Frances, C., 2001, Wet batch grinding of alumina hydrate in a stirred bead mill. *Powder Technol.*, **119**, 257–268.

[13] Yang, Y. and Sigmund, W.M., 2002, Expanded percolation theory model for the temperature induced forming (TIF) of alumina aqueous suspensions. *J. Eur. Ceram. Soc.*, **22**, 1791–1799.

[14] Omura, N., Hotta, Y., Sato, K., Kinemuchi, Y., Kume, S. and Watari, K., 2005, Characterization of Al_2O_3 slurries prepared by wet jet milling. *J. Ceram. Soc. Jpn.*, **494**, 491–494.

[15] Adegbite, S.A., 2012, Particle characterisation and grinding behaviour of gamma-alumina slurries prepared in a stirred media mill. *J. Mater. Sci. Res.*, **2**, 135–147.

[16] Yu, M., Luss, D. and Balakotaiah, V., 2013, Analysis of flow distribution and heat transfer in a diesel particulate filter. *Chem. Eng. J.*, **226**, 68–78.

[17] Nijhuis, T.A., Beers, A.E.W., Vergunst, T., Hoek, I., Kapteijn, F. and Moulijn, J.A., 2001, Preparation of monolithic catalysts. *Catal. Rev.*, **43**, 345–380.

[18] Vergunst, T., Kapteijn, F. and Moulijn, J.A., 2001, Monolithic catalysts—non-uniform active phase distribution by impregnation. *Appl. Catal., A*, **213**, 179–187.

[19] Meille, V., Pallier, S., Santa Cruz Bustamante, G.V., Roumanie, M. and Reymond, J.-P., 2005, Deposition of γ-Al_2O_3 layers on structured supports for the design of new catalytic reactors. *Appl. Catal., A*, **286**, 232–238.

[20] Hwang, S.-M., Kwon, O.J. and Kim, J.J., 2007, Method of catalyst coating in micro-reactors for methanol steam reforming. *Appl. Catal., A*, **316**, 83–89.

[21] Stefanescu, A., Veen, A.C. van, Mirodatos, C., Beziat, J.C. and Duval-Brunel, E., 2007, Wall coating optimization for microchannel reactors. *Catal. Today*, **125**, 16–23.

[22] Adegbite, S.A., Ph.D. Thesis, University of Birmingham, GB, 2010.

[23] Ostwald, W., 1929, Ueber die rechnerische darstellung des strukturgebietes der viskosität. *Kolloid-Z.*, **47**, 176–187.

[24] Herschel, W.H. and Bulkley, R., 1926, Konsistenzmessungen von gummi-benz-ollösungen. *Kolloid-Z.*, **39**, 291–300.

[25] Zapf, R., Becker-Willinger, C., Berresheim, K., Bolz, H., Gnaser, H., Hessel, V., Kolb, G., Pannwitt, A.-K. and Ziogas, A., 2003, Detailed characterization of various porous alumina-based catalyst coatings within microchannels and their testing for methanol steam reforming. *Chem. Eng. Res. Des.*, **81**, 721–729.

[26] Stejskal, E.O. and Tanner, J.E., 1965, Spin diffusion measurements: spin echoes in the presence of a time-dependent field gradient. *J. Chem. Phys.*, **42**, 288–292.

[27] Kärger, J. and Heink, W., 1983, The propagator representation of molecular transport in microporous crystallites. *J. Magn. Reson.*, **51**, 1–7.

[28] Maneval, J.E., Powell, R.L., McCarthy, M.J. and McCarthy, K.L., in *Particulate Two-phase Flow*, Butterworth-Heinemann, Boston, US, 1993, pp. 127–140.

[29] Collyer, A.A. and Clegg, D.W., *Rheological Measurement*, Springer, Dordrecht, NL, 1998.

[30] *PURALOX®/CATALOX® High-Purity Activated Aluminas*, Sasol Germany GmbH, Hamburg, DE, 2005.

[31] *PURALOX®/CATALOX® High-Purity Calcined Aluminas*, Sasol Germany GmbH, Hamburg, DE, 2017.

[32] Coulson, J.M., Richardson, J.F., Backhurst, J.R. and Harker, J.H., *Coulson & Richardson's Chemical Engineering: Fluid flow, heat transfer, and mass transfer*, Butterworth-Heinemann, Oxford, GB, 1999.

[33] Cotts, R.M., Hoch, M.J.R., Sun, T. and Markert, J.T., 1989, Pulsed field gradient stimulated echo methods for improved NMR diffusion measurements in heterogeneous systems. *J. Magn. Reson.*, **83**, 252–266.

[34] Gladden, L.F. and Sederman, A.J., 2013, Recent advances in flow MRI. *J. Magn. Reson.*, **229**, 2–11.

[35] Brunn, P.O. and Asoud, H., 2002, Analysis of shear rheometry of yield stress materials and apparent yield stress materials. *Rheol. Acta*, **41**, 524–531.

[36] Stokes, G.G., *Mathematical and Physical Papers*, Cambridge University Press, Cambridge, GB, 1880.

Chapter 7

Gravitational collapse of depletion-induced colloidal gels

A colloidal dispersion was defined in Chapter 1 as a dispersed phase, sized between 10 nm and 1 µm, distributed throughout a dispersion medium. In 1923, Perrin [1] used such dispersions to confirm Einstein's theory on Brownian motion [2] and demonstrate the existence of atoms and molecules. To this day, colloidal dispersions continue to be used to address long-standing fundamental questions due to the associated convenient length and time scales [3]. Furthermore, the ability to tune the interaction between colloids has enabled the formulation of colloidal gels, semi-solid colloidal dispersions with unique structural, mechanical, and rheological behaviour [4]. Many industrial products required to demonstrate specific behaviour are, for this reason, formulated as colloidal gels, from foodstuffs [5] to the specialist inks used for three-dimensional printing [6]. However, such gels are inherently unstable, with structural integrity maintained for a finite duration before the gel undergoes gravitational collapse.

A more detailed understanding of the mechanisms of colloidal gel collapse is not only of fundamental scientific interest but also of practical importance [7]. To this end, a multifaceted approach is used in this Chapter to investigate the ageing and ultimate collapse of colloidal gels. In particular, gel collapse was monitored using digital imaging and magnetic resonance (MR) imaging, with the latter used to provide a quantitative, spatio-temporally resolved measurement of the volume fraction. It is shown using MR imaging that gel collapse is initiated by processes at the top of the sample. This work was carried out in collaboration with the School of Physics and Astronomy, University of Edinburgh.

7.1 Introduction

Many industrial products are colloidal dispersions at volume fractions of, say, 5–40% in which the dispersed phase is denser than the dispersion medium. A key requirement is that the dispersed phase must not sediment appreciably during a shelf-life of months to years, but, when required, the colloidal dispersion must flow under a moderate applied shear stress. These, seemingly contradictory, requirements can be met by formulating the product as a colloidal gel; a space-spanning network of attractive particles with a yield stress, τ_0, high enough to support the weight of the particles and yet low enough to be overcome in use to give flowability. For comparison, Fig. 7.1 shows schematically the short-range spatial order of a colloidal fluid, with cluster formation, and the space-spanning network of a colloidal gel.

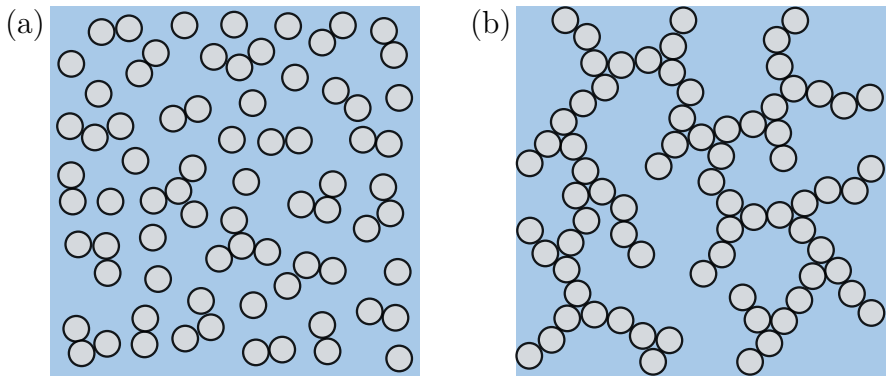

Fig. 7.1: Schematics showing (a) a typical colloidal fluid, with cluster formation, and (b) the space-spanning network of a colloidal gel.

It is now widely accepted [8] that there are two mechanisms of gelation; chemical gelation, involving the formation of chemical bonds, and physical gelation, originating from the short-range interactions between the particles. Considering chemical gelation, for example that of an epoxy resin, the gelation proceeds as irreversible chemical bonds form between the atoms of neighbouring polymer chains. If the average functionality of the polymer chains is greater than 2, *i.e.* the polymer chains demonstrate an ability to cross-link, a space-spanning network is formed at gelation [9]. Note that space-spanning networks are also known as percolating networks, with gelation a form of percolation. Since the colloidal gels under study in this Chapter are formed by physical gelation, a more detailed introduction to chemical gelation is beyond the scope of this thesis and the interested reader is directed towards the journal article of Zaccarelli [8]. Physical

gelation takes place due to the reversible, or transient, short-range interaction between particles. This is often induced by attractive van der Waals forces or electric double layers [10]. Alternatively, for an otherwise stable colloidal dispersion in which there is no direct interaction between the colloids, the addition of non-adsorbing polymer can induce percolation caused by an osmotic imbalance in a process termed the depletion effect [11,12].

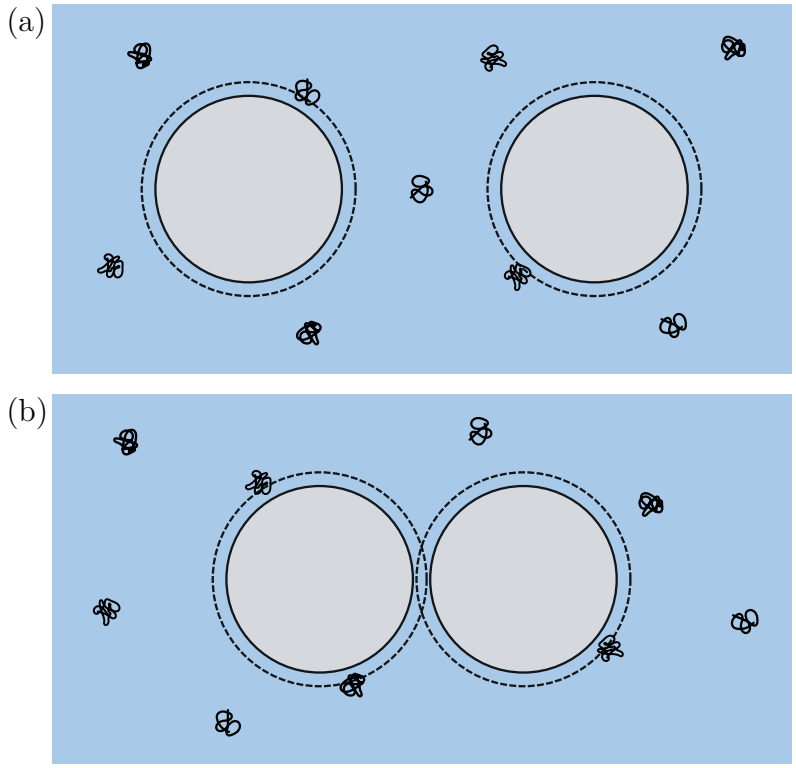

Fig. 7.2: A schematic representation of the depletion effect (a) before and (b) after the depletion of polymers from the region between the two colloids.

In understanding the depletion effect it is important to realise that the centre of a polymer molecule cannot be closer to a colloid than a certain distance, typically equal to the radius of gyration of the polymer molecule due to the high energy requirements associated with configurational distortion. Therefore, each colloid is surrounded by a depletion zone, within which there can be no polymer molecule centres. If two colloids move closer than twice the radius of gyration of the polymer molecule, there exists an overlap of depletion zones and exclusion of polymer molecules. This exclusion of polymer molecules, shown schematically in Fig. 7.2, is responsible for an osmotic imbalance which acts to press the colloids together [13]. The range and depth of this so-called

depletion attraction can be separately tuned by adjusting the molecular weight, *i.e.* the radius of gyration, and concentration of the polymer, respectively.

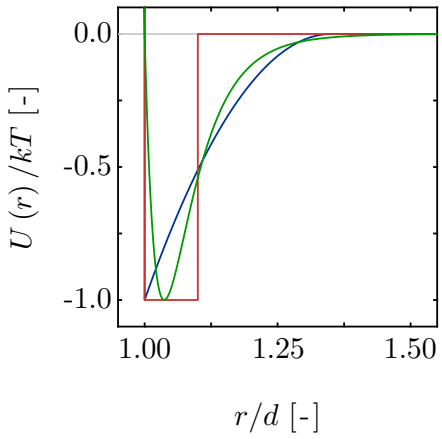

Fig. 7.3: A plot to show the (—) AO, (—) SW, and (—) generalised 2α-α LJ potentials, with $\alpha = 19$, for $b_2 = 0.43$, as determined using Eq. (7.7).

An understanding of the behaviour of colloid-polymer mixtures is challenging due to the difficulty associated with quantification of the depletion attraction with respect to the centre-to-centre separation, as is required for the comparison of experimental and simulated data [14,15]. To this end, theoretical models are often used to assume the shape of the depletion potential and the behaviour of colloid-polymer mixtures. For example, Asakura and Oosawa [12] derived a model to describe the depletion potential of colloids, modelled as hard spheres, in polymer mixtures from first principles. Due to the complexity of the Asakura–Oosawa (AO) model, Bergenholtz *et al.* [16] presented a simplification of the AO model suited to colloid-polymer mixtures with ξ, given by $2R_g/d$ and where R_g and d represent the polymer radius of gyration and the colloid diameter, respectively, of less than 0.1. In this simplified model,

$$U(r) = -\frac{3}{2}\Phi_P^{free} kT \left(\frac{1+\xi}{\xi^3}\right)\left(\frac{r}{d} - 1 - \xi\right)^2 \tag{7.1}$$

for $d < r \leq d(1+\xi)$, where $U(r)$ is the depletion potential as a function of the centre-to-centre separation, r, Φ_P^{free} is the volume fraction of the polymer in the free volume accessible in the mixture, and k and T represent Boltzmann's constant and absolute temperature, respectively. Note that Φ_P^{free} is related to the volume fraction of polymer

in the total volume, Φ_{P}, according to $\Phi_{\mathrm{P}} = \psi\Phi_{\mathrm{P}}^{\mathrm{free}}$, where

$$\psi = (1 - \Phi) \exp\left[-X\iota - Y\iota^2 - Z\iota^3\right], \tag{7.2}$$

with Φ the colloid volume fraction and

$$\iota = \frac{\Phi}{1 - \Phi}, \tag{7.3}$$

$$X = 3\xi + 3\xi^2 + \xi^3, \tag{7.4}$$

$$Y = \frac{9}{2}\xi^2 + 3\xi^3, \tag{7.5}$$

$$Z = 3\xi^3, \tag{7.6}$$

as determined by Lekkerkerker *et al.* [17]. Other models used to describe $U(r)$ include the square-well (SW) and generalised Lennard–Jones (LJ) models [18]. A comparison of the shapes of the AO, SW, and LJ potentials are shown in Fig. 7.3 for completeness. Fortunately, according to the extended law of corresponding states (ELCS), knowledge of the shape of the depletion potential is not required for comparison of experimental and simulated data, with the behaviour of a colloid-polymer mixture dependent only on Φ and the reduced second virial coefficient, b_2, given by

$$b_2 = 1 + 3\int_1^\infty \left(1 - \exp\left[-\frac{U(\tilde{r})}{kT}\right]\right)\tilde{r}^2\,\mathrm{d}\tilde{r}, \tag{7.7}$$

where $\tilde{r} = r/d$ [19]. Due to the radially-symmetric nature of the depletion attraction, the colloids exhibit a tendency to arrange in a locally-dense configuration, particularly as the strength of the depletion attraction is increased. Such behaviour is responsible for the formation of coexisting gas (colloid-poor) and liquid (colloid-rich) phases. The equilibrium phase behaviour of colloid-polymer mixtures will now be discussed. Note that according to ELCS, identical phase behaviour is expected for similar systems with short-range attraction, such as colloidal silica spheres [20] and micelles [21].

The equilibrium phase behaviour of colloid-polymer mixtures is sensitive to both Φ and b_2. Such phase behaviour is simple, particularly when the colloids do not crystallise quickly. Crystallisation, during which a colloidal fluid undergoes a disorder-order transition to a colloidal crystal demonstrating long-range spatial order, can be suppressed by selecting colloids with a sufficiently broad particle size distribution (PSD) [22,23]. The broadness of a PSD is often quantified using polydispersity, defined as the standard deviation of the PSD divided by the mean particle size. For a non-crystallising colloid-polymer mixture, an increase in depletion attraction strength causes the homogeneous colloidal fluid to give way, at a sharp boundary referred to as the binodal, to coexisting gas and liquid phases. The behaviour of the gas and liquid phases depends on the strength of the depletion attraction. At low depletion attraction strength, the randomly arranged colloids in the gas and liquid phases are ergodic; that is, they move throughout the phase volume. However, as the depletion attraction strength increases the liquid phase becomes glassy; although the structure resembles a liquid, motion of the colloids within the structure has been reduced to almost zero and equilibrium will no longer be reached on experimental time scales [24,25]. This sudden arrest is known as a glass transition. A more complete discussion of the glass transition can be found in the journal article of Hunter and Weeks [25].

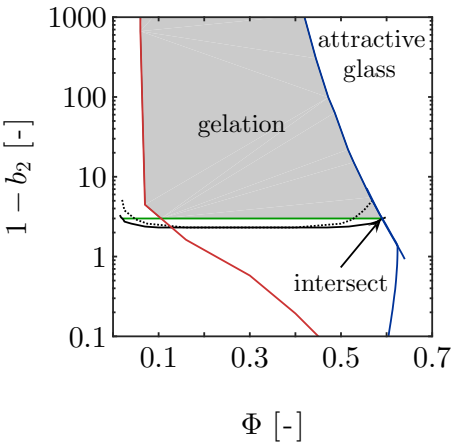

Fig. 7.4: Simulated universal (—) binodal and (·····) spinodal of non-crystallising particles, volume fraction Φ, with short-range attraction quantified by the reduced second virial coefficient, b_2. (—) Glass transition lines calculated from mode coupling theory (MCT) mapped to simulations [26,27] are shown. Percolation is observed in the simulations to the right of the so-called (—) percolation line. A percolated system below the (—) onset tie line was observed to reach equilibrium, whilst a percolated system above the onset tie line was unable to equilibrate.

Many studies suggest that there are at least two distinct classes of colloidal gels [7,8]. The first class of colloidal gels are formed when, during phase separation of a colloidal fluid into coexisting gas and liquid phases through spinodal decomposition, the liquid phase arrests due to a glass transition at high volume fractions [15,28–32]. In contrast, the second class of colloidal gels are equilibrium gels formed through the homogeneous percolation of a colloidal fluid, with homogeneous percolation known to form a space-spanning network without phase separation [33–39]. A mechanistic distinction between these two distinct classes of colloidal gels is not yet completely understood, although recent invention of the colloid-polymer mixtures described above represents an important step forward since these can be formulated to show either kind of gelation [7]. The colloid-polymer mixtures studied in this Chapter belong to the first class; that is, the mixtures gel only through arrested spinodal decomposition. To completely understand arrested spinodal decomposition, an understanding of the binodal and spinodal is required. According to ELCS, the binodals of all short-range attractive particles collapse onto a universal curve in (Φ, b_2)-space, as depicted in Fig. 7.4. Considering Fig. 7.4, a spinodal exists inside of a binodal, within which the homogeneous colloidal fluid is unstable against infinitesimal fluctuations in volume fraction, and phase separates *via* spinodal decomposition into a bicontinuous, space-spanning network when right of the percolation line. This coarsens with time. If the volume fraction of the liquid phase in this coarsening bicontinuous network reaches the attractive glass transition line, the liquid phase then arrests into a gel. Therefore, gelation is expected to occur above the onset tie line, where the binodal intersects the attractive glass boundary. For a more complete introduction to the second class of colloidal gels, so-called equilibrium gels, the interested reader is directed towards the journal article of Ruzicka *et al.* [38].

The two classes of colloidal gels previously introduced behave very differently under gravitational stress [39,40]. Since arrested spinodal gels are non-equilibrium states *en route* to phase separation, these gels can undergo gravitational collapse after a certain latency period [29,32]. Such gravitational gel collapse limits the shelf-life of products; a sedimented product is unsightly and leads to concentration gradients that can have catastrophic consequences, for example in drug formulations. Therefore, whether the gravitational collapse of arrested spinodal gels can be predicted is of both practical importance and fundamental scientific interest. In this Chapter, the ageing and ultimate gravitational collapse of arrested spinodal gels, in which the short-range attraction between the hard-sphere-like colloids is induced *via* the depletion effect, is investigated using a combination of techniques.

Previous workers have used a number of techniques to investigate the gravitational collapse of arrested spinodal gels with short-range attraction. For example, time-lapse video imaging was used by Starrs *et al.* [32] to quantify the height, H, of the interface between the gas and liquid phases as a function of time, t, with $H\left(t\right)$ observed to show three distinct stages; namely latency, collapse, and compaction, as shown in Fig. 7.5. Whilst H decreases linearly with time during sudden collapse, $H\left(t\right)$ during compaction can be estimated using a stretched exponential, as given by

$$\hat{H}\left(t\right) = \frac{H\left(t\right) - H_{\mathrm{rcp}}}{H\left(0\right) - H_{\mathrm{rcp}}} \propto \exp\left[-\left(\frac{t}{T_{\mathrm{str}}}\right)^{\beta}\right], \tag{7.8}$$

where T_{str} and β represent the characteristic time constant and stretching exponent, respectively, and H_{rcp} is the height of the gas-liquid interface at random close packing (RCP). Qualitative, two-dimensional (2D) images obtained by Starrs *et al.* [32] using dark-field imaging showed the formation of vertical channels within the network of the colloidal gel immediately before collapse. Such channels facilitate the flow of dispersion medium upwards and dispersed phase downwards. These results are in agreement with results obtained by Secchi *et al.* [41] using light scattering and novel ghost particle velocimetry. However, experiments performed on arrested spinodal gels with long-range attraction using conventional rheometry and confocal microscopy did not indicate the formation of vertical channels, instead the continuous microscopic restructuring of the space-spanning network was proposed to lead to macroscopic collapse [42].

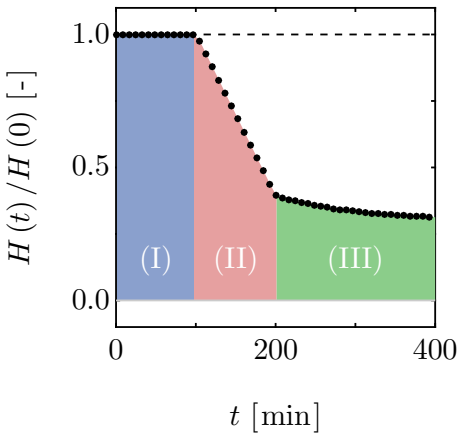

Fig. 7.5: A schematic representation of $H\left(t\right)$, normalised against $H\left(0\right)$, showing the (I) latency period, (II) sudden collapse, and (III) compaction stages.

In particular, the work reported in this Chapter, undertaken in collaboration with the School of Physics and Astronomy at the University of Edinburgh, combines Brownian dynamics (BD) and molecular dynamics (MD) simulations with visual observations and magnetic resonance (MR) experiments. Model colloid-polymer mixtures are prepared, namely poly(methyl methacrylate) (PMMA) colloids dispersed in a *cis*-decalin solvent with polystyrene (PS) polymers and varying Φ and $\Phi_{\mathrm{P}}^{\mathrm{free}}$, for the sampling of a suitable (Φ, b_2)-space range. Visual observations indicate that three distinct gel collapse regimes exist depending on Φ and $\Phi_{\mathrm{P}}^{\mathrm{free}}$. Secchi *et al.* [41] have shown, through work on colloid-polymer mixtures with identical ξ but different d, that these regimes are d-dependent. This contrasts strongly with equilibrium phase behaviour, which depends only on ξ [17]. For this reason, it is suggested in this Chapter that the ageing of these gels may be partly gravity-driven. Furthermore, a comparison between the MR experiments and BD and MD simulations suggests that hydrodynamics may drive sudden collapse. Spatially-resolved measurements of the volume fraction of the dispersion medium obtained during gravitational gel collapse using MR imaging reveal that gravitational gel collapse is initiated by processes at the top of the sample. Note that sample preparation, simulations, and visual observations were performed by collaborators at the University of Edinburgh, whilst MR imaging experiments were performed by the author of this thesis.

7.2 Materials and methods

7.2.1 Simulations

The simulation of interacting Brownian particles using BD simulation is an essential tool for investigating the behaviour of colloidal dispersions. In BD simulations, a finite simulation box containing N particles, of known d and Φ, is followed with time. Specifically, particle displacements are extracted at a fixed time step, Δt, according to a Gaussian distribution, with the mean squared displacement, $\langle \mathbf{R}^2 \rangle$, equal to $6D\Delta t$ for the case of a three-dimensional (3D) simulation, where D is the self-diffusivity of the particles. Note that the fictive velocity, $\mathbf{v}$, of each particle is then calculated from $\mathbf{R}$, where $\mathbf{R} = \mathbf{v}\Delta t$, and the system is evolved between t and $t + \Delta t$ using MD simulation. This process is then repeated until the system reaches equilibrium. By adjusting the range and depth of the interparticle interaction and Φ, (Φ, b_2)-space is traversed whilst testing for the formation of a space-spanning network. The binodal and spinodal can

also be quantified. A brief introduction to MD simulations, and an overview of the BD and MD simulations reported in this Chapter, is now given.

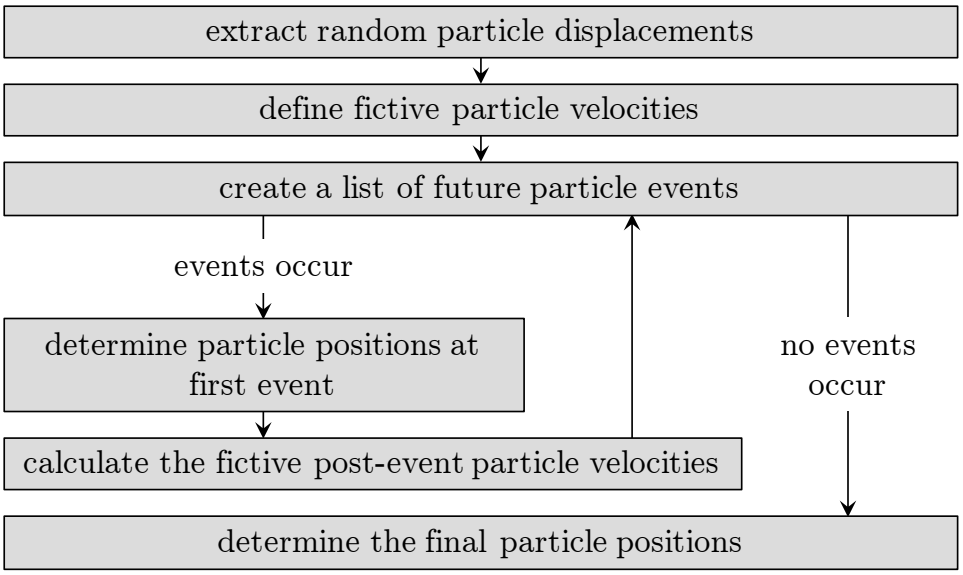

Fig. 7.6: A block diagram outlining the six key stages of ED-BD and MD simulations. This process is repeated and the simulation box evolves, with time, until the system reaches equilibrium. Adapted from Scala *et al.* [43].

There are two distinct approaches to MD simulation. The first approach, initially developed by Alder and Wainwright [44] and summarised in Fig. 7.6, is suitable when the interparticle interaction is described using a step potential. An example of a step potential is the SW potential, given by

$$U(r) = \begin{cases} \infty, & r < d, \\ -\epsilon, & d \leq r \leq d(1+\xi), \\ 0, & r > d(1+\xi), \end{cases} \tag{7.9}$$

where ϵ is the strength of the interaction. The particles move at constant $\mathbf{v}$ during Δt, except when two particles move closer than the range of the interparticle interaction or collide. To account for these events, all future particle interactions and collision times are calculated and sorted. If an event in the list of future events is scheduled to

take place between t and $t + \Delta t$, the system is evolved to the time of the first event; the positions of the particles are updated and the post-event $\mathbf{v}$ are calculated, with the particle collisions assumed to be elastic. The list of future events is then updated and the process repeated until no further events are scheduled to take place between t and $t + \Delta t$. At this point, $\mathbf{R}$ are again extracted as described above, with the entire process repeated until the system reaches equilibrium. The rate at which the system evolves between t and $t + \Delta t$ using this approach is, therefore, governed by the rate at which these events occur. For this approach to remain valid, a Δt must be selected that satisfies [43]

$$\Delta t \ll \frac{\langle r \rangle^2}{4D}, \tag{7.10}$$

where $\langle r \rangle$ is the average centre-to-centre separation, and

$$\Delta t \ll \frac{d^2}{4D}. \tag{7.11}$$

The reduction of Δt to a suitably small value decreases the average number of events occurring between t and $t + \Delta t$ to less than 1, although the number of steps required to reach equilibrium increases. However, the most time consuming stage of an event-driven (ED) MD simulation is determining the next event in the list of future events, which can be optimised using a binary search tree [45]. The second approach to MD simulations is suitable when the interparticle interaction is described using a smooth potential. Such potentials include the AO and LJ potentials. As an SW potential was chosen in these simulations, for which b_2 can be calculated analytically using Eq. (7.7), a detailed discussion of this second approach to MD simulations is beyond the scope of this thesis. For a more detailed discussion, the interested reader directed towards the journal article of Rahman [46]. Note that the simulations do not include hydrodynamic interactions (HI), due to a poor understanding of HI at high Φ and the associated time consuming simulations required, or gravitational effects.

The 3D ED-BD and MD simulations in this Chapter were performed by collaborators at the University of Edinburgh, and ξ was varied from 0.01 to 0.10, across which ELCS was expected to remain (at least) approximately valid [19]. Crystallisation was

prevented in the simulations by using either a 50:50 binary mixture of particles with a size ratio of 0.8 or a mixture with a quasi-continuous PSD of 10% polydispersity. An equilibrated configuration of 4×10^3 to 5×10^4 particles was obtained by performing simulations in the absence of an SW potential, *i.e.* with $\epsilon/kT = 0$. Note that periodic boundary conditions were utilised in all three spatial dimensions such that the effects of a finite simulation box were reduced. To determine the binodal, a single $\Phi = 0.27$ was selected, very close to the best theoretical estimate to date of the critical point at $\Phi = 0.29$ and $1 - b_2 = 2.17$ [47], and $1 - b_2$ was increased. In the presence of an SW potential, the simulation was allowed to reach equilibrium and Φ of the coexisting gas and liquid phases were measured. For the determination of the percolation line, the presence of a space-spanning network was investigated by identifying those particles within the SW of their neighbouring particles. The equilibrium percolation line has previously been obtained using simulations and theory [48,49] and follows the binodal at high $1 - b_2$. However, at a very low Φ it can take a long time for a space-spanning network to develop. If the colloids are severely affected by gravity in this time, a colloidal gel may never form due to sedimentation. Therefore, a dynamic percolation line was calculated as (Φ, b_2)-space was traversed, to the left of which the time it takes to form a space-spanning network is longer than the time taken for a particle to sediment by its radius.

For a given N and simulation box volume, V, the temperature of the system, which is related to the average kinetic energy of the particles, may fluctuate during the ED-BD and MD simulations due to the method used to extract $\mathbf{R}$. This fluctuation in T was prevented using a thermostat in which $\mathbf{R}$ and thus $\mathbf{v}$ were scaled accordingly [50].

7.2.2 Experimental

Materials

Samples were prepared by collaborators at the University of Edinburgh using PMMA colloids, with density, ρ, $1.15\,\mathrm{g\,cm^{-3}}$, sterically-stabilised using poly-12-hydroxystearic acid (PHSA) hairs to minimise any aggregation induced by van der Waals forces [51]. A polydispersity of 7.5% was selected, with $d = 652\,\mathrm{nm}$, too polydisperse to crystallise over experimental time scales. Linear PS was used, with a molecular weight, M_w, of $600\,\mathrm{kg\,mol^{-1}}$ and $R_\mathrm{g} = 21\,\mathrm{nm}$ such that $\xi = 0.06$. The colloids demonstrate near perfect hard-sphere equilibrium phase behaviour when dispersed in *cis*-decalin (Sigma Aldrich,

GB), a so-called theta solvent for PS; that is, there are no polymer-polymer interactions in *cis*-decalin with $1 - b_2$ of the polymers, given by Eq. (7.7), equal to zero [52]. Note that the density of *cis*-decalin, ρ_S, was $0.90\,\mathrm{g\,cm^{-3}}$ such that $\Delta\rho = 0.25\,\mathrm{g\,cm^{-3}}$. The equilibrium phase behaviour, phase separation, and arrest in this, and similar, colloid-polymer mixtures have previously been studied in detail [13]. In particular, they have been shown to form colloidal gels that collapse suddenly after a latency period [29,32]. Both Φ and Φ_P^{free} were varied, with b_2 calculated for a given Φ and Φ_P^{free} using Eqs. (7.1) to (7.7), to investigate a suitable range of (Φ, b_2)-space. The samples were homogenised on a roller mixer; care was taken to prevent air entrapment during this process, with Poon *et al.* [31] suggesting that air bubbles shorten the latency period.

Visual observations

Gravitational gel collapse of the samples was followed by collaborators at the University of Edinburgh using digital imaging until changes could no longer be resolved [32,40]. Samples were homogenised before transfer to $10\,\mathrm{mm} \times 10\,\mathrm{mm} \times 45\,\mathrm{mm}$ glass cuvettes for time-lapse observations at $20.0{\pm}1.0\,^{\circ}\mathrm{C}$ in a temperature-controlled cabinet. In gravitationally collapsing gels and samples phase separating into coexisting gas and liquid phases, as shown in Fig. 7.7, there is a sharp, horizontal interface. The height of this interface was detected using a Sobel edge-finding algorithm and plotted as a function of time, either normalised by $H(0)$ or represented as $\hat{H}$, as defined by Eq. (7.8).

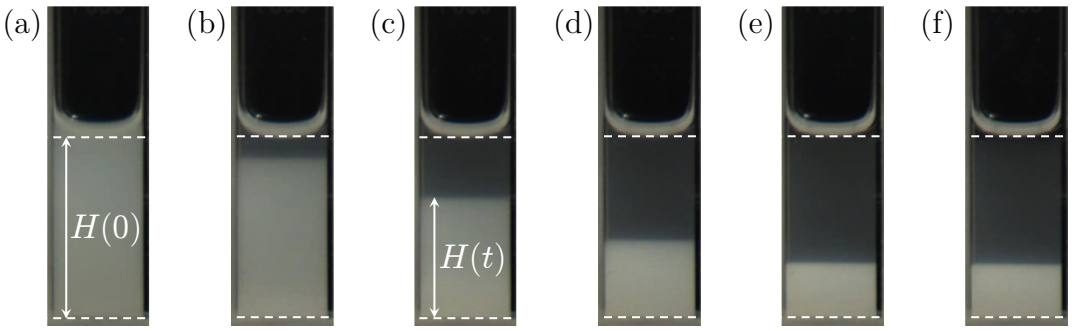

Fig. 7.7: Images of a colloid-polymer mixture phase separating at (a) 0, (b) 5, (c) 10, (d) 15, (e) 50, and (f) 100 min after homogenisation. Initial height, $H(0)$, and time-dependent interface height, $H(t)$, are as defined.

Visual observations performed in a chamber at $20.0{\pm}0.1\,^{\circ}\mathrm{C}$ suggest that the results do not depend on the accuracy of temperature control, with the $H(t)$ behaviour and latency period in the chamber falling within the scatter of the results of experiments

performed in the cabinet. Temperature gradients over the samples were too small to measure and their effect was excluded by repeating experiments with samples placed inside metal blocks.

Magnetic resonance

MR imaging has previously been used to quantify the local volume fraction of non-colloidal suspensions [53]. Here, the use of MR imaging is extended to provide a spatio-temporal measurement of the liquid phase volume fraction of the collapsing colloidal gels. MR imaging experiments were performed using a Bruker DMX300 spectrometer operating with a 7 T vertical-bore superconducting magnet and fitted with a 25 mm inner diameter (i.d.) radiofrequency (r.f.) coil tuned to a frequency of 300 MHz for the ^{1}H resonance. A three-axis gradient system with a maximum gradient strength of 98.7 G cm^{-1} was used for spatial encoding. Homogenised samples were placed in round, flat-bottomed, glass MR tubes of outer diameter (o.d.) 10 mm and i.d. 8.8 mm (Hilgenberg, DE). A polytetrafluoroethylene (PTFE) insert was used to reduce the i.d. of the r.f. coil to 10 mm and ensure optimum (and reproducible) positioning of the sample. Gravitational gel collapse in the glass MR tubes was observed to show the same, qualitative, $H(t)$ behaviour as the square cuvettes used for visual observations, although, particularly for low $1-b_2$, the latency period was observed to be systematically longer in the square cuvettes. In the MR sample environment, the temperature was controlled to 20.0±0.1 °C using gradient system cooling hardware.

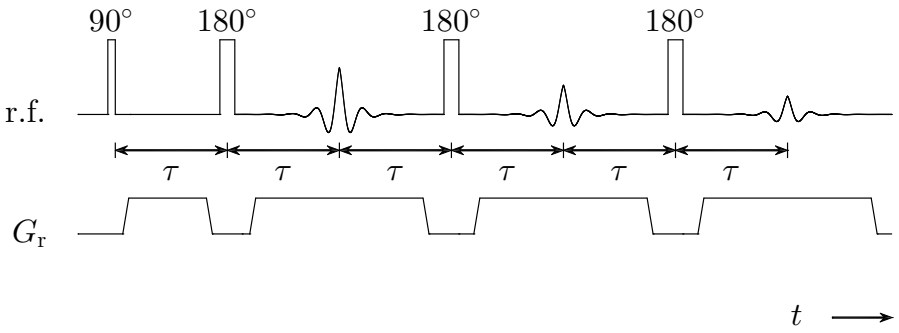

Fig. 7.8: A spatially-resolved T_2-mapping pulse sequence, with N echoes, used to characterise $S(t)$ as a function of sample height, H.

The measurement of the liquid phase, *i.e.* the solvent, volume fraction requires the quantitative measurement of spin density. In Chapter 2, MR imaging was introduced

in the absence of signal relaxation, with the measured signal directly proportional to the spin density. However, in practice, MR imaging is affected by both spin-lattice and spin-spin relaxation, as characterised by the time constants T_1 and T_2, respectively. For example, considering two regions with identical spin densities but different T_2, the signal measured in the region with the shorter T_2 will be lower than in the region with the longer T_2 due to greater signal decay. This is known as T_2-weighting. Likewise, a contrast in the image due to incomplete recovery of the signal as a result of differing T_1 is known as T_1-weighting. Whilst T_1-weighting can be removed by selecting a suitable recycle time, typically equal to 5 times T_1, T_2-weighting can only be removed if T_2 is known. In this Chapter, the signal is measured as a function of sample height and time using the spatially-resolved T_2-mapping pulse sequence shown in Fig. 7.8. If, for a given height, a single T_2 value is expected, then this value may be obtained through the non-linear least squares regression (NLLS) regression of

$$S\left(t\right) = S\left(0\right) \exp\left[-\frac{t}{T_2}\right] \tag{7.12}$$

to the experimentally-acquired signal, $S\left(t\right)$, where $S\left(0\right)$ is directly proportional to the spin density. Note that $S\left(0\right)$ is used in the calculation of volume fraction. However, a distribution of T_2 is here allowed for when calculating $S\left(0\right)$ due to the porous nature of the space-spanning network. The T_2 probability distribution, $p\left(T_2\right)$, was quantified by determining a numerical solution to the Fredholm integral equation of the first kind, as given by

$$\frac{S\left(t\right)}{\left|S\left(0\right)\right|} = \int_{-\infty}^{\infty} k_0\left(T_2, t\right) p\left(T_2\right) \, \mathrm{d}T_2 + e\left(t\right), \tag{7.13}$$

where $k_0\left(T_2, t\right)$ is the model function, or kernel, describing the expected signal for a given T_2 and t, and $e\left(t\right)$ is the random Gaussian noise in the experimental data. This process is often referred to as an inverse Laplace transform. In this work, Eq. (7.13) was solved on the logarithmic scale, such that

$$\frac{S\left(t\right)}{\left|S\left(0\right)\right|} = \int_{-\infty}^{\infty} k_0\left(T_2, t\right) w\left(T_2\right) \, \mathrm{d}\left(\log\left(T_2\right)\right) + e\left(t\right), \tag{7.14}$$

using regularisation, where

$$k_0\left(T_2, t\right) = \exp\left[-\frac{t}{T_2}\right] \tag{7.15}$$

and $w\left(T_2\right)$ is equivalent to $p\left(\log\left(T_2\right)\right)$. Equation (7.14) may be written in a vector-matrix form, such that

$$\mathbf{S} = \mathbf{k}_0\mathbf{w}, \tag{7.16}$$

where $\mathbf{S}$ is the experimentally-acquired data vector, $\mathbf{k}_0$ is a kernel matrix, and $\mathbf{w}$ is the probability vector of T_2 to be determined. A solution, $\hat{\mathbf{w}}$, is sought that minimises the residual sum of the squares, as given by

$$\hat{\mathbf{w}} = \arg\min_{\mathbf{w}\geq 0} \left\|\mathbf{S} - \mathbf{k}_0\mathbf{w}\right\|_2^2, \tag{7.17}$$

where $\left\|...\right\|_2$ is the l_2-norm of the data. However, as Eq. (7.17) is ill-conditioned, an unphysical solution may be obtained. A stable, physical solution may be obtained in the presence of noise if $\hat{\mathbf{w}}$ is constrained to be non-negative, within a specified range of T_2, and smooth. Although a number of regularisation methods exist, as reviewed in the journal article of Mitchell *et al.* [54], a Tikhonov regularisation method was used in this work [55]. This method introduces a penalty function to bias against unphysical solutions, as described by

$$\hat{\mathbf{w}} = \arg\min_{\mathbf{w}\geq 0} \left(\left\|\mathbf{S} - \mathbf{k}_0\mathbf{w}\right\|_2^2 + \alpha\left\|\mathbf{L}\mathbf{w}\right\|_2^2\right), \tag{7.18}$$

where $\left\|\mathbf{S} - \mathbf{k}_0\mathbf{w}\right\|_2^2$ is the residual, indicative of how close $\mathbf{w}$ is to being a true solution, and $\alpha\left\|\mathbf{L}\mathbf{w}\right\|_2^2$ is the penalty function, quantifying the degree of smoothing applied to $\hat{\mathbf{w}}$, with $\mathbf{L}$ an operator representing the choice of smoothness criterion and α the regularisation, or smoothing, parameter [56]. Note that α controls the degree of smoothness imposed on $\hat{\mathbf{w}}$; a large α increases the weighting towards $\left\|\mathbf{L}\mathbf{w}\right\|_2^2$ and a smooth solution, whilst a small α increases the weighting towards $\left\|\mathbf{S} - \mathbf{k}_0\mathbf{w}\right\|_2^2$ and a true solution.

For the quantification of $p(T_2)$ and $S(0)$ as a function of sample height, the second derivative was selected as the smoothness criterion and a fixed $\alpha = 0.1$ was chosen to enable the comparison of experimental datasets; T_2 was limited to 128 values sampled logarithmically between 0.001 and 1. The regularisation was implemented in MATLAB 2012b, operating under Windows 7, using code originally developed by Hollingsworth and Johns [57] for the measurement of droplet size distributions. A field-of-view (FOV) of 22.5 mm was selected, with 256 read points, to provide a spatial resolution of 88 µm, and 128 echoes (N) were utilised with $\tau = 2.23$ ms to sample the signal at 128 values of t linearly spaced between 4.46 ms and 571 ms. A recycle time of 10 s, equal to 6 times T_1 of pure *cis*-decalin (1.7 s), was used to eliminate any T_1-weighting and 8 scans were acquired giving a total acquisition time of 1 min 29 s. Measurements were repeated at 5 min intervals. Note that this technique is sensitive to the number of spatially-resolved data points used, with an increase in spatial resolution resulting in a reduction in the signal-to-noise ratio (SNR). The SNR in each liquid-filled pixel, with 256 data points, was > 1000. Spin density data were acquired over the duration of the gel collapse using this method, and comparison of this data with corresponding data for pure *cis*-decalin enabled the spatially-resolved measurement of the solvent volume fraction, Φ_S.

7.3 Results and discussion

7.3.1 Simulations

The equilibrium phase behaviour of particles with short-range attraction was simulated by collaborators at the University of Edinburgh, using ED-BD and MD, to predict the equilibrium phase and gelation state diagram. Firstly, the binodal was determined by increasing ϵ, and hence $1 - b_2$, for a fixed $\Phi = 0.27$. Shown in Fig. 7.9 are simulation boxes for short-range attractive particles with $1 - b_2$ of (a) 2.11, (b) 2.66, (c) 2.97, and (d) 3.32. For a low $1 - b_2$ that is below the binodal, the system remains single phase. However, the onset of phase separation is observed as $1 - b_2$ is increased above the binodal, giving rise to coexisting gas and liquid phases. The corresponding Φ profiles, showing Φ as a function of position along the z-axis, are included in Fig. 7.10, and it is shown that an increase in $1 - b_2$ from 2.66 to 3.32 causes a decrease in the gas phase Φ from 0.06 to 0.01, whilst the liquid phase Φ increases from 0.47 to 0.55. Measurements of the gas and liquid phase Φ as a function of $1 - b_2$ were then used to determine the binodal shown in Fig. 7.11.

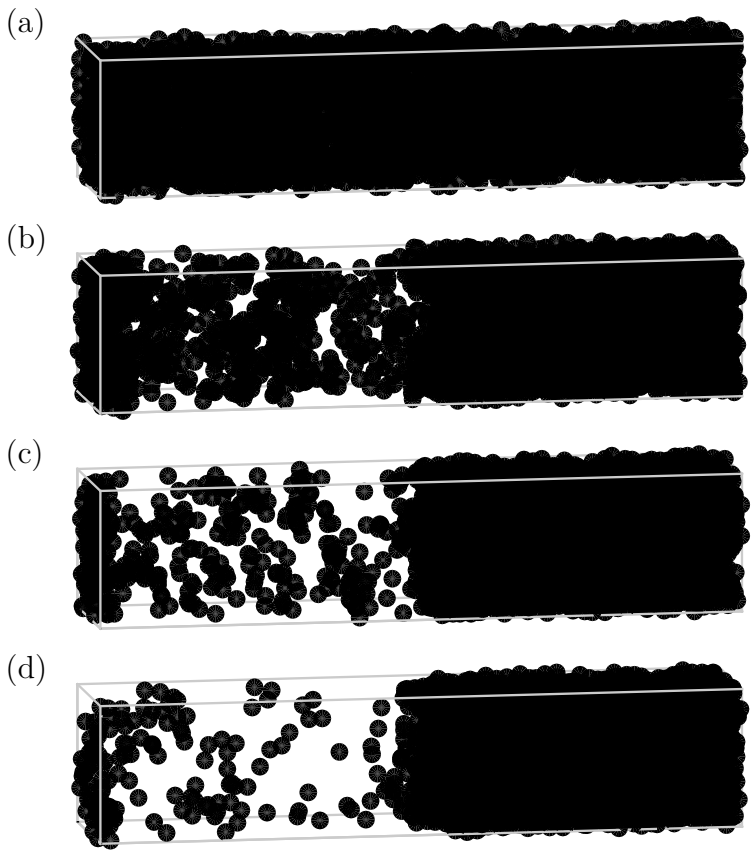

Fig. 7.9: Simulated equilibrium gas-liquid coexistence in simulation boxes containing 4×10^3 attractive particles and obtained using ED-BD and MD, with $1 - b_2$ of (a) 2.11, (b) 2.66, (c) 2.97, and (d) 3.32. In all cases, $\Phi = 0.27$ and $\xi = 0.10$.

Secondly, the spinodal was determined by calculating pressure as a function of Φ using the virial theorem derived by Clausius [58] and given by

$$PV = NkT + \frac{1}{3}\sum_{j=1}^{N} \mathbf{F}_j \cdot \mathbf{r}_j \tag{7.19}$$

for a 3D simulation, where $\mathbf{F}_j$ is the total force acting on the j^{th} particle with position vector $\mathbf{r}_j$. All parameters required by Eq. (7.19) are easily accessible in the simulations. Furthermore, Frenkel and Smit [59] showed Eq. (7.19) to be equivalent to

$$PV = NkT + \frac{1}{3}\sum_{j=2}^{N}\sum_{i=1}^{j-1} \mathbf{F}_{ij} \cdot \mathbf{r}_{ij} \tag{7.20}$$

for pairwise interactions, where $\mathbf{F}_{ij}$ is the force applied on the j^{th} particle by the i^{th} particle and $\mathbf{r}_{ij}$ is the separation. In the spinodal region, the system is unstable either due to a negative pressure or negative isothermal compressibility, W, where

$$W = -\frac{1}{V}\frac{\mathrm{d}V}{\mathrm{d}P}. \tag{7.21}$$

For either case, the system phase separates because many modes of infinitesimal Φ fluctuations grow with time. Note that the area of (Φ, b_2)-space between the binodal and spinodal is stable to such fluctuations, with phase separation instead occurring due to nucleation and growth. The resulting universal binodal and spinodal are observed in Fig. 7.11 to touch at the critical point of $\Phi = 0.29$ and $1 - b_2 = 2.17$.

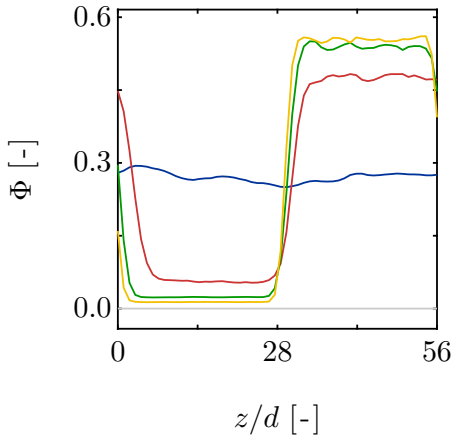

Fig. 7.10: Volume fraction profiles showing coexisting gas and liquid phases, calculated using the data shown in Fig. 7.9, with $1 - b_2$ of (—) 2.11, (—) 2.66, (—) 2.97, and (—) 3.32. In all cases, $\Phi = 0.27$ and $\xi = 0.10$.

To determine the dynamic percolation line, the Φ at which a space-spanning network was first formed in the simulation box as $1 - b_2$ was increased was also estimated. The presence of a space-spanning network was examined every Δt by identifying those particles within the SW of their neighbouring particles. For a low $1 - b_2$ that is below the critical point, the space-spanning network was able to equilibrate. However, at a high $1 - b_2$, above the critical point, the dynamic percolation line shifted to very low Φ and the space-spanning network was unable to equilibrate. The resulting dynamic percolation line is shown in Fig. 7.11.

7.3.2 Experimental

Visual observations

The colloid-polymer mixtures under study were confirmed by collaborators at the University of Edinburgh, using visual observations, to demonstrate the universal binodal expected for short-range attractive particles. All visual observations are reported in (Φ, b_2)-space, where $1-b_2$ for each sample was calculated numerically using the substitution of Eqs. (7.1) to (7.6) into Eq. (7.7). A sample with a sufficiently low $\Phi_{\mathrm{P}}^{\mathrm{free}}$—or, equivalently, a low $1-b_2$—remained single phase for an extended period of time. Over many hours, sedimentation was observed to occur due to the difference in density between the colloids and *cis*-decalin, producing a diffuse interface. However, as $\Phi_{\mathrm{P}}^{\mathrm{free}}$ was increased, a critical $1-b_2$ was reached and a sharp interface developed quickly and evolved, as shown in Fig. 7.7, to coexisting gas and liquid phases. The universal binodal simulated in Section 7.3.1 successfully passes between samples demonstrating single phase and phase separating behaviour, suggesting that the results of the ED-BD and MD simulations reported in Section 7.3.1 are, at least up to $\Phi = 0.40$, in agreement to within the experimental uncertainty of the visual observations. These results are summarised in Fig. 7.11.

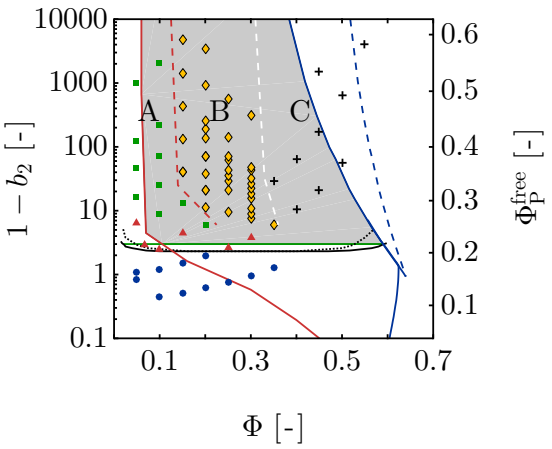

Fig. 7.11: The equilibrium phase and gelation state diagram, shown for mixtures of non-crystallising colloids and non-adsorbing polymers demonstrating (●) single phase and (▲) gas-liquid coexistence behaviour. Samples demonstrating regime (■) A, (◆) B, and (+) C gravitational gel collapse are also indicated. The predicted gelation region in the absence gravity is shaded. In the presence of gravity, the actual (- - -) glass transition and (- - -) percolation lines are expected to lie to the right of those determined using (—) MCT mapped to simulations and (—) simulations, respectively, as indicated.

Immediately across the gas-liquid phase boundary, samples phase separate into co-existing gas and liquid phases. Such behaviour ceases as $1 - b_2$ is increased above 5.00, with samples instead forming colloidal gels which subsequently undergo gravitational collapse. Interestingly, three different types of gravitational gel collapse are observed depending on Φ; namely regimes A, B, and C. These are indicated on Fig. 7.11, with the final Φ measured, Φ^{final}, also observed to be regime-dependent. To demonstrate the differences between these three regimes of gravitational gel collapse, Fig. 7.12 depicts $\hat{H}(t)$ for three different samples, where (a) $\Phi = 0.20$ and $1 - b_2 = 6.08$, (c) $\Phi = 0.20$ and $1 - b_2 = 255$, and (e) $\Phi = 0.30$ and $1 - b_2 = 7.68$. The low Φ regime, known as regime A, is characterised by a latency period of less than 3 min. An example of regime A gravitational collapse is shown in Fig. 7.12(a), showing an initial linear dependence of $\hat{H}$ with time during the sudden collapse followed by a stretched exponential, as given by Eq. (7.8), during compaction. The results of a NLLS regression to the experimental dataset are observed to be in agreement to within the uncertainty of the experimental data. Gravitational gel collapse of samples in regime A was seen to cease before Φ^{final} reached the glass transition line; Φ^{final} is dependent on Φ with samples with a higher Φ reaching a higher Φ^{final}, approaching the glass transition line. In the intermediate Φ regime, known as regime B, the colloidal gel is stable within a latency period of greater than 3 min. At the onset of gravitational gel collapse, as demonstrated in Fig. 7.12(c), $\hat{H}$ again demonstrates a linear dependence with time during sudden collapse followed by a stretched exponential at compaction. Unlike regime A gravitational collapse, however, Fig. 7.12(d) indicates that the compaction of samples in regime B stops abruptly at a well defined $\Phi^{\text{final}} = 0.55$. Such an abrupt stop suggests the presence of underlying physical phenomena, perhaps the formation of a quasi-crystalline space-spanning network. Samples in the high Φ regime, known as regime C, have long latency periods but do not undergo sudden collapse. Instead, the gravitational gel collapse of samples in regime C is shown in Fig. 7.12(e) to be described using only a stretched exponential. The samples in regime C had still not collapsed completely, as shown in Fig. 7.12(f), but all had reached $\Phi^{\text{final}} > 0.55$ and are likely to approach Φ^{rcp} of 0.64. Therefore, only regimes B and C demonstrate measurable latency periods; samples in these regimes are transient gels. This required Φ^{rcp} in Eq. (7.8) to be replaced with Φ^{final}.

In Fig. 7.11, the observed gelation region appears to be shifted with respect to that region obtained using ED-BD and MD simulations. There exists a clear discrepancy between the onset tie line expected at $1 - b_2 = 3.00$, as determined in the simulations, and that observed experimentally. This discrepancy can be explained by the presence

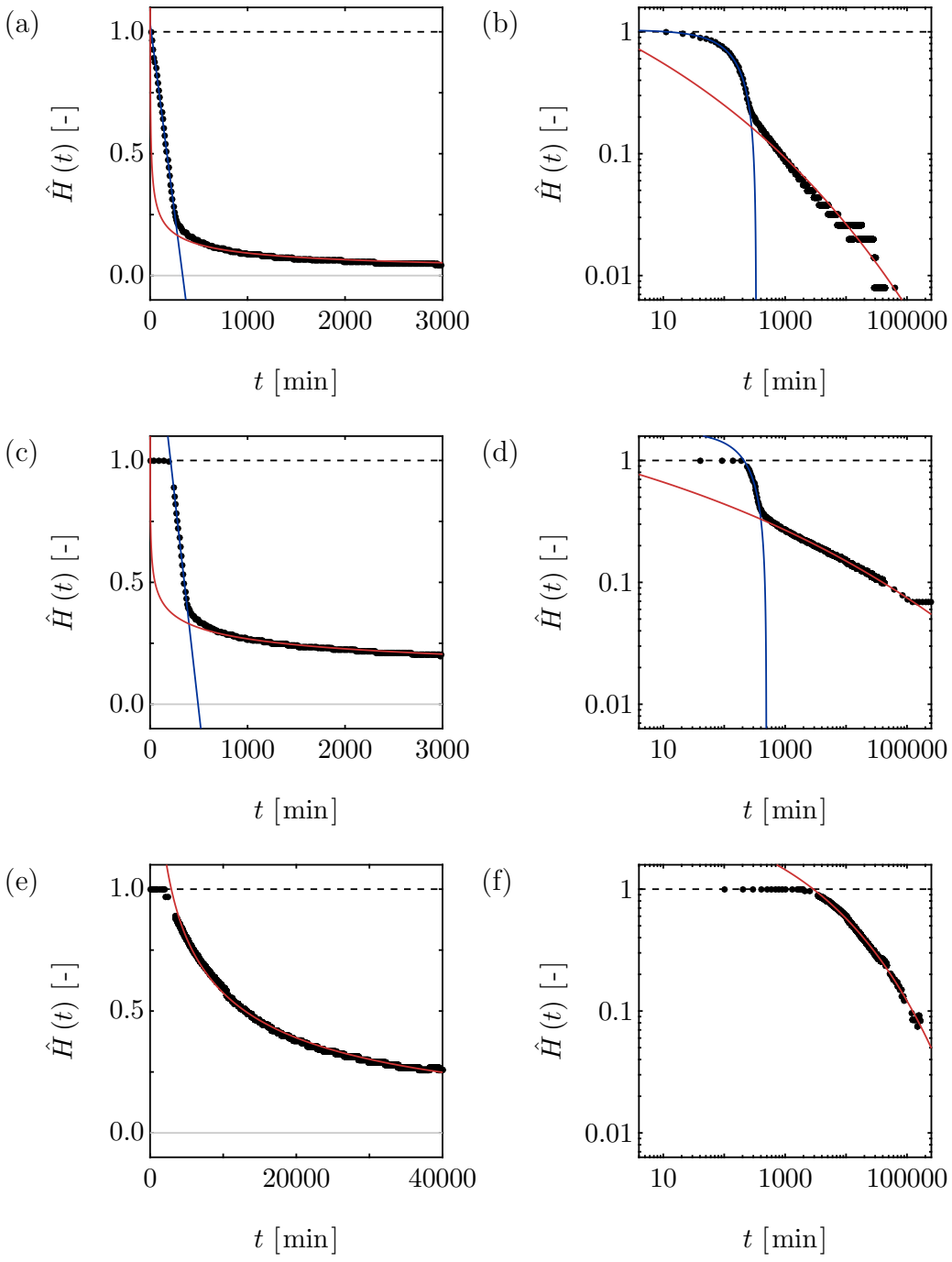

Fig. 7.12: The evolution of $\hat{H}$, defined by Eq. (7.8), with time, shown for three samples with (a) $\Phi = 0.20$ and $1 - b_2 = 6.08$, (c) $\Phi = 0.20$ and $1 - b_2 = 255$, and (e) $\Phi = 0.30$ and $1 - b_2 = 7.68$. In all cases, $\xi = 0.06$. Also shown is the (b,d,f) same data on a logarithmic scale and the (—) straight line and (—) stretched exponential regression data. The samples demonstrate regime A, B, and C gravitational gel collapse, respectively.

of gravity, which is omitted from simulations but would, experimentally, prevent the formation of a space-spanning network of particles immediately above the onset tie line due to an inability to support their own weight. Furthermore, the samples are observed to demonstrate gravitational gel collapse when to the right of the glass transition line, calculated according to MCT mapped to simulations [26,27]. Note that an introduction to MCT is beyond the scope of this thesis, with the interested reader directed towards the textbook of Götze [60]. It is possible that the true glass transition line lies to the right of that predicted by mapping MCT to simulations, with all samples investigated lying to the left of the true line. A shift in the glass transition line to the right would also cause the intersect highlighted in Fig. 7.4, *i.e.* the onset tie line, to shift to a higher $1 - b_2$. However, a detailed understanding of the difference between regime C colloidal gels and attractive glasses is not yet completely understood, with the proposed changes only suggestions at this time.

In the absence of gravity, transient gelation is expected immediately to the right of the percolation line. However, the experimental onset of transient gelation is observed only in regimes B and C, with regime A colloidal gels demonstrating an absence of a latency period. This is also likely due to gravity; a latency period requires a colloidal gel with τ_0 that is at least equal to the gravitational stress exerted by a single colloid, τ_G, to prevent sedimentation. Note that τ_G is given by

$$\tau_\mathrm{G} = \frac{2}{3}\Delta\rho a_\mathrm{G} d, \tag{7.22}$$

where a_G represents the acceleration due to gravity. Using Eq. (7.22), $\tau_\mathrm{G} = 1.1\,\mathrm{mPa}$ for the colloid-polymer mixtures under study in this Chapter. Kobelev and Schweizer [61] suggest that τ_0 of a depletion-induced colloidal gel is equal to

$$\tau_0 = u\left(\left(\frac{\Phi_\mathrm{P}^\mathrm{free}}{\Phi_\mathrm{P}^\mathrm{glass}}\right)^\varepsilon - 1\right)\left(\left(\frac{\Phi}{\Phi^\mathrm{perc}}\right)^\chi - 1\right), \tag{7.23}$$

where Φ^perc is the minimum Φ required for percolation at a given $\Phi_\mathrm{P}^\mathrm{free}$ or $1 - b_2$, $\Phi_\mathrm{P}^\mathrm{glass}$ is the Φ_P at the glass transition line for a particular Φ, u is the scale setting constant of the samples under study, and ε and χ take average values of 2.5 and 4.0, respectively. Using conventional rheometry to quantify τ_0, u was determined as 120 µPa.

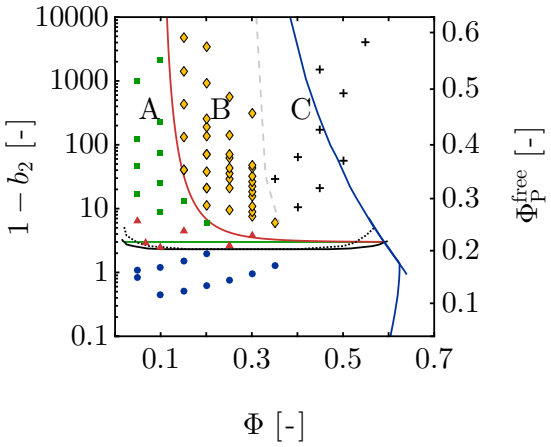

Fig. 7.13: An equilibrium phase and gelation state diagram shown for mixtures of non-crystallising colloids and non-adsorbing polymers. Lines and markers are as defined in Fig. 7.11, with exception to the (—) gravity-shifted percolation line.

According to Eq. (7.23), $\tau_0 = 0\,\text{mPa}$ at the onset tie line, where the glass transition line intersects the binodal, and at the percolation line. Further, equating Eqs. (7.22) and (7.23) gives the following expression,

$$\Phi_P^{free} = \Phi_P^{glass} \left(\frac{\frac{\tau_0}{u} + \left(\frac{\Phi}{\Phi^{perc}}\right)^{\chi} - 1}{\left(\frac{\Phi}{\Phi^{perc}}\right)^{\chi} - 1} \right)^{\frac{1}{\varepsilon}}, \tag{7.24}$$

which may be used to predict the effect of gravity on percolation. Figure 7.13 shows the percolation line, predicted by Eq. (7.24), in the presence of gravity with $\Phi_P^{glass} = 0.22$ and a maximum $\Phi^{perc} = 0.10$. It is observed that the gravity-shifted percolation line passes between regime A and B gravitational gel collapse. A shift in the onset tie line to a higher Φ_P^{glass}, or equivalently a higher $1 - b_2$, due to a shift in the glass transition line to a higher Φ would further explain these experimental observations. Furthermore, Eq. (7.24) implies that the three distinct gel collapse regimes are d-dependent, agreeing with previous work by Secchi *et al.* [41].

Magnetic resonance

Using the methodology outlined in Section 7.2.2, $p\left(\log\left(T_2\right)\right)$ was obtained as a function of H to measure $S\left(0\right)$ and quantify Φ_S. Figure 7.14 shows $p\left(\log\left(T_2\right)\right)$ obtained during phase separation of a colloid-polymer mixture with $\Phi = 0.15$ and $1 - b_2 = 4.41$. This is

below the experimentally-observed critical $1 - b_2 = 5.00$ needed for gelation. At 1.5 min after homogenisation, $p(\log(T_2))$ is shown in Fig. 7.14(a) to be independent of H, as expected, with a mean T_2 of 49 ms and standard deviation of 14 ms. However, the gas and liquid phases that form during phase separation are characterised by different T_2. In Fig. 7.14(b), acquired 101.5 min after homogenisation, a transition in $p(\log(T_2))$ is seen at the gas-liquid interface; above the interface, the gas phase is characterised by a T_2 of 55±19 ms, whilst below the interface, the T_2 of the liquid phase is 47±14 ms. This interface propagates down the sample, as shown in Figs. 7.14(c) and (d) at 201.5 and 401.5 min, respectively. During phase separation, T_2 of the gas phase remains constant at 55±19 ms, whilst T_2 of the liquid phase decreases to 40±14 ms. This was repeated for a subset of samples exhibiting regime A, B, and C gravitational gel collapse.

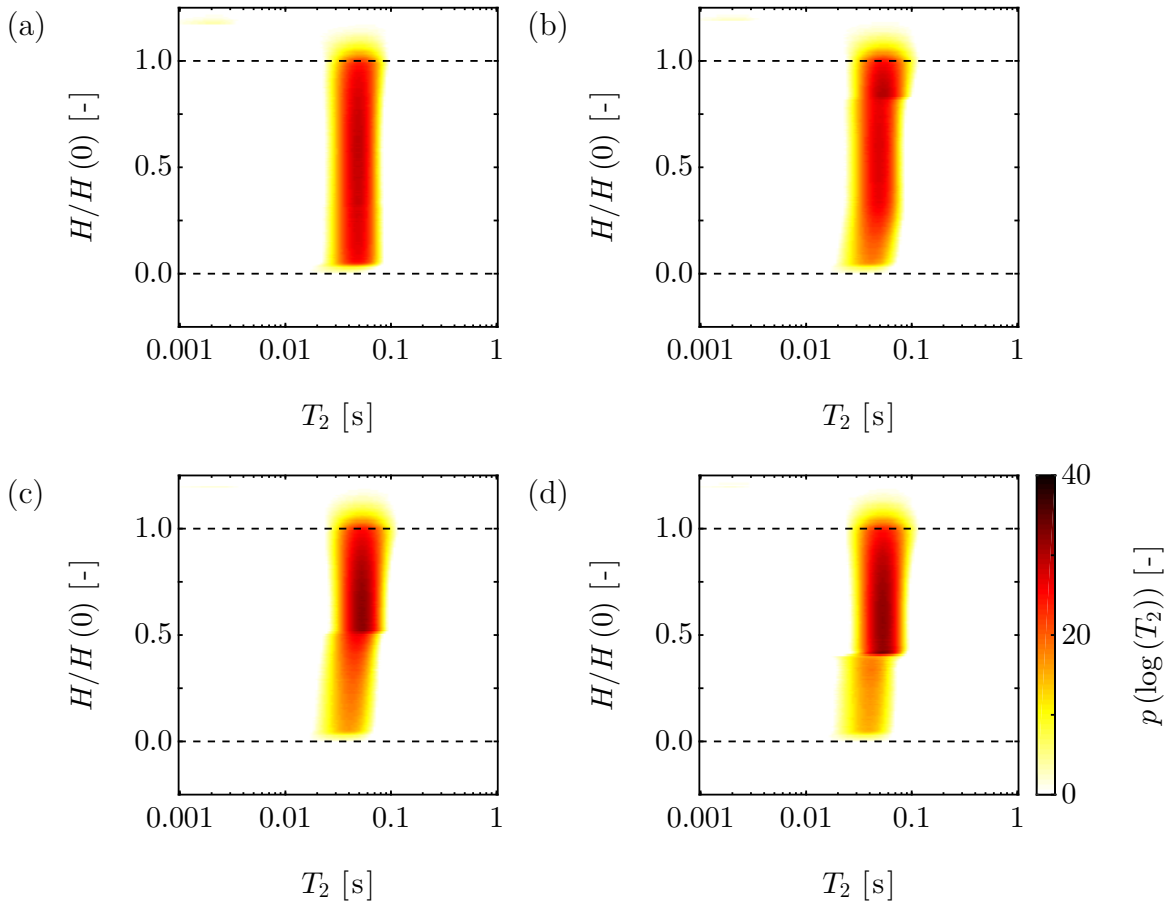

Fig. 7.14: Spatially-resolved $p(\log(T_2))$ data shown as a function of H, acquired (a) 1.5, (b) 101.5, (c) 201.5, and (d) 401.5 min after homogenisation for a non-gelling sample with $\Phi = 0.15$, $1 - b_2 = 4.41$, and where $\xi = 0.06$.

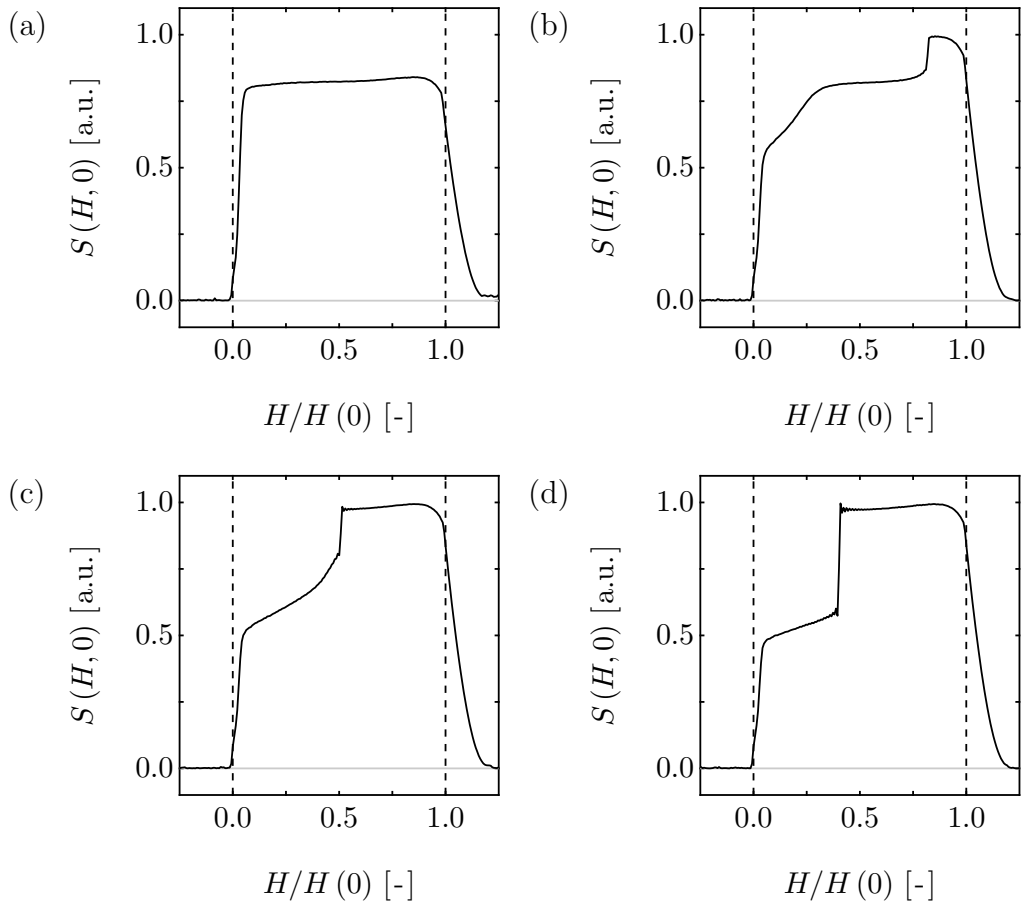

Fig. 7.15: Signal intensity profiles for a non-gelling sample acquired (a) 1.5, (b) 101.5, (c) 201.5, and (d) 401.5 min after homogenisation, with $\Phi = 0.15$, $1 - b_2 = 4.41$, and where $\xi = 0.06$.

Using the spatially-resolved $p(\log(T_2))$ data, volume-averaged T_2 distributions can be quantified by the integration of such data with respect to $H/H(0)$. The changes in the spatially-resolved $p(\log(T_2))$ discussed previously are observed to cause a broadening of the volume-averaged T_2 distributions with time. Alternatively, the integration of spatially-resolved $p(\log(T_2))$ with respect to T_2 can be used to quantify $S(0)$ as a function of H, here denoted $S(H,0)$. Figure 7.15 shows $S(H,0)$ data obtained (a) 1.5, (b) 101.5, (c) 201.5, (d) 401.5 min after homogenisation. As expected, $S(H,0)$ is observed to be almost independent of H immediately after homogenisation, except within the meniscus and at the bottom of the sample due to a reduction in sample volume, with a mean $S(0)$ of 0.82. Note that inhomogeneities in the B_0 and B_1 magnetic fields, introduced in Chapter 2, are responsible for the local fluctuations in $S(H,0)$ observed in Fig. 7.15(a). However, $S(H,0)$ becomes dependent on H during phase separation.

In Fig. 7.15(b), acquired 101.5 min after homogenisation, a sharp transition in $S(H,0)$ is seen at the gas-liquid interface; above the gas-liquid interface, the mean $S(0)$ of the gas phase is 0.99, whilst below the interface, the mean $S(0)$ of the liquid phase is 0.66. This interface propagates down through the sample, as shown in Figs. 7.15(c) and (d) after 201.5 and 401.5 min, respectively. During phase separation, the mean gas phase $S(0)$ increases from 0.82 to 0.99, whilst the mean $S(0)$ of the liquid phase decreases from 0.82 to 0.53. Fortunately, as the inhomogeneities in B_0 and B_1 are not expected to change significantly over the experimental time scale, a comparison of the $S(H,0)$ dataset with identical data obtained for pure *cis*-decalin was used to enable Φ_S of the sample under study to be determined as a function of both H and t, denoted $\Phi_S(H,t)$. In the subsequent discussion of the MR imaging results, $\Phi_S(H,t)$ has been converted to $\Phi(H,t)$, with $\Phi(H,t) + \Phi_S(H,t) = 1$.

Figure 7.16 shows $\Phi(H,t)$ for three samples, where (a) $\Phi = 0.15$ and $1 - b_2 = 13.2$, (c) $\Phi = 0.15$ and $1 - b_2 = 4810$, and (e) $\Phi = 0.30$ and $1 - b_2 = 7.68$. Figures 7.16(b), (d), and (f) show the corresponding $H(t)$ profiles extracted from $\Phi(H,t)$ using a Sobel edge-finding algorithm. As expected, these samples show regime A, B, and C gravitational gel collapse, respectively, with only regime B and C colloidal gels demonstrating a latency period. Although regime C gravitational gel collapse is partly understood as poroelastic compression, and accurately modelled by Eq. (7.8), delayed collapse of samples in regime B remains poorly understood. From $\Phi(H,t)$ data shown in Fig. 7.16(a), regime A gravitational gel collapse can be observed to proceed homogeneously; a high Φ region propagates upwards though the sample, whilst a very low Φ region propagates downwards. In contrast, regime B gravitational gel collapse proceeds heterogeneously in Fig. 7.16(c) and can be divided into three distinct regions; namely a foot, leg, and column. The high Φ foot is formed at the bottom of the sample due to slow compaction during the latency period. During sudden collapse, shown to occur after 561.5±5.0 min, the intermediate Φ leg is formed. The low Φ column describes the remaining space-spanning network, which ceases to exist after 751.5±5.0 min, *i.e.* during compaction. These regions are consistent with previous work [41]. Interestingly, detachment of the gel from the meniscus, where it is initially held due to the depletion effect, is observed to cause the formation of a high Φ region at the very top of the sample. This is shown in greater detail in Fig. 7.17 over a time scale of 450–600 min, where rapid sedimentation of the high Φ region after 541.5±5.0 min appears to initiate sudden collapse. The velocity, v, of this rapid sedimentation is $8.1 \pm 0.1\,\mu m\,s^{-1}$, over an order of magnitude greater than during sudden collapse, $500 \pm 11\,nm\,s^{-1}$, and over two orders of magnitude

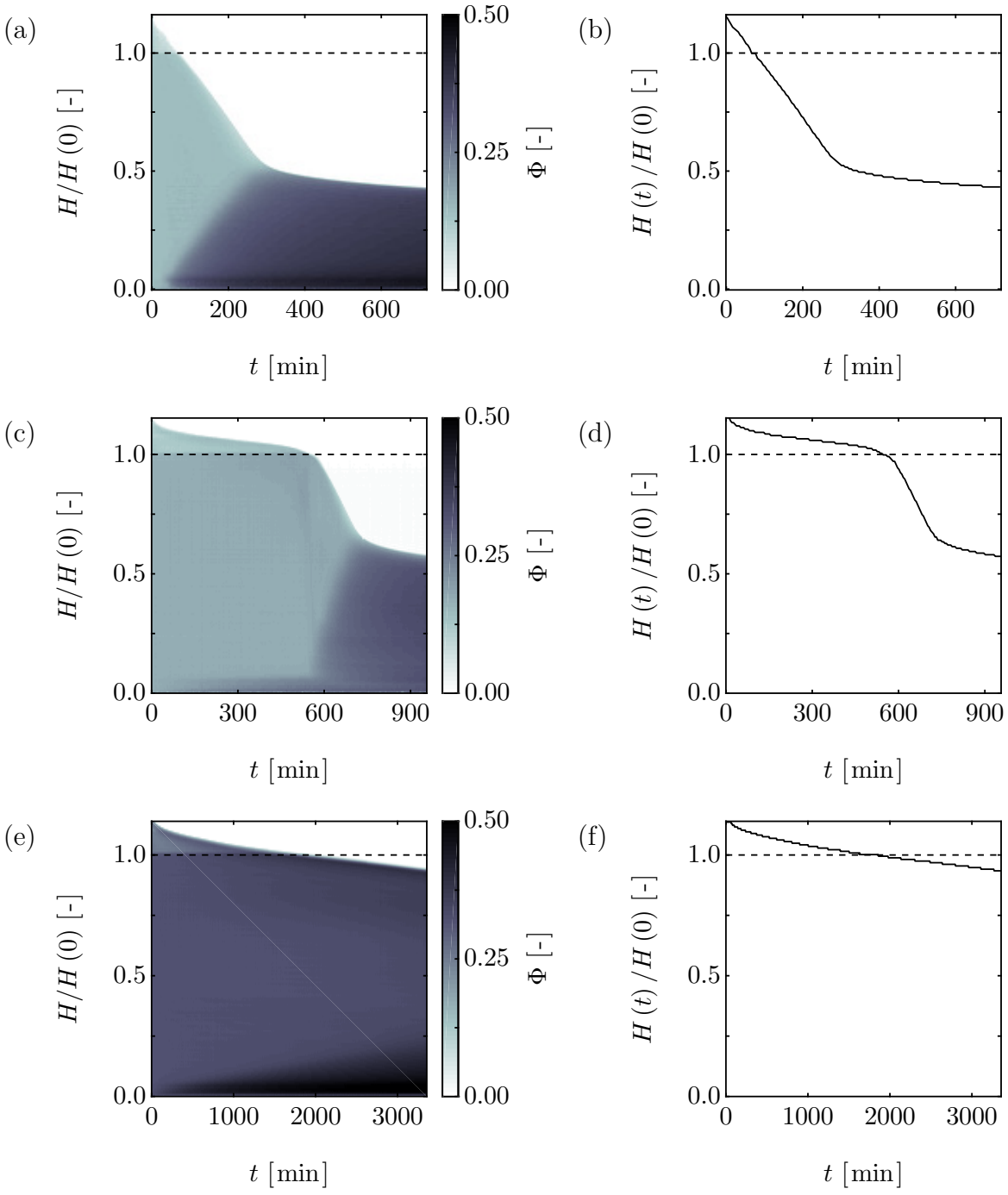

Fig. 7.16: The evolution of $\Phi\,(H)$ with time, shown for three samples with (a) $\Phi = 0.15$ and $1 - b_2 = 13.2$, (c) $\Phi = 0.15$ and $1 - b_2 = 4810$, and (e) $\Phi = 0.30$ and $1 - b_2 = 7.68$. In all cases, $\xi = 0.06$. Also depicted are the (b,d,f) corresponding $H\,(t)$ profiles extracted from $\Phi\,(H, t)$ using a Sobel edge-finding algorithm. The samples are expected to demonstrate regime A, B, and C gravitational gel collapse, respectively.

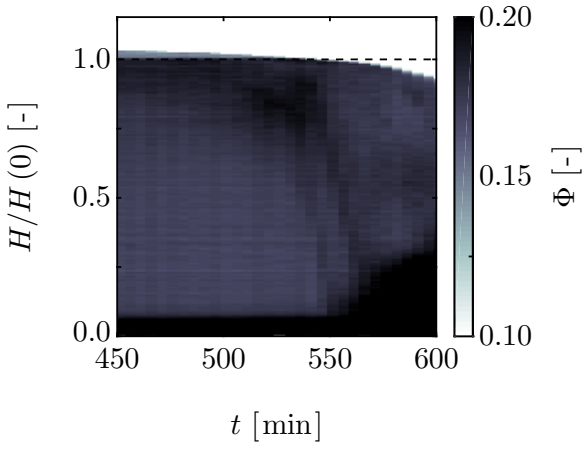

Fig. 7.17: A subset of $\Phi(H,t)$ data shown over a time scale of 450–600 min for a sample with $\Phi = 0.15$ and $1 - b_2 = 4810$. Rapid sedimentation of the high Φ region at the top of the sample occurs at 541.5±5.0 min, followed by sudden collapse at 561.5±5.0 min.

greater than during the latency period, $33 \pm 2\,\mathrm{nm\,s^{-1}}$, where the uncertainties are equal to the 95% confidence intervals in the individual fits. Although the formation of a high Φ region at the top of the sample has previously been observed [32,41], visualisation of the rapid sedimentation of this region is a new discovery and represents a significant step towards understanding the origins of gravitational gel collapse.

The origin of the high Φ region at the top of the sample is unclear, with Starrs *et al.* [32] suggesting that this region consists of a cluster of broken up and compacted gel debris. Since the settling of a cluster is only possible if the net force due to gravity exceeds the upwards force due to the yield stress of the colloidal gel, a theoretical size of cluster required to overcome τ_0 can be determined. Note that τ_0 was measured as 20 mPa by collaborators at the University of Edinburgh using conventional rheometry. The gravitational stress exerted by a cluster of N colloids, τ_N, with $\Phi = \Phi^{\mathrm{rcp}}$ can be determined using

$$\tau_N = \frac{2}{3}\Delta\rho a_{\mathrm{G}} d_N \Phi^{\mathrm{rcp}}, \tag{7.25}$$

where d_N is the theoretical diameter of the cluster. Therefore, equating the force due to gravity with that due to the yield stress of the colloidal gel suggests that a cluster of $d_N = 38\,\mu\mathrm{m}$ is capable of overcoming τ_0 and yielding the space-spanning network.

In addition, the force due to gravity, F_{G}, was calculated using

$$F_{\mathrm{G}} = \frac{1}{6}\pi\Delta\rho a_{\mathrm{G}} d_N^3 \Phi^{\mathrm{rcp}} \tag{7.26}$$

and, in the first instance, equated with the drag force, denoted F_{D} and given by Stokes' law [62] as

$$F_{\mathrm{D}} = 3\pi\eta d_N v, \tag{7.27}$$

where η is the shear viscosity, to provide an estimate of d_N based on v. This was used to suggest that the size of the experimental cluster was 30 ± 1 µm for an experimentally-observed $v = 8.1\pm0.1\,\mu\mathrm{m\,s^{-1}}$ and $\eta = 10\,\mathrm{mPa\,s}$. Therefore, the cluster size estimated using Eqs. (7.26) and (7.27) is comparable to that estimated based on τ_0. The absence of cluster formation in ED-BD and MD simulations, and in regime A gravitational gel collapse, suggests that these processes may be gravity- and HI-driven. A more detailed investigation into cluster formation is performed in Chapter 8 using 2D MR imaging, with Φ also quantified as a function of radial position.

The formation of a high Φ region at the top of the sample during regime C gravitational gel collapse is also observed in Fig. 7.16(e). However, unlike regime B gravitational gel collapse, this does not sediment rapidly. Such behaviour can be explained by the dependence of τ_0 on Φ, with an increase in Φ from 0.15 to 0.30 causing an almost twenty-fold increase in τ_0 according to Eq. (7.23), with

$$\chi = 2.45 + 15.4\Phi^{\mathrm{perc}} \tag{7.28}$$

for ξ in the range 0.03 to 0.09 [61]. The space-spanning network can, therefore, support the weight of these clusters. Furthermore, this suggests that the type of gravitational gel collapse demonstrated is d-dependent, due to the sensitivity of u to d. It is, perhaps, for this reason that Secchi *et al.* [41] did not observe regime B gravitational gel collapse for their samples with $d = 90\,\mathrm{nm}$. Further work is required to confirm the dependence of regime B gravitational gel collapse on both Φ and d.

7.4 Conclusions

In this Chapter, gravitational collapse of depletion-induced colloidal gels was investigated. Event-driven BD and MD simulations were performed to study the equilibrium phase behaviour of particles with short-range attraction. It was observed that samples with a $1-b_2$ of less than 3.00 remained single phase, whilst those samples with a $1-b_2$ of greater than 3.00 phase separated into coexisting gas and liquid phases. These data were used to characterise the binodal and dynamic percolation lines. The spinodal was also determined.

An experimental study on a model colloid-polymer mixture, consisting of PMMA colloids dispersed in a *cis*-decalin solvent with PS, was performed using visual observations. By adjusting Φ and $\Phi_{\mathrm{P}}^{\mathrm{free}}$ it was possible to traverse (Φ, b_2)-space. A comparison of the experimental state diagram with that obtained using simulations suggested the phase behaviour to be gravity-dependent. Interestingly, measurement of the height of the sharp interface between the coexisting gas and liquid phases indicated the presence of three distinct types of gravitational gel collapse; regime A demonstrating sudden collapse followed by slow compaction, regime B showing the same behaviour as regime A but with an initial latency period, and regime C showing only a latency period and slow compaction. Using MR imaging, a quantitative measurement of Φ as a function of H and t was performed for each regime. It has been shown, for the very first time, that a cluster of colloids, with high Φ, is formed at the very top of samples in regimes B and C as the gel detaches from the meniscus during the latency period. For a sample in regime B, this cluster is observed to fall though the sample rapidly, initiating the sudden collapse of the colloidal gel. This cluster falls at $8.1\pm0.1\,\mu\mathrm{m\,s^{-1}}$, corresponding to a theoretical cluster size of $30\pm1\,\mu\mathrm{m}$ at $\Phi = \Phi^{\mathrm{rcp}}$. The absence of sudden collapse in regime C gels can be explained by τ_0, which increases rapidly as Φ is increased.

Identifying the origins of such clusters will constitute a next significant step towards obtaining a full understanding of these colloidal gels and their ultimate gravitational collapse. To this end, Chapter 8 describes the use of 2D MR imaging to probe cluster formation as a function of radial position. Furthermore, collapse dynamics are investigated to provide insight into both the rapid sedimentation of such clusters and the ensuing sudden collapse. Despite this, further work is required to reinforce understanding, including investigating samples with varying ξ and d.

7.5 References

[1] Perrin, J., *Les atomes*, Constable, London, GB, 1923.

[2] Einstein, A., *Investigations on the Theory of the Brownian Movement*, Dover Publications, New York, US, 1926.

[3] Frenkel, D., 2002, Playing tricks with designer "atoms". *Science*, **296**, 65–67.

[4] Vermant, J. and Solomon, M.J., 2005, Flow-induced structure in colloidal suspensions. *J. Phys. Condens. Matter*, **17**, R187–R216.

[5] Mezzenga, R. and Fischer, P., 2013, The self-assembly, aggregation and phase transitions of food protein systems in one, two and three dimensions. *Rep. Prog. Phys.*, **76**, 046601.

[6] Conrad, J.C., Ferreira, S.R., Yoshikawa, J., Shepherd, R.F., Ahn, B.Y. and Lewis, J.A., 2011, Designing colloidal suspensions for directed materials assembly. *Curr. Opin. Colloid Interface Sci.*, **16**, 71–79.

[7] Helgeson, M.E., Gao, Y., Moran, S.E., Lee, J., Godfrin, M., Tripathi, A., Bose, A. and Doyle, P.S., 2014, Homogeneous percolation versus arrested phase separation in attractively-driven nanoemulsion colloidal gels. *Soft Matter*, **10**, 3122–3133.

[8] Zaccarelli, E., 2007, Colloidal gels: equilibrium and non-equilibrium routes. *J. Phys. Condens. Matter*, **19**, 323101.

[9] Corezzi, S., Palmieri, L., Kenny, J.M. and Fioretto, D., 2005, Clustering, glass transition and gelation in a reactive fluid. *J. Phys. Condens. Matter*, **17**, S3557–S3563.

[10] Verwey, E.J.W. and Overbeek, J.T.G., *Theory of the stability of lyophobic colloids: The interaction of sol particles having an electric double layer*, Elsevier, New York, US, 1948.

[11] Asakura, S. and Oosawa, F., 1954, On interaction between two bodies immersed in a solution of macromolecules. *J. Chem. Phys.*, **22**, 1255–1256.

[12] Asakura, S. and Oosawa, F., 1958, Interaction between particles suspended in solutions of macromolecules. *J. Polm. Sci*, **33**, 183–192.

[13] Poon, W.C.K., 2002, The physics of a model colloid-polymer mixture. *J. Phys. Condens. Matter*, **14**, R859–R880.

[14] Zaccarelli, E., Lu, P.J., Ciulla, F., Weitz, D.A. and Sciortino, F., 2008, Gelation as arrested phase separation in short-ranged attractive colloid-polymer mixtures. *J. Phys. Condens. Matter*, **20**, 294242.

[15] Lu, P.J., Zaccarelli, E., Ciulla, F., Schofield, A.B., Sciortino, F. and Weitz, D.A., 2008, Gelation of particles with short-range attraction. *Nature*, **453**, 499–503.

[16] Bergenholtz, J., Poon, W.C.K. and Fuchs, M., 2003, Gelation in model colloid-polymer mixtures. *Langmuir*, **19**, 4493–4503.

[17] Lekkerkerker, H.N.W., Poon, W.C.K., Pusey, P.N., Stroobants, A. and Warren, P.B., 1992, Phase behaviour of colloid + polymer mixtures. *Europhys. Lett.*, **20**, 559–564.

[18] Vliegenthart, G.A., Lodge, J.F.M. and Lekkerkerker, H.N.W., 1999, Strong weak and metastable liquids structure and dynamical aspects of the liquid state. *Physica A*, **263**, 378–388.

[19] Noro, M.G. and Frenkel, D., 2000, Extended corresponding-states behavior for particles with variable range attractions. *J. Chem. Phys.*, **113**, 2941–2944.

[20] Sztucki, M., Narayanan, T., Belina, G., Pignon, F. and Hoekstra, H., 2006, Kinetic arrest and glass-glass transition in short-ranged attractive colloids. *Phys. Rev. E*, **74**, 051504.

[21] Laflèche, F., Durand, D. and Nicolai, T., 2003, Association of adhesive spheres formed by hydrophobically end-capped PEO. 1. Influence of the presence of single end-capped PEO. *Macromolecules*, **36**, 1331–1340.

[22] Pusey, P.N. and Megen, W. van, 1986, Phase behaviour of concentrated suspensions of nearly hard colloidal spheres. *Nature*, **320**, 340–342.

[23] Pusey, P.N., 1987, The effect of polydispersity on the crystallization of hard spherical colloids. *J. Phys. Fr.*, **48**, 709–712.

[24] Pham, K.N., Puertas, A.M., Bergenholtz, J., Egelhaaf, S.U., Moussaïd, A., Pusey, P.N., Schofield, A.B., Cates, M.E., Fuchs, M. and Poon, W.C.K., 2002, Multiple glassy states in a simple model system. *Science*, **296**, 104–106.

[25] Hunter, G.L. and Weeks, E.R., 2012, The physics of the colloidal glass transition. *Rep. Prog. Phys.*, **75**, 066501.

[26] Sciortino, F., Tartaglia, P. and Zaccarelli, E., 2003, Evidence of a higher-order singularity in dense short-ranged attractive colloids. *Phys. Rev. Lett.*, **91**, 268301.

[27] Zaccarelli, E. and Poon, W.C.K., 2009, Colloidal glasses and gels: the interplay of bonding and caging. *Proc. Natl. Acad. Sci.*, **106**, 15203–15208.

[28] Carpineti, M. and Giglio, M., 1992, Spinodal-type dynamics in fractal aggregation of colloidal clusters. *Phys. Rev. Lett.*, **68**, 3327–3330.

[29] Poon, W.C.K., Pirie, A.D. and Pusey, P.N., 1995, Gelation in colloid-polymer mixtures. *Faraday Discuss.*, **101**, 65–76.

[30] Verhaegh, N.A.M., Asnaghi, D., Lekkerkerker, H.N.W., Giglio, M. and Cipelletti, L., 1997, Transient gelation by spinodal decomposition in colloid-polymer mixtures. *Physica A*, **242**, 104–118.

[31] Poon, W.C.K., Starrs, L., Meeker, S.P., Moussaïd, A., Evans, R.M.L., Pusey, P.N. and Robins, M.M., 1999, Delayed sedimentation of transient gels in colloid-polymer mixtures: dark-field observation, rheology and dynamic light scattering studies. *Faraday Discuss.*, **112**, 143–154.

[32] Starrs, L., Poon, W.C.K., Hibberd, D.J. and Robins, M.M., 2002, Collapse of transient gels in colloid-polymer mixtures. *J. Phys. Condens. Matter*, **14**, 2485–2505.

[33] Kruif, C.G. de and Miltenburg, J.C. van, 1990, Phase transitions in sterically stabilized silica colloids studied by adiabatic calorimetry. *J. Chem. Phys.*, **93**, 6865–6869.

[34] Grant, M.C. and Russel, W.B., 1993, Volume-fraction dependence of elastic moduli and transition temperature for colloidal silica gels. *Phys. Rev. E*, **47**, 2606–2614.

[35] Verduin, H. and Dhont, J.K.G., 1995, Phase-diagram of a model adhesive hard-sphere dispersion. *J. Colloid Interf. Sci.*, **172**, 425–437.

[36] Saika-Voivod, I., Zaccarelli, E., Sciortino, F., Buldyrev, S.V. and Tartaglia, P., 2004, Effect of bond lifetime on the dynamics of a short-range attractive colloidal system. *Phys. Rev. E*, **70**, 041401.

[37] Eberle, A.P.R., Wagner, N.J. and Castañeda-Priego, R., 2011, Dynamical arrest transition in nanoparticle dispersions with short-range interactions. *Phys. Rev. Lett.*, **106**, 105704.

[38] Ruzicka, B., Zaccarelli, E., Zulian, L., Sztucki, M., Moussaïd, A., Narayanan, T. and Sciortino, F., 2011, Observation of empty liquids and equilibrium gels in a colloidal clay. *Nat. Mater.*, **10**, 56–60.

[39] Kim, J.M., Fang, J., Eberle, A.P.R., Castañeda-Priego, R. and Wagner, N.J., 2013, Gel transition in adhesive hard-sphere colloidal dispersions: the role of gravitational effects. *Phys. Rev. Lett.*, **110**, 208302.

[40] Buscall, R., Choudhury, T.H., Faers, M.A., Goodwin, J.W., Luckham, P.A. and Partridge, S.J., 2009, Towards rationalising collapse times for the delayed sedimentation of weakly-aggregated colloidal gels. *Soft Matter*, **5**, 1345–1349.

[41] Secchi, E., Buzzaccaro, S. and Piazza, R., 2014, Time-evolution scenarios for short-range depletion gels subjected to the gravitational stress. *Soft Matter*, **10**, 5296–5310.

[42] Bartlett, P., Teece, L.J. and Faers, M.A., 2012, Sudden collapse of a colloidal gel. *Phys. Rev. E*, **85**, 021404.

[43] Scala, A., Voigtmann, T. and De Michele, C., 2007, Event-driven Brownian dynamics for hard spheres. *J. Chem. Phys.*, **126**, 134109.

[44] Alder, B.J. and Wainwright, T.E., 1959, Studies in molecular dynamics. I. General method. *J. Chem. Phys.*, **31**, 459.

[45] Rapaport, D.C., 1980, The event scheduling problem in molecular dynamic simulation. *J. Comput. Phys.*, **34**, 184–201.

[46] Rahman, A., 1964, Correlations in the motion of atoms in liquid argon. *Phys. Rev.*, **136**, A405–A411.

[47] Largo, J., Miller, M.A. and Sciortino, F., 2008, The vanishing limit of the square-well fluid: the adhesive hard-sphere model as a reference system. *J. Chem. Phys.*, **128**, 134513.

[48] Miller, M.A. and Frenkel, D., 2004, Phase diagram of the adhesive hard sphere fluid. *J. Chem. Phys.*, **121**, 535–545.

[49] Fantoni, R., Gazzillo, D. and Giacometti, A., 2005, Stability boundaries, percolation threshold, and two-phase coexistence for polydisperse fluids of adhesive colloidal particles. *J. Chem. Phys.*, **122**, 034901.

[50] Berendsen, H.J.C., Postma, J.P.M., Gunsteren, W.F. van, DiNola, A. and Haak, J.R., 1984, Molecular dynamics with coupling to an external bath. *J. Chem. Phys.*, **81**, 3684–3690.

[51] Napper, D.H., 1977, Steric stabilization. *J. Colloid Interf. Sci.*, **58**, 390–407.

[52] Poon, W.C.K., *Colloidal Suspensions*, Oxford University Press, New York, US, 2015.

[53] Ovarlez, G., Bertrand, F. and Rodts, S., 2006, Local determination of the constitutive law of a dense suspension of non-colloidal particles through MRI. *J. Rheol.*, **50**, 1–32.

[54] Mitchell, J., Chandrasekera, T.C. and Gladden, L.F., 2012, Numerical estimation of relaxation and diffusion distributions in two dimensions. *Prog. Nucl. Magn. Reson. Spectrosc.*, **62**, 34–50.

[55] Tikhonov, A.N. and Arsenin, V.Y., *Solutions of Ill-posed Problems*, V. H. Winston & Sons, Washington, US, 1977.

[56] Mitchell, J., Chandrasekera, T.C., Holland, D.J., Gladden, L.F. and Fordham, E.J., 2013, Magnetic resonance imaging in laboratory petrophysical core analysis. *Phys. Rep.*, **526**, 165–225.

[57] Hollingsworth, K.G. and Johns, M.L., 2003, Measurement of emulsion droplet sizes using PFG NMR and regularization methods. *J. Colloid Interf. Sci.*, **258**, 383–389.

[58] Clausius, R.J.E., 1870, XVI. On a mechanical theorem applicable to heat. *Philosophical Magazine Series 4*, **40**, 122–127.

[59] Frenkel, D. and Smit, B., *Understanding Molecular Simulation: From Algorithms to Applications*, Academic Press, London, GB, 2001.

[60] Götze, W., *Aspects of structural glass transitions*, North Holland, Amsterdam, 1991, pp. 287–503.

[61] Kobelev, V. and Schweizer, K.S., 2005, Nonlinear elasticity and yielding of depletion gels. *J. Chem. Phys.*, **123**, 164902.

[62] Stokes, G.G., *Mathematical and Physical Papers*, Cambridge University Press, Cambridge, GB, 1880.

Chapter 8

On the stability of colloidal gels using MR

Many industrial products are colloidal dispersions where the dispersed phase is denser than the dispersion medium. The sedimentation of a colloidal product over a shelf-life of months to years is typically prevented by formulating the product as a colloidal gel; a space-spanning network of attractive particles with a yield stress high enough to support the weight of the particle network but low enough to be overcome in use to give flowability. However, colloidal gels are known to undergo gravitational collapse after a latency period, again limiting the shelf-life of products. The mechanism of gravitational gel collapse remains poorly understood, with a more detailed understanding being of both fundamental interest and practical importance.

In Chapter 7, a combination of magnetic resonance (MR) imaging, visual observations, and event-driven Brownian dynamics (ED-BD) and molecular dynamics (MD) simulations were used to study gravitational gel collapse. Using one-dimensional (1D) measurements of colloid volume fraction, Φ, obtained using MR imaging as a function of sample height, it was seen that a high Φ region forms at the top of the sample and initiates sudden collapse. This work is extended in this Chapter by using two-dimensional (2D) MR imaging on a range of model colloid-polymer mixtures. Collapse dynamics, *i.e.* the duration of the latency period and rates of sudden collapse, are compared by measuring the height of the gas-liquid interface as a function of time. As an extension to work described in Chapter 7, the spatially-resolved Φ data show the formation of a high Φ region at the top of the sample, adjacent to the wall, during the latency period. Only small changes are observed at the centre of the sample until sudden collapse.

8.1 Introduction

Colloidal gels are formed when colloids aggregate into a space-spanning, percolating network. Although this process may be induced by attractive van der Waals forces or electric double layers [1], this Chapter is concerned only with colloidal gels in which the short-range interparticle attraction is induced by non-adsorbing polymers *via* the depletion effect.

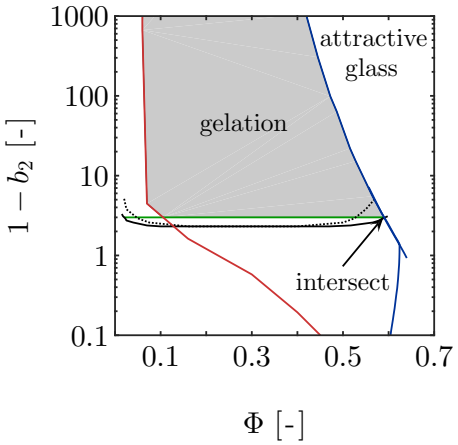

Fig. 8.1: Simulated universal (—) binodal and (·····) spinodal of non-crystallising particles, of volume fraction Φ, with short-range attraction quantified by the reduced second virial coefficient, b_2. The (—) glass transition lines calculated from mode coupling theory (MCT) mapped to simulations [2,3] are shown. Percolation is observed in the simulations to the right of the so-called (—) percolation line. A percolated system below the (—) onset tie line was observed to reach equilibrium, however, a percolated system above the onset tie line was unable to equilibrate.

The equilibrium phase behaviour of colloid-polymer mixtures is simple, particularly when the colloids do not crystallise quickly. An increase in depletion attraction strength causes the homogeneous colloidal fluid to phase separate at the binodal to coexisting gas (colloid-poor) and liquid (colloid-rich) phases. According to the extended law of corresponding states (ELCS), the binodals of all short-range attractive particles collapse onto a universal curve in (Φ, b_2)-space, as depicted in Fig. 8.1, where Φ is the colloid volume fraction and b_2 is the reduced second virial coefficient, as given by

$$b_2 = 1 + 3\int_1^\infty \left(1 - \exp\left[-\frac{U(\tilde{r})}{kT}\right]\right)\tilde{r}^2\,\mathrm{d}\tilde{r}, \tag{8.1}$$

with $U(\tilde{r})$ the depletion potential as a function of $\tilde{r}$, equal to the ratio of the centre-to-centre separation, r, and colloid diameter, d, and where k and T represent Boltzmann's constant and absolute temperature, respectively [4]. Although a number of models may be used, $U(\tilde{r})$ is here described using the simplified Asakura–Oosawa (AO) model [5] given by

$$U(\tilde{r}) = -\frac{3}{2}\Phi_{\mathrm{P}}^{\mathrm{free}} kT \left(\frac{1+\xi}{\xi^3}\right)\left(\frac{r}{d} - 1 - \xi\right)^2 \tag{8.2}$$

for $d < r \leq d(1+\xi)$, where $\Phi_{\mathrm{P}}^{\mathrm{free}}$ is the volume fraction of polymer in the free volume accessible in the mixture and ξ is given by $2R_{\mathrm{g}}/d$, with R_{g} equal to the polymer radius of gyration. Note that $\Phi_{\mathrm{P}}^{\mathrm{free}}$ is related to the volume fraction of polymer in the total volume, Φ_{P}, according to $\Phi_{\mathrm{P}} = \psi\Phi_{\mathrm{P}}^{\mathrm{free}}$, where

$$\psi = (1-\Phi)\exp\left[-X\iota - Y\iota^2 - Z\iota^3\right], \tag{8.3}$$

with

$$\iota = \frac{\Phi}{1-\Phi}, \tag{8.4}$$

$$X = 3\xi + 3\xi^2 + \xi^3, \tag{8.5}$$

$$Y = \frac{9}{2}\xi^2 + 3\xi^3, \tag{8.6}$$

$$Z = 3\xi^3, \tag{8.7}$$

as determined by Lekkerkerker *et al.* [6]. Considering Fig. 8.1, a spinodal exists within the binodal; a homogeneous colloidal fluid phase in the spinodal and to the right of the percolation line will phase separate *via* spinodal decomposition into a bicontinuous, space-spanning network that coarsens with time. If Φ of the liquid phase reaches the glass transition line then the liquid phase arrests into a gel. A second class of colloidal gels, known as equilibrium gels, also exist in which the space-spanning network forms

without phase separating. Equilibrium gels are briefly introduced in Chapter 7, with the interested reader directed towards the journal article of Ruzicka *et al.* [7] for a more complete introduction. The interested reader is also directed towards Chapter 7 for discussion of the event-driven (ED) Brownian dynamics (BD) and molecular dynamics (MD) simulations used for the determination of the binodal, spinodal, and percolation lines shown in Fig. 8.1.

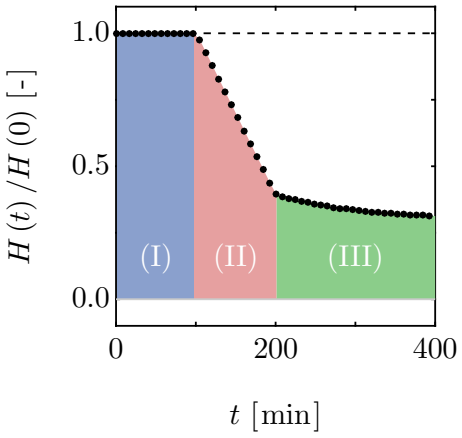

Fig. 8.2: A schematic representation of $H(t)$, normalised against $H(0)$, showing the (I) latency period, (II) sudden collapse, and (III) compaction stages.

Since arrested spinodal gels are non-equilibrium states *en route* to phase separation, these gels are known to demonstrate gravitational collapse after a latency period [8,9]. This gravitational gel collapse is typically monitored by measuring the height, H, of the sharp interface that develops as the sample phase separates into coexisting gas and liquid phases with time, t. Typically, $H(t)$ demonstrates three distinct stages; latency, sudden collapse, and compaction, as shown in Fig. 8.2, with $H(t)$ decreasing linearly during sudden collapse and according to a stretched exponential during compaction, as given by

$$\hat{H}(t) = \frac{H(t) - H_{\mathrm{rcp}}}{H(0) - H_{\mathrm{rcp}}} \propto \exp\left[-\left(\frac{t}{T_{\mathrm{str}}}\right)^{\beta}\right], \tag{8.8}$$

where T_{str} and β represent the characteristic time constant and stretching exponent, respectively, and H_{rcp} is the height at a random close packing (RCP) Φ of 0.64 [10].

Gravitational gel collapse limits the shelf-life of products, with a sedimented product both unsightly and responsible for concentration gradients that can have significant consequences, for example in drug formulations. Therefore, whether the gravitational collapse of arrested spinodal gels can be predicted is of both practical importance and fundamental scientific interest. Although the origins and mechanisms of gravitational gel collapse remain unclear, one popular hypothesis is that the sensitivity of physical gelation to thermal fluctuations provides an opportunity for the rearrangement of the space-spanning network over experimental time scales. Such rearrangements may include a coarsening of the gel with time [11] and/or localised micro-collapses [12], with these resulting in macroscopic structural changes and ultimate gravitational collapse. Confocal microscopy has provided clear experimental evidence of local rearrangements in transient gels [13], leading workers to consider how structural changes might facilitate the sudden gravitational collapse of colloidal gels. For example, Poon *et al.* [14] observed the formation of vertical channels within the network using dark-field imaging and suggested that coarsening of the space-spanning network with time is responsible for an increase in the permeability that facilitates the flow of solvent upwards through the sample and colloids downwards. This flow behaviour would encourage further rearrangements until the network is unable to support its own weight. Similar experiments performed using light scattering and novel ghost particle velocimetry also showed the formation of vertical channels [15].

In Chapter 7, one-dimensional (1D) magnetic resonance (MR) imaging was used to observe the formation of a high Φ region, or dense cluster, at the top of a transient gel during the latency period. Sudden collapse was only observed when the space-spanning network was unable to support the weight of this dense cluster, which subsequently sedimented rapidly. The rapid sedimentation of this cluster may result in the vertical channels described above, although the origins of such clusters remain unclear. The work reported in Chapter 7 is here extended using two-dimensional (2D) MR imaging to provide a spatially-resolved measurement of Φ. The gravitational collapse of model colloid-polymer mixtures, comprising of poly(methyl methacrylate) (PMMA) colloids dispersed in a *cis*-decalin solvent with polystyrene (PS) polymers, is studied and three distinct types of gel collapse are observed through measurement of $H(t)$. Furthermore, the characterisation of Φ with time suggests that the clusters responsible for delayed sudden collapse are formed at the wall of the sample, with no considerable changes in either Φ or H at the centre of the sample during the latency period. A more complete introduction to depletion-induced colloid-polymer mixtures is given in Chapter 7.

8.2 Materials and methods

8.2.1 Materials and experimental set-up

Samples were prepared using PMMA colloids, with a density of $1.15\,\mathrm{g\,cm^{-3}}$, sterically-stabilised using a layer of poly-12-hydroxystearic acid (PHSA) to minimise aggregation due to van der Waals forces [16]. A range of (Φ, b_2)-space was sampled by adjusting Φ and d of the PMMA colloids and $\Phi_{\mathrm{P}}^{\mathrm{free}}$, molecular weight, M_{w}, and R_{g} of the added PS. Note that the polydispersity was 7.5%, too polydisperse to crystallise over experimental time scales. The samples under study, prepared by collaborators at the University of Edinburgh, are outlined in Table 8.1 with b_2 calculated using Eqs. (8.1) to (8.7).

Table 8.1: Properties of the colloid-polymer mixtures under study.

d [µm]	R_{g} [nm]	ξ [-]	M_{w} [$\mathrm{kg\,mol^{-1}}$]	Φ [-]	$\Phi_{\mathrm{P}}^{\mathrm{free}}$ [-]	$1 - b_2$ [-]
0.652	21	0.06	600	0.15	0.24	4.41
0.652	21	0.06	600	0.15	0.35	13.2
0.652	21	0.06	600	0.15	0.59	4810
0.652	21	0.06	600	0.30	0.27	7.68
0.652	21	0.06	600	0.30	0.32	26.1
0.652	21	0.06	600	0.30	0.46	311
2.20	46	0.04	2500	0.30	0.00	0
2.20	46	0.04	2500	0.30	0.45	70 800

The colloids studied in this work demonstrate near perfect hard-sphere equilibrium phase behaviour when dispersed in *cis*-decalin (Sigma Aldrich, GB), a theta solvent for PS with a density of $0.90\,\mathrm{g\,cm^{-3}}$, such that $\Delta\rho = 0.25\,\mathrm{g\,cm^{-3}}$. The equilibrium phase behaviour, phase separation, and arrest of these model colloid-polymer mixtures was previously studied in Chapter 7. In particular, it was shown that they formed colloidal gels that collapsed suddenly after a latency period. For the experiments reported in this Chapter, approximately 10 mL of sample was placed in a round, flat-bottomed, glass MR tube of outer diameter (o.d.) 10 mm and inner diameter (i.d.) 8.8 mm (Hilgenberg, DE). The samples were homogenised before transfer to the superconducting magnet for MR imaging studies; care was taken to prevent air entrapment during this process, since previous work by Poon *et al.* [14] has indicated that air bubbles can shorten the latency period. Note that the Φ reported in Table 8.1 are accurate to ±3.0%.

8.2.2 Magnetic resonance

All MR experiments were performed using a Bruker DMX300 spectrometer operating with a 7 T vertical-bore superconducting magnet and fitted with a 25 mm i.d. radiofrequency (r.f.) coil tuned to a frequency of 300 MHz for the ^{1}H resonance. A three-axis gradient system with a maximum gradient strength of 98.7 G cm^{-1} was used for spatial encoding. An insert, constructed using polytetrafluoroethylene (PTFE), was used to reduce the i.d. of the r.f. coil to 10 mm and thus ensure the optimum and reproducible positioning of the sample. The temperature of the sample environment was controlled to 20.0±0.1 °C using gradient system cooling hardware.

Data were acquired using a slice selective, spin echo imaging pulse sequence with 64 read points and 32 phase increments. A field-of-view (FOV) of 22.5 mm was selected in the read direction and 11.25 mm in the phase direction to provide a spatial resolution of 352 µm × 352 µm. The signal-to-noise ratio (SNR) in the 2D intensity images was 100 for a slice thickness of 2 mm. A total of 4 signal averages were acquired with a recycle time of 1.6 s, equal to the T_1 of pure *cis*-decalin (1.7 s), to provide an acquisition time of 3 min 30 s. Measurements were repeated at regular intervals of 5 min for the duration of gravitational gel collapse, with the timings reported in this Chapter equal to the total duration at the end of the previous acquisition. Note that during processing in MATLAB 2012b, operating under Windows 7, the data were zero-filled to 512 × 256 before Fourier transformation. This process increased the apparent spatial resolution to 44 µm × 44 µm. For the spatio-temporally resolved quantification of Φ, the 2D intensity images acquired during gravitational gel collapse were compared with corresponding data for pure *cis*-decalin. Although T_1- and T_2-weighting is present in the 2D intensity images, the results shown in Chapter 7 suggest that the error in determining Φ using such images is $< 2.4\%$ for an echo time, 2τ, of 2.8 ms and with T_2 in the range 40–60 ms. This was determined according to

$$S\left(2\tau\right) = S\left(0\right)\exp\left[-\frac{2\tau}{T_2}\right], \tag{8.9}$$

where $S\left(2\tau\right)$ is the signal measured at a time 2τ and with $S\left(0\right)$ a measure of the spin density, or concentration. The spatially-resolved Φ data reported in this Chapter are, therefore, accurate to ±2.4%. This procedure was repeated for all samples described in Section 8.2.1 and summarised in Table 8.1.

8.3 Results and discussion

Using the methodology outlined in Section 8.2.2, signal intensity was measured during gravitational gel collapse as a function of sample height, H, and radial position, r, here denoted $S(H, r)$. Figure 8.3 shows the resulting 2D intensity images of a non-gelling sample, where $\Phi = 0.15$ and $1 - b_2 = 4.41$, that phase separates into coexisting gas and liquid phases with time. Immediately after homogenisation, it can be seen in Fig. 8.3(a) that $S(H, r)$ is almost independent of H and r, with a mean signal intensity of 0.71. Note that inhomogeneities in the B_0 and B_1 magnetic fields, introduced in Chapter 2, are responsible for the local fluctuations in $S(H, r)$ observed in Fig. 8.3(a). However, $S(H, r)$ becomes dependent on H during phase separation but remains independent of r. In Fig. 8.3(b), acquired 105 min after homogenisation, a sharp transition in $S(H, r)$ is observed at the gas-liquid interface; above the gas-liquid interface, the mean signal intensity of the gas phase is 0.79, whilst below the interface, the mean signal intensity of the liquid phase is 0.68. This interface propagates down the sample, as shown in Figs. 8.3(c) and (d) after 205 and 405 min, respectively, as the mean gas phase signal intensity increases from 0.71 to 0.84 and the mean signal intensity of the liquid phase decreases from 0.71 to 0.48. Since the inhomogeneities in B_0 and B_1 are not expected to change significantly over the experimental time scale, a comparison of the $S(H, r)$ data with identical data obtained for pure *cis*-decalin was used to determine the solvent volume fraction, Φ_S, as a function of H, r, and t, denoted $\Phi_S(H, r, t)$. The Φ_S data obtained are then converted to Φ, where $\Phi(H, r, t) + \Phi_S(H, r, t) = 1$, with Φ accurate to $\pm 2.4\%$, as described in Section 8.2.2.

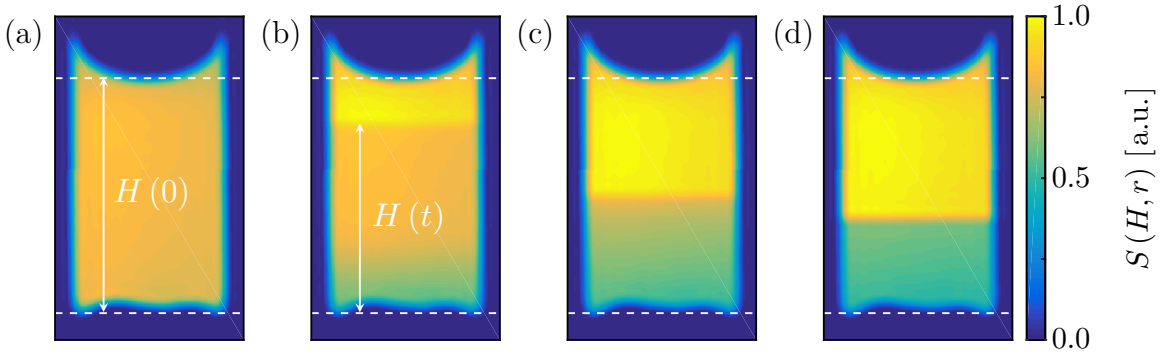

Fig. 8.3: 2D MR intensity images of a colloid-polymer mixture phase separating, with $\Phi = 0.15$ and $1 - b_2 = 4.41$, at (a) 5, (b) 105, (c) 205, and (d) 405 min after homogenisation. Initial height, $H(0)$, and time-dependent interface height, $H(t)$, are as defined. Note that $\xi = 0.06$.

This Section is arranged as follows. Firstly, $H(t)$ data are determined digitally as a function of r using a Sobel edge-finding algorithm. These data are discussed, providing insights into the origins of sudden collapse, with latency periods and rates of sudden collapse then calculated from the $H(r,t)$ data and reported in (Φ, b_2)-space. Secondly, Φ data are determined as a function of H, r, and t to investigate rearrangements of the space-spanning network with time. From $\Phi(H,r,t)$ data, the origins of the dense clusters introduced in Section 8.1 are considered. Finally, $H(r,t)$ and $\Phi(H,r,t)$ data are used to suggest a mechanism of gravitational gel collapse.

8.3.1 Time-dependent interface height

The origins of sudden collapse

Figure 8.4 shows 2D $H(r,t)$ data for three samples, with (a) $\Phi = 0.15$ and $1 - b_2 = 13.2$, (c) $\Phi = 0.15$ and $1 - b_2 = 4810$, and (e) $\Phi = 0.30$ and $1 - b_2 = 7.68$. As expected, $H(r,t)$ is dependent on t and demonstrates latency, sudden collapse, and compaction behaviour characteristic of the sample under study. Immediately after homogenisation, $H(r,t)$ is observed to be dependent on r due to the meniscus, decreasing from a maximum at the wall to a minimum at the centre of the sample, *i.e.* at $r = 0\,\text{mm}$. During latency, $H(t)$ decreases with time at the wall but is independent of t at $r = 0\,\text{mm}$ such that, at the onset of sudden collapse and during compaction, $H(r,t)$ is approximately independent of r. Interestingly, the $H(r,t)$ data appear to be practically symmetrical about $r = 0\,\text{mm}$ and suggest that gravitational gel collapse originates from the top of the meniscus before propagating into the centre of the sample.

The dependence of $H(r,t)$ on both r and t is presented more clearly in Figs. 8.4(b), (d), and (f), which show $H(t)$ profiles, extracted from the corresponding $H(r,t)$ data at radial positions of 4, 2, and 0 mm. As expected, the samples under study demonstrate three distinct types of gravitational gel collapse depending on both Φ and $1 - b_2$; namely regimes A, B, and C. These findings are consistent with previous work [15,17]. Such regimes were previously discussed in detail in Chapter 7 and will be introduced here for completeness. Regime A gravitational gel collapse is characterised by a latency period of less than 3 min. An example of regime A gravitational gel collapse is shown in Fig. 8.4(b), showing an initial linear sudden collapse followed by a stretched exponential at compaction. In contrast, regime B gravitational gel collapse is characterised by a latency period of greater than 3 min, as shown in Fig. 8.4(d), and demonstrates a linear

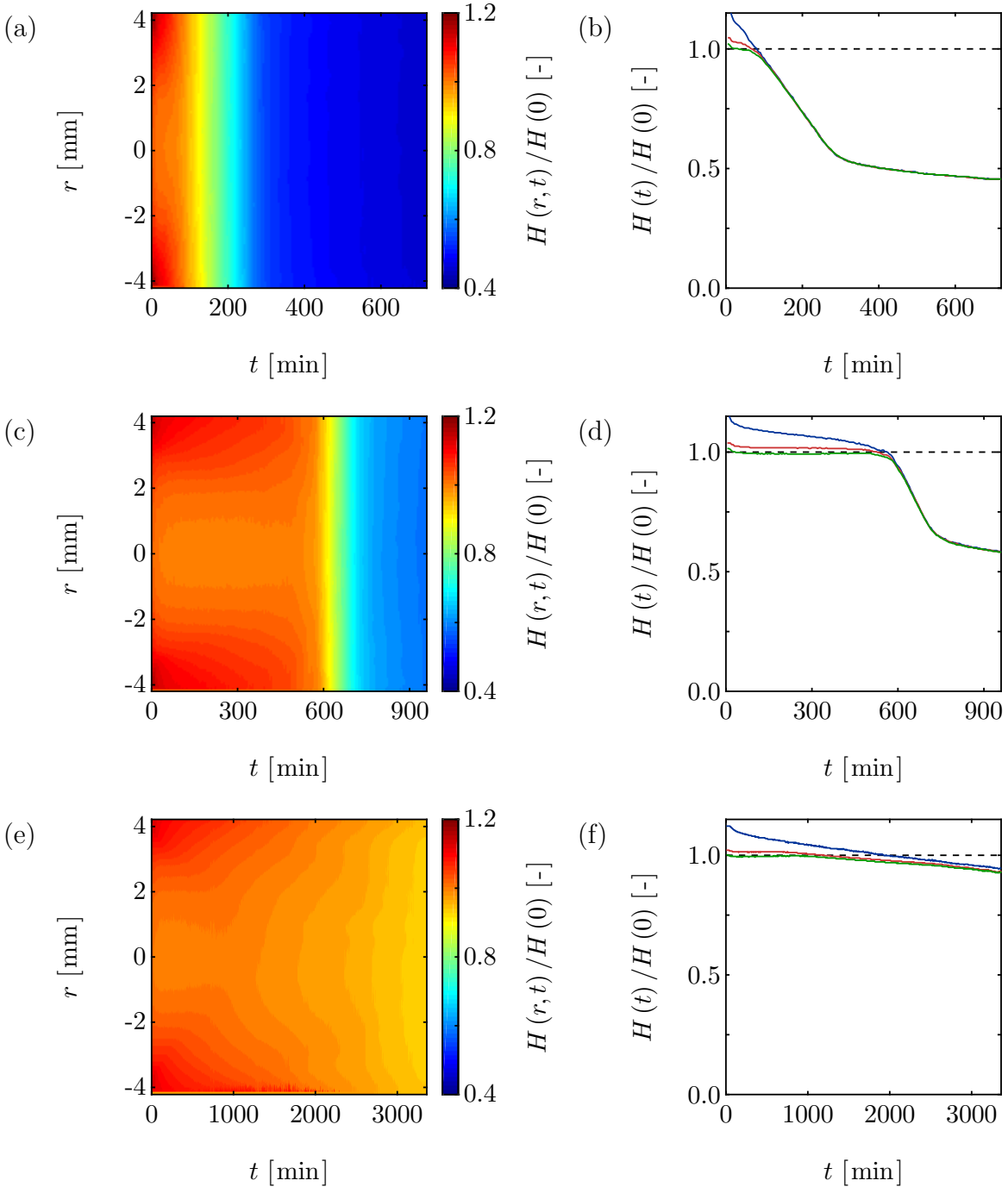

Fig. 8.4: The evolution of $H(r)$ with time for three samples, with (a) $\Phi = 0.15$ and $1 - b_2 = 13.2$, (c) $\Phi = 0.15$ and $1 - b_2 = 4810$, and (e) $\Phi = 0.30$ and $1 - b_2 = 7.68$. In all cases, $\xi = 0.06$. Also shown are the (b,d,f) corresponding $H(t)$ profiles extracted from $H(r,t)$ at r of (—) 4, (—) 2, and (—) 0 mm. The samples are expected to demonstrate regime A, B, and C gravitational gel collapse, respectively.

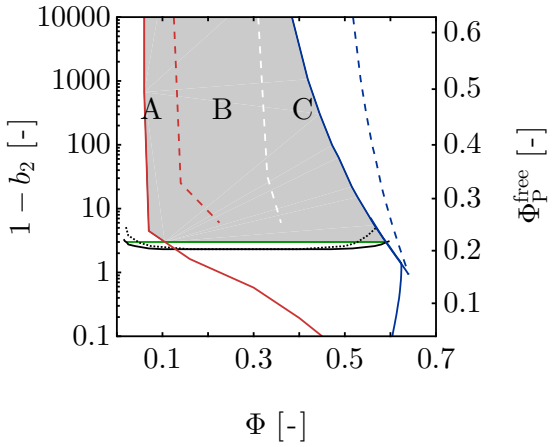

Fig. 8.5: The equilibrium phase and gelation state diagram, shown for mixtures of non-crystallising colloids and non-adsorbing polymers demonstrating regime A, B, and C gravitational collapse. The predicted gelation region in the absence of gravity is shaded. In the presence of gravity, the actual (- - -) glass transition and (- - -) percolation lines are expected to lie to the right of those determined using (—) MCT mapped to simulations and (—) simulations, respectively, as indicated.

dependence with time during sudden collapse followed by a stretched exponential during compaction. Unlike A and B, regime C gravitational gel collapse demonstrates an absence of sudden collapse, with a latency period followed immediately by a stretched exponential compaction. An example of regime C gravitational gel collapse is shown in Fig. 8.4(f). Such behaviour has been attributed to the increase in yield stress, τ_0, associated with increasing Φ [18]. The equilibrium phase and gelation state diagram, obtained in Chapter 7 using a combination of ED-BD and MD simulations and visual observations, is included in Fig. 8.5 and shows regimes A, B, and C in (Φ, b_2)-space.

Sudden collapse dynamics

Using the $H(r,t)$ data, the duration of the latency period, t_l, was measured in (Φ, b_2)-space. For each sample, t_l was determined as a function of r by measuring the time at which $H(r,t)/H(0)$ decreased to less than 1.0. The t_l values reported are equal to the mean of the spatially-resolved t_l values, with the uncertainties equal to the standard deviation. As reported in previous work [11,13,19], t_l increases with increasing Φ_P^{free}. Kilfoil *et al.* [13] accurately described the relationship between t_l and Φ_P^{free} using

$$t_l \propto \exp\left[\Psi \Phi_P^{free}\right], \tag{8.10}$$

where Ψ is a Φ-dependent parameter, although alternative expressions have also been proposed [11,19]. Figure 8.6(a) shows t_l as a function of Φ_P^{free} at Φ of 0.15 and 0.30. For $\Phi = 0.15$ and $\xi = 0.06$, an increase in t_l from 48.9±6.7 to 561±16 min is observed as Φ_P is increased from 0.19 to 0.48, corresponding to an increase in Φ_P^{free} from 0.24 to 0.59. This trend was expected. According to Eq. (8.2), an increase in Φ_P^{free} is responsible for an increase in $1 - b_2$ and a space-spanning network increasingly capable of supporting its own weight. Likewise, for a fixed $\Phi_P = 0.29$, the increase in $1 - b_2$ associated with an increase in Φ from 0.15 to 0.30, as given by Eqs. (8.3) to (8.7), is seen to cause an increase in t_l from 82.6±5.6 to 87 000±8800 min and an increase in Ψ from 7.7 to 23, as obtained through non-linear least squares (NLLS) regression of Eq. (8.10) to the t_l data. A decrease in ξ also causes a decrease in t_l due to a decrease in Φ_P^{free}.

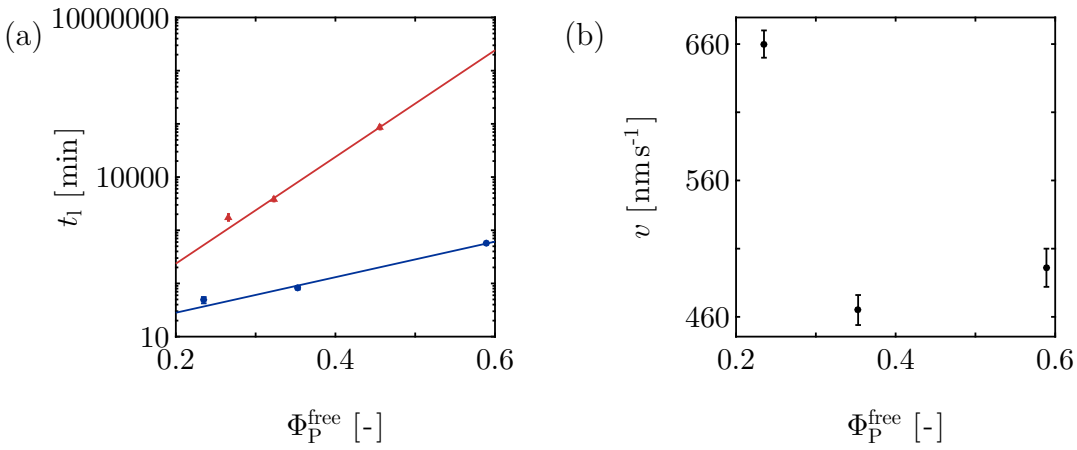

Fig. 8.6: Plots to demonstrate the relationship between (a) t_l and Φ_P^{free} for Φ of (—) 0.15 and (—) 0.30, and (b) v and Φ_P^{free} for $\Phi = 0.15$. In all cases, $\xi = 0.06$. The solid lines show the NLLS regression of Eq. (8.10) to the experimental t_l data.

The rate of sudden collapse, v, was quantified as a function of r through the linear least squares (LLS) of a straight line to the experimental $H(r,t)$ data over an appropriate time scale. Values of v reported correspond to the mean of the spatially-resolved v values and the uncertainties are equal to the standard deviation. Figure 8.6(b) shows v as a function of Φ_P^{free} for $\Phi = 0.15$ and $\xi = 0.06$. It is seen that v changes as Φ_P^{free} is increased, initially decreasing before subsequently increasing. Previous work by Kilfoil *et al.* [13] has suggested that v decreases with increasing Φ_P^{free}. However, the estimation of a trend in v with Φ_P^{free} is difficult in this case due to the limited data available, thus requiring further work.

8.3.2 Volume fraction

The origins of rapid sedimentation

In Section 8.2.2, a method was described to enable the spatio-temporal measurement of Φ. Figure 8.7 shows corresponding $\Phi(H, r)$ data for the non-gelling sample shown previously in Fig. 8.3. Immediately after homogenisation, it can be observed in Fig. 8.7(a) that $\Phi(H, r)$ is independent of position, with a mean Φ of 0.15. However, $\Phi(H, r)$ becomes dependent on position during phase separation into coexisting gas and liquid phases. Figure 8.7(b), acquired 105 min after homogenisation, shows a sharp transition in $\Phi(H, r)$ at the gas-liquid interface; above the gas-liquid interface, the mean Φ of the gas phase is 0.00, whilst below the interface, the mean Φ of the liquid phase is 0.20. This interface propagates down the sample, as shown in Figs. 8.7(c) and (d) after 205 and 405 min, respectively, as the mean Φ of the gas phase decreases from 0.15 to 0.00 and the mean Φ of the liquid phase increases from 0.15 to 0.40.

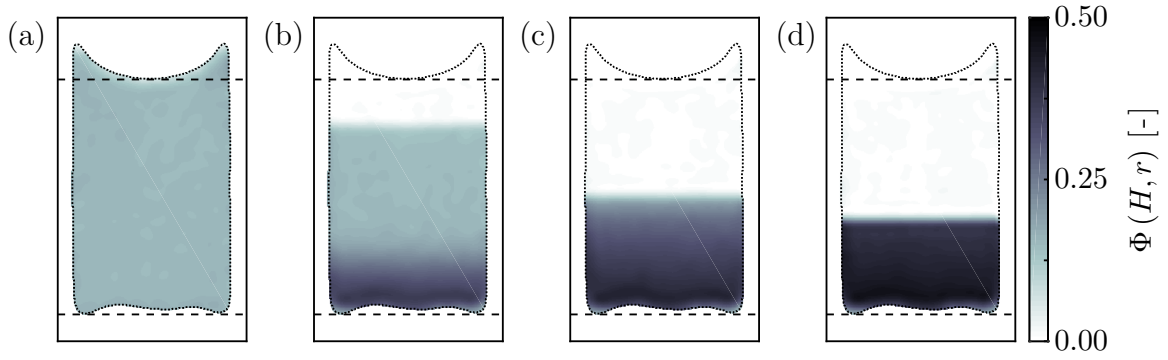

Fig. 8.7: 2D $\Phi(H, r)$ data acquired during the phase separation of a colloid-polymer mixture, with $\Phi = 0.15$ and $1 - b_2 = 4.41$, at (a) 5, (b) 105, (c) 205, and (d) 405 min after homogenisation. The dashed lines represent $H(0)$, as defined in Fig. 8.3, and the bottom of the sample. Note that $\xi = 0.06$. Dotted lines show the edge of the sample.

A 3D dataset was then generated for each sample investigated, with Fig. 8.8 showing $\Phi(H, t)$ at r of 4 and 0 mm for three samples, where (a) $\Phi = 0.15$ and $1 - b_2 = 13.2$, (c) $\Phi = 0.15$ and $1 - b_2 = 4810$, and (e) $\Phi = 0.30$ and $1 - b_2 = 7.68$. As was expected, these samples show regime A, B, and C gravitational gel collapse, respectively. From the $\Phi(H, t)$ data shown in Figs. 8.8(a) and (b), regime A gravitational gel collapse can be observed to proceed homogeneously; a high Φ region propagates upwards through the sample, whilst a very low Φ region propagates downwards. This behaviour appears

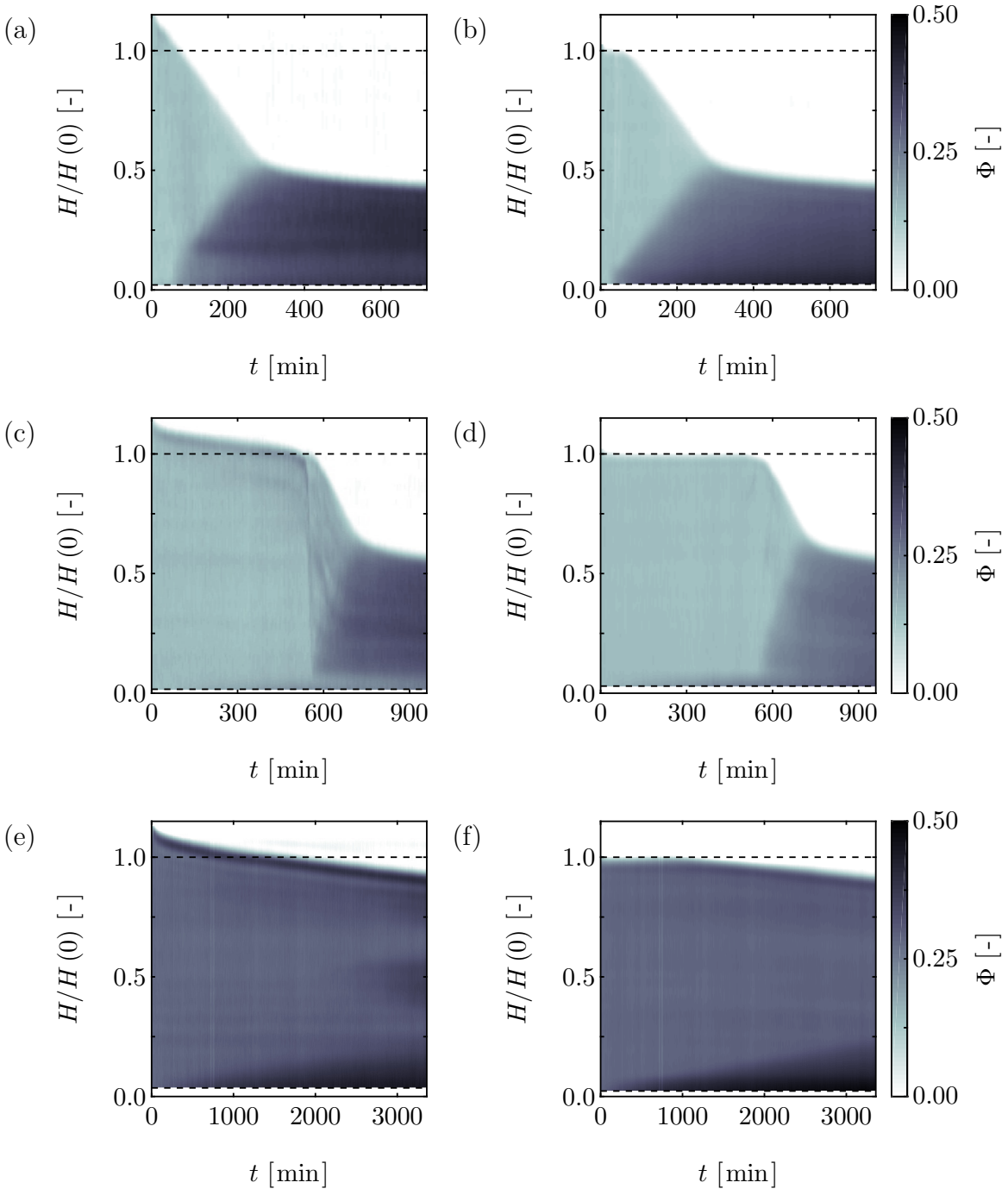

Fig. 8.8: The evolution of $\Phi(H)$ with time shown for three samples at $r = 4\,\mathrm{mm}$, with (a) $\Phi = 0.15$ and $1 - b_2 = 13.2$, (c) $\Phi = 0.15$ and $1 - b_2 = 4810$, and (e) $\Phi = 0.30$ and $1 - b_2 = 7.68$. In all cases, $\xi = 0.06$. Also shown are the (b,d,f) corresponding $\Phi(H, t)$ data at $r = 0\,\mathrm{mm}$. The samples are expected to demonstrate regime A, B, and C gravitational gel collapse, respectively.

to be almost independent of r. In contrast, regime B gravitational gel collapse is shown in Figs. 8.8(c) and (d) to proceed heterogeneously. Such gel collapse is typically divided into three distinct regions; namely a foot, leg, and column [15]. The slow compaction of the sample during the latency period causes a high Φ foot to develop with time at the very bottom of the sample. During sudden collapse at 560±5 min, an intermediate Φ leg is formed above the foot due to collapse of the space-spanning network in the low Φ column. The low Φ column ceases to exist at the onset of compaction at 750±5 min. Interestingly, rapid sedimentation of a dense cluster in Fig. 8.8(c) at 540±5 min appears to initiate sudden collapse of the space-spanning network, an observation consistent with the results acquired using 1D MR imaging described in Chapter 7. Furthermore, the absence of a dense cluster in Fig. 8.8(d) suggests that cluster formation depends on r. Unlike regimes A and B, regime C gravitational gel collapse is shown in Figs. 8.8(e) and (f) to demonstrate an absence of sudden collapse. Although the formation of dense clusters can be observed in Fig. 8.8(e), these clusters do not sediment rapidly. These observations imply that this behaviour is Φ and $1 - b_2$ dependent. The sudden collapse of samples in regimes A and B will now be investigated further.

Figures 8.9 and 8.10 show $\Phi\,(H, r)$ data at 5 and 10 min intervals before and after the onset of sudden collapse for samples demonstrating regime A and B gravitational gel collapse, respectively. Interestingly, the formation and rapid sedimentation of clusters is observed in both samples, suggesting that the origins of gravitational gel collapse are independent of the sample under study. In particular, Fig. 8.9 shows $\Phi\,(H, r)$ data between 20 and 75 min. Note that the height of the gas-liquid interface decreases with time, in accordance with those results reported in Section 8.3.1. The clusters, formed at the gas-liquid interface adjacent to the wall by collapse of the space-spanning network in the meniscus, increase in size with time. At only 25 min after homogenisation, shown in Fig. 8.9(b), the clusters begin to detach from the gas-liquid interface where they are initially held due to the depletion effect, here detaching first at the right side of the sample and then at the left, before subsequently sedimenting. Following rapid sedimentation and during sudden collapse, the formation of low Φ vertical channels is observed in Figs. 8.9(d) to (h), acquired 35 to 55 min after homogenisation, consistent with those observations made by Poon [14], Starrs [9], and Secchi *et al.* [15]. High Φ vertical channels are also observed in Figs. 8.9(b) to (d). For completeness, it is noted that Φ decreases from 0.15 to 0.11 in the low Φ channels, whilst increasing to 0.17 in the high Φ channels. It has previously been hypothesised that these vertical channels facilitate the movement of solvent upwards, initiating sudden collapse.

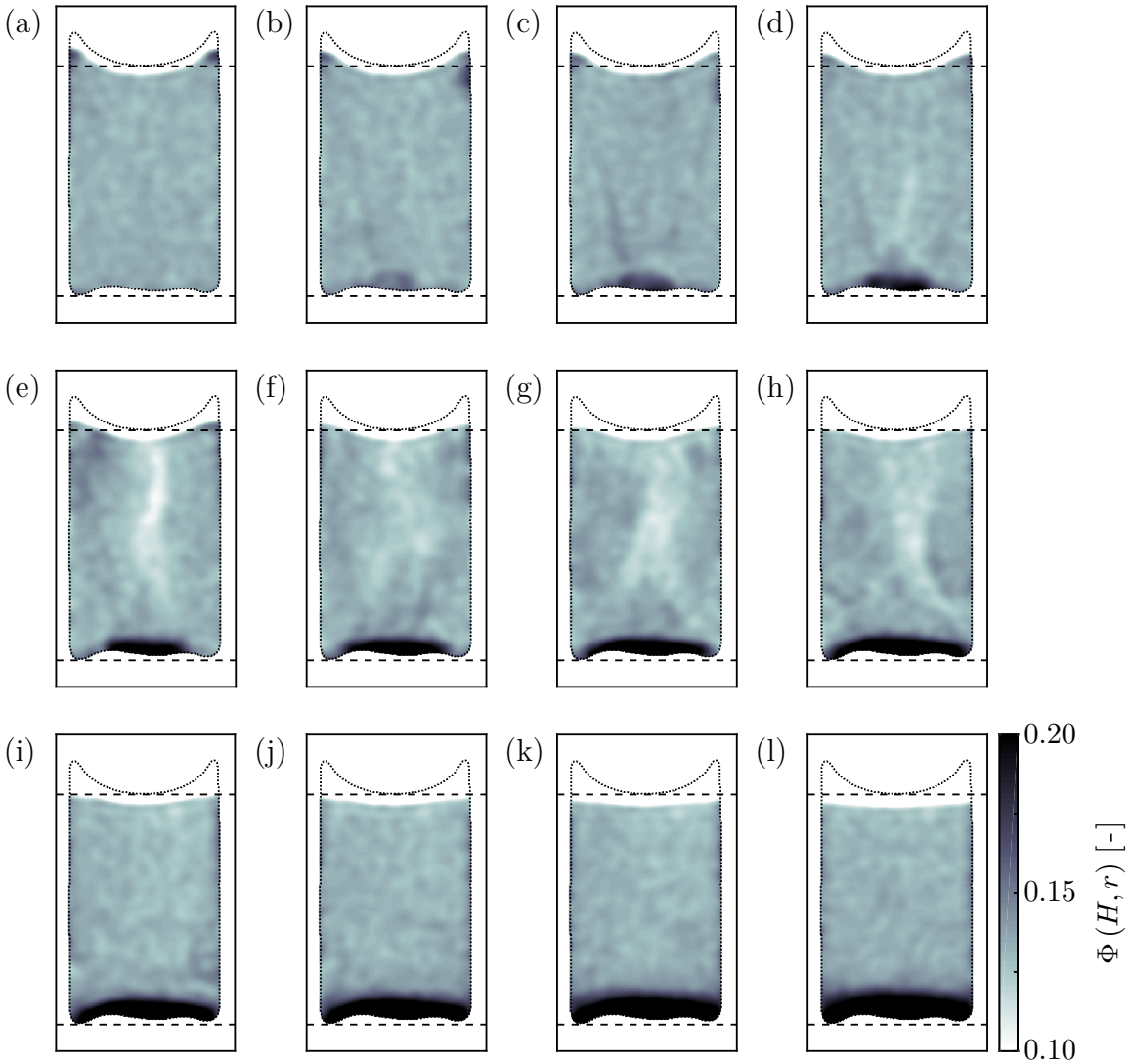

Fig. 8.9: 2D $\Phi\left(H, r\right)$ data acquired during the gravitational collapse of a colloidal gel, with $\Phi = 0.15$ and $1 - b_2 = 13.2$, at (a) 20, (b) 25, (c) 30, (d) 35, (e) 40, (f) 45, (g) 50, (h) 55, (i) 60, (j) 65, (k) 70, and (l) 75 min after homogenisation. The dashed lines represent $H\left(0\right)$, as defined in Fig. 8.3, and the bottom of the sample. Note that $\xi = 0.06$ and the dotted lines show the edge of the sample.

Considering now Fig. 8.10, showing $\Phi\left(H, r\right)$ data acquired between 510 and 620 min for a sample demonstrating regime B gravitational gel collapse, rapid sedimentation of the clusters occurs at 540 min, much later than was observed in Fig. 8.9 for a sample demonstrating regime A gravitational gel collapse. The clusters are also much larger in size, a possible explanation for which is provided in Section 8.3.3. It is interesting to note that Φ of these clusters is not constant, as was assumed in Section 7.3.2, but

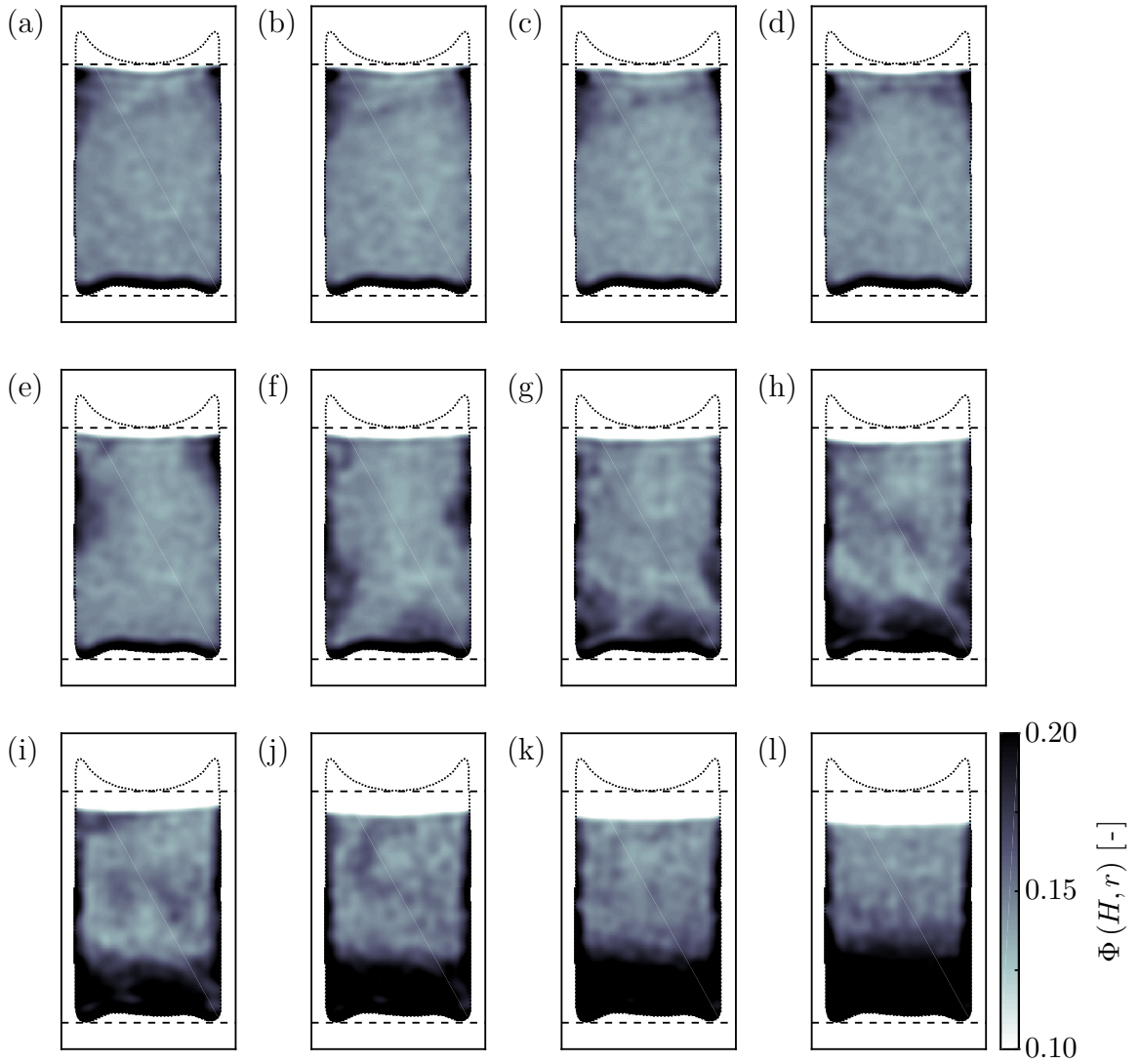

Fig. 8.10: 2D $\Phi\left(H, r\right)$ data acquired during the gravitational collapse of a colloidal gel, with $\Phi = 0.15$ and $1 - b_2 = 4810$, at (a) 510, (b) 520, (c) 530, (d) 540, (e) 550, (f) 560, (g) 570, (h) 580, (i) 590, (j) 600, (k) 610, and (l) 620 min after homogenisation. The dashed lines represent $H\left(0\right)$, as defined in Fig. 8.3, and the bottom of the sample. Note that $\xi = 0.06$ and the dotted lines show the edge of the sample.

increases with decreasing radius; $\Phi = 0.15$ at the edge of the cluster, whilst $\Phi = 0.20$ at the centre. After detaching from the gas-liquid interface, first at the left side of the sample and then at the right, rapid sedimentation of these clusters, shown in Figs. 8.10(e) to (h) at 550 to 580 min after homogenisation, proceeds with $v = 8.1 \pm 0.1\,\mu\mathrm{m\,s^{-1}}$. This is over an order of magnitude greater than during sudden collapse. In the absence of polymer, the sample phase separates without cluster formation.

Rapid sedimentation dynamics

In Chapter 7, the force due to gravity associated with a spherical cluster of N colloids, and theoretical diameter d_N, was assumed to equal that due to the yield stress of the colloidal gel. This assumption was used to determine that a theoretical cluster size of 38 µm at Φ^{rcp}, *i.e.* Φ at RCP, is sufficient to overcome τ_0. Note that the gravitational stress associated with a cluster, τ_N, is given by

$$\tau_N = \frac{2}{3}\Delta\rho a_{\text{G}} d_N \Phi, \tag{8.11}$$

where a_{G} is the acceleration due to gravity. The 3D $\Phi(H, r, t)$ data obtained are used in this Chapter to enable the direct determination of d_N of these clusters (if a spherical cluster shape is assumed). Since Φ within these clusters was spatially-dependent, the centre of the cluster was determined and Φ quantified as a function of radial position, r_N, with $d_N/2$ equal to the average r_N at which Φ had decreased to 0.15.

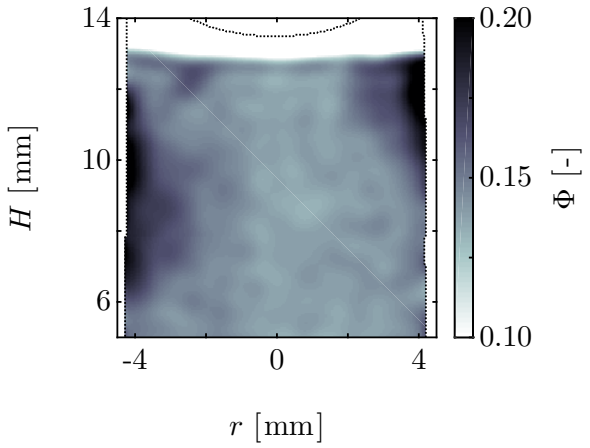

Fig. 8.11: 2D $\Phi(H, r)$ data showing cluster formation at the left side of the sample shown in Fig. 8.10, with $\Phi = 0.15$ and $1 - b_2 = 4810$, at 550 min after homogenisation. Note that $\xi = 0.06$ and the growth of a cluster at the right side of the sample can also be observed. The dotted line shows the edge of the sample.

Figure 8.11 shows the cluster formed at the left side of the sample in Fig. 8.10(e), with the formation of a cluster at the right of the sample also seen. The corresponding $\Phi(r_N)$ profile indicates that Φ is inversely proportional to r_N, decreasing from 0.20 at $r_N = 0.0$ mm to 0.15 at $r_N = 1.6$ mm such that $d_N = 3.2$ mm. Therefore, τ_N is more

accurately quantified using

$$\tau_N = \frac{16\Delta\rho a_{\mathrm{G}}}{d_N^2} \int_0^{d_N/2} \Phi\left(r_N\right) r_N^2 \, \mathrm{d}r_N, \tag{8.12}$$

which, for the experimentally-observed cluster, estimates $\tau_N = 860 \pm 60\,\mathrm{mPa}$, with the uncertainty representative of the error in Φ due to T_2-weighting. This is over an order of magnitude greater than τ_0 of the sample under study, estimated as 20 mPa using conventional rheometry, which suggests that τ_N is sufficient to overcome τ_0. Note that although only one cluster is considered at one point in time in this discussion, namely the cluster formed at the left of the sample at 550 min after homogenisation, analysis could also be performed on all clusters over the duration of gravitational gel collapse. Such analysis would enable the number of clusters and the size and Φ distributions of clusters to be investigated as a function of time.

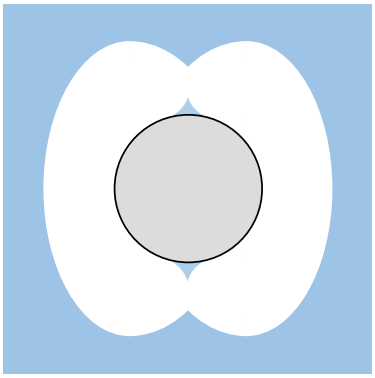

Fig. 8.12: A schematic representation of the flow surrounding a (◎) moving particle in a yield stress fluid, showing the (○) yielded (liquid) and (●) unyielded (solid) regions. Adapted from Beris *et al.* [20]. The particle is moving downwards.

The relationship between the force due to gravity and that due to the yield stress, in terms of τ_N and τ_0, respectively, was previously quantified by Beris *et al.* [20] using the dimensionless yield stress parameter, O, given by

$$O = \frac{2\tau_0}{\tau_N}, \tag{8.13}$$

which, for the experimentally-observed cluster, suggests O equals 0.046 ± 0.003. A value

of O of less than unity is expected since a cluster must yield a finite volume of space-spanning network during sedimentation, as shown schematically in Fig. 8.12; the size of the yielded region decreases to 0 as O tends to 1 and increases to infinity as O tends to 0. For fluids demonstrating yield stress behaviour, the sedimentation of a single particle will occur only if O is less than a critical O, denoted O_c. Previous works, using a number of yield stress fluids [21–23], have suggested that O_c ranges from 0.14 to 0.39 for polymeric fluids. Such polymeric fluids include the Carbopol 940-in-water solutions investigated in Chapter 5. However, more recent experiments by Emady *et al.* [24] have shown that $O_\mathrm{c} = 0.050$ for colloidal gels, with the decrease in O_c when compared to polymeric fluids attributed to rearrangements of the space-spanning network which act to strengthen the network immediately below the cluster [25]. Therefore, O calculated using the estimate of τ_N, determined from the 2D $\Phi\left(H, r\right)$ data reported in this Chapter, is just less than the O_c reported by Emady *et al.* [24] for colloidal gels. Whilst O_c might be expected to be sample-dependent, the excellent agreement between O_c and O is encouraging and suggests that a cluster of size 3.2 mm is not unrealistic. Further work is required to estimate O_c of the colloidal gels under study before more accurate conclusions can be made.

Equating the drag force, F_D, given in the first instance by Stokes' law [26] as

$$F_\mathrm{D} = 3\pi\eta d_N v, \tag{8.14}$$

where η is the shear viscosity, with the force due to gravity, F_G, given by

$$F_\mathrm{G} = 4\pi\Delta\rho a_\mathrm{G} \int_0^{d_N/2} \Phi\left(r_N\right) r_N^2 \,\mathrm{d}r_N, \tag{8.15}$$

was used to estimate the theoretical v of the experimentally-observed cluster. Using this initial approach, a theoretical $v = 23 \pm 1\,\mathrm{mm\,s^{-1}}$ was determined for $d_N = 3.2\,\mathrm{mm}$ and $\eta = 10\,\mathrm{mPa\,s}$. Note that the rheology of the colloidal gels, including both τ_0 and η, was characterised by collaborators at the University of Edinburgh using conventional rheometry. The theoretical v is over three orders of magnitude greater than the experimental $v = 8.1 \pm 0.1\,\mathrm{\mu m\,s^{-1}}$. Investigation of the discrepancy between the theoretical and experimental v requires consideration of the assumptions associated with Stokes' law. In particular, it is known that F_D can only be described using Eq. (8.14) for

- **Creeping flow.** Reynolds numbers, Re, much less than 1 are assumed.
- **Newtonian behaviour.** Any non-Newtonian behaviour must be considered.
- **Dilute dispersions.** Unhindered settling is assumed, *i.e.* very low Φ and absent of wall effects.
- **Spherical particles.** The clusters are assumed spherical, smooth, and rigid.

Whilst creeping flow can be assumed, since Re = 0.002, Newtonian behaviour cannot be assumed due to the non-Newtonian behaviour of the sample under study; colloidal gels demonstrate yield stress behaviour and their rheology can be described [27] using the Herschel–Bulkley model [28], given by

$$\tau\left(\dot{\gamma}\right) = \tau_0 + K\dot{\gamma}^n, \tag{8.16}$$

where τ and $\dot{\gamma}$ represent the shear stress and shear rate, respectively, K is the consistency factor, and n the flow behaviour index. The interested reader is directed towards Section 1.2 for a more complete introduction to the Herschel–Bulkley model. To this end, Merkak *et al.* [22] derived an expression for a smooth particle, given by

$$F_\mathrm{D} = \frac{\pi}{2}\frac{\tau_0 d_N^2}{O_\mathrm{c}} + 6\pi\tau_0^{\frac{n}{n+1}} K^{\frac{1}{n+1}} d_N^{\frac{n+2}{n+1}} v^{\frac{n}{n+1}} + 3\pi K d_N^{2-n} v^n o\left(n\right), \tag{8.17}$$

to describe F_D for a Herschel–Bulkley fluid, where $o\left(n\right)$ is a function of n and represents shear-thinning effects [29]. Assuming $n = 0.9$, consistent with Pandey and Conrad [27] and for which $o\left(n\right) = 1.14$, and $O_\mathrm{c} = 0.05$, as described previously, the theoretical v of the experimentally-observed cluster reduces to $74 \pm 22\,\mu\mathrm{m\,s^{-1}}$. Note that for Newtonian rheology, $n = 1.0$ and $\tau_0 = 0\,\mathrm{mPa}$ with Eq. (8.17) reducing to Eq. (8.14).

Although the non-Newtonian behaviour of the sample under study has been considered, the theoretical v remains an order of magnitude greater than the experimental v. It is, thus, necessary to consider the effect of Φ; as Φ increases, interactions restrict the motion of a single particle and cause a reduction in v. Richardson and Zaki [30] proposed a correction to account for so-called hindered settling, given by

$$v_\mathrm{H} = v\left(1 - \Phi\right)^c, \tag{8.18}$$

where v_{H} is the hindered v and c is a system-specific parameter, given by

$$c = 4.65 + \frac{19.5 d_N}{d_{\mathrm{t}}} \tag{8.19}$$

for $\mathrm{Re} < 0.2$, where d_{t} is the i.d. of the MR tube. Whilst other corrections are known to exist that account for both hydrodynamic interactions and the depletion potential [31–33], these are accurate only for dilute systems, typically $\Phi < 0.03$, and weak depletion potentials, *i.e.* where $1 - b_2$ is small [34]. In contrast, the theoretical correction given by Eqs. (8.18) and (8.19) has previously demonstrated good agreement with experimental observations up to $\Phi = 0.40$ for colloidal dispersions [35]. At $\Phi = 0.15$ and $d_N = 3.2\,\mathrm{mm}$, the theoretical v_{H} of the experimentally-observed cluster reduces to $11 \pm 3\,\mu\mathrm{m\,s^{-1}}$. Thus, despite the assumptions made, an experimental $v = 8.1 \pm 0.1\,\mu\mathrm{m\,s^{-1}}$ for a cluster size of 3.2 mm does not seem unrealistic. The theoretical estimation of v could be improved with knowledge of the three-dimensional (3D) shape of the cluster, perhaps using one of the fast 3D MR imaging techniques reviewed in Section 3.1. In the previous analysis the clusters were assumed spherical, although a torus might be expected in 3D due to the symmetry associated with collapse of the space-spanning network in the meniscus of a cylindrical geometry. Further improvements may also follow if diffusion is taken into account, with a tendency for clusters to prevent sedimentation and reduce v [36], or if wall effects are considered.

8.3.3 The origins of gravitational gel collapse

In Section 8.3.1, $H(r,t)$ was measured for three samples demonstrating regime A, B, and C gravitational gel collapse. For all samples, $H(t)$ is independent of t at the centre of the sample during the latency period, but dependent on t at the wall. This suggests that gravitational gel collapse is initiated by processes at the top of the sample; the space-spanning network detaches from the meniscus where it is initially held due to the depletion effect. Slow compaction during the latency period of a sample demonstrating regime B gravitational gel collapse, as indicated by the high Φ foot at the bottom of the sample in Fig. 8.10(a), may make this process possible. Collapse of detached space-spanning network in the meniscus leads to the formation of clusters at the walls that grow with time, as shown in the $\Phi(H,r,t)$ data in Fig. 8.10. The tendency of a sample to form clusters depends on Φ, which determines the frequency of colloidal collisions

and thus the rate of cluster formation, $1 - b_2$, and the Péclet number, Pe, given by

$$\mathrm{Pe} = \frac{1}{12}\frac{\pi\Delta\rho a_{\mathrm{G}} d^4}{kT}, \tag{8.20}$$

which quantifies the relative gravitational and thermal motion. According to Eq. (8.20), gravitational motion dominates at high Pe, with a tendency for the sample to phase separate; a space-spanning network might never form if Pe is too high [37]. Thermal motion dominates at low Pe, with cluster formation likely depending on $1 - b_2$; thermal motion is sufficient to overcome the interaction potential at low $1 - b_2$, whilst, at high $1 - b_2$, clusters are formed. A detailed discussion of the competition between Pe and $1 - b_2$ will not be provided here, with the interested reader directed towards the journal article of Whitmer and Luijten [38]. For completeness, Pe is 0.028 and 3.64 for single colloids with d of 0.652 and 2.20 µm, respectively.

The growth of clusters at the top of the sample depends on τ_0 and O_{c}, with the space-spanning network able to support only a finite τ_N. At low τ_0, the space-spanning network is unable to support the weight of large clusters, since $O < O_{\mathrm{c}}$ even for small clusters. In contrast, a space-spanning network with high τ_0 can support the weight of these large clusters. Therefore, whilst such clusters are formed and may continue to grow, rapid sedimentation of these clusters might never occur providing $O > O_{\mathrm{c}}$. This is observed for regime C gels, which demonstrate only slow compaction behaviour that can be described as poroelastic compression where the rate of compaction decreases exponentially with time [39]. Those samples with intermediate τ_0, *i.e.* where $O \approx O_{\mathrm{c}}$, are of particular importance and display sudden collapse after a latency period. The samples investigated in Figs. 8.9 and 8.10, demonstrating regime A and B gravitational gel collapse, respectively, both show the formation of clusters at the top of the sample. Since τ_0 varies with Φ and $\Phi_{\mathrm{P}}^{\mathrm{free}}$ according to

$$\tau_0 = u\left(\left(\frac{\Phi_{\mathrm{P}}^{\mathrm{free}}}{\Phi_{\mathrm{P}}^{\mathrm{glass}}}\right)^{\varepsilon} - 1\right)\left(\left(\frac{\Phi}{\Phi^{\mathrm{perc}}}\right)^{\chi} - 1\right), \tag{8.21}$$

where Φ^{perc} is the minimum Φ required for percolation at a given $\Phi_{\mathrm{P}}^{\mathrm{free}}$ or $1 - b_2$, $\Phi_{\mathrm{P}}^{\mathrm{glass}}$ is the Φ_{P} at the glass transition line for a particular Φ, u is the scale setting constant of the samples under study, and ε and χ take average values of 2.5 and 4.0, respectively,

τ_0 is expected to increase with an increase in both Φ and $\Phi_{\mathrm{P}}^{\mathrm{free}}$. All other things being equal, an increase in $\Phi_{\mathrm{P}}^{\mathrm{free}}$ from 0.35 to 0.59 causes a five-fold increase in τ_0. Therefore, the sample investigated in regime B can support a τ_N up to 5 times greater than the sample in regime A; it is seen that a small cluster with low Φ is sufficient to overcome τ_0 in Fig. 8.9, whilst a larger cluster with a higher Φ is required in Fig. 8.10. For this reason, it is here hypothesised that the greatest difference between regime A, B, and C gravitational gel collapse is the time at which O_{c} exceeds O; in the case of regime A gels, $O_{\mathrm{c}} > O$ is reached almost instantaneously, whilst $O_{\mathrm{c}} > O$ might never be reached over experimental time scales for regime C gels. This hypothesis is supported by the experimentally-acquired $\Phi\left(H, r, t\right)$ data, showing the initial slow compaction of both regime B and regime C gels. A more detailed investigation of the sudden collapse that ensues requires further experimental study, although the presence of vertical channels in Fig. 8.9 suggests that local increases in permeability are responsible for the flow of solvent upwards, consistent with previous work [9,14,15].

8.4 Conclusions

In this Chapter, 2D MR imaging has successfully been applied for investigation of the gravitational collapse of a model colloid-polymer mixture, consisting of PMMA colloids dispersed in a *cis*-decalin solvent with PS polymer, over a wide range of (Φ, b_2)-space. In particular, the height of the sharp interface between the coexisting gas and liquid phases was determined as a function of r and t to investigate sudden collapse dynamics, whilst a quantitative measurement of Φ as a function of H, r and t was used to probe cluster formation and rapid sedimentation.

It has been shown, from $H\left(r, t\right)$ data, that gravitational gel collapse begins at the top of the sample, within the meniscus. Using the $H\left(r, t\right)$ data obtained, three distinct types of gravitational gel collapse were observed, namely regimes A, B, and C, consistent with previous work using 1D MR imaging reported in Chapter 7. Furthermore, the study of the collapse dynamics indicated an increase in v during sudden collapse with $\Phi_{\mathrm{P}}^{\mathrm{free}}$, as expected. It was observed, from $\Phi\left(H, r, t\right)$ data, that clusters of colloids with comparatively high Φ are formed within the meniscus during the latency period in all regimes. This represents a significant step forward, extending previous work utilising 1D MR imaging described in Chapter 7, and is, to the best of the author's knowledge, the first observation of the formation of such clusters in colloidal gels in 2D. For sam-

ples demonstrating regime A and B gravitational gel collapse, these clusters sediment rapidly and initiate sudden collapse. Interestingly, although rapid sedimentation is not seen over experimental time scales, the formation of high Φ clusters is also observed for a sample in regime C. Preliminary analysis of the size and velocity of a cluster during rapid sedimentation indicates that such behaviour is τ_0-dependent, with τ_0 known to increase strongly with both Φ and $\Phi_{\mathrm{P}}^{\mathrm{free}}$. Therefore, for samples demonstrating regime A and B gravitational gel collapse, with low-to-intermediate Φ, a low-to-intermediate τ_0 is expected, sufficient to support the weight of small-to-medium sized clusters. In contrast, high Φ samples demonstrating regime C gravitational gel collapse are capable of supporting the weight of even larger clusters.

For completeness, it is noted that, for a sample in regime B, a cluster of size 3.2 mm was observed to sediment at $v = 8.1 \pm 0.1\,\mu\mathrm{m\,s^{-1}}$. A more accurate estimate of v can be obtained through the measurement of n and O_{c} of the sample under study. Whether gravitational gel collapse is initiated at the top of the sample due to the meniscus or the depletion interaction with the wall remains the subject of future work.

8.5 References

[1] Verwey, E.J.W. and Overbeek, J.T.G., *Theory of the stability of lyophobic colloids: The interaction of sol particles having an electric double layer*, Elsevier, New York, US, 1948.

[2] Sciortino, F., Tartaglia, P. and Zaccarelli, E., 2003, Evidence of a higher-order singularity in dense short-ranged attractive colloids. *Phys. Rev. Lett.*, **91**, 268301.

[3] Zaccarelli, E. and Poon, W.C.K., 2009, Colloidal glasses and gels: the interplay of bonding and caging. *Proc. Natl. Acad. Sci.*, **106**, 15203–15208.

[4] Noro, M.G. and Frenkel, D., 2000, Extended corresponding-states behavior for particles with variable range attractions. *J. Chem. Phys.*, **113**, 2941–2944.

[5] Bergenholtz, J., Poon, W.C.K. and Fuchs, M., 2003, Gelation in model colloid-polymer mixtures. *Langmuir*, **19**, 4493–4503.

[6] Lekkerkerker, H.N.W., Poon, W.C.K., Pusey, P.N., Stroobants, A. and Warren, P.B., 1992, Phase behaviour of colloid + polymer mixtures. *Europhys. Lett.*, **20**, 559–564.

[7] Ruzicka, B., Zaccarelli, E., Zulian, L., Sztucki, M., Moussaïd, A., Narayanan, T. and Sciortino, F., 2011, Observation of empty liquids and equilibrium gels in a colloidal clay. *Nat. Mater.*, **10**, 56–60.

[8] Poon, W.C.K., Pirie, A.D. and Pusey, P.N., 1995, Gelation in colloid-polymer mixtures. *Faraday Discuss.*, **101**, 65–76.

[9] Starrs, L., Poon, W.C.K., Hibberd, D.J. and Robins, M.M., 2002, Collapse of transient gels in colloid-polymer mixtures. *J. Phys. Condens. Matter*, **14**, 2485–2505.

[10] Huh, J.Y., Lynch, M.L. and Furst, E.M., 2011, Poroelastic consolidation in the phase separation of vesicle-polymer suspensions. *Ind. Eng. Chem. Res.*, **50**, 78–84.

[11] Gopalakrishnan, V., Schweizer, K.S. and Zukoski, C.F., 2006, Linking single particle rearrangements to delayed collapse times in transient depletion gels. *J. Phys. Condens. Matter*, **18**, 11531–11550.

[12] Bartlett, P., Teece, L.J. and Faers, M.A., 2012, Sudden collapse of a colloidal gel. *Phys. Rev. E*, **85**, 021404.

[13] Kilfoil, M.L., Pashkovski, E.E., Masters, J.A. and Weitz, D.A., 2003, Dynamics of weakly aggregated colloidal particles. *Philos. Trans. R. Soc. Lond. A*, **361**, 753–766.

[14] Poon, W.C.K., Starrs, L., Meeker, S.P., Moussaïd, A., Evans, R.M.L., Pusey, P.N. and Robins, M.M., 1999, Delayed sedimentation of transient gels in colloid-polymer mixtures: dark-field observation, rheology and dynamic light scattering studies. *Faraday Discuss.*, **112**, 143–154.

[15] Secchi, E., Buzzaccaro, S. and Piazza, R., 2014, Time-evolution scenarios for short-range depletion gels subjected to the gravitational stress. *Soft Matter*, **10**, 5296–5310.

[16] Napper, D.H., 1977, Steric stabilization. *J. Colloid Interf. Sci.*, **58**, 390–407.

[17] Harich, R., Blythe, T.W., Hermes, M., Zaccarelli, E., Sederman, A.J., Gladden, L.F. and Poon, W.C.K., 2016, Gravitational collapse of depletion-induced colloidal gels. *Soft Matter*, **12**, 4300–4308.

[18] Kobelev, V. and Schweizer, K.S., 2005, Nonlinear elasticity and yielding of depletion gels. *J. Chem. Phys.*, **123**, 164902.

[19] Blijdenstein, T.B.J., Linden, E.D. van, Vliet, T. van and Aken, G.A. van, 2004, Scaling behavior of delayed demixing, rheology, and microstructure of emulsions flocculated by depletion and bridging. *Langmuir*, **20**, 11321–11328.

[20] Beris, A.N., Tsamopoulos, J.A., Armstrong, R.C. and Brown, R.A., 1985, Creeping motion of a sphere through a Bingham plastic. *J. Fluid Mech.*, **158**, 219–244.

[21] Atapattu, D.D., Chhabra, R.P. and Uhlherr, P.H.T., 1995, Creeping sphere motion in Herschel–Bulkley fluids: flow field and drag. *J. Non-Newton. Fluid Mech.*, **59**, 245–265.

[22] Merkak, O., Jossic, L. and Magnin, A., 2006, Spheres and interactions between spheres moving at very low velocities in a yield stress fluid. *J. Non-Newton. Fluid Mech.*, **133**, 99–108.

[23] Tabuteau, H., Coussot, P. and Bruyn, J.. de, 2007, Drag force on a sphere in steady motion through a yield-stress fluid. *J. Rheol.*, **51**, 125–137.

[24] Emady, H., Caggioni, M. and Spicer, P., 2013, Colloidal microstructure effects on particle sedimentation in yield stress fluids. *J. Rheol.*, **57**, 1761–1772.

[25] Rich, J.P., Lammerding, J., McKinley, G.H. and Doyle, P.S., 2011, Nonlinear microrheology of an aging, yield stress fluid using magnetic. *Soft Matter*, **7**, 9933–9943.

[26] Stokes, G.G., *Mathematical and Physical Papers*, Cambridge University Press, Cambridge, GB, 1880.

[27] Pandey, R. and Conrad, J.C., 2012, Effects of attraction strength on microchannel flow of colloid-polymer depletion mixtures. *Soft Matter*, **8**, 10695–10703.

[28] Herschel, W.H. and Bulkley, R., 1926, Konsistenzmessungen von gummi-benz-ollösungen. *Kolloid-Z.*, **39**, 291–300.

[29] Gu, D. and Tanner, R.I., 1985, The drag on a sphere in a power-law fluid. *J. Non-Newton. Fluid Mech.*, **17**, 1–12.

[30] Richardson, J.F. and Zaki, W.N., 1997, Sedimentation and fluidisation: part I. *Trans. Inst. Chem. Eng.*, **75**, S82–S100.

[31] Steinour, H.H., 1944, Rate of sedimentation: concentrated flocculated suspensions of powders. *Ind. Eng. Chem.*, **36**, 901–907.

[32] Batchelor, G.K., 1972, Sedimentation in a dilute dispersion of spheres. *J. Fluid Mech.*, **52**, 245–268.

[33] Jansen, J.W., Kruif, C.G. de and Vrij, A., 1986, Attractions in sterically stabilized silica dispersions. *J. Colloid Interf. Sci.*, **114**, 501–504.

[34] Moncho-Jordá, A., Louis, A.A. and Padding, J.T., 2010, Effects of interparticle attractions on colloidal sedimentation. *Phys. Rev. Lett.*, **104**, 068301.

[35] Tuinier, R. and Kruif, C.G. de, 1999, Phase separation, creaming, and network formation of oil-in-water emulsions induced by an exocellular polysaccharide. *J. Colloid Interf. Sci.*, **218**, 201–210.

[36] Abel, J.S., Stangle, G.C., Schilling, C.H. and Aksay, I.A., 1994, Sedimentation in flocculating colloidal suspensions. *J. Mater. Res.*, **9**, 451–461.

[37] Kim, J.M., Fang, J., Eberle, A.P.R., Castañeda-Priego, R. and Wagner, N.J., 2013, Gel transition in adhesive hard-sphere colloidal dispersions: the role of gravitational effects. *Phys. Rev. Lett.*, **110**, 208302.

[38] Whitmer, J.K. and Luijten, E., 2011, Sedimentation of aggregating colloids. *J. Chem. Phys.*, **134**, 034510.

[39] Buscall, R. and White, L.R., 1987, The consolidation of concentrated suspensions. *J. Chem. Soc., Faraday Trans. 1*, **83**, 873–891.

Chapter 9

Conclusions and future work

Magnetic resonance (MR) is a highly versatile technique that enables the non-invasive study of structure, reaction, and dynamics without limitation on optical opacity. For this reason, MR has great potential for use in industrial applications; from the *in situ* study of unit operations, for the development and refinement of theoretical models, to the optimisation of product properties. In this thesis, MR has been applied with the aim of optimising product properties in two different areas:

- **Rheological characterisation.** Many industrial processes, particularly those involving flow [1], are sensitive to only small changes in process fluid rheology. To this end, the online, or inline, application of MR for the rheological characterisation of process fluids in real-time has been investigated, and novel processing strategies developed, to enable improved process control and optimisation. This has been demonstrated on a washcoating slurry used by Johnson Matthey in the manufacture of catalysts for exhaust emissions control.
- **Gravitational collapse of colloidal gels.** Many industrial products are formulated as colloidal gels, a space-spanning network of attractive particles. However, colloidal gels are known to undergo gravitational collapse after a latency period, limiting the shelf-life of many products. To this end, MR has been applied offline to provide insights into the origins of gravitational gel collapse with the aim of improving understanding and extending the shelf-life of products.

This Chapter is arranged as follows. Firstly, the conclusions presented in the experimental Chapters of this thesis are summarised. Secondly, suggestions for future work in this field are described.

9.1 Conclusions

The use of magnetic resonance (MR) in industrial applications can be divided into two categories; namely the *in situ* study of unit operations and the optimisation of product properties. This thesis was concerned only with the latter category, with a particular focus on the rheological characterisation of process fluids and the gravitational collapse of colloidal gels.

Many industrial processes are sensitive to process fluid rheology, particularly those involving flow, *e.g.* spraying, mixing, and coating [1]. For example, during the manufacture of catalysed diesel particulate filters (cDPFs) by Johnson Matthey (JM), as used in the automotive industry for the abatement of harmful exhaust gas emissions, a catalyst-containing washcoating slurry is applied to the surface of bare wall-flow or flow-through monoliths in a process called washcoating. This is subsequently dried [2]. Whilst catalyst uniformity is known to be sensitive to the drying process, the catalyst thickness is affected by the rheology of the washcoating slurry. The rheological characterisation of such slurries is typically performed offline using conventional rheometry methods. However, an online, or inline, method is sought for real-time process control and optimisation. Until recently, MR has been an unlikely choice for this application due to the requirement of high field strength, expensive, superconducting magnet technology. However, recent developments in low field strength, inexpensive, permanent magnet technology mean that the online, or inline, application of MR in industry can now be realised.

Since the washcoating slurry was expected to demonstrate non-Newtonian rheology, experiments were performed initially on model fluids with increasing complexity. Chapter 3 reports initial experiments performed on model power-law fluids; namely xanthan gum-in-water solutions. In the first instance, MR flow imaging was employed to acquire two-dimensional (2D) velocity images across a pipe geometry during flow. Regression of an analytical expression describing the velocity of a power-law fluid as a function of flow behaviour index, n, was then used to provide an estimate of n describing the fluid under study. The estimates of n obtained were accurate to within 5% of those values obtained using conventional rheometry. However, the implementation of MR flow imaging requires expensive three-axis gradient hardware, is time-consuming, and can be problematic when using low-field MR due to a reduction in signal-to-noise ratio (SNR). To this end, a volume-averaged, high SNR approach utilising pulsed field gradient (PFG) MR was developed, requiring only single-axis gradient hardware, with

a cumulant analysis of the signal in q-space, $S(q)$, then providing an estimate of n describing the rheology of the fluid under study. Direct analysis of $S(q)$ data negates the requirement of Fourier transform and removes the associated sampling restrictions and long acquisition times. The numerical simulations indicated the cumulant MR approach to be robust to reduced sampling and noisy data, with only 8 points required to be sampled in q-space for SNR = 100 to provide estimates of n accurate to within 5% of the ground truth. Experimental study on xanthan gum-in-water solutions revealed that an estimate of n can be obtained with the same accuracy using only 4 sampled q-space points if SNR $>$ 1000. This corresponds to a reduction in acquisition time of 94% when compared to the acquisition of an MR flow image using a single spin echo sequence. Furthermore, the high SNR associated with this approach has potential for application on low-field MR hardware. This approach could also be combined with a measurement of pressure drop to determine the consistency factor, K.

The cumulant MR approach developed was then extended in Chapter 4 to Herschel–Bulkley rheology, characterised by n, K, and yield stress, τ_0. Numerical simulations indicated that the cumulant MR approach was unable to unambiguously estimate the Herschel–Bulkley rheological parameters due to the interdependence that exists between the parameters n, K, and τ_0. For this reason, errors in the estimates of n and τ_0 of up to 50% were typical and an alternative approach sought. To this end, a Bayesian analysis approach was developed, again using PFG MR, whereby a Bayesian analysis of $S(q)$ data was utilised to obtain a posterior probability distribution describing the probability of parameters n and τ_0. Note that $S(q)$ was required to be sampled over a wider range of q-space for the purpose of Bayesian analysis. Numerical simulations indicated that the Bayesian MR approach was able to unambiguously estimate the Herschel–Bulkley rheological parameters, with typical errors in the estimates of n and τ_0 of 0.50% when utilising complex $S(q)$ data, over two orders of magnitude less than the corresponding errors associated with the cumulant MR approach. These simulations were then extended in Chapter 5 to investigate the robustness of the proposed Bayesian MR approach to reduced sampling and noisy data. It was demonstrated that 16 points are required to be sampled in q-space for SNR = 100 to provide estimates of n accurate to within 5% of the ground truth. Furthermore, experimental study on model Herschel–Bulkley fluids, namely Carbopol 940-in-water solutions, revealed that an accurate estimate of n and τ_0 can be obtained with the same accuracy using only 8 sampled q-space points if SNR $>$ 1000. This corresponds to a reduction in acquisition time of 88% when compared to the acquisition of an MR flow image. Measurement of

the pressure drop was also performed to enable the estimation of K and recovery of the full flow curve. Interestingly, differences between the estimates of the Herschel–Bulkley parameters obtained using MR methods and those obtained using conventional rheometry were observed and attributed to the shear-history dependent nature of Carbopol 940-in-water solutions and the different geometries used. Note that the Bayesian MR approach outlined is applicable to Herschel–Bulkley, power-law, and Newtonian fluids, but may be readily extended to different constitutive equations.

The suitability of the Bayesian MR approach developed in Chapter 4 for the study of real process fluids was investigated in Chapter 6 through experimental study on an alumina-in-acetic acid slurry provided by JM and used in the manufacture of cDPFs. It has been shown that the rheology of such slurries is sensitive to the pH value, solids concentration, and particle size distribution (PSD) of the milled alumina [3]. To this end, the Bayesian MR approach was used to characterise the rheology of the alumina-in-acetic acid washcoating slurry online during the addition of acetic acid. A reduction in pH from 6.0 to 5.0 was observed to cause only a small change in n and τ_0, although K decreased by an order of magnitude. The rheological parameters n and τ_0 estimated using Bayesian MR were accurate to within 13% of those parameters obtained using MR flow imaging and $<8\%$ of those determined using conventional rheometry. This implies that the Bayesian MR approach can be used online to accurately characterise the rheology of real process fluids, potentially using low-field MR hardware. Note that sedimentation, observed to occur over the experimental time scale, did not affect the rheological characterisation using MR rheometry in this instance.

In Chapters 7 and 8, MR was applied to study the gravitational collapse of colloidal gels. Many industrial products are colloidal dispersions formulated as colloidal gels; a space-spanning network of attractive particles with a yield stress high enough to support the weight of the particles but low enough to be overcome in use to provide flowability. However, such colloidal gels have been shown to undergo sudden collapse after a latency period, causing phase separation into coexisting gas (colloid-poor) and liquid (colloid-rich) phases and limiting the shelf-life of many products. Despite this, gravitational gel collapse remains poorly understood, with a detailed understanding of its origins and mechanisms of both fundamental interest and practical importance. To this end, a multifaceted approach using molecular dynamics (MD) simulations, visual observations, and MR imaging was employed in Chapter 7 to investigate the gravitational collapse of a model colloidal gel; namely a colloid-polymer mixture consisting of poly(methyl methacrylate) colloids dispersed in a *cis*-decalin solvent with polystyrene

polymers. In particular, collaborators at the University of Edinburgh performed MD simulations in the absence of gravity and hydrodynamics to quantify an equilibrium phase and gelation state diagram as a function of both colloid volume fraction, Φ, and interaction strength, $1 - b_2$. This was then compared to the experimental phase diagram obtained using visual observations, performed by collaborators at the University of Edinburgh, and it was demonstrated that gravitational gel collapse is gravity-driven. Interestingly, measurement of the height of the sharp interface between the coexisting gas and liquid phases revealed the presence of three distinct types of gravitational gel collapse depending on Φ and $1 - b_2$; regime A, demonstrating sudden collapse followed by slow compaction, regime B, with an initial latency period, and regime C, showing a latency period and slow compaction. Using one-dimensional (1D) MR imaging, the author of this thesis characterised Φ as a function of sample height during gravitational gel collapse. The formation of a cluster of colloids at the top of the sample during the latency period was observed for colloidal gels in regimes B and C. For colloidal gels in regime B, these clusters subsequently sedimented rapidly, initiating sudden collapse. The absence of rapid sedimentation for a colloidal gel in regime C was attributed to τ_0, which increases strongly as Φ and $1 - b_2$ are increased. These findings represent a significant step forward in understanding the origins and mechanisms of gravitational gel collapse.

The gravitational collapse of colloidal gels was investigated further in Chapter 8. Using 2D MR imaging, Φ was characterised as a function of both sample height and radial position during the gravitational gel collapse. Measurement of the height of the sharp interface between the coexisting gas and liquid phases revealed that gravitational gel collapse begins within the meniscus. Interestingly, corresponding Φ data indicate the subsequent formation of clusters in these regions for colloidal gels in regimes A, B, and C. Whether gravitational gel collapse is initiated in this region due to the meniscus or due to the depletion interaction with the wall is unclear and requires further work. For colloidal gels in regimes A and B, these clusters grow in size and sediment rapidly, initiating sudden collapse. This is, to the author's best knowledge, the first observation of the formation and sedimentation of such clusters in 2D. For colloidal gels in regime C, rapid sedimentation of such clusters did not occur. Therefore, it is here hypothesised that gravitational gel collapse is τ_0-dependent; colloidal gels in regimes A and B possess a low-to-intermediate τ_0 and can support the weight of small-to-medium sized clusters, whilst colloidal gels in regime C have a high τ_0 and so the rapid sedimentation of these clusters might never occur. This is consistent with observations made in Chapter 7.

9.2 Future work

The Bayesian MR approach developed in Chapter 4 and applied in Chapters 5 and 6 enables the rheological characterisation of real process fluids over a time scale of up to 88% less than spin echo MR flow imaging. Furthermore, the numerical simulations reported in Chapter 5 indicated that a robust measurement of the Herschel–Bulkley rheological parameters can be obtained with SNR as low as 100. This new approach is, therefore, ideally suited to low-field, permanent magnet hardware. However, since such hardware was unavailable, experiments presented in this thesis were performed on an intermediate-field, superconducting magnet. For this reason, the implementation of the Bayesian MR approach on low-field MR hardware must remain the subject of future work. If implemented successfully, this approach has potential for use in a large number of industrial applications, providing an online, or inline, measurement of rheology. This data could be used for process control and optimisation, thus facilitating a transition from batch to continuous processing. Alternatively, the high temporal resolution of the Bayesian MR approach could be exploited in the laboratory to study the thixotropy or anti-thixotropy of process fluids.

Considering only the application of low-field MR to the characterisation of alumina-in-acetic acid slurry, MR should be viewed not as a unique tool but a versatile toolkit. It is known that the rheology of these slurries is dependent not only on the pH value, but also on the solids concentration and PSD. Therefore, the Bayesian MR approach developed in Chapter 4 for rheological characterisation could be interleaved with measurements of the PSD—perhaps utilising an alternative Bayesian MR approach previously described by Holland *et al.* [4], Ross *et al.* [5], and Ziovas *et al.* [6]—and solids concentration. A series of such measurements online, or inline, would enable complete characterisation of the alumina-in-acetic acid slurry under study. Such data could be used in an industrial application, to provide information necessary for process control and optimisation, or in the laboratory, for investigation into the relationship between the PSD, solids concentration, and the rheology of the washcoating slurry.

In Chapters 7 and 8, MR imaging was applied to provide insights into the origins and mechanisms of the gravitational collapse of colloidal gels. It was demonstrated that the rapid sedimentation of clusters of colloids, formed within the meniscus during the latency period, appears to initiate sudden collapse. However, whether the formation of clusters in this region is caused by the meniscus or the depletion interaction with the wall remains unclear. To this end, the experimental procedures outlined in Chapter 7

could be applied and extended to samples in which the meniscus has been removed. Alternatively, experiments could be performed using MR tubes with walls of increasing roughness to investigate wall effects directly. Depending on the outcome of these studies, the packaging or containers of industrial products formulated as colloidal gels could be altered to extend the shelf-life of such products.

The link from rapid sedimentation to sudden collapse is yet to be made, although the observation of vertical channels with low Φ during sudden collapse of a colloidal gel in regime A offers one hypothesis; the high permeability vertical channels facilitate the flow of solvent upwards and colloids downwards. This hypothesis could be tested using MR flow imaging. However, since velocities are expected to be very small, care must be taken to ensure that displacements due to coherent motion exceed those due to incoherent motion. This could be ensured through use of long flow contrast times, with displacement due to incoherent motion increasing with the square root of time, but that resulting from coherent motion increasing linearly with time. The long T_1 of the solvent would allow for long flow contrast times, although the short T_2 would need to be addressed by using a stimulated echo, as described in Section 2.1.4. This would provide further insights into the origins and mechanisms of sudden collapse.

9.3 References

[1] Collyer, A.A. and Clegg, D.W., *Rheological Measurement*, Springer, Dordrecht, NL, 1998.

[2] Nijhuis, T.A., Beers, A.E.W., Vergunst, T., Hoek, I., Kapteijn, F. and Moulijn, J.A., 2001, Preparation of monolithic catalysts. *Catal. Rev.*, **43**, 345–380.

[3] Adegbite, S.A., Ph.D. Thesis, University of Birmingham, GB, 2010.

[4] Holland, D.J., Blake, A., Tayler, A.B., Sederman, A.J. and Gladden, L.F., 2011, A Bayesian approach to characterising multi-phase flows using magnetic resonance: application to bubble flows. *J. Magn. Reson.*, **209**, 83–87.

[5] Ross, J.G., Holland, D.J., Blake, A., Sederman, A.J. and Gladden, L.F., 2012, Extending the use of Earth's field NMR using Bayesian methodology: application to particle sizing. *J. Magn. Reson.*, **222**, 44–52.

[6] Ziovas, K., Sederman, A.J., Gehin-Delval, C., Gunes, D.Z., Hughes, E. and Mantle, M.D., 2016, Rapid sphere sizing using a Bayesian analysis of reciprocal space imaging data. *J. Colloid Interf. Sci.*, **462**, 110–122.